Conversion of 2,3-butanediol over bifunctional catalysts

by

QUANXING ZHENG

B.S., Xiamen University, 2002
M.S., Xiamen University, 2005

AN ABSTRACT OF A DISSERTATION

submitted in partial fulfillment of the requirements for the degree

DOCTOR OF PHILOSOPHY

Department of Chemical Engineering
College of Engineering

KANSAS STATE UNIVERSITY
Manhattan, Kansas

2016

Abstract

In this study, Cu/ZSM-5 catalysts were used to catalyze the hydrodeoxygenation of 2,3-butanediol to butenes in a single reactor in the presence of hydrogen. The carbon selectivity of butenes increased with increasing SiO_2/Al_2O_3 ratio (lowering acidity of zeolite) and H_2/2,3-butanediol ratio. Cu/ZSM-5 with a SiO_2/Al_2O_3 ratio of 280 showed the best activity toward the production of butenes. On zeolite ZSM-5(280), the carbon selectivity of butenes increased with increasing copper loading and 19.2wt% of CuO showed the highest selectivity of butenes (maximum 71%). The optimal reaction temperature is around 250 ^{o}C. Experiments demonstrated that methyl ethyl ketone (MEK) and 2-methylpropanal are the intermediates in the conversion of 2,3-butanediol to butenes. The optimal performance toward the production of butene is the result of a balance between copper and acid catalytic functions.

Due to the functionalized nature of 2,3-butanediol, a variety of reactions can occur during the conversion of 2,3-butanediol, especially when multiple catalyst functionalities are present. To investigate the role of the metal (Cu) and acid sites in the process of reaction, the reaction kinetics for all major intermediate products (acetoin, MEK, 2-methylpropanal, 2-butanol and 2-methyl-1-propanol) were measured over Cu/ZSM-5(280), HZSM-5(280), and Cu/SiO_2 at 250 ^{o}C. The results showed that Cu is the active site for hydrogenation reactions, while the acidic sites on the zeolite are active for dehydration reactions. In addition, dehydration of alcohols over the zeolite is much faster than hydrogenation of ketone (MEK) and aldehyde (2-methylpropanal). A kinetic model employing Langmuir-Hinshelwood kinetics was constructed in order to predict 2,3-butanediol chemistry over Cu/ZSM-5(280). The goal of this model was to predict the trends for all species involved in the reactions. Reactions were assumed to occur on two sites (acid and metal sites) with competitive adsorption between all species on those sites.

Two different types of mesoporous materials (Al-MCM-48, Al-SBA-15) and hierarchical zeolite (meso-ZSM-5) were loaded with ~20wt% CuO and investigated in the conversion of 2,3-butanediol to butenes. The results showed that the existence of mesopores on the catalysts (Al-MCM-48 and Al-SBA-15 types) could decrease the selectivities of products from cracking reactions, especially $C_3^=$ and $C_5^=-C_7^=$ by comparison with the catalyst with ~20wt% CuO loaded on the regular HZSM-5(280); meanwhile, the selectivity of $C_8^=$ from oligomerization of butenes was found to increase with increasing pore size of the catalysts. With respect to Cu/meso-ZSM-

5(280) catalyst, it can be seen that the catalyst performs in a similar way to both Cu/ZSM-5(280) catalyst and mesoporous copper catalysts (Cu/Al-MCM-48 and Cu/Al-SBA-15) since both micropores (diameter of ~0.55 nm) and mesopores (pore size of ~23 nm) exist on meso-ZSM-5(280).

The results from Cu catalysts were compared with four other metal catalysts (Ni, Pd, Rh and Pt). It was found that Cu is not very active for hydrogenation of butenes, but is active for hydrogenation of carbonyl groups (C=O) to form hydroxyl groups (−OH). Pd, on the other hand, is active in further hydrogenating butenes and other unsaturated hydrocarbons. Both Ni and Rh catalysts are good for hydrogenation of olefins and cracking of heavy hydrocarbons; however, Rh is not as good as Ni for the hydrogenation of the carbonyl group (C=O) of MEK. In addition, Pt favors the formation of heavy aromatics such as 5-ethyl-1,2,3,4-tetrahydro-naphthalene, while Pd is active for the production of xylene.

Conversion of 2,3-butanediol over bifunctional catalysts

by

QUANXING ZHENG

B.S., Xiamen University, 2002
M.S., Xiamen University, 2005

A DISSERTATION

submitted in partial fulfillment of the requirements for the degree

DOCTOR OF PHILOSOPHY

Department of Chemical Engineering
College of Engineering

KANSAS STATE UNIVERSITY
Manhattan, Kansas

2016

Approved by:

Major Professor
Keith L. Hohn

Copyright

Abstract

In this study, Cu/ZSM-5 catalysts were used to catalyze the hydrodeoxygenation of 2,3-butanediol to butenes in a single reactor in the presence of hydrogen. The carbon selectivity of butenes increased with increasing SiO_2/Al_2O_3 ratio (lowering acidity of zeolite) and H_2/2,3-butanediol ratio. Cu/ZSM-5 with a SiO_2/Al_2O_3 ratio of 280 showed the best activity toward the production of butenes. On zeolite ZSM-5(280), the carbon selectivity of butenes increased with increasing copper loading and 19.2wt% of CuO showed the highest selectivity of butenes (maximum 71%). The optimal reaction temperature is around 250 ^{o}C. Experiments demonstrated that methyl ethyl ketone (MEK) and 2-methylpropanal are the intermediates in the conversion of 2,3-butanediol to butenes. The optimal performance toward the production of butene is the result of a balance between copper and acid catalytic functions.

Due to the functionalized nature of 2,3-butanediol, a variety of reactions can occur during the conversion of 2,3-butanediol, especially when multiple catalyst functionalities are present. To investigate the role of the metal (Cu) and acid sites in the process of reaction, the reaction kinetics for all major intermediate products (acetoin, MEK, 2-methylpropanal, 2-butanol and 2-methyl-1-propanol) were measured over Cu/ZSM-5(280), HZSM-5(280), and Cu/SiO$_2$ at 250 ^{o}C. The results showed that Cu is the active site for hydrogenation reactions, while the acidic sites on the zeolite are active for dehydration reactions. In addition, dehydration of alcohols over the zeolite is much faster than hydrogenation of ketone (MEK) and aldehyde (2-methylpropanal). A kinetic model employing Langmuir-Hinshelwood kinetics was constructed in order to predict 2,3-butanediol chemistry over Cu/ZSM-5(280). The goal of this model was to predict the trends for all species involved in the reactions. Reactions were assumed to occur on two sites (acid and metal sites) with competitive adsorption between all species on those sites.

Two different types of mesoporous materials (Al-MCM-48, Al-SBA-15) and hierarchical zeolite (meso-ZSM-5) were loaded with ~20wt% CuO and investigated in the conversion of 2,3-butanediol to butenes. The results showed that the existence of mesopores on the catalysts (Al-MCM-48 and Al-SBA-15 types) could decrease the selectivities of products from cracking reactions, especially $C_3^=$ and $C_5^=-C_7^=$ by comparison with the catalyst with ~20wt% CuO loaded on the regular HZSM-5(280); meanwhile, the selectivity of $C_8^=$ from oligomerization of butenes was found to increase with increasing pore size of the catalysts. With respect to Cu/meso-ZSM-

5(280) catalyst, it can be seen that the catalyst performs in a similar way to both Cu/ZSM-5(280) catalyst and mesoporous copper catalysts (Cu/Al-MCM-48 and Cu/Al-SBA-15) since both micropores (diameter of ~0.55 nm) and mesopores (pore size of ~23 nm) exist on meso-ZSM-5(280).

The results from Cu catalysts were compared with four other metal catalysts (Ni, Pd, Rh and Pt). It was found that Cu is not very active for hydrogenation of butenes, but is active for hydrogenation of carbonyl groups (C=O) to form hydroxyl groups (−OH). Pd, on the other hand, is active in further hydrogenating butenes and other unsaturated hydrocarbons. Both Ni and Rh catalysts are good for hydrogenation of olefins and cracking of heavy hydrocarbons; however, Rh is not as good as Ni for the hydrogenation of the carbonyl group (C=O) of MEK. In addition, Pt favors the formation of heavy aromatics such as 5-ethyl-1,2,3,4-tetrahydro-naphthalene, while Pd is active for the production of xylene.

Table of Contents

List of Figures

List of Tables

Acknowledgements

Dedication

This thesis is dedicated to my parents, my wife and children.

Chapter 1 - Introduction

As the crude oil reserves become increasingly deficient, there is a stringent need for processes that could produce hydrocarbons from renewable resources rather than petroleum [1–3]. Such processes could produce essentially the same product currently made in petroleum refineries, eliminating the need for modifications to vehicles or to the distribution infrastructure. Hence, the utilization of renewable resources guarantees a long-term supply of hydrocarbons even when the petroleum reserves are depleted sometime in the future. A number of routes for producing hydrocarbons from sustainable resources have been proposed [4]. These routes convert biomass-derived sugars to oxygenated intermediates, which are then upgraded to fuel-range hydrocarbons [5–8]. The key to developing a successful process of this nature is to select intermediate compounds that can be selectively produced from sugars, and can easily be converted to fuel-range hydrocarbons.

Recently, many chemicals, like 2,3-butanediol (2,3-BDO), could be produced biologically from renewable resources. A great deal of microorganism species, such as *Klebsiella oxytoca* [9–11], *Enterobacter aerogenes* [12], *Bacillus licheniformis* [13] and *Enterobacter cloacae* [14] have been investigated for fermentation of glucose and xylose, which can be obtained through hydrolysis of corn starch, to produce 2,3-butanediol. 2,3-butanediol (2,3-BDO) is an odorless, colorless and transparent liquid at normal temperature, which is widely used in chemical, food, fuel, aeronautical and other fields [15].

2,3-butanediol (2,3-BDO) can be used to produce methyl ethyl ketone (MEK)[16], which is the main dehydration product of 2,3-BDO. MEK can be used for resins, paints and other solvents. Further dehydration of 2,3-BDO yields 1,3-butadiene [17], which can be dimerized to produce the aromatic intermediate styrene by Diels-Alder reaction [18].

The goal of this research is to convert 2,3-butanediol to another valuable chemical, butene, which is a basic building block of fuels as well as many chemicals. As a precursor, butene can be converted to a variety of oligomers (dimer, trimer, tetramer,etc)[19,20], which can be further converted to saturated hydrocarbons through hydrogenation reactions. In this way, butene can serve as an intermediate to produce high-grade liquid fuel with specific types of saturated hydrocarbons [20,21].

1.1. Production of 2,3-butanediol from fermentation

Recently, 2,3-butanediol has attracted considerable attention because it can be produced via fermentation of sugars with a high productivity by using a variety of microorganisms, such as *Klebsiella oxytoca* [9–11,22], *Enterobacter aerogenes* [12], *Bacillus licheniformis* [13] and *Enterobacter cloacae* [14].

Ji et al. [9] developed two-stage agitation control strategy for efficient production of 2,3-butanediol via fermentation by *Klebsiella oxytoca*. In the first phase (15 h), higher agitation speed (300 rpm) was used to accelerate cell growth, during this period of time, glucose was mainly used for cell growth; in the second phase (after 15 h), lower agitation speed (200 rpm) was employed to enhance 2,3-butanediol production when glucose was mainly consumed for production of 2,3-butanediol. By using this strategy, he obtained a maximum 2,3-BDO concentration of 95.5g/L with productivity of 1.71g/L/h by fermentation of media containing 200g/L of glucose in a 3 L batch fermentor. In addition, they used an industrial medium containing urea as a sole nitrogen source to produce 2,3-butanediol through co-fermentation of glucose and xylose (wt/wt, 2:1) by *Klebsiella oxytoca* ME303, and a maximum yield of 2,3-butanediol and acetoin was 0.428 $g/g_{(glucose+xylose)}$, which was 85.6% of theoretical value [11].

Since 2,3-butanediol is the end-product of the "anaerobic" pathway, minimizing the oxygen supply may be favorable for the production of 2,3-butanediol. However, the oxygen supply rate is important because it determines the respiratory pathway, in which xylose is catabolized, but influences the "anaerobic" pathway for production of 2,3-butanediol at the same time. Jansen et al. [23] controlled the oxygen supply rate and the xylose concentration, and they obtained a final concentration of 2,3-BDO of 12.63g/L by fermentation of media containing 50g/L of xylose in a 7-L batch fermentor using *Klebsiella oxytoca* ATCC 8724.

Perego et al. [12] investigated the optimization of the operating conditions for 2,3-butanediol production by *Enterobacter aerogenes* in synthetic glucose solutions and also in food industry wastes. The results show that the optimal temperature is 39 ^{o}C and the optimal pH value is 6.0. In addition, they obtained the final 2,3-butanediol concentration of 33g/L by fermentation of a glucose solution with a starting concentration of 100g/L in 29.2 days. As for the different food industry wastes tested in the experiment, they found that the starch hydrolysate coming from corn transformation and whey from cheese manufacture had the best results based on the product yield and productivity. Perego et al. [13] also investigated the effects of carbon sources

(glucose, sucrose and cornstarch hydrolysate), temperature, inoculum size and starting substrate concentration on the production of 2,3-butanediol by *Bacillus licheniformis*. The result show that the highest 2,3-butanediol yield is 0.87 mol/mol and the average productivity (2,3-butanediol + acetoin) is 0.58 g/L/h from the fermentation of cornstarch hydrolysate at 37 ^{o}C with the pH of 6.0, inoculum size of 10 g/L, starting substrate concentration of 30 g/L. Saha and coworkers [14] obtained a yield of 2,3-BDO of 0.4g/g arabinose with a corresponding productivity of 0.63g/L/h by fermentation of media with an initial arabinose concentration of 50g/L by using *Enterobacter cloacae.*

In the past few years, many researchers have attempted to get butanol from fermentation [24]. Qureshi et al. [25] studied the production of butanol (acetone+butanol+ethanol, or ABE) via fermentation by *Clostridium beijerinckii*. The results showed that the ABE production from fermentation of 25g/L glucose and 25g/L xylose was 9.9 ± 0.4 and 9.6 ± 0.4 g/L, respectively. In addition, Qureshi et al. [26] also investigated the production of butanol (ABE) from wheat straw hydrolysate in batch cultures using *Clostridium beijerinckii* P260, and the ABE productivity was 0.63 g/L/h with a yield of 0.42g/g with the starting glucose concentration of 35 g/L. Yu et al. [27] investigated the production of butanol (ABE) from fermentation of sweet sorghum bagasse (total sugar 55g/L) via *Clostridium acetobutylicum* and final concentration of 19.21 g/L of ABE was obtained (butanol 9.34g, ethanol 2.5g and acetone 7.36g). Lu et al. [28] studied the butanol production from fermentation of concentrated cassava bagasse hydrolysate containing 584.4 g/L glucose via *Clostridium acetobutylicum* strain, and the yield of butanol was 0.23 g/g$_{glucose}$ with the productivity of 0.32 g/L/h. In contrast, 2,3-butanediol has more advantages than butanol to be the resource of biofuel, based on the selectivity and productivity of fermentation.

1.2. Dehydration of 2,3-butanediol to MEK and 1,3-butadiene

Dehydration of 2,3-BDO to methyl ethyl ketone (MEK) and 1,3-butadiene has been well studied, and occurs readily over a number of catalysts [16,22]. The first attempt was published in 1945. Winfield et al. studied the catalytic dehydration of 2,3-butanediol to 1,3-butadiene and methyl vinyl carbinol (3-buten-2-ol) over ThO_2 [29], and they found that ThO_2 can catalyzed the dehydration of 2,3-BDO to 3-buten-2-ol at a temperature little above 50 ^{o}C, which was then dehydrated to 1,3-butadiene. 1,3-butadiene can be dimerized to produce the aromatic intermediate styrene (Diels-Alder reaction) [18] and hydrogenated to butene.

Trans and Chambers [16] investigated dehydration of 2,3-butanediol (50g/L) to methyl ethyl ketone (MEK) over $HSO_3^-/SiO_2-Al_2O_3$ catalysts at 210 ^{o}C in the packed bed reactor. They found the catalysts with higher sulfonic groups had higher reaction activity. The results showed that the activity of the catalysts decreased over time. They attributed the deactivation of catalysts to the loss of sulfonic groups in the reaction, because they used hydrochloric acid (HCl) to regenerate the catalysts, which, however, did not improve the catalyst activity. In addition, they suggested that the catalysts could lose more external sulfonic groups than the internal ones during the dehydration reaction, indicating that the dehydration reaction in the packed bed reactor proceeded first with the external, then later with the internal sulfonic groups. Emerson and co-workers [30] used sulfuric acid to dehydrate 2,3-butanediol to MEK in the liquid phase The results showed that elevated temperature and higher concentration of acid were beneficial for conversion of 2,3-butanediol to MEK.

Bourns and Nicholls [31] investigated the effect of different combination of 2,3-butanediol/H_2O and MEK/H_2O feed rates on the dehydration of 2,3-butanediol in the gas phase over activated Morden bentonite. The results indicated that MEK was obtained with a yield of 86%, but only very small amounts of butadiene were produced when the dry 2,3-butanediol was passed over the catalysts. Butadiene yields were 0.8%, 2.0%, 4.1% and 6.7%, at 450 ^{o}C, 550 ^{o}C, 650 ^{o}C and 700 ^{o}C, respectively; and the yield of butadiene was increased when water vapour was used as a diluent. The yield was 18.8% when the 2,3-butanediol to H_2O molar ratio was 1:10.02, while the yield of butadiene increased to 25.3% when the 2,3-butanediol to H_2O molar ratio decreased to 1:44.95 at 700 ^{o}C. In the presence of water vapor, butadiene was formed in considerable quantities from both MEK and 2,3-butanediol (700 ^{o}C, 29.1% of the yield, MEK to H_2O molar ratio 1:13.7; 44.8% of the yield, MEK to H_2O ratio 1:39.9). Hence, they suggested that MEK was the intermediate in the conversion of 2,3-butanediol to butadiene.

Bucsi [32] investigated the transformation of diols over perfluorinated resinfulfonic acids (Nafion-H) in a fixed-bed reactor and compare the catalytic properties of Nafion-H and NaHX zeolite. The results showed that the conversion of 2,3-butanediol over Nafion-H at 175 ^{o}C was greater than that over NaHX at 250 ^{o}C (100% on Nafion-H vs. 59% on NaHX). They ascribed this to the stronger acidity of Nafion-H. In addition, the transformation of 2,3-butanediol yielded a very complex mixture of products via the pinacol rearrangement. The selectivity to 2-ethyl-2,4,5-trimethyl-1,3-dioxolane isomers and 4,5-dimethyl-2-propyl-1,3-dioxolane isomers over

Nafion-H at 125 ^{o}C was 43% and 13%, respectively; however, when the temperature was increased to 175 ^{o}C, the selectivity was decreased to 4% and 2% respectively. These cyclic ketals and acetals derived from the intermolecular dehydration of unreacted 2,3-butanediol with carbonyl compounds MEK or isobutyraldehyde (IBH) formed during the primary dehydration step. Harvey et al. developed a pathway to selectively convert 2,3-butanediol by acid catalyst Amberlyst-15 to a complex mixture of 2-ethyl-2,4,5-trimethyl-1,3-dioxolanes and 4,5-dimethyl-2-isopropyl dioxolanes, which can be used as a gasoline-range fuel and diesel oxygenate due to an anti-knock index of 90.5, high combustion value, low solubility in water and full miscibility with both gasoline and diesel fuel [33].

Zhang et al. [34] investigated the dehydration of 2,3-BDO over zeolite HZSM-5 and HZSM-5 modified with boric acid, and studied the effect of framework Si/Al ratio and addition of boric acid on 2,3-BDO dehydration. They reported that high Si/Al ratio was beneficial to low-temperature activation of 2,3-BDO and the methyl migration to 2-methylpropanal, and the addition of boric acid enhanced the catalytic stability. Lee et al. [35] utilized in situ DRIFTS to investigate the dehydration of 2,3-BDO over a series of zeolites ZSM-5, mordenite, β- and Y-type zeolites, and found that dehydration of 2,3-BDO to MEK was favored on ZSM-5. Duan et al. [36] investigated the dehydration of 2,3-BDO over monoclinic ZrO_2 and the result showed that 3-buten-2-ol was produced with a maximum selectivity of 59.0% along with major byproducts such as MEK and 3-hydroxy-2-butanone.

More recently, Liu et al. [37] used γ-alumina to catalyze the direct production of 1,3-butadiene from 2,3-butanediol. They suggested that under the optimized kinetic reaction conditions (trace amount of γ-alumina, high flow rate), the production of MEK and 2-methylpropanal was significantly reduced, while the selectivity of 1,3-butadiene could be obtained up to 80%. Sato and coworkers investigated dehydration of 2,3-BDO to 1,3-butadiene over Sc_2O_3 [38], and dehydration of other diols, such as 1,3-butanediol and 1,4-butanediol over rare earth oxides [39,40], ZrO_2 [41] and Cu-based catalysts [42].

1.3. Zeolites

1.3.1. Zeolite structure

Zeolites are porous, hydrated aluminosilicates with a framework based on an extensive three-dimensional network constructed from TO_4 tetrahedra (T= Si or Al). Each oxygen atom situated at the corners of the tetrahedral unit is shared by two adjacent tetrahedra. The AlO_2^- tetrahedra in the structure determine the framework charge, which is generally balanced by cations that occupy non-framework sites. The general chemical composition of a zeolite is written as:

$$M_{2/n}O \cdot Al_2O_3 \cdot xSiO_2 \cdot yH_2O$$
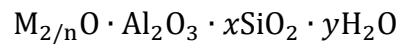
where M is the exchangeable cation (typically Na^+, K^+, Mg^{2+}, Ca^{2+}, NH_4^+, H^+, etc), n represents the cation valence, x accounts for the SiO_2/Al_2O_3 ratio and y is the water content in the hydrated form of zeolite. Zeolites' open-structure framework contains channels or cavities, which are occupied by cations and water molecules[43,44].
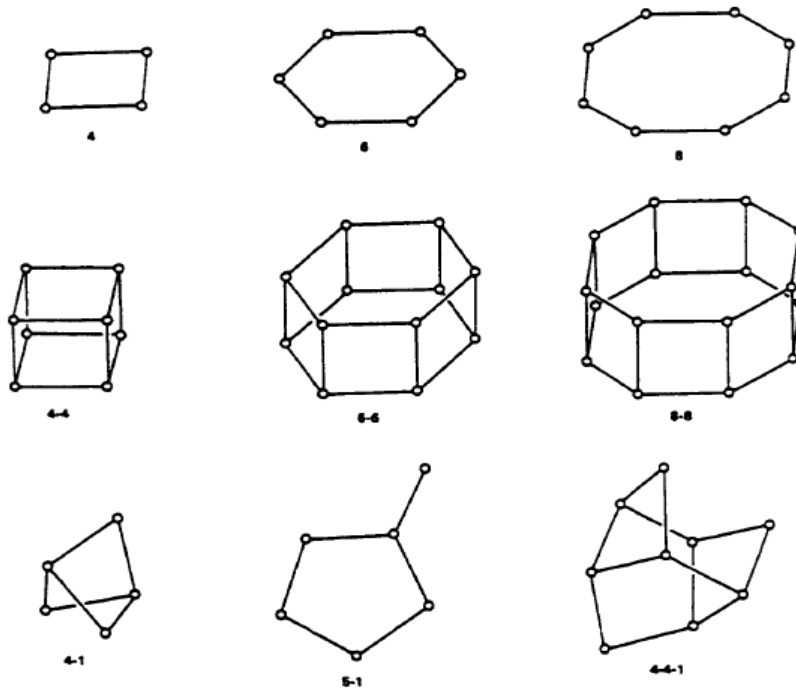
Figure 1.1.Secondary building units of zeolites [44]**.**

As mentioned above, the primary building unit of a zeolite structure is the individual

tetrahedral TO_4 unit, where T is either Si or Al. The symmetry of zeolite unit cells leads to nine secondary building units (repeating unit cells), which can be used to describe all of the known zeolites. The secondary building units consist of 4, 6 and 8-member single rings, 4-4, 6-6 and 8-8-member double rings and 4-1, 5-1, and 4-4-1 branched rings (**Figure 1.1**)[43,44]. Zeolite ZSM-5 consists of 5-1 building units and Y-type zeolite can be described by 4-ring, 6-ring and 6-6-double ring building units. Besides these building units, characteristic chains can be observed in zeolite structures, such as zig-zag, sawtooth, crankshaft and pentasil chains (**Figure 1.2**), and so forth. Typically, zeolites can be discriminated based on their pore size, namely the number of Si or Al atoms forming the ring openings, such as small (8-member ring), medium (10-member ring) and large (12-member ring) pore zeolites.

ZSM-5 is classified as a medium-pore zeolite, which possesses a zigzag channel system intersecting a straight 10 ring channel to form the three-dimensional pore system[44,45]. The structure of ZSM-5 is built up from the pentasil units (**Figure 1.2a**). These units connect to form chains (**Figure 1.2b**), which further link to form sheet building units (**Figure 1.2c**). The ZSM-5 crystalline structure (**Figure 1.2d**) is formed when these sheet units are linked across a center of inversion[46]. This three-dimensional pore system consists of sinusoidal 10-ring (elliptical openings, 5.1×5.5 Å) and perpendicularly intersecting straight 10-ring (near-circular openings, 5.3×5.6 Å) channels. All of the framework ions (both Al and Si) occupy the sites that define the channel intersections, and none solely occupies a site within the "channel"[44]. The typical unit cell content of ZSM-5 is:

$Na_nAl_nSi_{96-n}O_{192}$~16H_2O (n~3).[43]
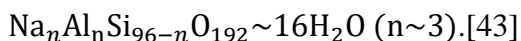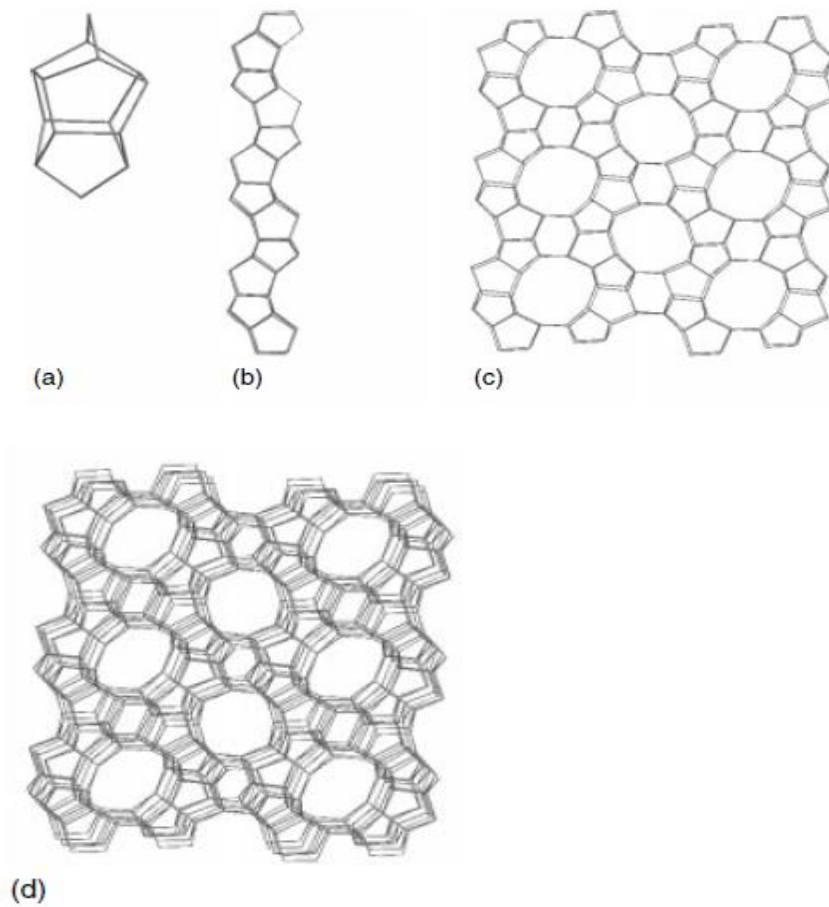
Figure 1.2.The ZSM-5 structure can be built up successively: (a) the pentasil unit; (b) chains of pentasil units; (c) layers of the chains; and (d) layers linked across inversion centers. [45]
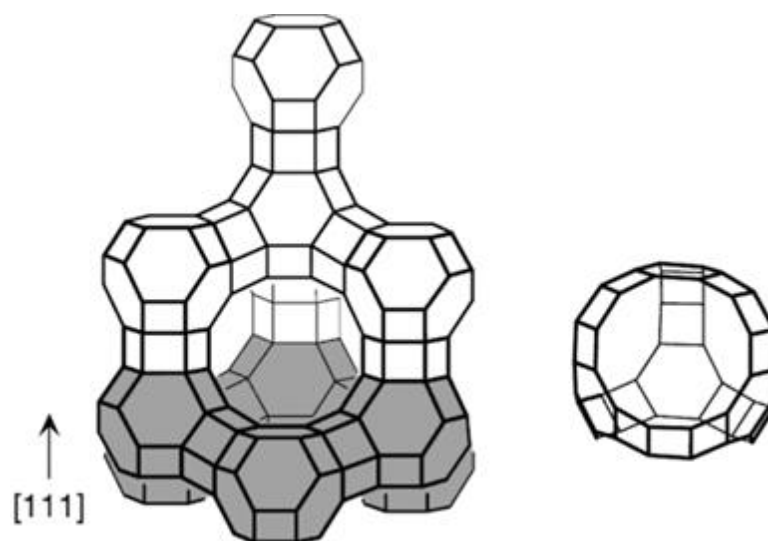
Figure 1.3.Y-zeolite framework (left) and its supercage (right) [47]**.**

Y-type zeolite (Faujasite) is a large pore zeolite containing a 12-membered ring pore opening. The Y zeolite framework consists of a hexagonal prism (6-6 double ring), the sodalite cage (β cage) and the Type II 26-hedron (spherical supercage, approximatey diameter of 11.4 Å). Sodalite cages are connected to one another by hexagonal prisms. This creates the supercage with four tetrahedrally oriented 12-membered oxygen ring windows (approximately diameter of 7.4 Å) and a 3-dimensional channel system. The 6-membered oxygen ring on the sodalite cage (β cage) has an approximately diameter of 2.6 Å (**Figure 1.3**)[43,47]. The combination of supercage, 12-ring pore openings and 3-dimensional channel system makes the Y type zeolite thermally stable.

1.3.2. Acid sites of zeolite

As is mentioned above, the AlO_2^- tetrahedra in the framework impart an overall negative charge to the framework. This is balanced by the presence of extra-framework charge-compensating cations. A Bronsted acid site is where the aluminum site is bridged with its associated silanol group (Si-OH). Brönsted acid sites can be converted to Lewis acid sites by dehydration of zeolite at high temperature, leading to coordinatively unsaturated Al^{3+} sites,

which are strong Lewis acid sites (**Scheme 1.1**) [48]. Lewis acid sites are unstable, and can be converted to Brönsted acid sites when water is present. Therefore, the acidity of zeolite is determined by the content of Al (or SiO_2/Al_2O_3) in the zeolite framework. The higher content of Al (lower SiO_2/Al_2O_3) leads to the stronger acidity of the zeolite.
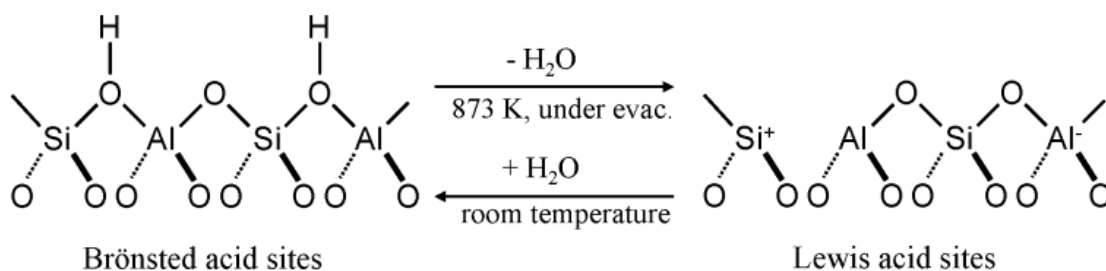
Scheme 1.1. Brönsted and Lewis acid sites on zeolite [48]**.**

1.4. Mesoporous aluminosilicate and hierarchical zeolite

The mesoporous silicate material MCM-41 has received widespread attention due to its extremely high surface area (around $1100 m^2/g$) combined with large and uniform pore sizes since it was invented in 1992[49]. It possesses a 2-D hexagonally arranged mesopores with long-range order (**Figure 1.4,** pore size 15 Å-100 Å), which is synthesized by condensation of silicates around the self-assembled micelles by surfactant molecules ($C_nH_{2n+1}(CH_3)_3N^+$). The carbon chain length plays an important role in determining the dimensions of pores of MCM-41. In comparison to microporous zeolites, ordered mesoporous materials overcome the pore size constraint of zeolites and could allow the more facile diffusion of bulk molecules. However, purely siliceous MCM-41 has been found to have low thermal stability in hot water. The mesoporous structure collapsed in hot water due to the amorphous character of the pore walls [50]. It is reported that the incorporation of Al in the framework could enhance the thermal stability; the mesoporous structure remained even after treatment in boiling water for 300 h [51]. Moreover, incorporation of Al leads to acid sites associated with the presence of Al in the framework position similar to microporous zeolite. Hence, Al-MCM-41 is expected to be a suitable solid acid in this project. Besides MCM-4, mesoporous materials MCM-48 (3-D cubic structure, **Figure 1.4**) and SBA-15 (cubic structure, **Figure 1.4**) can also be used as solid acids

after incorporation of Al, both of which are reported to exhibit higher thermal stability than MCM-41[52–54]. In addition, SBA-15 has a micropore-mesopore network, which can lower diffusion limitations normally observed for microporous zeolite.
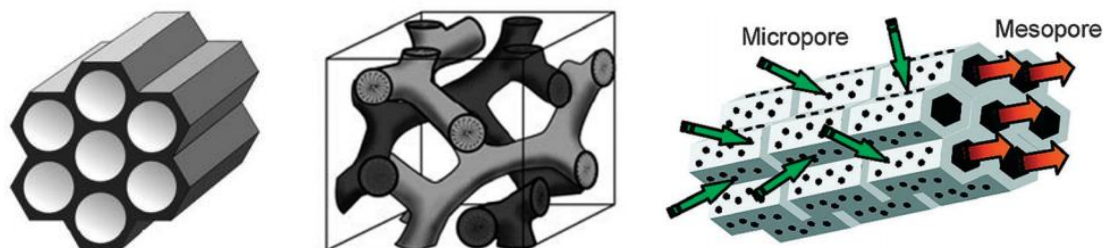
Figure 1.4. Different structures of MCM-41(left), MCM-48 (middle) and SBA-15 (right) [55].

1.5. Catalytic performance of different metals

Copper is well known as a hydrogenation catalyst. Brands et al. [56] investigated a series of Cu/SiO_2 catalysts promoted with Mn, Fe, Co, Ni, Mo, Mg and Y(yttrium) in the hydrogenation reaction of methyl acetate, and the results showed that Cu-containing catalysts have high activity for vapor-phase hydrogenation reaction, particularly the selective hydrogenation of C−O bonds; however, copper catalysts are relatively inactive for hydrogenolysis of C−C bonds. They found that Ni, Co and Mo promoted catalysts showed high activity in hydrogenolysis of C−C bonds, especially the Ni-promoted catalyst, which exhibited high methane formation (up to 70%), which was due to C-C cleavage.

Guo et al.[57] investigated hydrogenolysis of glycerol to propanediols over Cu catalysts and found that $γ-Al_2O_3$ supported Cu catalysts showed excellent performance and successfully suppressed the scission of C-C bonds. The Cu/ $γ-Al_2O_3$ catalyst with an optimized amount of Cu showed a selectivity to propanediol up to 96.8% with glycerol conversion about 49.6% at 220 $^{\circ}$C.

Sitthisa et al.[58] investigated the hydrodeoxygenation of furfural over Cu, Pd and Ni supported on SiO_2, and found that the Cu catalyst mainly produced furfuryl alcohol via hydrogenation of the carbonyl group (C=O) due to the weak interaction of Cu with C=C. However, Pd/SiO_2 catalyst catalyzed the hydrodeoxygenation of furfural to produce a large

11

amount of furan by decarbonylation, which is more favorable than hydrogenation over Pd catalysts. Ni/SiO$_2$ was beneficial for the formation of ring opening products such as butanal, butanol and butane. They suggested that the different product distribution was due to the strength of interaction of the furan ring with the metal surface and the type of intermediates on the surface that each metal can stabilize.

Vasiliadou et al.[59] investigated the hydrogenolysis of glycerol to propylene glycol over highly dispersed Cu/SiO$_2$ catalysts. Their results showed that Cu selectively converted glycerol to propylene glycol with selectivity of 92−97% via consecutive dehydration-hydrogenation reactions with a conversion up to 50% at 240 ^{o}C. They demonstrated that the weak activity of Cu in C−C bond cleavage limited the formation of ethylene glycol. Sato et al.[60] reported that reduced Cu catalyst could effectively catalyze the dehydration of glycerol to hydroxyacetone in N$_2$, and the hydrogenation of hydroxyacetone followed by hydrogenolysis in H$_2$ to form ethylene glycol, acetaldehyde and ethanol.

Chapter 2 - Conversion of 2,3-butanediol to butenes over bifunctional catalysts in a single reactor

2.1. Introduction

Because petroleum is a finite resource, there is growing interest in processes that produce hydrocarbons from renewable resources for use as fuels [1–3,6]. Such processes could produce essentially the same product currently made in petroleum refineries, eliminating the need for modifications to vehicles or to the hydrocarbon distribution infrastructure. A number of routes for producing hydrocarbons from sustainable resources have been proposed [4,6,21]. These routes convert biomass-derived sugars to oxygenated intermediates, which are upgraded to fuel-range hydrocarbons. The key to developing a successful process of this nature is to select intermediate compounds that can be selectively produced from sugars, and can easily be converted to fuel-range hydrocarbons.

A potential intermediate compound that has not previously been considered for production of hydrocarbons from biomass-derived sugars is 2,3-butanediol (2,3-BDO). 2,3-BDO is an intriguing intermediate because it can be produced via fermentation of sugars with a high productivity at high concentration by using a variety of microorganisms, such as Klebsiella oxytoca [9–11,22], Enterobacter aerogenes [12], Bacillus licheniformis [13] and Enterobacter cloacae [14]. Ji et al. [9] obtained a maximum 2,3-BDO concentration of 95.5g/L with productivity of 1.71g/L/h by fermentation of media containing 200g/L of glucose in a 3 L batch fermentor using Klebsiella oxytoca. Jansen et al. [23] obtained a final concentration of 2,3-BDO of 12.63g/L by fermentation of media containing 50g/L of xylose in a 7-L batch fermentor using Klebsiella oxytoca ATCC 8724. Saha and coworkers [14] obtained a yield of 2,3-BDO of 0.4g/g arabinose with a corresponding productivity of 0.63g/L/h by fermentation of media with an initial arabinose concentration of 50g/L.

Once 2,3-butanediol (2,3-BDO) is produced via fermentation, routes to convert it to hydrocarbons would be needed. However, there is little research in this area. Dehydration of 2,3-BDO to methyl ethyl ketone (MEK) has been well studied, and occurs readily over a number of catalysts [16,22]. Zhang et al. [34] investigated the dehydration of 2,3-BDO over zeolite HZSM-5 and HZSM-5 modified with boric acid, and studied the effect of framework Si/Al ratio and

addition of boric acid on 2,3-BDO dehydration. They reported that high Si/Al ratio was beneficial to low-temperature activation of 2,3-BDO and the methyl migration to 2-methylpropanal, and addition of boric acid enhanced the catalytic stability. Lee et al. [35] utilized in situ DRIFTS to investigate the dehydration of 2,3-BDO over a series of zeolites ZSM-5, mordenite, β- and Y-type zeolites, and found that dehydration of 2,3-BDO to MEK was favored on ZSM-5. Duan et al. [36] investigated the dehydration of 2,3-BDO over monoclinic ZrO_2 and the result showed that 3-buten-2-ol was produced with a maximum selectivity of 59.0% along with major byproducts such as MEK and 3-hydroxy-2-butanone. In addition, further dehydration of 2,3-BDO yields 1,3-butadiene [17], which can be dimerized to produce the aromatic intermediate styrene (Diels-Alder reaction) [18] and hydrogenated to butene. Sato and coworkers investigated dehydration of 2,3-BDO to 1,3-butadiene over Sc_2O_3 [38], and dehydration of other diols, like 1,3-butanediol and 1,4-butanediol over rare earth oxides [39,40], ZrO_2 [41] and Cu-based catalysts [42].

The approach reported here is to convert 2,3-BDO to butene, which is a basic building block of fuels as well as many chemicals. As a precursor, butene can be converted to a variety of oligomers (dimer, trimer, tetramer,etc) [19,20], which can be further converted to saturated hydrocarbons through hydrogenation reaction. In this way, butene can serve as an intermediate to produce high-grade liquid fuel with specific type of saturated hydrocarbons [20,21].

The major challenge is to remove the two hydroxyl groups of 2,3-butanediol (2,3-BDO) in a single step to produce butene. This process involves a bifunctional pathway, in which 2,3-butanediol is dehydrated on an acid site to methyl ethyl ketone (MEK), 2-methylpropanal, and butadiene, which can be further hydrogenated to butene on the metal sites. Copper is interesting for use as the hydrogenation catalyst. Cu-containing catalysts show high activity for vapor-phase hydrogenation reaction particularly the selective hydrogenation of carbon-oxygen bonds; however, copper catalysts are relatively inactive for hydrogenolysis of carbon-carbon bonds [56]. Guo et al.[57] investigated hydrogenolysis of glycerol to propanediols over Cu catalysts, and found that γ-Al_2O_3 supported Cu catalysts showed excellent performance (selectivity to propanediol, 96.8%) and successfully suppressed the scission of C-C bonds. Sitthisa et al.[58] investigated the hydrodeoxygenation of furfural over Cu, Pd and Ni supported on SiO_2, and found that the Cu catalyst mainly produced furfuryl alcohol via hydrogenation of the carbonyl group due to the weak interaction of Cu with C=C. Vasiliadou et al.[59] investigated the

hydrogenolysis of glycerol to propylene glycol over highly dispersed Cu/SiO_2 catalyst. The result showed that Cu selectively converted glycerol to propylene glycol with selectivity of 92-97% via consecutive dehydration-hydrogenation reactions. Sato et al.[60] reported that reduced Cu catalyst could effectively catalyze the dehydration of glycerol to hydroxyacetone in N_2, and the hydrogenation of hydroxyacetone followed by hydrogenolysis in H_2 to form ethylene glycol, acetaldehyde and ethanol.

Based on the excellent hydrogenation performance of copper, we have studied a high copper loading catalyst supported on ZSM-5 to convert 2,3-butanediol to butenes in a single reactor. The impact of reaction conditions (temperature and hydrogen to 2,3-butanediol ratio) and the Si/Al ratio of the ZSM-5 catalyst are reported and it is demonstrated for the first time that 2,3-BDO can be converted to butenes in a single step at a high yield.

2.2. Experimental section

2.2.1. Materials

Ammonium-type ZSM-5 with SiO_2/Al_2O_3 ratios of 23, 50 and 280 were obtained from Zeolyst International. ZSM-5 is referred to as ZSM-5(n), where n is the SiO_2/Al_2O_3 ratio. 2,3-butanediol (>97%) was purchased from TCI America. $Cu(NO_3)_2 \cdot 3H_2O$ (99%) was purchased from Fisher scientific.

2.2.2. Catalyst preparation

As previously reported, the ion exchange of zeolite ZSM-5 with Cu(II) in ammonia could result in excessively exchanged copper on zeolites with high copper dispersion [61,62]. The catalysts used in this work were synthesized by the ion exchange method as follows, which is similar to the deposition precipitation (DP) method [63,64] or ammonia evaporation (AE) methods [65,66]. First, the ammonium-type ZSM-5 was calcined at 550 ^{o}C for 4 hours to convert it to HZSM-5. Then the desired amount of $Cu(NO_3)_2 \cdot 3H_2O$ was dissolved in 100 mL of deionized water at room temperature. Ammonia was added to the solution until the pH was about 9.1 to form a dark blue cupric ammine complex $[Cu(NH_3)_4(H_2O)_2]^{2+}$, and then water was added to make 250 mL of a copper-ammonia complex solution. 20 grams of HZSM-5 zeolite was added to the solution and then the container was capped to avoid the evaporation of ammonia

and stirred for 4 hours at room temperature. After that, the container was transferred to an oil bath and heated to 60 ^{o}C for 2 hours. Then the solution was filtered and the precipitate was washed at least five times by water and dried at 110 ^{o}C overnight followed by calcination at 550 ^{o}C for 4 hours. Finally, the calcined catalyst was pelletized, crushed and sieved to obtain a particle size distribution in the range 40-60 mesh. To make 10%CuO/ZSM-5, the amount of $Cu(NO_3)_2 \cdot 3H_2O$ added to the solution was 24.16 g. The content of CuO was determined to be 9.5wt%, 9.7wt% and 9.2wt% on ZSM-5 with SiO_2/Al_2O_3 ratios of 23, 50 and 280, respectively, by the inductively coupled plasma (ICP) method. Two Cu/ZSM-5(280) catalysts with high loading of CuO were prepared by increasing the amount of $Cu(NO_3)_2 \cdot 3H_2O$ to 36.24 g, and extending the time of ion exchange in the oil bath to 12 hours and 24 hours. For these two catalysts, the content of CuO was determined by ICP to be 19.2wt% and 29.1wt%, respectively. For the catalyst Cu/ZSM-5(280) with low loading of CuO, the amount of $Cu(NO_3)_2 \cdot 3H_2O$ was decreased to 12.0 g and the time of ion exchange was shortened to about 1 hour in the oil bath, and the content of CuO was determined by ICP to be 6.0wt%.

2.2.3. Catalytic reactions

The catalytic reactions were performed in a conventional continuous flow fixed-bed reactor made of stainless steel (id=8 mm) under atmospheric pressure. Prior to reaction, the catalyst sample (weight=1.0 g) was reduced in the reactor in the H_2/N_2 flow (flow rate of $H_2/N_2=1/5$) at 300 ^{o}C for 2 hours. The H_2 flow of 24 cm^3/min (standard ambient temperature and pressure, SATP) and the N_2 flow of 120 cm^3/min (SATP) were controlled with mass-flow controllers (Brooks). 2,3-BDO was fed via a micropump (Eldex 1SMP) at 3 mL/hour together with a H_2 flow of 67.2 cm^3/min (SATP) and N_2 flow of 15.4 cm^3/min (SATP). Reactor temperature was set between 200 and 300 ^{o}C. Product compositions were analyzed by an on-line gas chromatograph (SRI 8610C) equipped with an MXT-1 column (nonpolar phase, 60m, ID 0.25 mm, film thickness 0.25 μm), TCD and FID detectors for the analysis of hydrocarbons and oxygenated chemicals, and quantified by injecting calibration standards to the GC system. The temperature of the tubing from the bottom of the reactor to the inlet of GC was maintained at 230 ^{o}C to avoid the condensation of liquid products. The products were injected through the sample loop (0.2 mL), which was controlled by a high temperature ten-port valve. The oven was kept at 40 ^{o}C for 5 min, and then raised to 120 ^{o}C at a ramp rate of 40 ^{o}C/min, finally raised to 250 ^{o}C at

a rate of 20 $^{\circ}$C/min, and held at this temperature for 10 min. As MXT-1 column is not capable of separating some hydrocarbons, such as 1-butene and isobuene, to determine the distribution of butenes (1-butene, isobutene, trans-2-butene and cis-2-butene) over catalysts with different SiO_2/Al_2O_3 ratios, additional experiments were performed where the MXT-1 column was replaced with an MXT-Alumina BOND/MAPD column (30m, ID 0.53 mm, film thickness 10 μm), which is capable of separating the four isomers of butenes. To ensure the identification of products, GC-MS analyses were also carried out by using an Agilent 7890A GC system equipped with an Agilent 5975C MS detector and HP-1 capillary column. The carbon selectivity [67,68] and conversion of 2,3-BDO were calculated in the following methods.

$$\text{Carbon selectivity} = \frac{\text{Moles of carbon in specific product}}{\text{Total carbon atoms in identified products}} \times 100\%$$

$$\text{Conversion} = \frac{(\text{moles of 2,3-BDO})_{in} - (\text{moles of 2,3-BDO})_{out}}{(\text{moles of 2,3-butanediol})_{in}} \times 100\%$$

Two repeat runs were performed at each reaction condition and the two trials were generally within 5% of each other. The relative difference between the sum of butene selectivity from MXT-1 column and MXT-Alumina BOND/MAPD column is about 5%-6%. The carbon balances closed with above 90% for all runs in this paper.

2.2.4. Catalyst characterization

2.2.4.1. NH$_3$ temperature-programed desorption (NH$_3$-TPD)

The surface acidity of catalysts was investigated by temperature programmed desorption of ammonia (NH$_3$-TPD). NH$_3$-TPD was carried out in an Altamira AMI-200 system. Prior to adsorption, 0.2 g of copper catalyst was loaded in a quartz U-tube reactor and pre-treated at 550 $^{\circ}$C in helium for 1 hour followed by cooling to 100 $^{\circ}$C. Then the catalyst was reduced in a flow of H$_2$/Ar (10v/v%) at a constant rate of 10 $^{\circ}$C/min to 300 $^{\circ}$C and then maintained for 2 hours followed by cooling to 100 $^{\circ}$C. 10 mL/min of ammonia (anhydrous, 99.99%) was then introduced at 100 $^{\circ}$C for 30 min. Physisorbed NH$_3$ molecules were removed by flowing pure helium at 100 $^{\circ}$C for 2 hours. Finally, the temperature was raised to 700 $^{\circ}$C at10 $^{\circ}$C/min. Desorbed ammonia was detected with a thermal conductivity detector (TCD).

2.2.4.2. H$_2$ temperature-programed reduction (H$_2$-TPR)

H$_2$-TPR was measured in the same system as NH$_3$-TPD. 0.1 g of sample was loaded in a quartz U-tube reactor and treated at 550 $^{\circ}$C in Ar (99.999%) at a flow of 40 mL/min for an hour. After cooling, the temperature was ramped from 50 $^{\circ}$C to 900 $^{\circ}$C at a ramp rate of 5 $^{\circ}$C/min in H$_2$/Ar flow (10v/v%, 40 mL/min). H$_2$ consumption was recorded by a thermal conductivity detector (TCD). H$_2$ consumption was calibrated by reducing 0.03 g of pure CuO.

2.2.4.3. Brunauer-Emmett-Teller (BET)

Surface area measurements of catalysts were conducted according to the Brunauer-Emmett- Teller (BET) gas (nitrogen) adsorption method. About 0.06 g of catalyst powder was poured into the sample cell and degassed at 350 $^{\circ}$C for 4 hours before determining the exact mass of the sample, which was then confirmed after degassing. The adsorption/desorption isotherms were measured using a Quantachrome Autosorb1 instrument at -196 $^{\circ}$C and analyzed with Autosorb1 software. The total surface area was determined from N$_2$ adsorption branch in the linear range of relative pressure from 0.007 to 0.03. The micropore surface area and micropore volume were evaluated by the t-plot method [69]. The total pore volume was evaluated by single point pore volume at a relative pressure of 0.95.

2.2.4.4. X-ray diffraction (XRD)

XRD analysis was conducted using a Rigaku Miniflex II desktop x-ray diffractometer. Scans of two theta angles were from 5° to 90° for all catalysts with a step size of of 0.02° and scan speed of 0.75 $^{\circ}$/min. All samples were well ground before analysis in order to provide a significant number of oriented particles to fulfill the Bragg condition of reflection.

2.2.4.5. Scanning electron microscopy (SEM)

Scanning electron microscopy (SEM) experiments were performed on a FEI Nova NanoSEM 430 to identify the morphology of Cu/ZSM-5 catalysts.

2.2.4.6. X-ray photoelectron spectroscopy (XPS)

XPS data were obtained with a PerkinElmer PHI 5400 using achromatic Al Kα radiation (1486.60 eV). The pressure in the analysis chamber was typically 8.0×10^{-8} Torr. Cu $2p_{3/2}$ (932.7 eV) and Au $4f_{7/2}$ (84.0 eV) were used as standards to calibrate the binding energy (BE) range, and the binding energy of carbon 284.6 eV was used as the BE standard to correct for charging on the substrate [70]. XPS spectra were curve fitted by the software CasaXPS based on the centered position, full width at half maximum (FWHM) and peak intensity.

2.2.4.7. N$_2$O adsorption

Copper surface area (SA$_{Cu}$) and dispersion (D$_{Cu}$) were determined by dissociative N$_2$O adsorption method at 90 ^oC [71,72] using the same system as H$_2$-TPR and NH$_3$-TPD. Prior to N$_2$O adsorption, the catalysts (0.1 g) were first treated at 550 ^oC in Ar at a flow of 40 mL/min for an hour. After cooling, the temperature was ramped from 50 ^oC to 400 ^oC at a ramp rate of 5 ^oC/min in H$_2$/Ar flow (10v/v%, 40 mL/min) by the H$_2$-TPR procedure described above and decreased to 90 ^oC in Ar (99.999%, 30 mL/min). In this step, the amount of hydrogen consumption was denoted as X. Then the pre-reduced catalysts were exposed to N$_2$O/He (5 v/v%, 40 mL/min) isothermally at 90 ^oC for 1 hour to oxidize surface copper atoms to Cu$_2$O followed by cooling to 50 ^oC in Ar (30 mL/min). After this process, the second H$_2$-TPR was carried out on the freshly oxidized catalysts from 50 ^oC to 400 ^oC at a ramp rate of 5 ^oC/min in H$_2$/Ar flow (10v/v%, 40 mL/min) in order to reduce Cu$_2$O back to metallic Cu. The hydrogen consumption in this step was denoted as Y. Copper dispersion (D$_{Cu}$), is calculated as D$_{Cu}$ =2Y/X, which is defined as the ratio of the surface copper atoms to the total copper atoms present in the catalyst. Copper surface area SA$_{Cu}$ (m^2/g$_{Cu}$) is calculated as described in literatures [71,72] by the following equation:

$$SA_{Cu} = \frac{2 \cdot Y \cdot N_{av}}{X \cdot M_{Cu} \cdot SD_{Cu}} \approx 1353 \ Y/X \ (m^2/g_{Cu})$$

where N$_{av}$ = Avogadro's constant = 6.02×10^{23} atoms/mol, M$_{Cu}$ = Atomic weight of Cu = 63.546 g/mol, SD$_{Cu}$ = copper surface density = 1.47×10^{19} atoms/m^2 (the average value for Cu(111), Cu(110), and Cu(100) crystal surfaces).

2.2.4.8. Thermogravimetric analysis (TGA)

Thermogravimetric analysis (TGA) was performed with a thermogravimetric analyzer (Shimadzu TGA-50). The used catalyst samples were collected after a specific reaction time (40 min or 280 min). After the feed of 2,3-BDO was stopped, the flow of hydrogen and nitrogen (the same flow rate as reaction) was maintained for about 30 min to remove residual 2,3-BDO in the reactor and the products adsorbed on the catalysts as well. Catalyst was recovered after cooling to room temperature. Prior to TGA analysis, the used catalysts were kept in the oven at 100 ^{o}C for 3 days so that the copper in catalysts could be oxidized completely. Typically, about 20 mg of used catalyst sample was heated in air (air flow: 10 mL/min) from room temperature to 600 ^{o}C at a ramp rate of 10 ^{o}C/min. The coke content for each sample was then determined from the weight loss between 300 ^{o}C and 600 ^{o}C [73].

2.3. Characterization of catalyst

2.3.1. X-ray diffraction

Figure 2.1 shows the XRD patterns of the Cu/ZSM-5 catalysts with different SiO_2/Al_2O_3 ratios and those of the parent HZSM-5 calcined at 550 ^{o}C, and **Figure A.1** and **A.2** display the XRD patterns and relative crystallinity, respectively, of the calcined catalysts with different CuO loadings on zeolite HZSM-5(280). As seen in these figures, although a slight decrease in the intensity of the main peaks was noticed after introduction of copper, all the characteristic peaks of the parent HZSM-5 were observed in Cu/ZSM-5 catalysts, which indicated that the introduction of copper did not destroy the structure of the parent HZSM-5. In addition, two characteristic peaks related to CuO (35.7º and 38.55º) were only observed on 9.5%CuO/ZSM-5(23), which indicated that Cu species were well dispersed on HZSM-5(50) and HZSM-5(280). This is in accordance with the SEM result (see **Figure A.3**), copper clusters were observed only on 9.5%CuO/ZSM-5(23) with the size of 0.5 µm-1.0µm and the weight percent of CuO in these clusters was estimated at ~ 43% obtained by EDS detector.
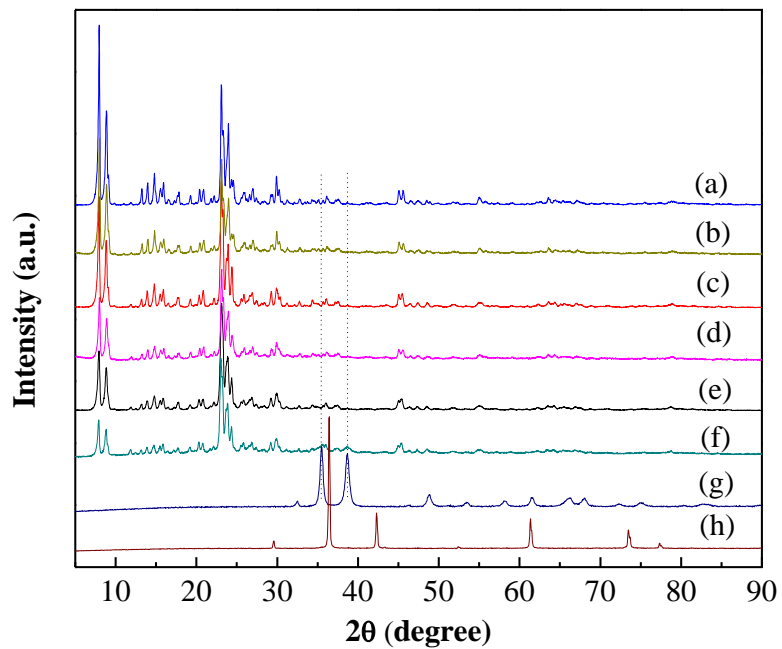
Figure 2.1. XRD patterns of the calcined catalysts with different SiO$_2$/Al$_2$O$_3$ ratios.(a) HZSM-5(280), (b) 9.2%CuO/ZSM-5(280), (c) HZSM-5(50), (d) 9.7%CuO/ZSM-5(50), (e) HZSM-5(23), (f) 9.5%CuO/ZSM-5(23), (g) CuO, (h) Cu$_2$O.

2.3.2. H$_2$ temperature-programmed reduction
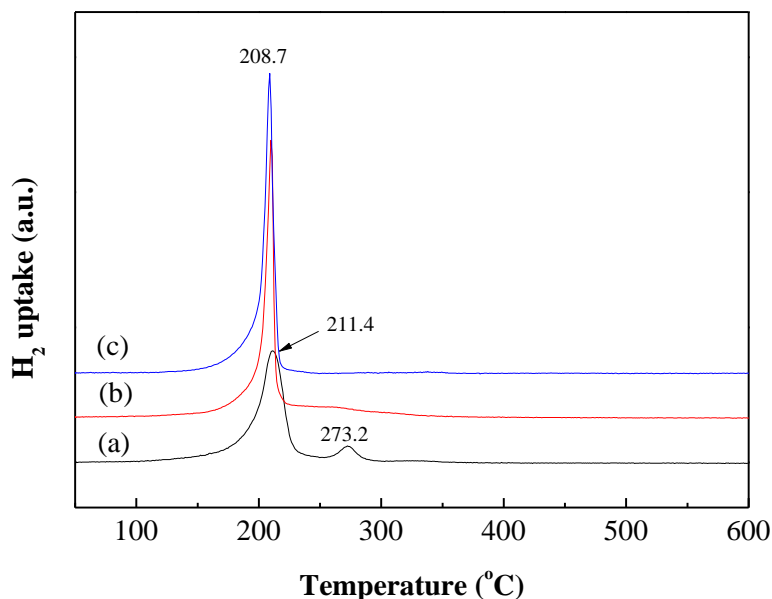
Figure 2.2. H$_2$-TPR profiles of calcined Cu/ZSM-5 with different SiO$_2$/Al$_2$O$_3$ ratios. (a) 9.5%CuO/ZSM-5(23), (b) 9.7%CuO/ZSM-5(50), (c) 9.2%CuO/ZSM-5(280).
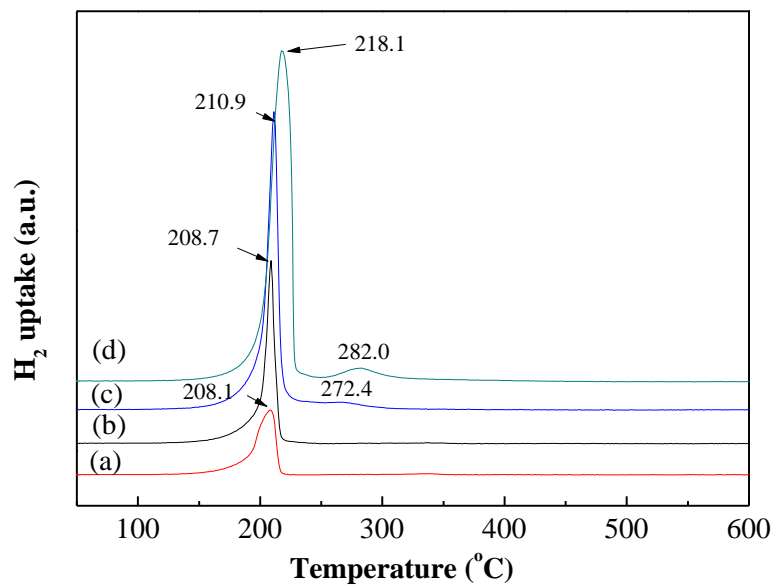
Figure 2.3. H$_2$-TPR profiles of calcined Cu/ZSM-5(280) with various CuO loadings. (a) 6.0%, (b) 9.2%, (c) 19.2%, (d) 29.1%.

In order to investigate the reducibility of Cu on zeolite ZSM-5, H_2-TPR measurements were performed. **Figure 2.2** shows the H_2-TPR profiles of Cu/ZSM-5 with SiO_2/Al_2O_3 ratios of 23, 50 and 280. It is reported that Cu/ZSM-5 catalysts undergo a stepwise reduction process [74–77]. Generally, the peak at the low temperature (170 ºC -210 ºC) may be attributed to the reduction of CuO in one step to metallic Cu^0, and the reduction of isolated Cu^{2+} ions to Cu^+ as well; and the high temperature peak (normally > 350 ºC) may be ascribed to the reduction of Cu^+ to metallic Cu^0. However, in Figure 2.2 and Figure 2.3, the high-temperature peak was not observed. As seen in Figure 2.2, catalyst 9.5%CuO/ZSM-5(23) was seen to exhibit two separate reduction peaks. The main peak at low temperature peak (211.4 ºC) is assigned to the well dispersed CuO on zeolite ZSM-5 and the small peak at higher temperature (273.2 ºC) is assigned to the reduction of bulk CuO. The assignment of the reduction peaks is similar to the catalyst Cu/SiO_2 prepared by ammonia evaporation (AE) method [63,66,78]. The main reduction peaks of CuO/ZSM-5 catalysts with SiO_2/Al_2O_3 ratios of 50 and 280 (see Figure 2.2b and Figure 2.2c) became sharper than on Cu/ZSM-5(23) and shift to a lower temperature (208.7 ºC). The shoulder peak at high temperature for 9.7%CuO/ZSM-5(50) was smaller than that of CuO/ZSM-5(23). For the catalyst 9.2%Cu/ZSM-5(280), only one low-temperature reduction peak was identified. Figure 2.3 exhibits the H_2-TPR profiles of catalysts CuO/ZSM-5(280) with various CuO loadings. With increasing CuO loadings from 6.0% to 29.1%, the intensity of the main reduction peak was observed to increase and the temperature was shifted from 208.1 to 218.1 ºC. For all trials, the H_2 consumption of catalysts is proportional to the CuO loading and the ratio of H_2/CuO is almost close to 1 (see supplementary information, Table A.1), which indicates that Cu is divalent. On the catalysts with CuO loadings of 19.2% and 29.1% (Figure 2.3c and Figure 2.3d), the shoulder peak at high temperature related to bulk CuO was observed. From the result of TPR measurement, it can be concluded that most Cu species on zeolite HZSM-5 are well dispersed Cu based on the large reduction peak at low temperature.

2.3.3. N_2 adsorption

The structure properties of the zeolites and copper catalysts can be derived from the results of N_2 adsorption-desorption measurements at -196 ºC. The surface area and pore volume are summarized in Table 2.1. As is shown in Table 2.1, both mesopores and micropores exist for the zeolites. The external surface area and mesopore volume of HZSM-5(23) (148 m^2/g, 0.199

cm^3/g) are higher than those of HZSM-5(50) (115 m^2/g, 0.150 cm^3/g) and HZSM-5(280) (105 m^2/g, 0.121 cm^3/g). It is seen that introduction of copper into zeolite HZSM-5(23) leads to nearly unchanged micropore area, but lowers both external area and mesopore volume. The external surface area dropped from 148 m^2/g to 130 m^2/g and mesopore volume decreased from 0.199 cm^3/g to 0.165 cm^3/g, which indicated that most of the copper species were deposited in the mesopores, reducing the contributions of these pores to the total surface area and total pore volume as a result. However, introduction of copper on zeolite HZSM-5(50) and HZSM-5(280) lowers the micropore surface area (203 m^2/g and 220 m^2/g for 9.7%CuO/ZSM-5(50) and 9.2%CuO/ZSM-5(280), respectively), and micropore volume (0.107 cm^3/g and 0.146 cm^3/g for 9.7%CuO/ZSM-5(50) and 9.2%CuO/ZSM-5(280), respectively) (see **Table 2.1**). Moreover, as shown in **Table 2.1**, when the addition of CuO was increased from 6.0% to 29.1% on zeolite HZSM-5(280), the BET surface area remained almost unchanged; however, the micropore area dropped from 258 to 198 m^2/g, which is assumed to be caused by copper deposition in the micropores of the zeolite. The external surface area increased from 167 to 231 m^2/g and the mesopore volume increased from 0.214 to 0.298 cm^3/g.

Table 2.1. Surface area, pore volume, copper dispersion and ammonia uptake of catalysts and supports.

sample	surface area			pore volume			NH_3 uptake (mmol/g)	SA_{Cu} (m^2/g_{Cu})	D_{Cu}
	S_{BET} $(m^2/g)^a$	S_{micro} $(m^2/g)^b$	$S_{external}$ $(m^2/g)^c$	V_{total} $(cm^3/g)^d$	V_{micro} $(cm^3/g)^b$	V_{meso} $(cm^3/g)^e$			
HZSM-5(23)	431	283	148	0.411	0.212	0.199	1.167	–	–
HZSM-5(50)	447	333	115	0.319	0.169	0.150	0.746	–	–
HZSM-5(280)	437	332	105	0.301	0.180	0.121	0.145	–	–
9.5%CuO/ZSM-5(23)	414	284	130	0.299	0.134	0.165	1.462	20.3	0.03
9.7%CuO/ZSM-5(50)	423	203	220	0.426	0.107	0.319	0.922	155.6	0.23
6.0%CuO/ZSM-5(280)	425	258	167	0.358	0.144	0.214	0.314	209.7	0.31
9.2%CuO/ZSM-5(280)	445	220	226	0.426	0.146	0.280	0.356	162.4	0.24
19.2%CuO/ZSM-5(280)	437	215	222	0.455	0.173	0.282	0.487	148.8	0.22
29.1%CuO/ZSM-5(280)	429	198	231	0.482	0.184	0.298	0.668	67.7	0.10

[a] The Brunauer-Emmett-Teller (BET) surface area (S_{BET}) was calculated from the linear part of BET plot from 0.007 to 0.03.
[b] The micropore area (S_{micro}) and volume (V_{micro}) were obtained by the t-plot method.
[c] The external surface area $S_{external}=S_{BET}-S_{micro}$.
[d] The total pore volume (V_{total}) was evaluated by single point total pore volume at a relative pressure of 0.95.
[e] The mesopore volume $V_{meso}=V_{total}-V_{micro}$.

2.3.4. NH$_3$-TPD
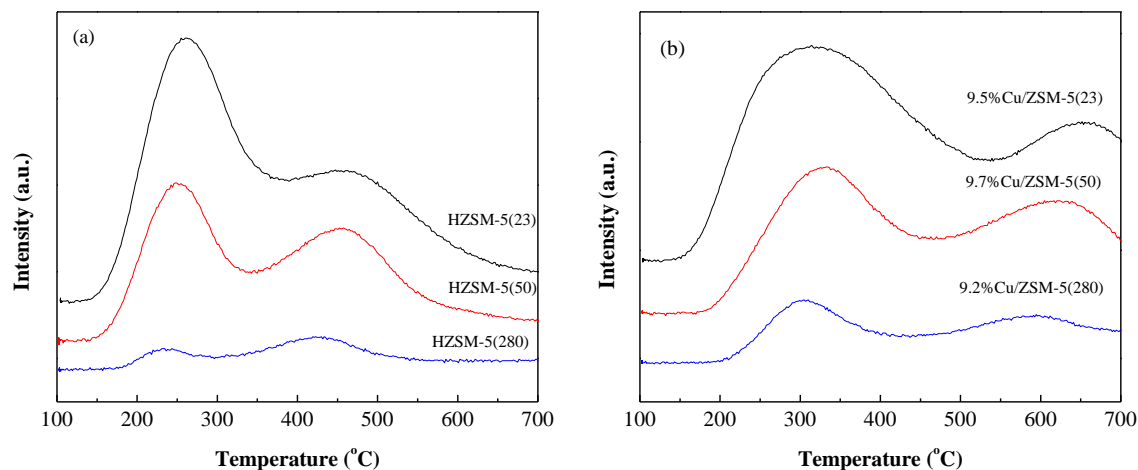
Figure 2.4. NH$_3$-TPD profiles of (a) HZSM-5 with different SiO$_2$/Al$_2$O$_3$ ratios and (b) reduced Cu/ZSM-5 with different SiO$_2$/Al$_2$O$_3$ ratios.

The acidity of the zeolites and reduced copper catalysts were determined by NH$_3$-TPD, as shown in **Figure 2.4**. **Figure A.4** displays the NH$_3$-TPD profiles of reduced Cu/ZSM-5(280) catalysts with various CuO loadings. The amount of ammonia uptake is given in **Table 2.1**. NH$_3$-TPD curves with regard to the temperature can provide information of the strength of acid sites of the zeolites. As seen in **Figure 2.4a**, the NH$_3$-TPD profiles of parent zeolite HZSM-5 with different SiO$_2$/Al$_2$O$_3$ ratios exhibited two distinct desorption peaks centering at around 250 and 450 ºC, which are the characteristic peaks of zeolite with MFI structure [79]. However, in Nanba's work, the corresponding two desorption temperature of NH$_3$ from HZSM-5 were 200 and about 400 ºC [80]. The temperature difference (50 ºC) was probably due to the different flow rate of carrier gas and different ramp rate of heating when NH$_3$-TPD was performed (in this work, the flow rate of He is 25 mL/min, ramp rate is 10 ºC/min). The peak at low temperature is assigned to ammonia weakly held or physically adsorbed on the Lewis acid sites of zeolite, whereas the peak at high temperature is ascribable to the desorption of ammonia strongly adsorbed on and/or interacting with the dislodged Al, and decomposition of NH$_4^+$ on the Brönsted acid sites [81–84]. As is shown, with increasing SiO$_2$/Al$_2$O$_3$ ratios of the zeolite from 23 to 280, the peak intensity of ammonia desorption, especially the peak at low temperature decreased dramatically and the total acid concentration dropped from 1.167 mmol/gcat to 0.145

mmol/gcat (see **Table 2.1**), which is consistent with the idea that the acidity of a zeolite is inversely proportional to the SiO_2/Al_2O_3 ratio.

As is reported, copper catalyst exhibits a strong capability of oxidizing NH_3 to NO or N_2 [85,86]. However, Nanba et al. demonstrated that only N_2 was formed over Cu^{2+} species, which was accompanied by the reduction of Cu^{2+} to Cu^+ [80]. Therefore, to reduce the possibility of oxidization of NH_3 prior to an NH_3-TPD experiment, all copper catalysts in this work were reduced by H_2 at temperature of 300 ℃ for two hours. As seen in **Figure 2.4b**, NH_3-TPD profiles of reduced Cu/ZSM-5 with various SiO_2/Al_2O_3 ratios also exhibited two distinct peaks, both of which shifted to higher temperatures (about 300-350 ℃ and 600-650 ℃) compared to characteristic peaks of the parent zeolites; meanwhile, the peaks of low temperature became larger and broader, which can be ascribable to the combination of NH_3 desorption from both Lewis acid sites of zeolites and copper sites on the surface. The higher temperature peak above 600 ℃ is not shown in the NH_3-TPD profiles of parent zeolites, which indicates that some copper species strongly adsorb NH_3, and is probably due to NH_3 adsorbed on Cu that only binds to one Al [86]. The high temperature peak exhibits a slight shift to low temperature from 650 to 600 ℃ with increasing SiO_2/Al_2O_3 ratios from 23 to 280. In addition, the total acid concentration of Cu/ZSM-5 catalyst is higher than that of the corresponding parent zeolite and decreases with increasing SiO_2/Al_2O_3 ratio (from 1.462 mmol/g_{cat} to 0.356 mmol/g_{cat}, see **Table 2.1**).

2.3.5. X-ray photoelectron spectroscopy
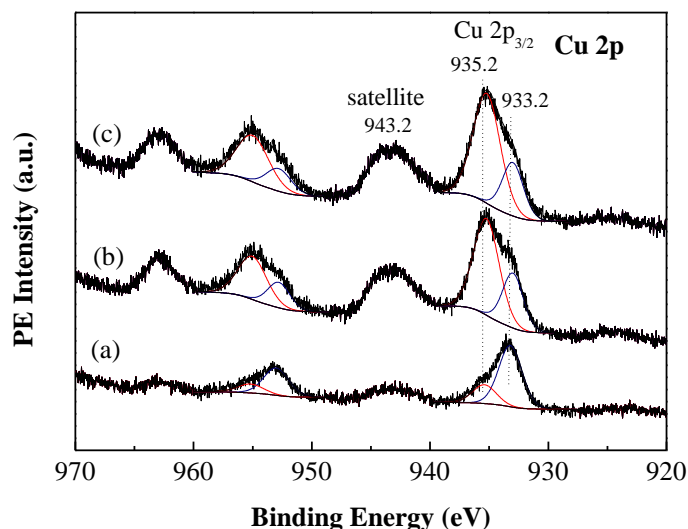
Figure 2.5. XPS spectra of the calcined CuO/ZSM-5 with different SiO$_2$/Al$_2$O$_3$ ratios. (a) 9.5%CuO/ZSM-5(23), (b) 9.7%CuO/ZSM-5(50), (c) 9.2%CuO/ZSM-5(280). Spectra were curve fitted by the software CasaXPS.

XPS analysis was employed to elucidate the chemical states of copper on the Cu/ZSM-5 catalysts. The Cu 2p photoelectron spectra of the calcined Cu/ZSM-5 with various SiO$_2$/Al$_2$O$_3$ ratios are shown in **Figure 2.5**. The asymmetric peaks of Cu 2p$_{3/2}$ were deconvoluted into two peaks centering about 935.2 and 933.2 eV. It is seen from **Figure 2.5** that the Cu 2p$_{3/2}$ peak of CuO/ZSM-5(23) is centered around 933.2 eV; however, the peaks of the other two catalysts CuO/ZSM-5(50) and CuO/ZSM-(280) are at 935.2 eV. Typically, peaks observed at 935.2 eV are assigned to well dispersed Cu(II) species [87]. The binding energy of the bulk CuO species is 933.6 eV (Cu 2p$_{3/2}$), and the shift to higher binding energy of well dispersed Cu(II) species is indicative of a charge transfer from the metal ion to the support oxide [87]. The presence of the Cu 2p shake-up satellite peak (942-944 eV) is characteristic of Cu^{2+} with electron configuration of (d^9) [66]. However, the Cu 2p$_{3/2}$ at about 933.2 eV is difficult to discriminate between Cu(I) and Cu(II). It was reported that X-ray irradiation from XPS could cause the reduction of the CuO particles [70] and X-ray sensitivity to metal ion reduction depends strongly on the chemical environment of the metal ion [88]. Gervasini et al.[87] suggested that the peak of lower binding energy (Cu 2p$_{3/2}$ 933.15 eV) could be attributed to Cu(I) when they compared the valence state of Cu on the catalysts Cu/Al$_2$O$_3$ and Cu/SiO$_2$-Al$_2$O$_3$. Interestingly, one peak at 933.15 eV was

observed on $Cu/SiO_2-Al_2O_3$, which is similar to our Cu/ZSM-5(23) (see **Figure 2.5a**) and two peaks (932 and 935.3 eV) were displayed on Cu/SiO_2, which is analogous to our Cu/ZSM-5 catalysts with SiO_2/Al_2O_3 ratios of 50 and 280 (**Figure 2.5b and 5c**). Contarini et al.[88] reported that the lower binding energy peak (933-934 eV) and the higher binding energy peak (935-936 eV) were assigned to the tetrahedrally and octahedrally coordinated Cu^{2+}, respectively, and the shake-up satellites have a stronger correlation with the octahedrally species when they studied the valence state of Cu on dehydrated and hydrated copper-exchanged X- and Y-zeolite. In addition, they pointed out that different Si/Al ratios in zeolites might affect the symmetry and water coordination around the exchanged Cu ion. Espinós et al. [89] pointed out that, for the same oxidation state of Cu, the binding energy can change depending on the dispersion degree. They suggested that the higher binding energy (935.4 eV) and lower binding energy (933.6 eV) were related to the dispersed and bulk Cu species, respectively. Böske et al.[90] investigated the binding energy of various cuprate crystals by high-resolution XPS and found out that the Cu $2p_{3/2}$ peak varied due to the changes with the linking arrangement of Cu-O networks within the lattice, like linear chain, zigzag chain and CuO_2 plane, which resulted in the shifts in the position of binding energy and the relative intensity between the satellite and the main peak.
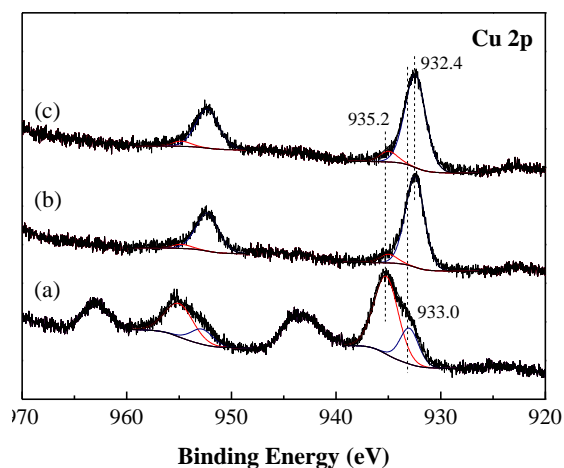
Figure 2.6. XPS spectra of 19.2%CuO/ZSM-5(280) catalyst. (a) without reduction, (b) after reduction, (c) after reaction. Spectra were curve fitted by the software CasaXPS.

In this work, if the peak at 933.2 eV is ascribable to Cu(I), the H_2 consumption of catalyst 9.5%CuO/ZSM-5(23) should be much smaller than the other two catalysts (9.7%CuO/ZSM-5(50)

and 9.2%CuO/ZSM-5(280)). However, from the TPR results, it is clearly seen that the H_2 consumption area of catalyst 9.5%CuO/ZSM-5(23) is very close to the other two catalysts and the molar ratio of H_2/Cu is close to 1 (see **Table A.1**). Based on the results of XPS, TPR and XRD, we can safely conclude that the difference between the binding energy of Cu on HZSM-5 with various SiO_2/Al_2O_3 ratios is due to the dispersion of Cu or the structural environment where Cu is located. The binding energy of Cu on ZSM-5(23) tends to shift to the lower energy level (see **Figure A.6a** for 18.6%CuO/ZSM-5(23)); however, the binding energy of Cu on ZSM-5 with SiO_2/Al_2O_3 ratios of 50 and 280 shifts to the higher energy level.

XPS results for Cu/ZSM-5(280) with higher CuO loadings (see **Figure A.5**) show no significant change in the Cu binding energy. **Figure 2.6** displays the XPS spectra of reduced and used 19.2%CuO/ZSM-5(280) compared to the fresh one. The satellite peaks (943.2 eV) disappeared for the reduced and used catalyst. For the used catalyst, the peak of Cu $2p_{3/2}$ was symmetric and found at 932.4 eV, which is assigned to Cu^0 species [66]. This indicates that the valence state of Cu on the catalyst did not change during reaction.

2.3.6. N_2O adsorption

Copper surface area (SA_{Cu}) and dispersion (D_{Cu}) were calculated by the N_2O decomposition method [71,72]. As is shown in **Table 2.1**, the catalyst 9.5%CuO/ZSM-5(23) has the worst copper dispersion (0.03) and lowest copper surface area (20.3 m^2/g_{Cu}), which is in agreement with the results of H_2-TPR, SEM (**Figure A.3**) and XPS. On ZSM-5(280), the dispersion of copper decreases slightly from 0.31 to 0.22 with increasing CuO loadings from 6.0% to 19.2%, and the copper surface area decreases from 209.7 to 148.8 m^2/g_{Cu}. However, when the CuO loading was increased to 29.1%, the copper dispersion and the copper surface area drastically decreased to 0.10 and 67.7 m^2/g_{Cu}, respectively. This is in accordance with the result of H_2-TPR (**Figure 2.3**). High loading of copper is not favorable for the copper dispersion [91].

2.4. Results and discussion

2.4.1. Reaction of 2,3-butanediol over catalysts with different SiO_2/Al_2O_3 ratio

Prior to study the effect of SiO_2/Al_2O_3 ratio on the conversion of 2,3-butanediol, the control experiments were performed on the parent zeolites HZSM-5 with different SiO_2/Al_2O_3 ratios (23, 50 and 280) in the absence of hydrogen (N_2 flow: 82.6 cm^3/min, SATP) and the presence of hydrogen (H_2: 67.2 cm^3/min, SATP; N_2: 15.4 cm^3/min, SATP), respectively, at temperature 250 ^{o}C. The conversion of 2,3-butanediol and selectivities of the main products taken at 40 min and 100 min are shown in **Table 2.2**. As is reported [16,34–36], the dehydration reaction of 2,3-butanediol occurs readily on acid catalysts. It can be seen in **Table 2.2**, the conversions of 2,3-butanediol over HZSM-5 under all conditions are very high (>99.0%), and the main products are MEK, 2-methylpropanal and 1,3-butadiene, which is in accordance with the result reported in the literature [34]. In addition, the minor products including 2-methyl-1-propanol, 3-hydroxy-2-butanone and 2-ethyl-2,4,5-trimethyl-1,3-dioxolane were detected, but the selectivities were much lower than the main products mentioned above (see **Table 2.2**). 3-hydroxy-2-butanone was produced via dehydrogenation of 2,3-butanediol, while 2-methyl-1-propanol was from hydrogenation of 2-methylpropanal. The formation of the cyclic ketal 2-ethyl-2,4,5-trimethyl-1,3-dioxolane was reported from the intermolecular condensation of 2,3-butanediol and MEK [32]. However, the selectivities of butenes, which are of interest, are negligible through the conversion of 2,3-butanediol over HZSM-5. Moreover, it can be seen, running the reactions of 2,3-butanediol over each HZSM-5 in the absence or presence of hydrogen led to almost the same result, which indicates that hydrogen is not involved in the conversion of 2,3-butanediol over HZSM-5.

To explore the effect of the framework Si/Al ratio on the catalytic performance in the conversion of 2,3-butanediol to butenes, the reactions were performed over reduced catalysts with about 10wt% of CuO loaded on ZSM-5 zeolites with silica to alumina (SiO_2/Al_2O_3) ratios of 23, 50 and 280 at the same reaction conditions (feed rate of 2,3-butanediol of 3.0 mL/hour, hydrogen to 2,3-butanediol molar ratio of 5, and a reaction temperature 250 ºC). The selectivities of the major reaction products as a function of time on stream for the catalysts with different SiO_2/Al_2O_3 ratios are shown in **Figure 2.7**, and the conversion of 2,3-butanediol and selectivities to the products taken at 40 min and 280 min are shown in **Table 2.3**.

Table 2.2. Conversion of 2,3-butanediol (%) and carbon selectivity of main products (%) on the parent H-ZSM-5 with different SiO_2/Al_2O_3 ratios in 40min and 100 min (shown in parentheses).

	zeolite (without H_2)[a]			zeolite (with H_2)[b]		
	HZSM-5(23)	HZSM-5(50)	HZSM-5(280)	HZSM-5(23)	HZSM-5(50)	HZSM-5(280)
1,3-butadiene (C_4H_6)	10.05 (10.42)	11.11 (11.32)	13.87 (15.36)	10.61 (11.06)	10.42 (12.08)	14.00 (14.48)
butenes (C_4H_8)	0.85 (0.65)	0.64 (0.51)	0.80 (0.50)	0.85 (0.67)	0.67 (0.48)	0.81 (0.48)
MEK (C_4H_8O)	55.30 (54.69)	56.21 (54.36)	52.77 (49.87)	56.32 (55.1)	56.13 (53.65)	53.69 (51.51)
2-methylpropanal (C_4H_8O)	27.95 (27.30)	29.25 (28.21)	29.38 (26.00)	28.79 (28.62)	29.80 (28.44)	28.41 (25.59)
2-methyl-1-propanol ($C_4H_{10}O$)	0.53 (1.23)	0.68 (0.98)	0.68 (1.02)	0.77 (1.24)	0.71 (1.02)	0.67 (0.95)
3-hydroxy-2-butanone ($C_4H_8O_2$)	0.71 (1.68)	0.60 (1.04)	0.76 (1.30)	0.64 (1.37)	0.62 (1.01)	0.81 (1.27)
2-ethyl-2,4,5-trimethyl-1,3-dioxolane ($C_8H_{16}O_2$)	0.36 (0.62)	0.24 (1.71)	0.38 (3.39)	0.10 (0.53)	0.29 (1.36)	0.36 (3.24)
others[c]	4.25 (3.41)	1.27 (1.87)	1.36 (2.56)	1.92 (1.41)	1.36 (1.96)	1.25 (2.48)
conversion	100 (99.65)	100 (99.70)	100 (99.50)	100 (99.71)	100 (99.81)	100 (99.00)

[a] Reaction condition: feed rate of 2,3-butanediol, 3.0 mL/hour; catalyst weight, 1.0 g; temperature, 250 ℃; N_2 flow, 82.6 cm^3/min.

[b] Reaction condition: feed rate of 2,3-butanediol, 3.0 mL/hour; catalyst weight, 1.0 g; temperature, 250 ℃; H_2 flow, 67.2 cm^3/min; N_2 flow, 15.4 cm^3/min.

[c] Other products: acetone, tetramethylfuran, 3,4,5-trimethyl-2-cyclopentenone and aromatics.

It can be seen in **Table 2.3**, the conversion of 2,3-butanediol on all three catalysts were extremely high, especially in the beginning of the reaction, because the dehydration reaction of 2,3-butanediol occurs readily on acid catalysts [16,34–36]. It is reported, dehydration of diols will occur on silica-supported copper catalysts since Cu is a Lewis acid [91]. Hence, Cu in the catalysts will be the active sites for both hydrogenation [56–60] and dehydration reactions. Interestingly, it is observed that the conversion of 2,3-butanediol on 9.5%CuO/ZSM-5(23) is 98.95% at 40 min, which is lower than that of the other two catalysts (almost 100% at 40 min) and the control data of HZSM-5(23) as well (see **Table 2.2**). This is probably due to the deactivation of the Cu/ZSM-5 catalyst.

It can be observed that the selectivities of MEK (**Figure 2.7b**) and 2-methylpropanal (**Table 2.3**), both of which are the main products from dehydration reaction of 2,3-butanediol (see **Table 2.2**) by a pinacol rearrangement [16,30,34–36], decreased with increasing SiO_2/Al_2O_3 ratio in the beginning of reaction (40 min), which is inconsistent with the report that high Si/Al ratio is favorable for the high yield of MEK and high selectivity of 2-methylpropanal [34]. As we can see, on the catalyst with a SiO_2/Al_2O_3 ratio of 23, the MEK (**Figure 2.7b**) selectivity decreased slightly from 35% to 27% over time and the selectivity of 2-methylpropanal (**Table 2.3**) was extremely high (10.65% at 40 min, 9.03% at 280 min); however, on catalyst with SiO_2/Al_2O_3 of 280, the selectivity of MEK was found to be about 20% and the selectivity of 2-methylpropanal was negligible even at 280 min of time on stream. In addition, as seen in **Figure 2.7a**, the catalyst with SiO_2/Al_2O_3 of 280 was found to have significantly higher butene selectivity, which is the sum of the selectivities of 1-butene, cis-2-butene, trans-2-butene and isobutene, than the other two catalysts; butene selectivity increased from 48% at initial 10 min to 65% at 100 min and then tended to be relatively stable. However, the highest butene selectivity over catalysts with SiO_2/Al_2O_3 ratios of 50 and 23 was approximately 50% and 40%, which dropped slightly to 45% and dramatically to 10%, respectively, in 280 min of time on stream.
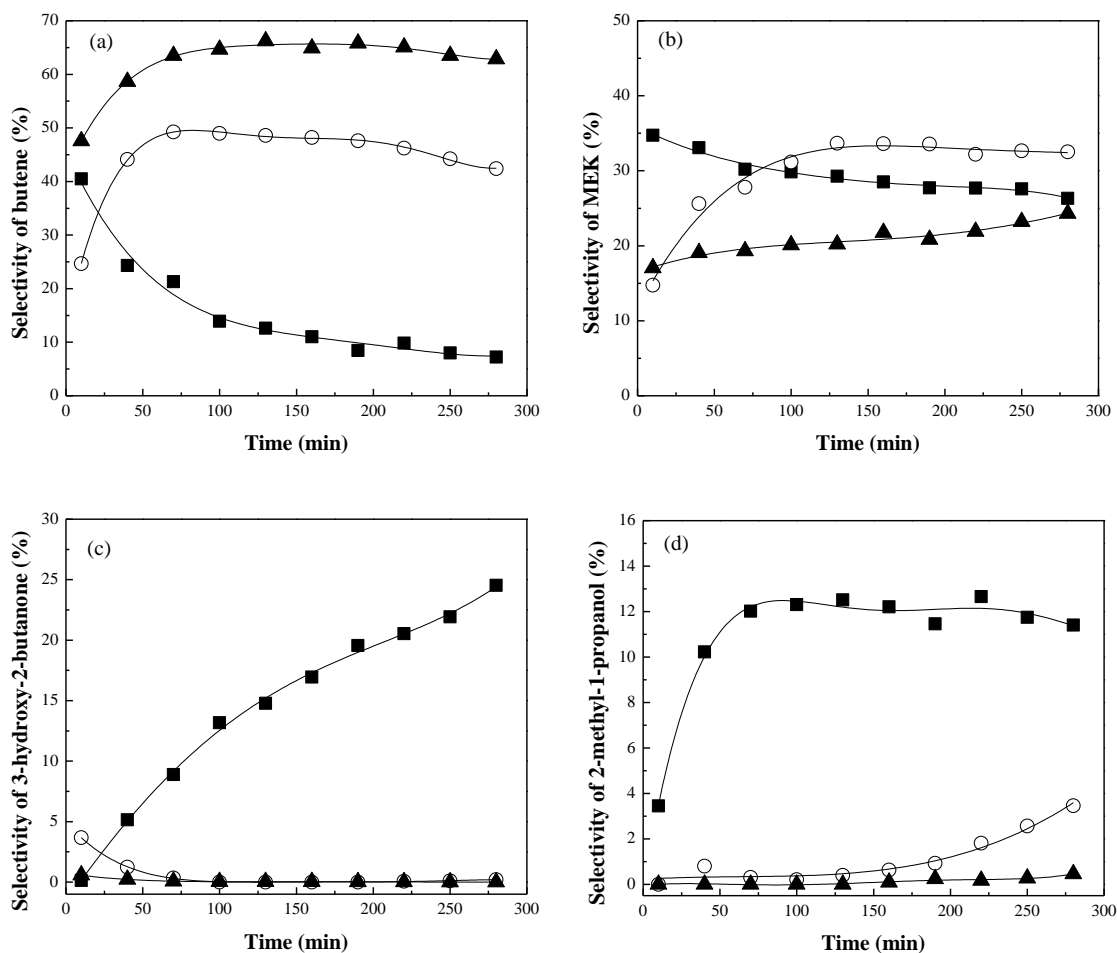
Figure 2.7.Catalytic results as a function of time on stream for the conversion of 2,3-butanediol over reduced copper supported on ZSM-5 with different SiO_2/Al_2O_3: (■) 9.5%CuO/ZSM-5(23), (○) 9.7%CuO/ZSM-5(50), (▲) 9.2%CuO/ZSM-5(280). Carbon selectivity to main products (a) butene, (b) MEK, (c) 3-hydroxy-2-butanone, (d) 2-methyl-1-propanol. Reaction conditions: feed rate of 2,3-butanediol, 3.0 mL/hour; catalyst weight, 1.0 g; H_2/2,3-butanediol (molar ratio), 5:1; temperature: 250 ºC.

Table 2.3. Conversion of 2,3-butanediol (%) and carbon selectivity of the products (%) on reduced Cu/ZSM-5 with different SiO$_2$/Al$_2$O$_3$ ratios in 40 min and 280 min (shown in parentheses)[a].

	catalysts		
	9.5%CuO/ZSM-5(23)	9.7%CuO/ZSM-5(50)	9.2%CuO/ZSM-5(280)
ethylene (C$_2$H$_4$)	0.04 (0.01)	0.36 (0.13)	0.21 (0.15)
propylene (C$_3$H$_6$)	0.38 (0.13)	2.80 (0.79)	1.90 (0.75)
isobutane and butane (C$_4$H$_{10}$)	0.04 (0.03)	0.32 (0.09)	0.18 (0.11)
butenes (C$_4$H$_8$)	24.30 (7.23)	44.13 (42.41)	58.65 (62.84)
C$_5$ olefins (C$_5$H$_{10}$)	0.16 (0.02)	6.02 (0.66)	3.74 (0.79)
C$_6$ olefins (C$_6$H$_{12}$)	0.05 (0.02)	0.16 (0.34)	2.10 (0.12)
C$_7$ olefins (C$_7$H$_{14}$)	0.10 (0.02)	0.52 (0.19)	0.38 (0.19)
C$_8$ olefins (C$_8$H$_{16}$)	0.62 (0.27)	3.37 (1.61)	1.24 (0.72)
MEK (C$_4$H$_8$O)	33.07 (26.31)	25.62 (32.52)	19.06 (24.30)
2-methylpropanal (C$_4$H$_8$O)	10.65 (9.03)	0.03 (4.21)	0 (0.17)
2-methyl-1-propanol (C$_4$H$_{10}$O)	10.23 (11.40)	0.80 (3.46)	0 (0.46)
2,3-butanedione (C$_4$H$_6$O$_2$)	0.21 (1.41)	0.35 (0.02)	0.14 (0.01)
3-hydroxy-2-butanone (C$_4$H$_8$O$_2$)	5.14 (24.53)	1.24 (0.20)	0.22 (0)
2-butanol (C$_4$H$_{10}$O)	0.87 (1.64)	1.00 (0.41)	0.57 (0.22)
2-ethyl-2,4,5-trimethyl-1,3-dioxolane (C$_8$H$_{16}$O$_2$)	1.84 (3.52)	0.05 (0.03)	0.15 (0.01)
ethylbenzene (C$_8$H$_{10}$)	0.45 (0.79)	1.07 (0.71)	0.55 (0.57)
p-xylene (C$_8$H$_{10}$)	0 (0)	1.12 (0.58)	0.72 (0.43)
tetramethylfuran (C$_8$H$_{12}$O)	9.36 (8.37)	2.75 (7.25)	0.98 (3.43)
1-ethyl-3-methyl-benzene (C$_9$H$_{12}$)	0.03 (0.88)	0 (0.10)	0.19 (0.08)
1,3,5-trimethyl-benzene (C$_9$H$_{12}$)	0.12 (0.07)	0.42 (0.15)	0.19 (0.09)
conversion of 2,3-butanediol	98.95 (91.69)	100 (99.80)	100 (99.67)
Distribution of butenes			
1-butene (C$_4$H$_8$)	3.85 (2.40)	4.61 (3.67)	7.62 (7.97)
isobutene (C$_4$H$_8$)	6.82 (0.43)	11.03 (10.90)	11.54 (12.80)
trans-2-butene (C$_4$H$_8$)	7.58 (2.27)	14.45 (13.17)	20.22 (21.43)
cis-2-butene (C$_4$H$_8$)	5.97 (1.80)	12.20 (12.95)	16.91 (18.12)

[a] Reaction conditions: feed rate of 2,3-butanediol, 3.0 mL/hour; catalyst weight, 1.0 g; H$_2$/2,3-butanediol (mol ratio), 5:1; temperature, 250 °C.

Table 2.3 also shows the distribution of the different butene isomers made over all catalysts. All four isomers of butene (1-butene, trans-2-butene, cis-2-butene, and isobutene) were detected. The selectivity of 1-butene is much smaller than the other three isomers (isobutene, trans-2-butene and cis-2-butene) in the initial 40 min. In this work, 1,3-butadiene, which is a major product from dehydration of 2,3-butanediol (see **Table 2.2**), was not detected, suggesting that either it is not formed over the Cu/ZSM-5 catalysts, or that it was immediately hydrogenated to butenes after forming. In addition, the selectivities of butane and isobutene, which could be produced by further hydrogenation of the butenes, were very small (see **Table 2.3**), which indicates that copper catalysts are not favorable for the hydrogenation of butenes to C_4 alkanes in this work.

As discussed above, there is a trend that increasing the Si/Al ratio (lowering acidity of HZSM-5) increases butene selectivity. However, it was also observed that during the first ten minutes of reaction, the selectivity of butene over catalyst with SiO_2/Al_2O_3 of 23 (40%) is higher than with ratio of 50 (25%). This is likely due to the influence of dimerization and cracking reactions that occurred during this period of time. As we can see in **Table 2.3**, the catalyst with a SiO_2/Al_2O_3 of 50 showed the highest selectivity of C_8 olefins (3.37%), which is from dimerization of butenes [19], and highest selectivities of propylene (2.80%) and C_5 olefins (6.02%, the sum of the selectivities of 2-methyl-1-butene, 3-methyl-1-butene and 2-methyl-2-butene), both of which are from cracking reactions [19]. It seems that catalyst with modest acidity (SiO_2/Al_2O_3=50, acidity 0.746 mmol/g) is beneficial for the oligomerization of butenes to form dimers, with subsequent cracking reaction to form ethylene, propylene, C_5, C_6 and C_7 olefins, which reduced the production of butenes especially at the beginning of reaction. It has to be mentioned that the selectivities of products from dimerization and cracking reactions decreased over time due to the deactivation of catalysts.

As mentioned above, a small amount of 3-hydroxy-2-butanone can be seen in the control experiment of conversion of 2,3-butanediol over HZSM-5 (see **Table 2**). which is a product from the dehydrogenation reaction of 2,3-butanediol [36]. Over Cu/ZSM-5 catalyst, 3-hydroxy-2-butanone was also observed (see **Figure 2.7c**) even in the excess of hydrogen present in the reactor (molar ratio of H_2/2,3-BDO=5). Over the catalyst with SiO_2/Al_2O_3 of 23, the selectivity of 3-hydroxy-2-butanone increased dramatically with increasing time on stream (increased from almost 0% to about 25%), which is probably due to deactivation of catalyst. However, the

catalyst with SiO_2/Al_2O_3 ratio of 50 presented activity for dehydrogenation reaction only in the first 70 min on stream, while the selectivity of 3-hydroxy-2-butanone over the catalyst with SiO_2/Al_2O_3 ratio of 280 was negligible. The reaction mechanism will be discussed later.
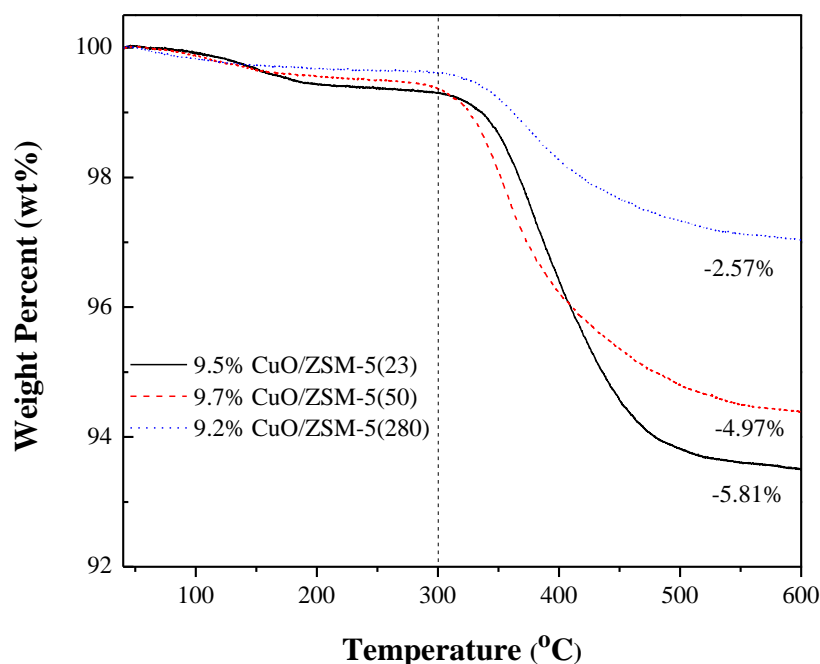
Figure 2.8. Thermogravimetric profile of catalysts after 280 min of reaction. Reaction conditions: feed rate of 2,3-butanediol, 3.0 mL/hour; catalyst weight, 1.0 g; H_2/2,3-butanediol (molar ratio), 5:1; temperature: 250 ºC.

Over the catalyst with a SiO_2/Al_2O_3 ratio of 23, the increase of 2-methyl-1-propanol selectivity is a result of deactivation of catalyst (**Figure 2.7d**). Deactivation of zeolite-based catalysts is mainly due to the formation of coke [92,93], which is a non-desorbed product that prevents access to the acid sites of catalysts. To determine the coke content of the used catalysts, a quantitative analysis of coke formation over the used catalysts after the reaction was investigated by thermogravimetric analysis (TGA). **Figure 2.8** shows the TGA results of the catalysts after 280 min of reaction. As is shown, the coke content on 9.5%CuO/ZSM-5(23) was 5.81%, which was higher than that on 9.7%CuO/ZSM-5(50) (4.97%) and 9.2%CuO/ZSM-5(280) (2.57%). This indicates that the acidity of catalyst is an important cause in coke formation.

Indeed, with more acid sites, the coke formation will occur faster. The coke content on 9.5%CuO/ZSM-5(23) was 4.29% after 40 min of reaction, which was much higher than the other two catalysts (see **Figure A.7**). Hence, the catalyst will deactivate sooner as a result. For this reason, the catalyst with a SiO_2/Al_2O_3 ratio of 23 deactivated faster than the other two catalysts. As is shown in **Table 2.3**, the conversion of 2,3-butanediol over 9.5%CuO/ZSM-5(23) decreased from 98.95% at 40 min to 91.69% at 280 min, while conversion over the other two catalysts remained above 99.0% even after 280 min. In addition, deactivation of catalyst results in the loss of acid sites, decreasing the possibility of dehydration reaction over acid sites, therefore, the selectivity of MEK over the catalyst with a SiO_2/Al_2O_3 ratio of 23 decreased over time. Meanwhile, the selectivity of 2-methyl-1-propanol increased dramatically from 3.5% to 12.0% with time on stream (**Figure 2.7d**), which was accompanied by the decrease of isobutene selectivity from 6.82% at 40 min to 0.43% at 280 min (see **Table 2.3**). Consequently, the selectivity of butenes on 9.5%CuO/ZSM-5(23) showed a decreasing trend over time. It has been reported that copper catalysts are also active in dehydrogenation [42]. Hence, as is seen in **Figure 2.7c** and **Table 2.3**, when deactivation occurred, Cu on 9.5%CuO/ZSM-5(23) turned into the active sites in conversion of 2,3-butanediol to 3-hydroxy-2-butanone and 2,3-butanedione, both of which showed an increasing trend in selectivity with time on stream.

As is mentioned above, large copper clusters were observed on the surface of 9.5%CuO/ZSM-5(23) (see SEM image, **Figure A.3**), which is in accordance with the copper dispersion result (0.03) shown in **Table 2.1**. It is possible that poor copper dispersion and large Cu particle sizes could affect the catalytic reaction, as shown in the literature [59,94]. However, in this work, we believe that the differences noted for the different SiO_2/Al_2O_3 ratios are due to differences in catalyst acidity rather than Cu dispersion or Cu size, since the activity of catalyst 9.7%CuO/ZSM-5(50) was not good as catalyst 9.2%CuO/ZSM-5(280) even though it exhibited a good dispersion of Cu on the surface (0.23, see **Table 2.1**). Over a catalyst with SiO_2/Al_2O_3 of 280, only a trace amount of 2-methyl-1-propanol and 3-hydroxy-2-butanone were found in 280 min of time on stream. Also, it was seen to exhibit the highest selectivity of butenes and lowest selectivites to other byproducts, such as aromatics, 2-ethyl-2,4,5-trimethyl-1,3-dioxolane and tetramethylfuran (**Table 2.3**). Based on the discussion above, it can be concluded that zeolite ZSM-5 with SiO_2/Al_2O_3 ratio of 280 can be chosen as the best support for catalyzing the

hydrodeoxygenation of 2,3-butanediol to butene in a single reactor. Next, we will focus on this zeolite to examine other catalytic properties of catalyst.

2.4.2. Effect of copper content

Figure 2.9 shows the impact of copper loading on catalytic conversion of 2,3-butanediol to main products as a function of time on stream under the same reaction conditions as used in **Figure 2.7** and **Table 2.3** for ZSM-5(280) with four different CuO loadings: 6.0%, 9.2%, 19.2%, and 29.1%. The conversion of 2,3-butanediol and selectivities to the products are shown in **Table A.2**. As is seen, the conversion of 2,3-butanediol was high (> 99%) over all four catalysts.

As is shown in **Figure 2.9a**, the selectivity of butene increased with increasing copper loading, and the catalyst with 19.2wt% of CuO showed the highest catalytic activity toward the production of butene; the selectivity gradually increased from 60% in the initial 10 min to reach a maximum of approximately 71% at 70 min and then dropped slightly to 65% after 310 min on stream. However, it does appear that the catalyst with highest weight loading (29.1wt%) of CuO deactivated faster than the catalysts with lower loadings of CuO (9.2wt% and 19.2wt%). This suggests that it is not necessary to have excessively high loadings of CuO to get high selectivities of butenes.

As seen in **Figure 2.9b**, the selectivity of MEK showed a decreasing trend with increasing weight loading of copper. As copper is the active site of hydrogenation reaction, higher copper loading is expected to favor the hydrogenation of MEK to butenes, resulting in a lower selectivity of MEK. It can also be seen that the selectivity of MEK over catalysts showed a general tendency to increase gradually with increasing time on stream, which can be ascribed to the deactivation of catalysts.
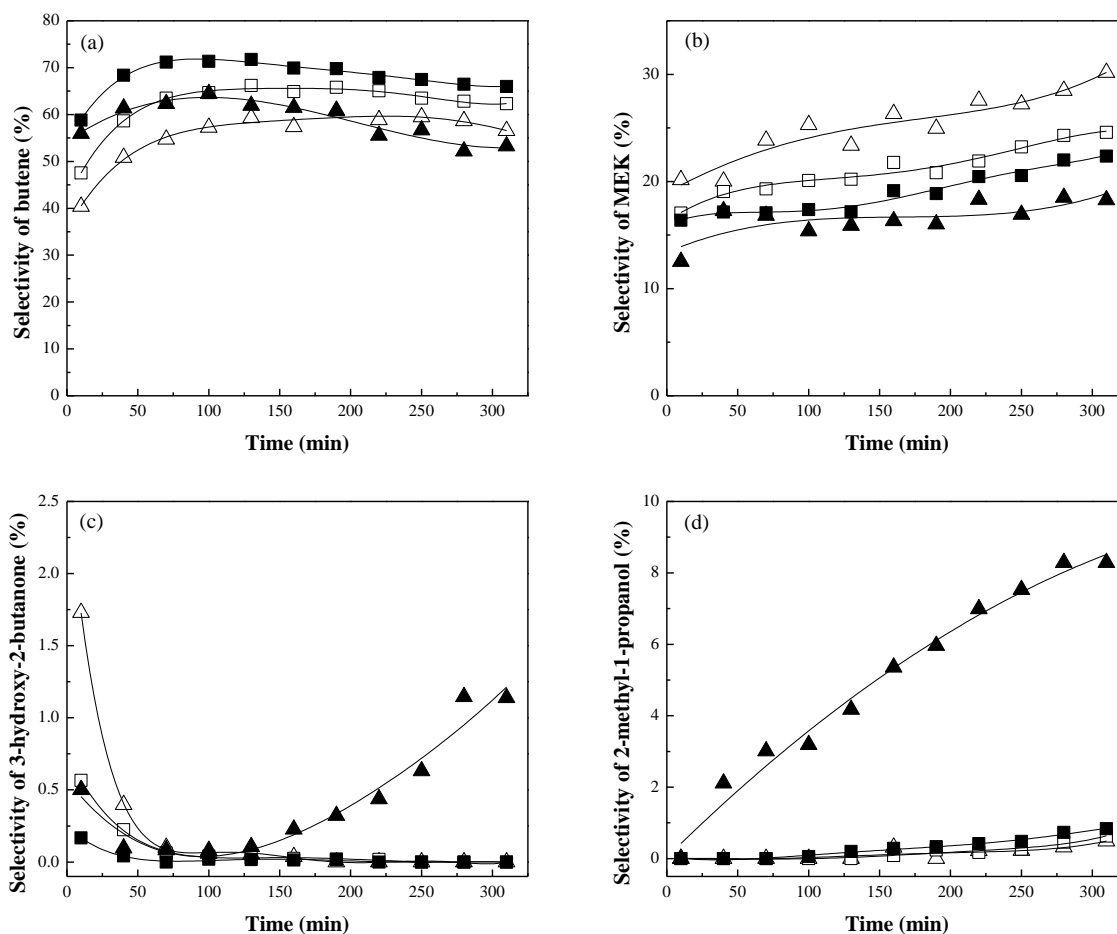
Figure 2.9. Catalytic results for the conversion of 2,3-butanediol to butene over different copper loadings on ZSM-5 (SiO₂/Al₂O₃=280). (△) 6.0%CuO/ZSM-5(280), (□) 9.2%CuO/ZSM-5(280), (■) 19.2%CuO/ZSM-5(280), (▲) 29.1%CuO/ZSM-5(280). Carbon selectivity to main products (a) butene, (b) MEK, (c) 3-hydroxy-2-butanone, (d) 2-methyl-1-propanol. Reaction conditions: feed rate of 2,3-butanediol, 3.0 mL/hour; catalyst weight, 1.0 g; H₂/2,3-butanediol (molar ratio), 5:1; temperature: 250 °C.

Figure 2.9d shows the selectivity of 2-methyl-1-propanol over catalysts with time on stream. With the exception of the catalyst with 29.1wt% of CuO loading, catalysts showed similar behaviors towards the selectivity of 2-methyl-1-propanol, which increased slightly from 0% to about 0.6% with time on stream. However, over the catalyst with highest loading of CuO (29.1wt%) in this work, the selectivity of 2-methyl-1-propanol increased dramatically from 0 to 8.5%. In addition, the selectivity of 2-methylpropanal (**Table A.2**) was negligible except on the catalyst with highest CuO loading (29.1wt%). These trends may be due to the low copper

dispersion (0.10, see **Table 2.1**) on the catalyst with 29.1% CuO, which is not favorable for dehydration of alcohols to butenes and hydrogenation of 2-methylpropanal, leading to high selectivities of 2-methyl-1-propanol and 2-methylpropanal.

The selectivity of 3-hydroxy-2-butanone with time on steam is depicted in **Figure 2.9c**. As seen in **Figure 2.9c**, in the initial 10 min, the catalyst with the lowest CuO loading (6wt%) exhibited the highest selectivity of 3-hydroxy-2-butanone (1.8%), however, catalyst with 19.2wt% of copper loading presented the lowest, 0.2%. By comparison with the control data of HZSM-5(280) (see **Table 2.2**), we suggest that the formation of 3-hydroxy-2-butanone in the initial reaction is probably from the dehydrogenation of 2,3-butanediol over HZSM-5(280). The selectivities of 3-hydroxy-2-butanone tended to decrease with time on stream, reaching 0 after 100 min, with the exception of the catalyst with 29.1wt% CuO, on which selectivity was observed to decrease from 0.5% to 0.1% at 100 min, and then increased steadily to 1.2% at 310 min, which probably can be attributed to low copper dispersion. Torresi et al investigated the conversion of 1,3-butanediol by dehydrogenation and dehydration reactions on CuO/SiO_2, and found that dehydrogenation predominated over catalysts with high copper loading [91], which is similar to our finding in this work.

In addition, over catalysts with different copper loadings, it can be seen that the selectivities of C_8, C_7, C_5 and C_3 olefins and 2-butanol (**Table A.2**) were higher on the catalyst with lower CuO loadings (6.0% and 9.2%), which indicates that lower copper loadings favored the dimerization of butenes, and subsequent cracking reaction and the formation of 2-butanol (the intermediate to form butenes), especially in the first 40 min of stream. The optimal amount of copper is not yet clear. As discussed in the literature [91], on SiO_2, the copper monolayer surface coverage is about 13.5wt% of Cu (e.g. 16.9wt of CuO), which is close to the CuO loading (19.2wt%) on the catalyst that gave the highest butene selectivity. The optimal performance is the result of a balance between copper and acid catalytic functions.

2.4.3. Effect of hydrogen to 2,3-butanediol ratio

The impact of hydrogen to 2,3-butanediol ratio on the catalytic performance of 19.2wt%CuO/ZSM-5(280) for conversion of 2,3-butanediol to main products with time on stream is depicted in **Figure 2.10** and the selectivities of the products are shown in **Table A.3**.

All conditions exhibit high conversion of 2,3-butanediol, though these is a general increasing trend with increasing hydrogen to 2,3-butanediol ratio.

As expected, the dehydrogenation reaction is an important reaction at low H_2/2,3-BDO ratio, especially when the ratio is below 2 (see **Figure 2.10c** and 2,3-butanedione in **Table A.3**). The selectivity of 3-hydroxy-2-butanone generally increased with increasing time on stream and decreased when H_2/2,3-BDO ratio was increased from 0 to 5. The selectivities of 2,3-butanedione at 40 min and 280 min also decreased with increasing H_2/2,3-BDO ratios. At H_2/2,3-BDO of 5, it can be seen that the dehydrogenation was suppressed, as indicated by the negligible amount of 3-hydroxy-2-butanone and 2,3-butanedione present.

The main trend of interest is that butene selectivity increases as H_2/2,3-BDO ratio increases (see **Figure 2.10a**), which is attributed to the fact that hydrogen has a positive impact on catalytic activity towards the hydrogenation reaction. Also, it was observed that the selectivity of butene decreases with increasing time on stream, which is due to the deactivation of catalysts especially with low H_2/2,3-BDO ratios of 0 and 1. Interestingly, butenes can be formed even in the absence of H_2 (H_2/2,3-BDO=0), which are higher than the control data of HZSM-5(280) without H_2 (see **Table 2.2**). As mentioned above, the dehydrogenation reaction became the main reaction at low H_2/2,3-BDO ratios. We suggest that H_2 formed in the process of dehydrogenation of 2,3-BDO is involved in the hydrogenation reactions to produce the butenes.

The impact of H_2/2,3-BDO ratio towards MEK selectivity is shown in **Figure 2.10b**. It is observed that the selectivity of MEK decreases with increasing H_2/2,3-BDO ratios from 2 to 5, and H_2/2,3-BDO ratio of 2 exhibits the highest and most stable selectivity (about 30%-34%) of MEK. At H_2/2,3-BDO ratios of 0 and 1, the selectivities of MEK decreased dramatically over time due to the deactivation of catalysts which lead to decreasing catalytic activity for dehydration. Meanwhile, the selectivities of 3-hydroxy-2-butanone and 2,3-butanedione increased dramatically over time in such conditions. This indicates that the dehydrogenation reaction became dominant at the conditions with low hydrogen.
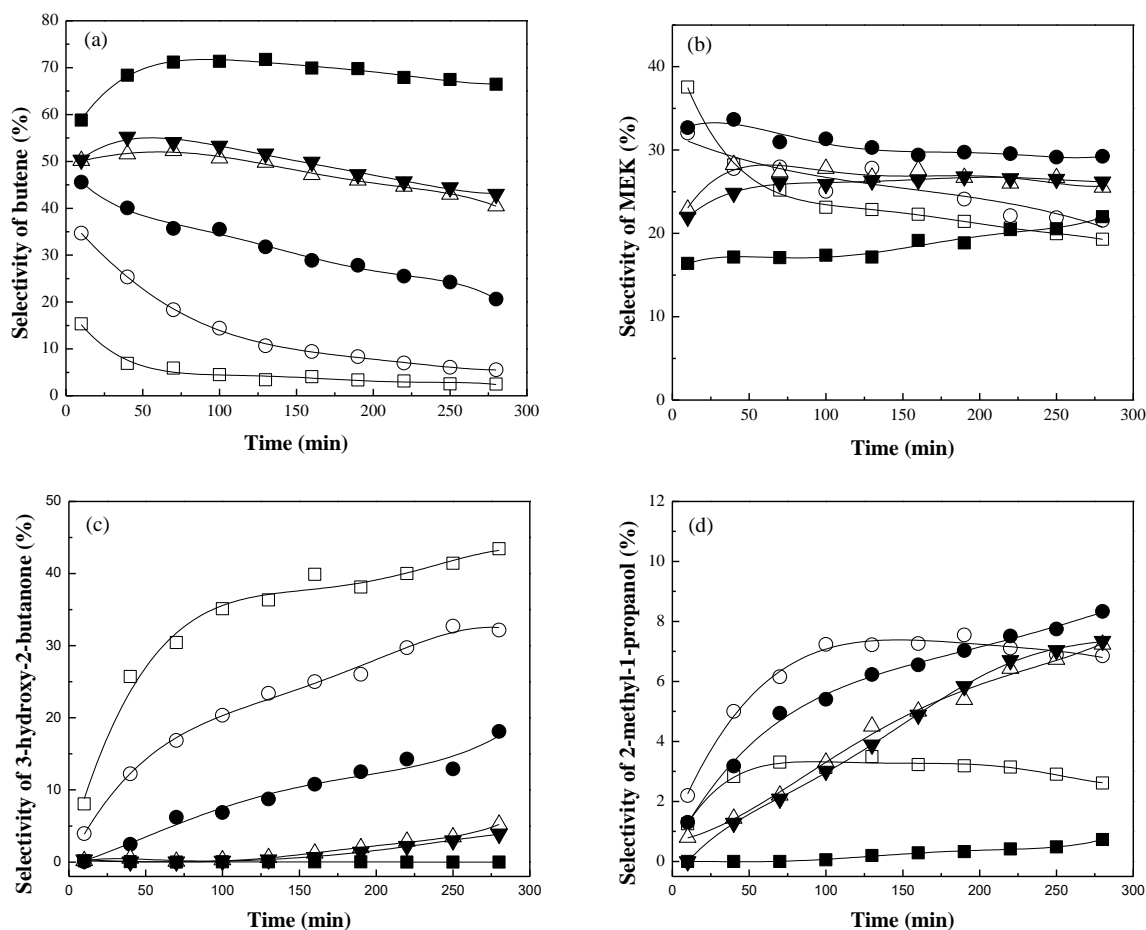
Figure 2.10. Catalytic results for the conversion of 2,3-butanediol to butene over 19.2 wt% copper supported on ZSM-5 (Si/Al$_2$O$_3$=280) at a hydrogen to 2,3-BDO ratio of: (□)0, (○)1, (●) 2, (△) 3, (▼) 4, (■) 5. Carbon selectivity to main products (a) butene, (b) MEK, (c) 3-hydroxy-2-butanone, (d) 2-methyl-1-propanol. Reaction conditions: feed rate of 2,3-butanediol, 3.0 mL/hour; catalyst: 19.2wt%CuO/ZSM-5(280); catalyst weight, 1.0 g; temperature, 250 °C.

The selectivity of 2-methyl-1-propanol with time on stream is depicted in **Figure 2.10d**. This selectivity increases with decreasing H$_2$/2,3-BDO ratio from 5 to 2. It is well known that hydrogen can improve the catalytic stability of zeolite catalysts due to the inhibition effect of the hydrogen on coke formation [95–97] by reacting with carbenium ions to limit the formation of carbonaceous compounds responsible for deactivation, which is in agreement with the TGA results (see **Figure A.8**). With decreasing H$_2$/2,3-BDO ratio, more coke is formed (**Figure A.8**), and faster catalyst deactivation is observed, resulting in increasing selectivity of 2-methyl-1-propanol over time. At the H$_2$/2,3-BDO ratio of 5, the catalyst exhibited extremely high catalytic

43

activity for hydrogenation and dehydration reactions, resulting in negligible selectivity of 2-methyl-1-propanol, which is expected to be converted to isobutene. As is shown in **Figure 2.10d**, however, when the H_2/2,3-BDO ratio is decreased from 1 to 0, the selectivity of 2-methyl-1-propanol decreases. This is because dehydrogenation of 2,3-butanediol to 3-hydroxy-2-butanone and 2,3-butanedione becomes the dominant reaction pathway under the conditions with low hydrogen. As is seen in **Table A.3**, with different H_2/2,3-BDO ratios, it can be seen that lower H_2 partial pressures is not favorable for the cracking reaction. Another product from dehydration reaction, 2-methylpropanal, exhibited a decreasing trend of selectivity with increasing H_2/2,3-BDO ratios from 0 to 5, decreasing from 13.15% to 0 at 40 min, which is the source of 2-methyl-1-propanol and isobutene.

In conclusion, hydrogenation reactions are essential towards getting high butene selectivities. Higher H_2/2,3-BDO ratios are better for catalyzing hydrogenation reactions because hydrogen can improve catalytic stability of zeolite catalysts.

2.4.4. Effect of temperature

The impact of temperature on the selectivities of the main product on 19.2wt%CuO/ZSM-5(280) as functions of time on stream is depicted in **Figure 2.11**. The conversion of 2,3-butanediol and selectivities of the products in 40 min and 310 min are shown in **Table A.4**. All temperatures except 230 ^{o}C exhibit the stable and high conversion of 2,3-butanediol, with conversions of nearly 100%. However, at lower temperature (230 ^{o}C), the conversion is relatively lower at 310 min (93.11%) due to deactivation.

As seen in **Figure 2.11a,** with the exception of 230 ^{o}C, the selectivity of butene decreased with increasing temperature, which is mainly due to oligomerization of butenes, and subsequent cracking reactions, resulting in lower selectivity of butene and higher seletivities of C_3, C_5, C_6, C_7 and C_8 olefins (see **Table A.4**). In particular, at a temperature of 250 ^{o}C, the catalyst exhibits the highest selectivity of butene. A high butene selectivity (55%) is initially observed for the lowest temperature (230 ^{o}C), but it dramatically decreased to 10% over 310 min.

Figure 2.11b displays the selectivity of MEK at various reaction temperatures. The initial selectivity of MEK decreases with increasing temperature. However, at 300 ^{o}C, the selectivity of MEK increased from 0 during the initial 10 min to 26% at 310 min, indicating catalyst deactivation. As we can see, low temperature (230 ^{o}C) favored the production of 2-methyl-1-

propanol over time (**Figure 2.11d)** and formation of 2-methylpropanal (**Table A.4**), accompanied by low selectivity of butenes. This is also due to the deactivation of catalyst. From TGA results (see **Figure A.9**), we can see the sharp weight loss (-0.8%) between 220 ^{o}C and 300 ^{o}C on the used catalyst after reaction at 230 ^{o}C, which is reported due to the formation of heavy oligomers from butenes that do not evaporate on zeolites [19]. However, at higher temperature, the heavy products can evaporate or be cracked into smaller molecules, reducing coke deposition [19]. And at extremely higher temperatures (270 ^{o}C and 300 ^{o}C), the deactivation of catalyst is due to hard coke formation at high temperature [92]. From the TGA (**Figure A.9**), we can see the weight loss on the used catalysts after reaction at 270 ^{o}C and 300 ^{o}C are mainly between 400 ^{o}C and 600 ^{o}C, which are due to the combustion of "hard coke" [98–100].

The selectivity of 3-hydroxy-2-butanone at various temperatures with time on stream is depicted in **Figure 2.11c**. Clearly, low temperatures favor the dehydrogenation reaction of 2,3-butanediol to lose one hydrogen atom from one hydroxyl group, especially after 100 min of stream. However, at higher temperatures like 270 ^{o}C and 300 ^{o}C, 2,3-buanediol is likely to lose two hydrogen atoms from both hydroxyl groups to form 2,3-butanedione (see **Table A.4**).

As discussed above, higher temperatures (270 ^{o}C and 300 ^{o}C) are beneficial for the oligomerization and cracking reactions, resulting in significantly higher selectivities of C_3 and C_5^+ olefins. Moreover, it should be noted that higher temperatures lead to higher selectivities of heavy products, such as aromatic compounds (**Table A.4**) and C_4 alkanes (isobutene and butane, see **Table A.4**).
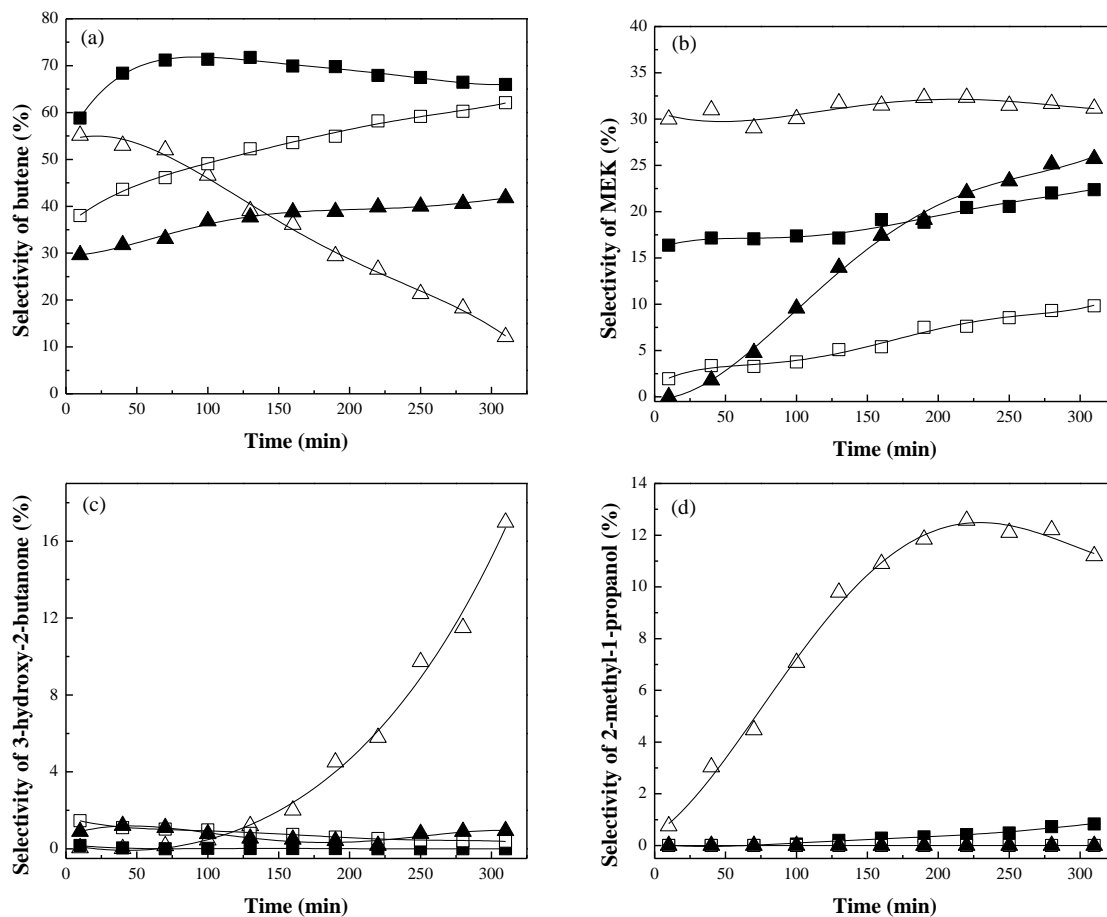
Figure 2.11. Catalytic results for the conversion of 2,3-butanediol to butene over 19.2 wt% CuO supported on ZSM-5 (Si:Al$_2$O$_3$=280) at a hydrogen to 2,3-BDO ratio of 5 at different reaction temperatures: (△) 230 ºC, (■) 250 ºC, (□) 270 ºC, (▲) 300 ºC. Carbon selectivity to main products, (a) butene, (b) MEK, (c) 3-hydroxy-2-butanone, (d) 2-methyl-1-propanol. Reaction conditions: feed rate of 2,3-butanediol, 3.0 mL/hour; catalyst: 19.2wt%CuO/ZSM-5(280); catalyst weight, 1.0 g; H$_2$/2,3-BDO (molar ratio)=5.

2.4.5. Regeneration of catalysts
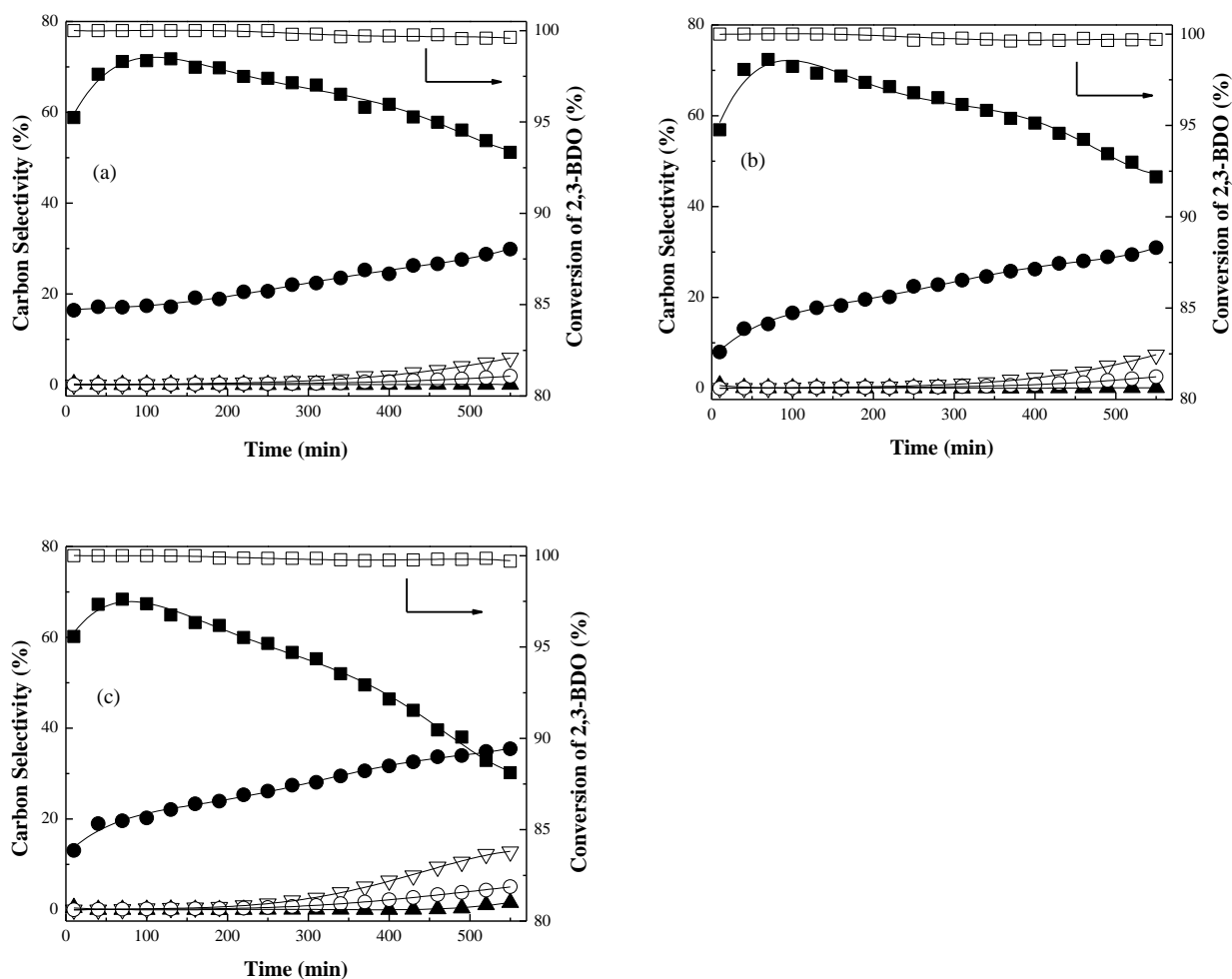
Figure 2.12.Catalytic results for the conversion of 2,3-butanediol over reduced catalysts (a) fresh catalyst 19.2%CuO/ZSM-5(280), (b) 19.2%CuO/ZSM-5(280) after first regeneration, (c) 19.2%CuO/ZSM-5(280) after second regeneration. Selectivity to products: (■) butene, (●)MEK, (▲) 3-hydroxy-2-butanone, (▽) 2-methyl-1-propanol, (○)2-methylpropanal, (□) conversion of 2,3-butanediol. Reaction conditions: feed rate of 2,3-butanediol, 3.0 mL/hour; catalyst weight, 1.0 g; H$_2$/2,3-BDO (molar ratio)=5; reaction temperature, 250 ºC.

Since deactivation of the catalyst was shown to be an issue, we have investigated whether the catalyst can be regenerated by heating in air. Deactivation by coke is reversible, because generally coke can be removed by oxidation [101,102]. This would be expected to regenerate the catalyst if coke deposition is the main source of deactivation [103], but not if sintering or other structural rearrangement was responsible. Experiments were run where 19.2% CuO on ZSM-5 (280, Si/Al$_2$O$_3$ ratio) was regenerated twice under air with air flow 120 cm^3/min at 550 ºC for 3

47

hours. **Figure 2.12a** shows the initial catalytic performance, while **Figure 2.12b** and **Figure 2.12c** show the performance after the first and second regenerations, respectively. As seen by comparison of these three Figures, regeneration under air is capable to yielding a catalyst with almost identical performance as the initial fresh catalyst. It is remarkable that high conversion of 2,3-butanediol (almost 100%) is exhibited by the catalysts, even ones displaying signs of deactivation. However, after a second regeneration, the catalytic activity, especially the selectivity of butene, is shown to drop faster than the fresh or used catalyst after the first regeneration, which is probably due to the formation of stable or hard coke species agglomerated on the zeolite in the first and second runs which cannot be removed by the regeneration procedure.

2.4.6. Hydrogenation of MEK
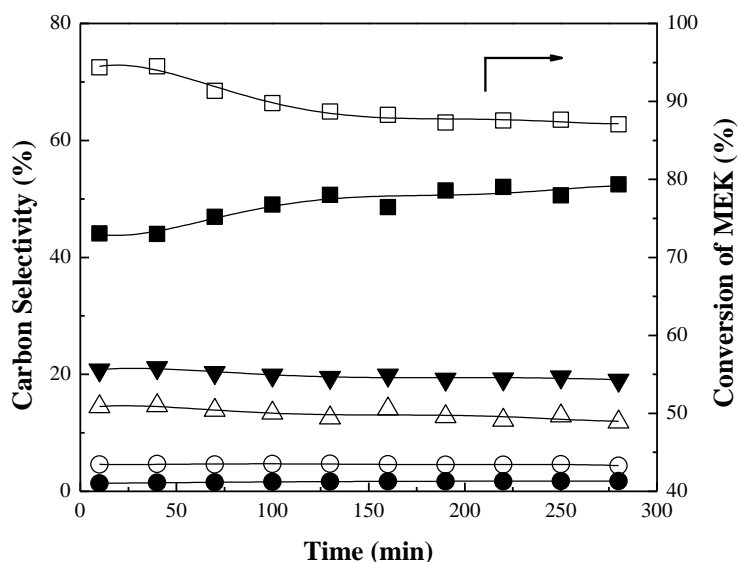
Figure 2.13.Catalytic results for the conversion of MEK over reduced catalyst 19.2%CuO/ZSM-5(280) with time on stream. Selectivity to products: (■)butene, (○)propylene, (△)pentene, (▼)C$_6^=$-C$_8^=$, (●)2-butanol, (□)conversion of MEK. Reaction conditions: feed rate of MEK, 3.0 mL/hour; catalyst weight, 1.0 g; H$_2$/MEK (molar ratio)=5.

As discussed above, the results suggest that MEK and 2-methylpropanal are the intermediates in the conversion of 2,3-butanediol to butene. To explore the roles of the intermediate in conversion of 2,3-butanediol, hydrogenation reactions of MEK and 2-

methylpropanal were conducted under similar reaction conditions to those used for 2,3-butanediol conversion. **Figure 2.13** shows the catalytic results of conversion of MEK over 19.2wt% CuO/ZSM-5(280) with time on stream. As we can see, the selectivity of butene is high (about 50%), although it is not as high as when 2,3-butanediol was the reactant. Interestingly, the results show that the selectivities of C_5-C_8 olefins are significantly higher in comparison with the result from 2,3-butanediol. Similar results are also observed in hydrogenation reaction of 2-methylpropanal, in which, the oligomerization and cracking reactions became dominant catalytic processes (see **Figure A.10**), with selectivities of C_5-C_8 olefins higher than butenes. The reason why the formation of C_6-C_8 olefins are favorable when MEK and 2-methylpropanal are used as reactants is likely because no acid sites are required to dehydrate 2,3-BDO to MEK and 2-methylpropanal, so more acid sites are available for dehydration of 2-methyl-1-propanol and 2-butanol to butenes, and the subsequent oligomerization and cracking reactions as well.
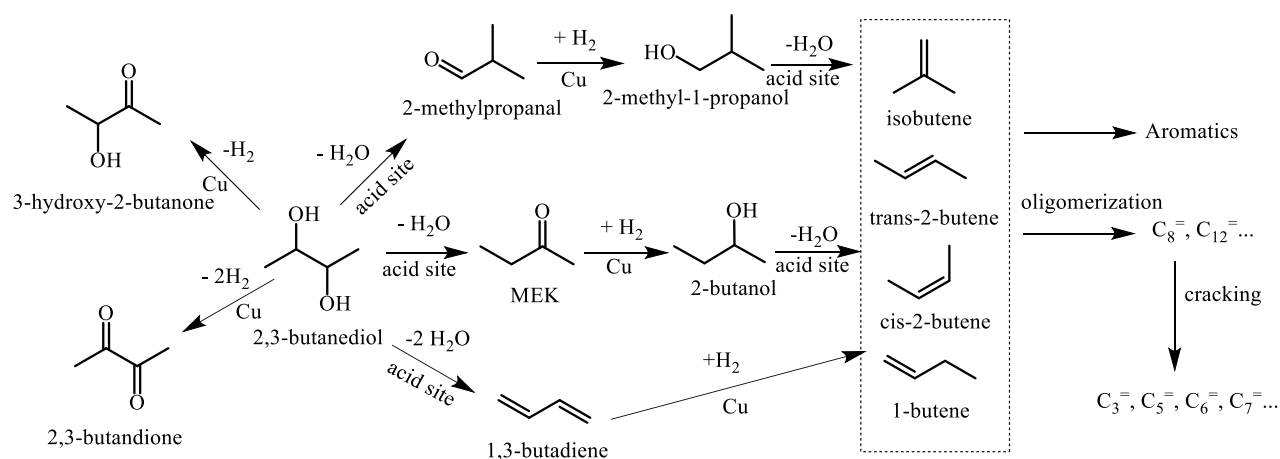
Scheme 2.1. Probable reaction pathways in the hydrodeoxygenation of 2,3-butanediol to products.

Based on the results discussed above, we summarize the probable reaction pathways in the hydrodeoxygenation of 2,3-butanediol in **Scheme 2.1**. The primary pathways involve dehydration and hydrogenation reactions. Over acid sites (including Cu sites), 2,3-butanediol is dehydrated to form primarily MEK and 2-methylpropanal [34]. MEK and 2-methylpropanal are converted to 2-butanol and 2-methyl-1-propanol, respectively, over copper sites through

hydrogenation. Finally, 2-butanol is dehydrated to form 1-butene, trans-2-butene and cis-2-butene and 2-methyl-1-propanol is converted to isobutene through dehydration. 1,3-butadiene, which is a product from dehydration of 2,3-BDO [34], is undetectable in this work. For this reason, a route to butenes via 1,3-butadiene as an intermediate is possible, but likely not very important. Once butenes are formed, they can be oligomerized to form dimers, trimers, etc, via a carbenium-ion mechanism [104], which can further be cracked to other olefins like propylene, pentene, etc. In addition, 2,3-butanediol can be converted to 3-hydroxy-2-butanone and 2,3-butandione via dehydrogenation reactions on copper sites.

2.5. Conclusions

The conversion of 2,3-butanediol to butenes in a single reactor has been demonstrated with a 70% yield over Cu/ZSM-5. Enhanced butene yields were achieved with a high SiO_2/Al_2O_3 ratio, with the best results achieved at $SiO_2/Al_2O_3=280$. This is attributed to the lower acidity of the high silica catalysts. Increasing copper loading had a relatively minor impact on catalytic results, though in general butene yield increased with copper loading. Deactivation of the catalysts due to coke formation was noted on all catalysts as product selectivities changed over a five-hour run time, but the original activity could be restored by heating the catalyst in air.

The impact of reaction conditions showed that the optimal temperature is around 250 ^{o}C. Lower temperature (230 ^{o}C) is beneficial for dehydrogenation of 2,3-butanediol; higher temperatures (270 ^{o}C and 300 ^{o}C) favor the oligomerization and cracking reactions, resulting in significantly higher selectivities of C_3 and C_5^+ olefins. The results show that hydrogenation reactions are essential towards getting high butene selectivities, and higher hydrogen to 2,3-butanediol ratios are favorable for catalyzing hydrogenation reactions. Dehydrogenation reactions become dominant for conditions with low hydrogen, especially when $H_2/2,3$-BDO ratios are below 2. The reaction mechanism demonstrated that MEK and 2-methylpropanal are the intermediates in the conversion of 2,3-butanediol to butenes. The optimal performance toward the production of butene is the result of a balance between copper and acid catalytic functions.

Chapter 3 - Kinetic study of 2,3-butanediol to butenes

3.1. Introduction

Recently 2,3-butanediol (2,3-BDO) has attracted substantial interest as a potential renewable feedstock for the production of fuels and chemicals. Zhang et al. [34] investigated the dehydration of 2,3-BDO over zeolite HZSM-5 and HZSM-5 modified with boric acid, and they reported that high Si/Al ratio was beneficial to low-temperature activation of 2,3-BDO and the methyl migration to 2-methylpropanal, and the addition of boric acid enhanced the catalytic stability. Duan et al. [36] investigated the dehydration of 2,3-BDO over monoclinic ZrO_2 and the result showed that 3-buten-2-ol was produced with a maximum selectivity of 59.0% along with major byproducts such as MEK and 3-hydroxy-2-butanone. Duan and coworkers [38] also investigated dehydration of 2,3-BDO to 1,3-butadiene over Sc_2O_3 and the maximum butadiene selectivity they obtained was 94 % with 100 % BDO conversion on a two-bed catalyst system (Sc_2O_3 +Al_2O_3) [38]. More recently, Liu et al. [37] used γ-alumina to catalyze the direct production of 1,3-butadiene from 2,3-butanediol and they suggested that under the optimized kinetic reaction conditions (trace amount of γ-alumina, high flow rate), the production of MEK and 2-methylpropanal was significantly reduced, while the selectivity of 1,3-butadiene could be obtained up to 80%. Harvey et al. [33] developed a pathway to selectively convert 2,3-butanediol by acid catalyst Amberlyst-15 to a complex mixture of 2-ethyl-2,4,5-trimethyl-1,3-dioxolanes and 4,5-dimethyl-2-isopropyl dioxolanes, which can be used as a gasoline-range fuel and diesel oxygenate due to an anti-knock index of 90.5, high combustion value, low solubility in water and full miscibility with both gasoline and diesel fuel. Our previous work has shown that bifunctional catalyst Cu/ZSM-5 can convert 2,3-butanediol to butenes with high selecitivty (~70%) in the presence of H_2 at 250 ^{o}C, and the optimal performance is the result of a balance between copper and acid catalytic functions [105].

The functionalized nature of 2,3-butanediol means that a variety of reactions can occur, especially when multiple catalyst functionalities are present. For example, our recent work to produce butene from 2,3-butanediol in the presence of hydrogen over an acid-metal bifunctional catalyst involved complex chemistry where 2,3-BDO could be dehydrogenated to acetoin and butanedione, dehydrated to MEK and 2-methylpropanal which could in turn be hydrogenated to butanol which can then be dehydrated to butenes. Even further reactions are possible from the

butenes. This complicated reaction scheme suggests a need for a systematic measurement of reaction kinetics for 2,3-BDO and its products over catalysts of interest. Such work could impact not only our approach of producing butenes from 2,3-BDO, but also other research to produce butadiene and MEK.

This research studies the reaction kinetics of 2,3-BDO and other key intermediates in 2,3-BDO chemistry (including methyl ethyl ketone, 2-methylpropanal, acetoin, 2-butanol, and 2-methyl-1-propanol) over acidic zeolites (ZSM-5 and Y-type), supported copper zeolites, and copper supported on silica. Through these experiments, the roles of acid and metal sites can be elucidated and possible reaction pathways to specific products can be proposed.

3.2. Experimental

3.2.1. Materials

Commercial zeolites NH_4^+-ZSM-5 (CBV 2314, SiO_2/Al_2O_3=23; CBV 5524G, SiO_2/Al_2O_3=50; CBV 28014, SiO_2/Al_2O_3=280, Zeolyst International), H-ZSM-5 (Zeocat PZ-2/500H, SiO_2/Al_2O_3=500, Zeochem), H-ZSM-5 (HSZ-890HOA, SiO_2/Al_2O_3=1500, Tosoh Corporation), HY (CBV 400, SiO_2/Al_2O_3=5.1; CBV 760, SiO_2/Al_2O_3=60, Zeolyst International), HY (HSZ-390HUA, SiO_2/Al_2O_3=500, Tosoh Corporation) and commercial fumed SiO_2 (Cab-O-Sil EH-5, Cabot Corporation) were employed as supports or catalysts. ZSM-5 and HY are referred to as ZSM-5(n) and HY(n), respectively, where n stands for the SiO_2/Al_2O_3 ratio. $Cu(NO_3)_2 \cdot 3H_2O$ (99%, Fisher scientific) was used as metal precursor. 2,3-butanediol (>97%, TCI America), acetoin (96%, Fisher Scientific), methyl ethyl ketone (>99%, Fisher Scientific), 2-methylpropanal (>99%, Fisher Scientific), 2-butanol (99.5%, Sigma-Aldrich) and 2-methyl-1-propanol (99.5%, Sigma-Aldrich) were used as reactants to investigate the reaction rate of each reaction. As acetoin exists as a solid dimer (2,3,5,6-tetramethyl-1,4-dioxane-2,5-diol) at room temperature, acetoin was used in the reaction as aqueous solution with concentration of 85 wt% in order to avoid clogging the pump. Quartz sand (40-60 mesh, X-fine, Quartz Plus, Inc) was used as an inert to dilute the catalysts.

3.2.2. Catalyst preparation

Preparation of catalysts has been described in the previous report [105]. To make 20wt% of CuO loading catalysts, typically, 36.24 g of $Cu(NO_3)_2 \cdot 3H_2O$ was dissolved in 100 mL of deionized water at room temperature, followed by adding ammonia hydroxide (28-30wt%, Fisher Scientific) until the pH reached 9.1 to form a dark blue cupric ammine complex $[Cu(NH_3)_4(H_2O)_2]^{2+}$, and then water was added to make 250 mL of a copper-ammonia complex solution. 20 g of zeolite (or SiO_2) was added to the solution and then the container was capped to avoid the evaporation of ammonia and stirred for 4 hours at room temperature. After that, the container was transferred to an oil bath and heated to 60 ^{o}C (for Cu/Y zeolites, the temperature is room temperature) for 2 hours. Then the solid was recovered by filtration, washed, dried at 110 ^{o}C, and calcined in air at 550 ^{o}C for 4 h. Finally, the calcined catalyst was pelletized, crushed and sieved to obtain a particle size distribution in the range 40-60 mesh. The content of CuO was determined (shown in **Table 3.2**) by the inductively coupled plasma (ICP) method. The copper catalysts were named as Cu/ZSM-5(n), Cu/Y(n) and Cu/SiO_2, where n is the SiO_2/Al_2O_3 ratio.

3.2.3. Catalyst characterization

BET surface area and porosity of catalysts were determined from Brunauer−Emmett−Teller (BET) gas (nitrogen) adsorption method measured on Quantachrome Autosorb-1 instrument at -196°C and analyzed with Autosorb-1 software. Before measurement, the samples were evacuated at 350 ^{o}C for 4 h. The acid properties of samples were investigated by temperature programmed desorption of ammonia (NH_3-TPD) in an Altamira AMI-200 system equipped with a thermal conductivity detector. Powder X-ray diffraction (XRD) patterns of the samples were recorded using Rigaku Miniflex II desktop x-ray diffractometer. Scans of two theta angles were from 5° to 90° for all catalysts with a step size of 0.02^o and scan speed of 0.75 ^{o}/min. The reducibility of the calcined catalysts was determined by temperature programmed reduction (H_2-TPR), which was carried out on the same system as NH_3-TPD. Copper surface area and dispersion were determined by dissociative N_2O adsorption method at 90 ^{o}C using the same system as H_2-TPR and NH_3-TPD. (The detailed procedures of all characterization are described in ref [105].)

3.2.4. Catalytic reaction

The catalytic reactions were performed in a conventional continuous flow fixed-bed reactor made of stainless steel (id=8 mm) under atmospheric pressure [105]. Prior to reaction, the catalyst sample was reduced in the reactor in the H_2/N_2 flow (flow rate of $H_2/N_2=1/5$) at 300 ^{o}C for 2 h. The H_2 flow of 24 cm^3/min (standard ambient temperature and pressure, SATP) and the N_2 flow of 120 cm^3/min (SATP) were controlled with mass-flow controllers (Brooks). Different chemicals, such as 2,3-butanediol, acetoin, MEK, 2-methylpropanal, 2-butanol and 2-methyl-1-propanol, were employed as reactants to investigate the reaction rate or turnover frequency (TOF) of each reaction over various catalysts (or supports). Typically, the reactant was fed via a micropump (Eldex 1SMP) at 3 mL/h together with a H_2 flow of 67.2 cm^3/min (SATP) and N_2 flow of 15.4 cm^3/min (SATP). The reaction temperature was set at 250 ^{o}C according to the previous report [105]. For the kinetic study, the catalyst was diluted with inert quartz sand to a total weight of 1 g to adjust the conversion to a comparable level (30%-80%). Product compositions were analyzed by an on-line gas chromatograph (SRI 8610C) equipped with an MXT-1 column (nonpolar phase, 60m, ID 0.25 mm, film thickness 0.25 µm), TCD and FID detectors for the analysis of hydrocarbons and oxygenated chemicals, and quantified by injecting calibration standards to the GC system. The temperature of the tubing from the bottom of the reactor to the inlet of GC was maintained at 230 ^{o}C to avoid the condensation of liquid products. The detailed procedure see the previous report [105]. To confirm the identification of products, GC-MS analyses were also carried out by using an Agilent 7890A GC system equipped with an Agilent 5975C MS detector and HP-1 capillary column. The carbon selectivity and conversion were calculated in the following methods.

$$\text{Carbon selectivity} = \frac{\text{Moles of carbon in specific product}}{\text{Total carbon atoms in identified products}} \times 100\%$$

$$\text{Conversion} = \frac{(\text{moles of reactant})_{in} - (\text{moles of reactant})_{out}}{(\text{moles of reactant})_{in}} \times 100\%$$

The carbon balances were maintained above 90% for all runs in this paper.

3.3. Results and discussion

3.3.1. Characterization of catalysts

3.3.1.1. X-ray diffraction
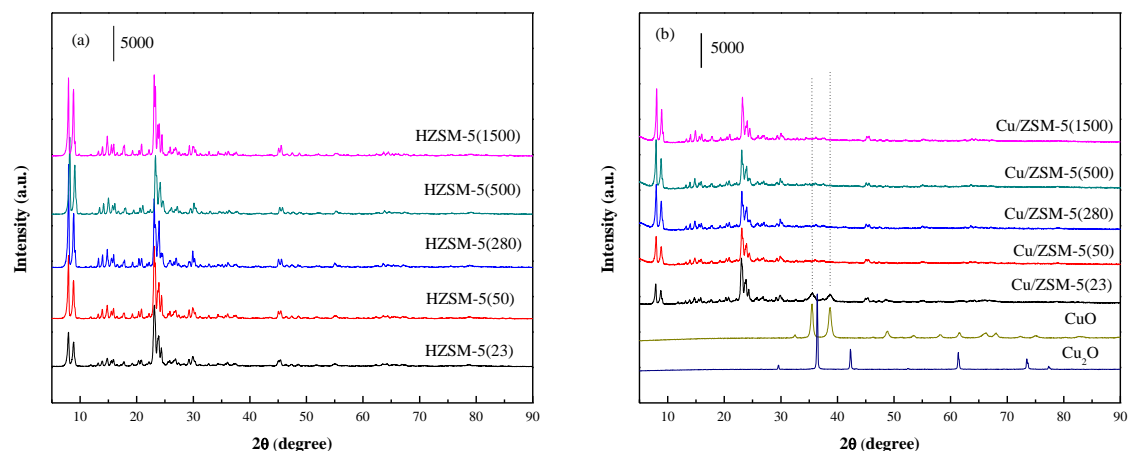
Figure 3.1. XRD patterns of the calcined (a) parent HZSM-5 zeolites with different SiO$_2$/Al$_2$O$_3$ ratios and (b) the corresponding Cu catalysts.

Figure 3.1 shows the XRD patterns of the parent HZSM-5 with different SiO$_2$/Al$_2$O$_3$ ratios (**Figure 3.1a**) and the corresponding Cu/ZSM-5 with approximately 20wt% of CuO loadings (**Figure 3.1b**) calcined at 550 $^{\circ}$C. By comparison, the addition of Cu slightly decreased the intensity of the main peaks of zeolites, which is in good agreement with the previous study [105]. However, the introduction of Cu did not significantly destroy the structure of the parent HZSM-5 since all characteristic peaks were observed in Cu/ZSM-5 catalysts. Additionally, two characteristic peaks related to CuO crystallite (35.7º and 38.55º) were observed on Cu/ZSM-5(23) because zeolite ZSM-5 with high acidity is not favorable for the dispersion of CuO on the surface [105]. In addition, no diffraction peaks for any crystalline phases of CuO were observed on Cu/ZSM-5 with SiO$_2$/Al$_2$O$_3$ ratios of 50, 280, 500 and 1500, indicating that the copper species are well dispersed on ZSM-5 even the loadings are approximately 20%.

55
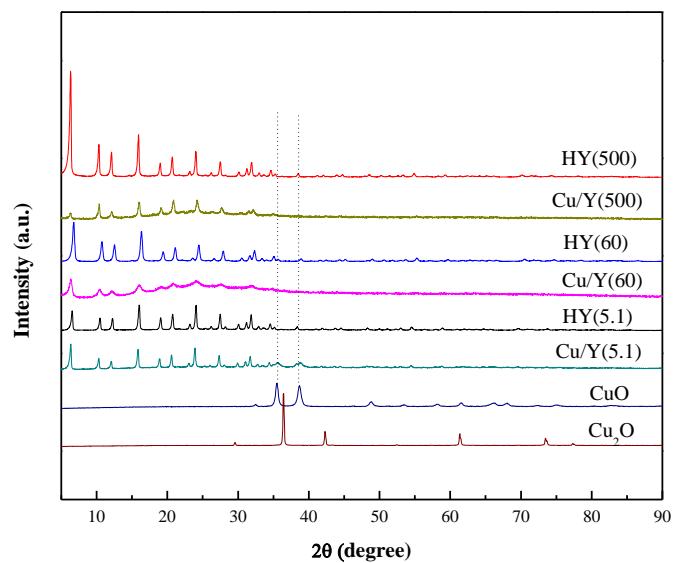
Figure 3.2. XRD patterns of the calcined parent HY zeolites and the corresponding Cu catalysts.
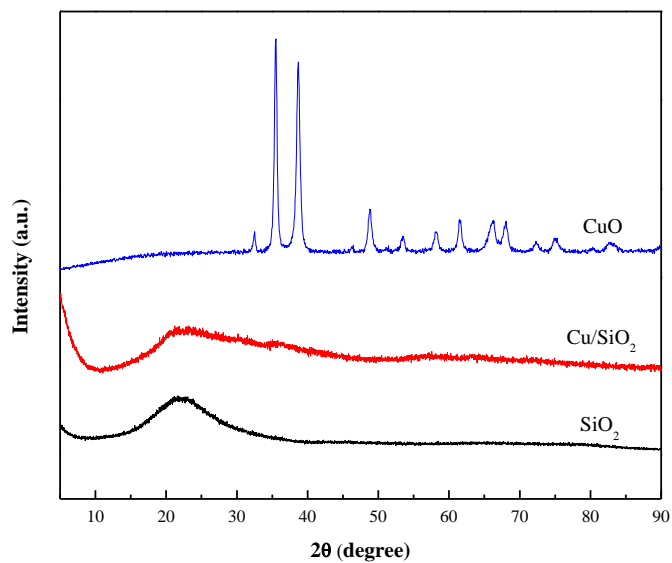
Figure 3.3. XRD patterns of the calcined SiO₂ and Cu/SiO₂ catalyst.

Figure 3.2 shows the XRD patterns of the parent HY zeolites with different SiO_2/Al_2O_3 ratios and the corresponding 20wt% Cu/Y zeolites. Similar to that observed on Cu/ZSM-5 catalysts, the characteristic peaks of CuO (35.7º and 38.55º) were only observed on Cu/Y with the highest acidity ($SiO_2/Al_2O_3=5.1$). The XRD patterns of SiO_2 and Cu/SiO_2 are shown in **Figure 3.3**. As seen, the broad diffraction peak at 2θ of 22° was exhibited on Cu/SiO_2, which was the characteristic of amorphous silica [66,106]. Apart from that, no discernible characteristic peaks related to CuO were observed, which indicated the presence of CuO with high dispersion on Cu/SiO_2 prepared by the method we suggested. As seen in **Figure 3.2**, the slightly increased background of XRD patterns at around 25° were observed on the catalysts Cu/Y(60) and Cu/Y(500), which were caused by the formed amorphous silica [107]. As reported, decomposition of structure occurs on Si-rich HY zeolite ($SiO_2/Al_2O_3=60$ and 500 in this study) when it is treated by steam [107–109] or alkali [109] at high temperature ($> 150\ ^oC$) due to the hydrothermally instability of HY zeolite. In this case, part of the HY framework will be collapsed and transformed into the amorphous species (SiO_2). Hence, when Cu/Y zeolites were prepared, the temperature should be carefully controlled below 60 ^oC or even at room temperature.

3.3.1.2. H$_2$-TPR
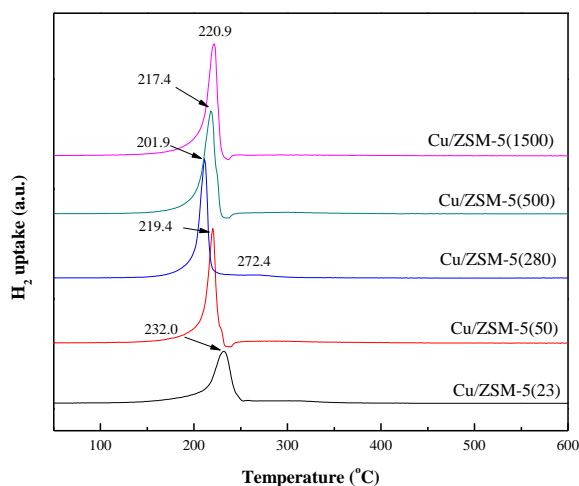
Figure 3.4. H$_2$-TPR profiles of the calcined Cu/ZSM-5 with different SiO$_2$/Al$_2$O$_3$ ratios.
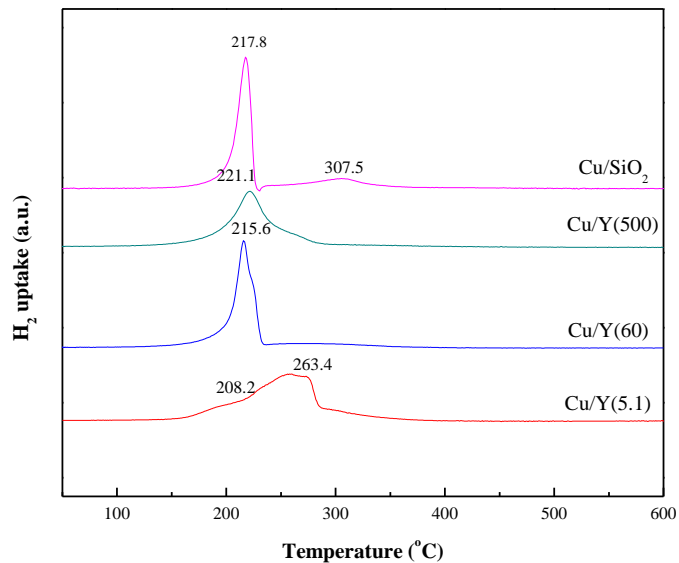
Figure 3.5. H$_2$-TPR profiles of the calcined Cu/Y with different SiO$_2$/Al$_2$O$_3$ ratios and the control catalyst Cu/SiO$_2$.

Figure 3.4 shows the H$_2$-TPR profiles of Cu/ZSM-5 with different SiO$_2$/Al$_2$O$_3$ ratios. As reported in the previous study [105], for Cu/ZSM-5(280), the peak at the low temperature (around 201.9 ℃) is assigned to the well dispersed CuO on zeolite ZSM-5, while the peak at high temperature (272.4 ℃) is assigned to the reduction of bulk CuO. As seen, on the catalysts Cu/ZSM-5 with SiO$_2$/Al$_2$O$_3$ of 50, 500 and 1500, the low reduction peak was shifted to around 220 ℃. However, on Cu/ZSM-5(23), the reduction peak was shifted to 232 ℃; more importantly, the peak was not as sharp as that of the other catalysts. As shown in **Figure 3.1b**, CuO crystallite was detected on the XRD pattern of Cu/ZSM-5(23), we can conclude that the reduction peak at 232 ℃ should be attributed to the combined contribution of well dispersed and bulk CuO species on ZSM-5(23).

Figure 3.5 shows H$_2$-TPR profiles of Cu/Y with different SiO$_2$/Al$_2$O$_3$ ratios and the control catalyst Cu/SiO$_2$ as well. As seen, the control catalyst Cu/SiO$_2$ was seen to exhibit two separate reduction peaks. The main peak at low temperature (217.8 ℃) is ascribed to the well dispersed CuO on SiO$_2$, and the small peak at high temperature (307.5 ℃) is attributed to the reduction of the bulk CuO [63,66,78]. Interestingly, the H$_2$-TPR profiles are different for all the Cu/Y catalysts. As seen, the reduction profile of Cu/Y(60) is similar to those of Cu/ZSM-5

catalysts, and also, the reduction temperature of the main peak is 215.6 ℃, which is close to that of Cu/ZSM-5 catalysts; by comparison, H_2-TPR profile of Cu/Y(500) is much broader, even though the reduction temperature is 221.1 ℃. However, the catalyst Cu/Y(5.1) displayed a main reduction peak at 263.4 ℃ together with a shoulder peak at low temperature 208.2 ℃. As discussed above, the low-temperature shoulder peak is assigned to the reduction of well dispersed CuO, while the reduction peak at high temperature is assigned to the bulk CuO on HY(5.1), which is accordance to the XRD pattern of Cu/Y(5.1) shown in **Figure 3.2**. This result confirmed the fact that zeolite with high acidity is not favorable for the dispersion of CuO on the surface further.

3.3.1.3. N_2 adsorption

The structural properties of the zeolites and copper catalysts can be derived from the results of N_2 adsorption-desorption measurements at -196 ℃. The surface area and porosity are summarized in **Table 3.1**. As shown, over Cu/ZSM-5 catalysts, the introduction of copper lowers the micropore surface area and volume, but increases the mesopore surface area and volume, which is assumed to be caused by copper deposition in the micropores of ZSM-5. However, on Cu/Y catalysts, the addition of copper not only decreases the micropore surface area and volume, but also lowers the mesopore area and volume, and the BET surface area as a result, indicating that most of copper species were deposited in both micropores and mesopores, reducing the contributions of these pores to the total surface area and volume as a whole. Moreover, it is seen that the existence of micropore is negligible on SiO_2 (surface area: 26 m^2/g). The addition of copper leads to significantly decrease of the total pore volume, which decreases from 1.352 to 0.834 cm^3/g, indicating that most of copper species deposited on the mesopore of SiO_2.

Table 3.1. BET surface area and porosity of catalysts.

Sample	Surface area			Pore volume		
	S_{BET} $(m^2/g)^a$	S_{micro} $(m^2/g)^b$	$S_{external}$ $(m^2/g)^c$	V_{total} $(cm^3/g)^d$	V_{micro} $(cm^3/g)^b$	V_{meso} $(cm^3/g)^e$
HZSM-5(23)[f]	431	283	148	0.411	0.212	0.199
HZSM-5(50)[f]	447	333	115	0.319	0.169	0.15
HZSM-5(280)[f]	437	332	105	0.301	0.180	0.121
HZSM-5(500)	415	325	90	0.305	0.188	0.117
HZSM-5(1500)	424	385	39	0.225	0.168	0.057
20%CuO/ZSM-5(23)	357	160	197	0.297	0.07	0.227
20%CuO/ZSM-5(50)	438	244	194	0.479	0.161	0.318
20%CuO/ZSM-5(280)[f]	437	215	222	0.455	0.173	0.282
20%CuO/ZSM-5(500)	411	226	185	0.392	0.157	0.235
20%CuO/ZSM-5(1500)	427	312	115	0.35	0.155	0.195
HY(5.1)	773	638	135	0.41	0.253	0.157
HY(60)	898	671	227	0.593	0.296	0.297
HY(500)	928	743	185	0.599	0.311	0.288
20%CuO/Y(5.1)	633	511	122	0.398	0.211	0.187
20%CuO/Y(60)	725	590	135	0.465	0.254	0.211
20%CuO/Y(500)	738	571	167	0.511	0.244	0.267
SiO_2	505	26	479	1.352	0.008	1.344
20%CuO/SiO_2	482	0	482	0.834	0.000	0.834

[a] The Brunauer-Emmett-Teller (BET) surface area (S_{BET}) was calculated from the linear part of BET plot from 0.007 to 0.03.
[b] The micropore area (S_{micro}) and volume (V_{micro}) were obtained by the t-plot method.
[c] The external surface area $S_{external}=S_{BET}-S_{micro}$.
[d] The total pore volume (V_{total}) was evaluated by single point total pore volume at a relative pressure of 0.95.
[e] The mesopore volume $V_{meso}=V_{total}-V_{micro}$.
[f] It is reproduced from ref [105].

3.3.1.4. NH₃-TPD
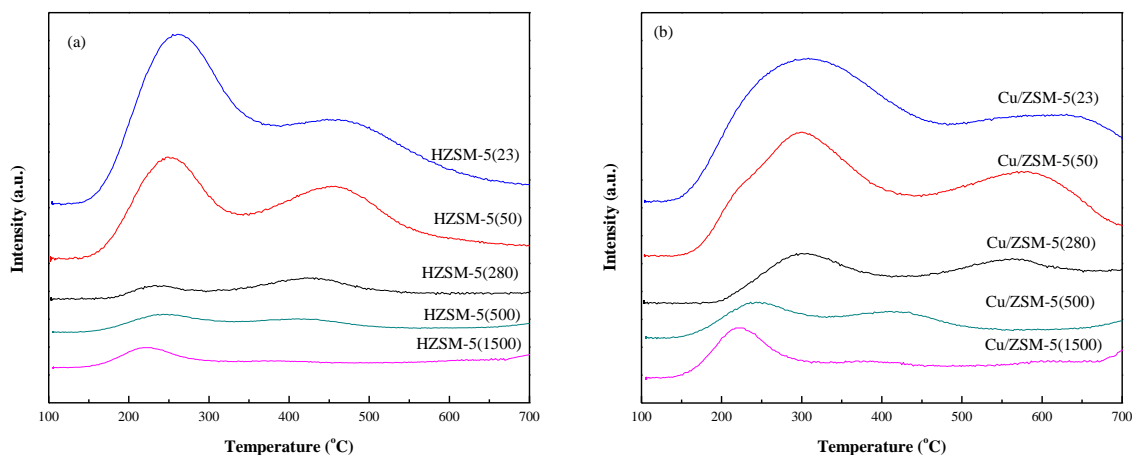
Figure 3.6. NH₃-TPD profiles of (a) HZSM-5 with different SiO₂/Al₂O₃ ratios and (b) reduced Cu/ZSM-5 with different SiO₂/Al₂O₃ ratios.

The acidity of ZSM-5 zeolites and the reduced Cu/ZSM-5 (~20wt% of CuO) was determined by NH₃-TPD, as shown in **Figure 3.6**. The amount of NH₃ uptake is summarized in **Table 3.2**. As shown, two distinct desorption peaks centering at around 250 and 450 ℃ were exhibited on the parent zeolite (**Figure 3.6a**), which are the characteristic of zeolite with MFI structure [79,105]. The peak at low temperature is assigned to ammonia weakly held or physically adsorbed on the Lewis acid sites of zeolite, while the peak at high temperature is ascribable to the desorption of ammonia strongly adsorbed on and/or interacting with the dislodged Al, and decomposition of NH^{4+} on the Brönsted acid sites [81–83]. As shown in **Figure 3.6a**, with increasing SiO_2/Al_2O_3 ratios from 23 to 280, the peak intensity of ammonia desorption decreased significantly, especially the peak at high temperature nearly vanished on HZSM-5 with SiO_2/Al_2O_3 ratio of 1500 and the total acid concentration dropped from 1.167 to 0.046 mmol/g$_{cat}$ (see **Table 3.2**). **Figure 3.6b** shows the NH₃-TPD profiles of reduced 20wt%Cu/ZSM-5 with various SiO_2/Al_2O_3 ratios. As seen, 20wt%Cu/ZSM-5 with SiO_2/Al_2O_3 of 23, 50 and 280, exhibited two distinct peaks, however, both of which shifted to higher temperature compared to the parent zeolites, which is similar to the previous report regarding the samples with 10wt% of CuO loading on the same zeolites [105]. As reported, the peak at low temperature is attributed to the combined contribution of NH₃ desorption from both Lewis acid

sites of zeolites and copper sites on the surface, while the higher temperature peak above 600 ºC is probably due to NH_3 adsorbed on Cu that only binds to one Al [86]. As shown, the shift of temperature is not obvious for the NH_3-TPD profiles of Cu/ZSM-5(500) and Cu/ZSM-5(1500) because of the weak acidity of the parent zeolites (0.092 mmol/g_{cat} for HZSM-5(500) and 0.046 mmol/g_{cat} for HZSM-5(1500), see **Table 3.2**); however, the intensity of the desorption peaks became stronger and broader, and the acidity increased to 0.614 and 0.564 mmol/g_{cat} on Cu/ZSM-5(500) and Cu/ZSM-5(1500), respectively.
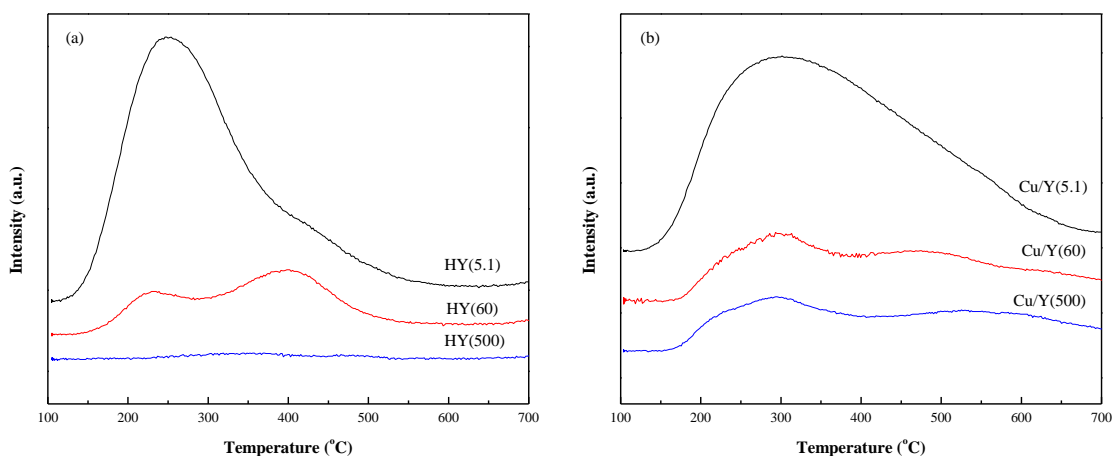
Figure 3.7. NH_3-TPD profiles of (a) HY with different SiO_2/Al_2O_3 ratios and (b) reduced Cu/HY with different SiO_2/Al_2O_3 ratios.
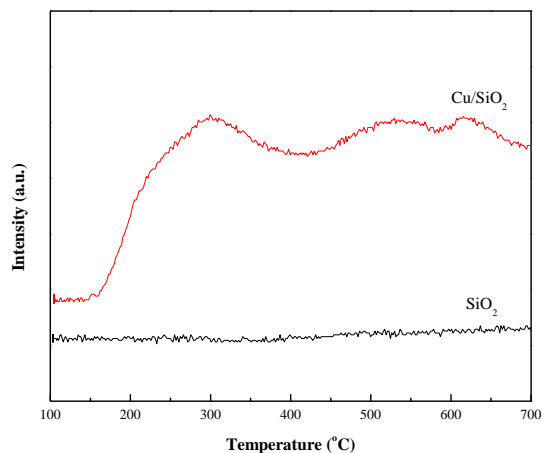
Figure 3.8. NH_3-TPD profiles of SiO_2 and Cu/SiO_2.

Table 3.2. Copper loading, copper dispersion and ammonia uptake of catalysts and supports.

	CuO loading (%)[a]	NH$_3$ uptake (mmol g^{-1})[b]	Cu area (m^2 g$_{Cu}^{-1}$)[c]	Cu Dispersion[c]
HZSM-5(23)	—	1.167	—	—
HZSM-5(50)	—	0.746	—	—
HZSM-5(280)	—	0.145	—	—
HZSM-5(500)	—	0.092	—	—
HZSM-5(1500)	—	0.046	—	—
20%CuO/ZSM-5(23)	17.8	1.549	28.2	0.04
20%CuO/ZSM-5(50)	18.3	1.144	50.5	0.07
20%CuO/ZSM-5(280)	19.2	0.487	209.7	0.22
20%CuO/ZSM-5(500)	18.0	0.614	85.2	0.13
20%CuO/ZSM-5(1500)	18.4	0.564	76.0	0.11
HY(5.1)	—	1.218	—	—
HY(60)	—	0.360	—	—
HY(500)	—	0.017	—	—
20%CuO/Y(5.1)	20.2	1.801	49.3	0.07
20%CuO/Y(60)	20.3	0.722	55.6	0.08
20%CuO/Y(500)	22.4	0.568	69.1	0.10
SiO$_2$	—	0	—	—
20%CuO/SiO$_2$	17.6	0.524	83.2	0.12

[a] The CuO loading was determined by ICP.
[b] NH$_3$ uptake was obtained by NH$_3$-TPD.
[c] Cu dispersion and Cu area were calculated by N$_2$O decomposition method.

Figure 3.7 shows the NH_3-TPD curves of HY with different SiO_2/Al_2O_3 ratios together with the corresponding Cu/Y catalysts. As shown, the NH_3-TPD profile of HY(5.1) zeolite exhibited a major desorption peak at around 250 ^{o}C with a shoulder peak at about 400 ^{o}C. The low- temperature peak is assigned to desorption of NH_3 from weak (Brönsted and/or Lewis) acid sites, while the high-temperature peak (shoulder) is due to strong Brönsted acid sites [110,111]. By comparison, the low-temperature peak of HY(60) is much smaller than the one of HY(5.1), indicating that the lower concentration of the weak acid sites exist on HY(60). Note that, the NH_3-TPD curve of HY(500) is almost flat due to the high SiO_2/Al_2O_3 ratio, and the acidity is 0.017 mmol/g_{cat} (shown in **Table 3.2**).

Figure 3.7b shows the NH_3-TPD curves of the reduced 20%Cu/Y with different SiO_2/Al_2O_3 ratios. As seen, Cu/Y(5.1) exhibits a broad NH_3 desorption peak, and the maximum temperature is shifted to higher temperature (300 ^{o}C) compared to the parent HY(5.1). Clearly, the peaks related to the weak and strong acid sites overlap, which makes it difficult to distinguish from each other; however, it can be considered as a combined contribution of NH_3 desorption from both acid sites of zeolite and copper sites on the surface. NH_3-TPD profiles of Cu/Y(60) shows two distinct peaks, both of which shift to higher temperature, which can also be ascribable to the combination of NH_3 desorption from both acid sites of zeolite and copper sites on the surface. As shown, the NH_3-TPD curve of Cu/Y(500) is similar to that of Cu/Y(60). However, most of NH_3 desorbed could be contributed from the interaction of NH_3 and copper species since the acidity of zeolite Y(500) is negligible.

Figure 3.8 shows the NH_3-TPD profiles of the control catalyst Cu/SiO_2 and the support SiO_2. No obvious desorption peak of NH_3 could be observed on SiO_2 since it is a relatively inert support. From **Figure 3.8**, it can be seen that three desorption peaks existed on Cu/SiO_2. The peak at low temperature (300 ^{o}C) was attributed to the weak acid sites, while the peak at high temperature (around 500 ^{o}C) was assigned to the strong acid sites. For the third peak with the temperature of 620 ^{o}C, the reason is still unclear. However, based on our previous report, we suggested it is probably due to the formation of N_2, which is from oxidation of NH_3 over unreduced Cu^{2+} species [80,105].

3.3.1.5. N_2O adsorption

Copper surface area and dispersion were calculated by the N_2O decomposition method [71,72]. As shown in **Table 3.2**, Cu/ZSM-5(23) has the worse copper dispersion (0.04) and lowest copper surface area (28.2 m^2/g_{Cu}) among Cu/ZSM-5 series catalysts, and Cu/Y(5.1) presents the lowest copper dispersion (0.07) and copper surface area (49.3 m^2/g_{Cu}) among Cu/Y catalysts, both of which are in agreement with the results of H_2-TPR and XRD. Hence, it is concluded that high acidity of zeolite is not good for the dispersion of copper. Cu/ZSM-5(280) exhibited the best dispersion of copper and copper surface area as well.

3.3.2. Conversion of 2,3-butanediol over Cu loaded on different supports

In our previous study, the impact of reaction conditions (temperature and hydrogen to 2,3-butanediol ratio) and CuO loading were investigated, and 20 wt% of CuO loaded on zeolite ZSM-5 with SiO_2/Al_2O_3 ratio of 280 presented the best catalytic activity on the conversion of 2,3-butanediol to butenes [105]. To get further insights into the catalytic performance of catalyst in the hydrodeoxygenation process of 2,3-butanediol to butenes, additional reactions were carried out over reduced catalysts with approximately 20 wt% of CuO loaded on ZSM-5 and Y zeolites with different SiO_2/Al_2O_3 ratios, and the reference support SiO_2 as well. The conversion of 2,3-butanediol and selectivities of the main products taken at 40 min and 190 min are shown in **Table 3.3**.

Table 3.3. Conversion of 2,3-butanediol to the main products on reduced catalysts in 40 min and 190 min (shown in parentheses).[a]

Catalysts	Conversion (%)	Selectivity (%)						
		Butenes	MEK	2-MPA[b]	IBA[c]	2-Butanol	Acetoin	Others[e]
20%CuO/ZSM-5(23)	99.86	46.26	37.30	2.38	1.57	0.00	0.00	12.49
	(99.58)	(26.32)	(35.55)	(8.45)	(14.90)	(0.81)	(0.40)	(13.57)
20%CuO/ZSM-5(50)	100.00	53.11	28.90	0.03	0.34	0.00	0.00	17.62
	(99.57)	(47.32)	(32.64)	(1.25)	(1.65)	(0.00)	(0.00)	(17.14)
20%CuO/ZSM-5(280)[d]	100.00	70.30	17.16	0.00	0.00	0.00	0.00	12.54
	(100.00)	(70.10)	(18.86)	(0.16)	(0.33)	(0.00)	(0.00)	(10.55)
20%CuO/ZSM-5(500)	100.00	61.41	22.96	0.36	1.27	0.70	0.00	13.3
	(99.48)	(39.48)	(30.69)	(3.76)	(12.25)	(1.58)	(0.93)	(11.31)
20%CuO/ZSM-5(1500)	93.59	10.28	33.53	5.36	11.74	2.44	24.20	12.45
	(85.10)	(3.47)	(28.16)	(3.00)	(7.98)	(3.86)	(45.00)	(8.53)
20%CuO/Y(5.1)	94.30	3.04	24.99	9.65	12.93	1.51	23.97	23.91
	(88.54)	(1.83)	(19.56)	(9.86)	(11.46)	(1.73)	(35.87)	(19.69)
20%CuO/Y(60)	100.00	21.90	43.97	5.61	0.81	0.00	0.17	27.54
	(99.47)	(9.76)	(38.06)	(10.54)	(5.35)	(0.00)	(5.14)	(31.15)
20%CuO/Y(500)	93.08	3.03	37.20	2.27	9.84	8.63	21.32	17.71
	(89.57)	(1.12)	(38.77)	(1.85)	(7.73)	(9.09)	(27.35)	(14.09)
20%CuO/SiO$_2$	88.23	0.81	39.83	1.09	4.70	9.52	31.21	12.84
	(86.23)	(0.72)	(38.64)	(0.78)	(3.03)	(8.95)	(34.20)	(13.68)

[a] Reaction conditions: feed rate of 2,3-butanediol, 3.0 mL/h; catalyst weight, 1.0g; H$_2$/2,3-butanediol (molar ratio), 5:1; temperature, 250 $^{\circ}$C, space time W/F$_{A0}$=30 g h mol^{-1}.
[b] 2-MPA: 2-methylpropanal.
[c] IBA: 2-methyl-1-propanol.
[d] It is reproduced from ref [105].
[e] Other products: Including tetramethylfuran, aromatics, 1-acetyl-2-methyl-1-cyclopentene, 1-ethyl-5-methylcyclopentene, propylene, C5$^=$−C8$^=$.

It can be seen in **Table 3.3** that the conversion of 2,3-butanediol was almost 100% on all Cu/ZSM-5 catalysts with different SiO$_2$/Al$_2$O$_3$ ratios except the one with the ratio of 1500: the conversion dropped dramatically from 93.59% at 40 min to 85.10% at 190 min. It should be noted that the catalyst 20%CuO/ZSM-5 with SiO$_2$/Al$_2$O$_3$ of 280 presented the highest selectivity of butenes (>70%) in 190 min of stream; in contrast, the catalysts with lower or higher SiO$_2$/Al$_2$O$_3$ ratios (23, 50, 500 and 1500) exhibited lower butene selectivityand higher MEK selectivity. As demonstrated in the previous study, the catalytic performance of Cu/ZSM-5 catalyst toward the formation of butenes is highly dependent on the balance between copper and acid catalyst functions [105]; the deactivation of zeolite-based catalysts is mainly due to the formation of coke: with more acid sites on the zeolite, the coke formation will occur faster

[92,93,105], hence, zeolite catalyst with higher acidity tends to deactivate faster. However, Cu/ZSM-5(1500) with the lowest acidity (0.564 mmol NH_3/g, see **Table 3.2**) was observed to show the lowest selectivity of butenes, 10.28% and 3.47% at 40 min and 190 min, respectively. This is probably due to the extremely low acidity of zeolite HZSM-5(1500) (0.046 mmol NH_3/g, see **Table 3.2**). As we know, deactivation of zeolite will result in the loss of acid sites, leading to insufficient acid sites for dehydration over the zeolite HZSM-5(1500). In this case, Cu sites on Cu/ZSM-5(1500) will be the active sites for dehydrogenation when deactivation takes place [105]. Therefore, it is concluded that moderate acidity in a zeolite is beneficial for selective conversion of 2,3-butanediolto butenes.

The trend relating butene selectivity to zeolite selectivity is also born out on Cu/Y catalyst. As shown in **Table 3.3**, 20%Cu/Y(60) with moderate acidity (0.722 mmol NH_3/g, see **Table 3.2**) presented the higher activity than the other two catalysts with higher or lower acidity. The conversion of 2,3-butanediol at 40 min and 190 min over Cu/Y(60) were 100% and 99.47%, respectively, which were higher than those on Cu/Y(5.1) (94.30% and 88.54%) and Cu/Y(500) (93.08% and 89.57%). In addition, catalyst Cu/Y(60) exhibited the higher selectivity of butenes (21.9% and 9.76% at 40 min and 190 min, respectively) than the other two Cu/Y catalysts. However, in comparison with the selectivity of butenes over Cu/ZSM-5 catalysts with similar acidity, Cu/Y catalysts gave lower selectivity of butenes, especially the catalysts 20%Cu/Y(5.1) and 20%Cu/Y(500) are shown to be nearly inactive in producing butenes: the selectivity of butenes is lower than 4% even in the initial 40 min of reaction. Interestingly, Cu/Y(5.1) and Cu/Y(500) are observed to be active in the production of acetoin (3-hydroxy-2-butanone), which is a side product from dehydrogenation of 2,3-butanediol over Cu catalyst. This is probably because Cu sites on catalysts can be the active sites for dehydrogenation of 2,3-butanediol when deactivation occurred [105]. As seen in **Table 3.3**, the selectivity of acetoin over these two catalysts are more than 20% even in the initial 40 min of reaction.

Additionally, a control catalyst Cu/SiO_2 was employed to examine the behavior of the metal function during 2,3-butanediol conversion. Torresi reported that dehydration of diols will occur on Cu/SiO_2 catalyst since Cu is a Lewis acid [91]. Hence, the products MEK and 2-methylpropanal, which are from dehydration of 2,3-butanediol, can be found over Cu/SiO_2 catalyst, and the selectivities are 39.83% and 1.09% at 40 min of reaction, respectively. In addition, 2-butanol and 2-methyl-1-propanol can be seen in the conversion of 2,3-butanediol

over Cu/SiO$_2$, which are from hydrogenation of MEK and 2-methylpropanal, and the selectivities are 9.52% and 4.7%, respectively. However, by comparison, the significantly lower selectivity of butenes (<1%) and conversion of 2,3-butanediol (<88.23%) observed when approximately 20% of CuO loaded on the inert SiO$_2$ (0 NH$_3$/g, see **Table 3.2**) compared to the acidic HZSM-5 and HY zeolites, highlights the crucial role oF the acid sites of zeolite in the process of converting 2,3-butanediol to butenes. Furthermore, acetoin is seen to be a main product in reacting 2,3-butanediol over Cu/SiO$_2$, and the selectivities are 31.21% and 34.20% at 40 min and 190 min, respectively. It should be noted that the conversion of 2,3-butanediol over SiO$_2$ at the same reaction conditions was less than 1%, which is not shown here.
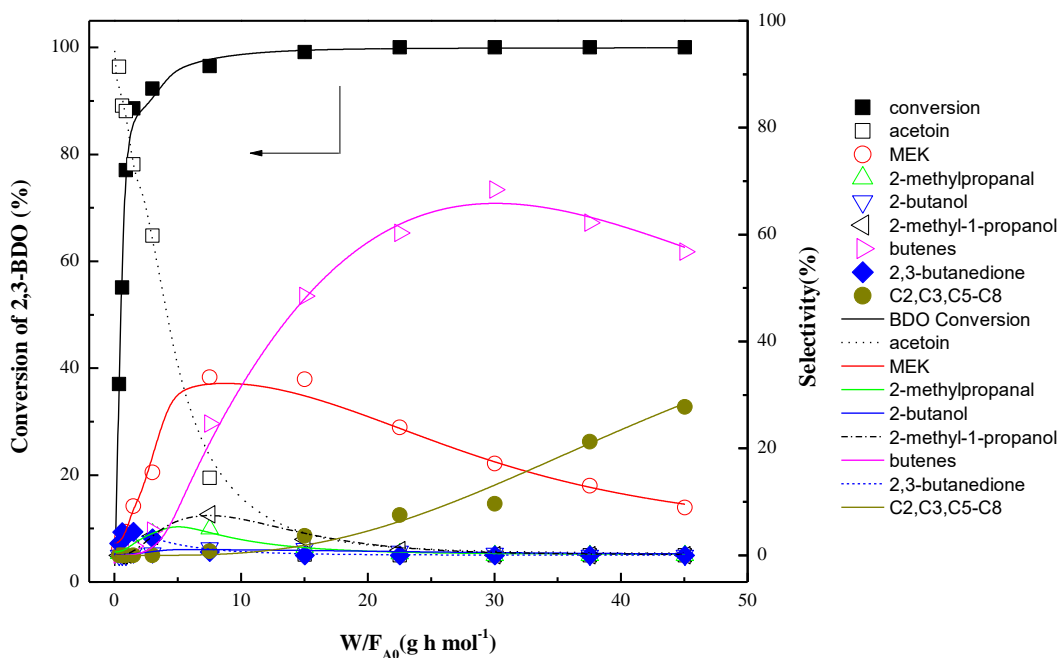
Figure 3.9. Catalytic results as a function of space time (W/F$_{A0}$) for the conversion of 2,3-butanediol over reduced catalyst 20%CuO/ZSM-5(280). Reaction conditions: feed rate of 2,3-butanediol, 3.0 mL/h; H$_2$/2,3-butanediol (molar ratio), 5:1; temperature, 250 ^{o}C; time on stream=40 min. All fitting lines were obtained from kinetic model (will be discussed later).

To better understand the reaction mechanism, we evaluated the effect of space time W/F$_{A0}$ (where W is the weight of catalyst (in unit of gram), and F$_{A0}$ is the molar flow rate of 2,3-

butanediol (in unit of mol h^{-1})) on conversion of 2,3-butanediol and the distribution of products over reduced catalyst 20%CuO/ZSM-5(280) at a feed rate of 2,3-butanediol of 3 mL h^{-1} in the presence of H$_2$ at 250 ^{o}C (see **Figure 3.9**). As seen in **Figure 3.9**, the conversion of 2,3-butanediol was exhibited to increase dramatically from 37% to 92% when the space time was increased from 0.36 to 3 g h mol^{-1}, and then tended to increase slowly until 2,3-butanediol was completely consumed when space time W/F$_{A0}$ reached 22.5 g h mol^{-1}. Interestingly, we can see that low space times are beneficial for the production of acetoin (the mechanism will be discussed later). At the space time of 0.36 g h mol^{-1}, acetoin (3-hydroxy-2-butanone) was observed to be the dominant product, and the selectivity was approximately 92%. However, with increasing space time, acetoin selectivity was seen to decrease dramatically to 0 when the space time reached 22.5 g h mol^{-1}, which was accompanied by the increase of the selectivities of the other products, such as MEK, butenes, 2-methylpropanal and 2-methyl-1-propanol. It should be noted that the selectivities of MEK, 2-methylpropanal and 2-methyl-1-propanol increased with increasing space time, reaching amaximum of 33.3%, 4.9% and 7.5%, respectively, at the space time of 7.5 g h mol^{-1}. The selectivities of butenes, which are of interest, showed an increasing trend with increasing space time, reaching the maximum selectivity 68.4% at the space time of 30 g h mol^{-1}, followed by decreasing to 56.8% at the space time of 45 g h mol^{-1}. By comparison, its decrease was accompanied by an increase of selectivities in the products from cracking reaction (C$_3^=$, C$_5^=$, C$_6^=$ and C$_7^=$) and oligomerization (C$_8^=$). Clearly, these results indicate that high space time increases the possibility that, given sufficient time, butenes react with each other over the acid sites of catalyst, producing the dimer (C$_8^=$) through oligomerization and cracking products (C$_3$, C$_5$, C$_6$ and C$_7$ olefins) by the subsequent cracking of the dimer. Interestingly, the selectivity of 2-butanol, which is thought to be a key intermediate in the pathway of MEK to butenes, is negligible under all W/F$_{A0}$. This result will be discussed later.

Apart from the reaction of 2,3-butanediol over 20%Cu/ZSM-5(280) mentioned above, a series of reactions were carried out by varying space time (W/F$_{A0}$) over HZSM-5(280), HY(60), 20%CuO/Y(60) and the control catalyst 20%CuO/SiO$_2$ (see **Figure 3.10**) under the same reaction conditions, in order to discern the role of the individual function (metallic or acidic) of the catalyst, and further determine the rate-limiting step of the reaction and the effect of the catalyst structure on the reaction. The space time over each catalyst was adjusted in the low range to obtain a comparable conversion level (30%-80%).
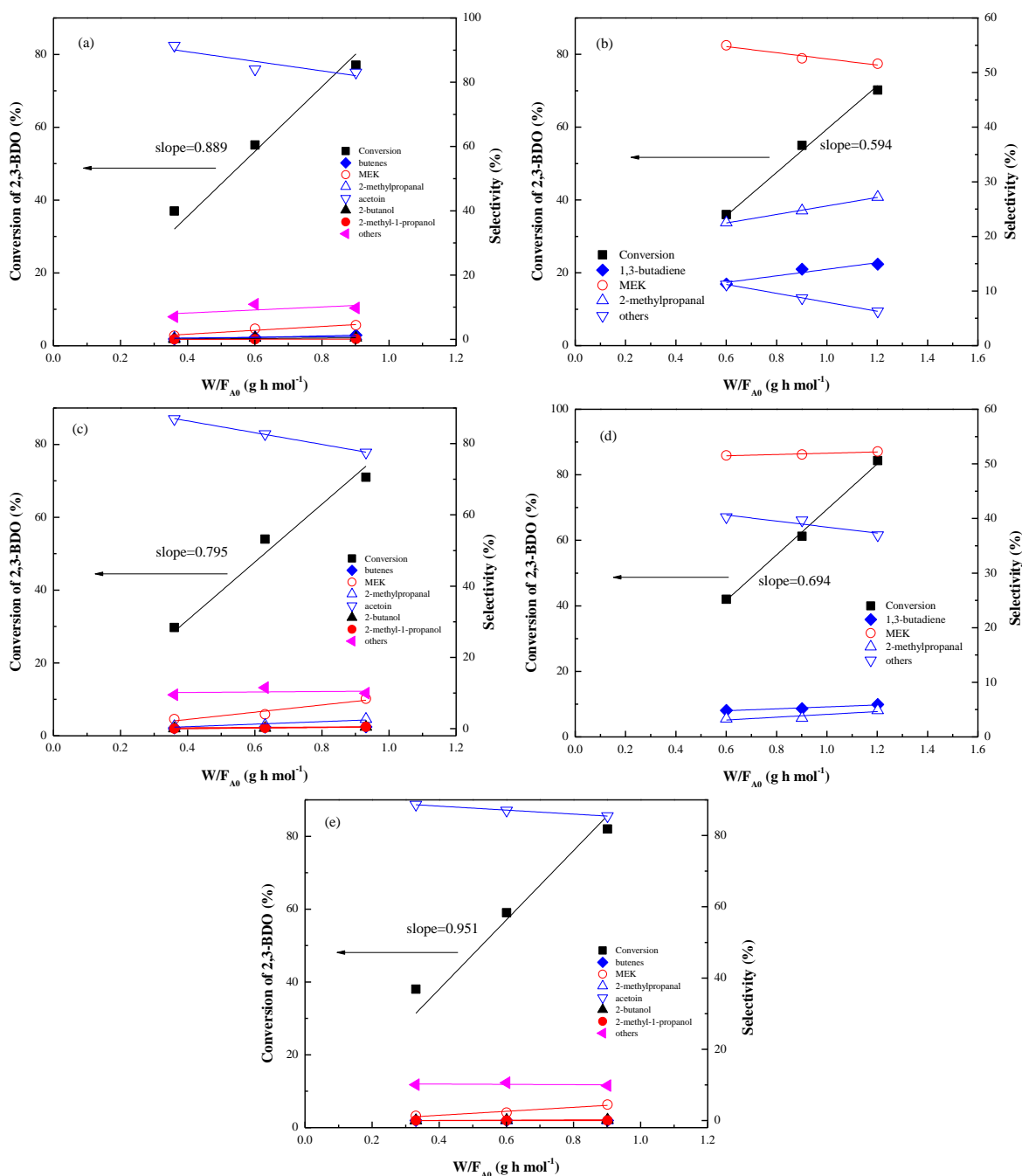
Figure 3.10. Conversion of 2,3-BDO and selectivities of the main products as a function of space time (W/F$_{A0}$) over different catalysts (a) Cu/ZSM-5(280), (b) HZSM-5(280), (c) Cu/Y(60), (d) HY(60), (e) Cu/SiO$_2$. Reaction conditions: feed rate of 2,3-butanediol, 3.0 mL/h; H$_2$/2,3-butanediol (molar ratio), 5:1; temperature, 250 ^{o}C; time on stream=40 min. Other minor products in (a), (c) and (e): 2,3-butanedione, tetramethylfuran, 3,4,5-trimethyl-2-cyclopentenone, aromatics and unknown products; in (b) and (d): tetramethylfuran, 3,4,5-trimethyl-2-cyclopentenone, 2-ethyl-2,4,5-trimethyl-1,3-dioxolane, aromatics and some unknown products.

Figure 3.10 shows the conversion of 2,3-butanediol and the selectivities of the main products over different catalysts as a function of space time under the same reaction conditions. As shown in **Figure 3.10**, the conversion of 2,3-butanediol on all catalysts increased with increasing space time. Note that, for conversion lower than 80%, a similar behavior was observed on all copper catalysts (see **Figure 3.10a**, **Figure 3.10c** and **Figure 3.10e**) and no significant production of butenes was seen; in contrast, the main product obtained was acetoin. In this case, we can see that the predominant reaction at the low space time was dehydrogenation, which indicates that the metallic function (Cu) of catalyst was performing the catalysis at low space time. In addition, the low selectivity of MEK implied that dehydration of 2,3-butanediol over Cu catalysts at low space times occurred only to a limited extent.

The data in **Figure 3.10** can also be used to calculate the reaction rate of 2,3-butanediol. The mole balance for a packed bed reactor can be represented by **Equation 3.1** [112]:

$$\frac{dF_A}{dW} = r_A'$$
(**Equation 3.1**)

where W is the catalyst weight, F_A is the molar flow rate of 2,3-butanediol, and r_A' is the reaction rate for the reactant. Expressing the molar flow rate as a function of reactant conversion, X, gives:

$$F_{A0}\frac{dX}{dW} = -r_A'$$
(**Equation 3.2**)

where F_{A0} is the initial molar flow rate of the reactant.

Rearranging this equation gives:

$$-r_A' = \frac{dX}{d(W/F_{A0})}$$
(**Equation 3.3**)

Equation 3.3 shows that the reaction rate of the reactant can be calculated by plotting the conversion versus the space time (W/F_{A0}) and finding the slope. This equation was used to find reaction rates in the kinetic studies.

Figure 3.10b and **Figure 3.10d** display the conversion of 2,3-butanediol together with the product distribution over parent zeolites HZSM-5(280) and HY(60), respectively. As shown, the product distribution is different at low space times. The major products over HZSM-5(280) are MEK (selectivity >50%), 2-methylpropanal (>20%) and 1,3-butadiene (>10%), which are from dehydration of 2,3-butanediol [34,105]; however, over zeolite HY(60) , the major products are MEK and other heavy products. By comparison, it seems that Y type zeolite is beneficial for

71

the production of heavy products at low space time, such as oxygenates and aromatics. This is probably because HY zeolite could provide sufficient space with large channels (0.74 nm) and super cage (1.3 nm) for the reactants or intermediates by comparison to HZSM-5 (channels with diameter of 0.51 nm, channel intersections of 0.9 nm) [113,114], which makes it easier for 2,3-butanediol or MEK to proceed further reaction to produce heavy products such as tetramethylfuran, 3,4,5-trimethyl-2-cyclopentenone, 2-ethyl-2,4,5-trimethyl-1,3-dioxolane, xylene and other aromatics. In addition, the total reaction rates over zeolites (HZSM-5, 0.594 mol g^{-1} h^{-1}, HY: 0.694 mol g^{-1} h^{-1}) are smaller than the corresponding copper loaded zeolite catalysts (**Figure 3.10a** and **Figure 3.10c**) and copper loaded SiO_2 catalyst (**Figure 3.10e**), which suggests that the reaction rate of dehydration of 2,3-butanediol over zeolite is slower than the dehydrogenation of 2,3-butanediol over copper catalysts.

3.3.3. Conversion of acetoin
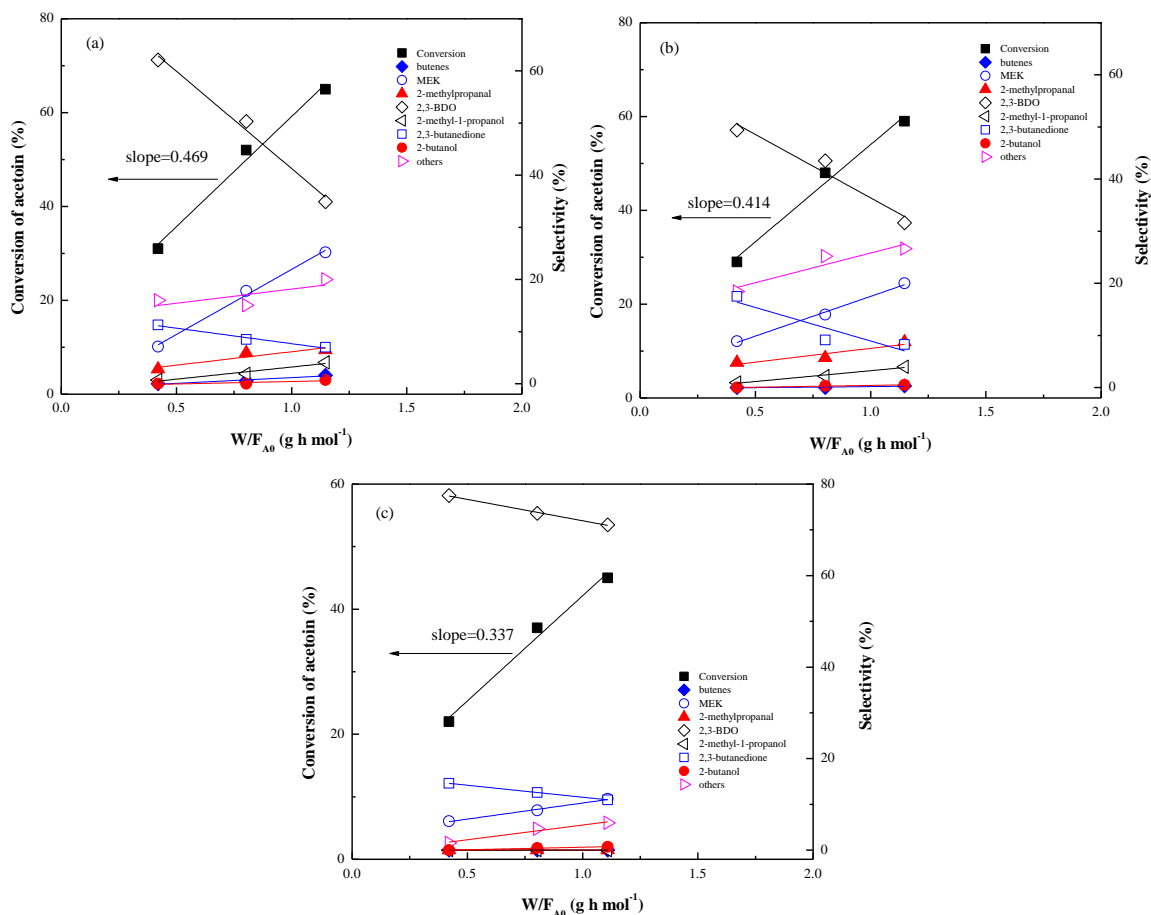
Figure 3.11. Conversion of acetoin and selectivities of the main products as a function of space time (W/F_{A0}, F_{A0} is the molar flow rate of acetoin) over different catalysts (a) Cu/ZSM-5(280), (b) Cu/Y(60), (c) Cu/SiO$_2$. Reaction conditions: feed rate of acetoin (85 wt%), 3 mL/h; H$_2$/acetoin (molar ratio), 5.7:1; temperature, 250 ^{o}C; time on stream=40 min. Other products: 1,2,3-trimethyl-cyclopentene, 1-ethyl-5-methylcyclopentene, 1-(2-methyl-1-cyclopenten-1-yl)-ethanone, 3,4,5-trimethyl-2-cyclopentenone, tetramethylfuran, aromatics and unknown products.

As mentioned above, acetoin can be selectively produced by dehydrogenation of 2,3-butanediol over copper catalysts even in the excess of H$_2$ present in the reactor at low space times; however, at high space time (see **Table 3.3** and W/F_{A0}>20 g h mol^{-1} in **Figure 3.9**), in the initial 40 min, the selectivity of acetoin decreased dramatically, essentially to 0% over Cu/ZSM-5 catalysts. To investigate the reaction mechanism between 2,3-butanediol and acetoin, additional reactions were carried out over the same reduced catalysts by using acetoin as the

reactant. As acetoin exists as a solid dimer (2,3,5,6-tetramethyl-1,4-dioxane-2,5-diol) at room temperature, acetoin was used in the reaction as aqueous solution with concentration of 85 wt% in order to avoid clogging the pump.

Figure 3.11 displays the conversion of acetoin and the selectivities of the main products as functions of space time (W/F$_{A0}$) over the reduced copper catalysts. As seen in **Figure 3.11a**, over Cu/ZSM-5(280) catalyst, the overall reaction rate is about 0.469 mol g^{-1} h^{-1} with the main product 2,3-butanediol, which shows a decreasing trend in selectivity from 62% to 35% when the space time increased from 0.42 to 1.14 g h mol^{-1}. Besides 2,3-butanediol, some other products obtained over Cu/ZSM-5(280) are similar to those observed in conversion of 2,3-butanediol over copper catalysts (see **Figure 3.10**) as discussed above, which include MEK, 2-methylpropanal and 2-methyl-1-propanol. All of these products showed an increasing trend of selectivity with increasing space time, which was accompanied by an decreasing selectivity of 2,3-butanediol (see **Figure 3.11a**). This indicates that, over Cu/ZSM-5(280), acetoin was firstly hydrogenated to 2,3-butanediol, which was further converted to MEK, 2-methylpropanal and some other products by dehydration or hydrogenation subsequently. In addition, the selectivity of 2,3-butanedione, which is from dehydrogenation of acetoin, decreased with increasing space time. It should be noted, only trace amounts of butene (<1.6%) and 2-butanol (<0.7%) were observed at low space time (W/F$_{A0}$<1.14 g h mol^{-1}), which is in agreement with the results obtained from conversion of 2,3-butanediol over Cu/ZSM-5(280) (see **Figure 3.10a**).

Figure 3.11b showed the catalytic performance of catalyst Cu/Y(60) in the conversion of acetoin. As seen, similar to the behavior observed over Cu/ZSM-5(280), 2,3-butanediol was observed to be the main product over catalyst Cu/Y(60) as well, especially at the low space time of 0.42 g h mol^{-1}. The selectivity decreased from 49% to 32% with increasing space time from 0.42 to 1.14 g h mol^{-1}. Meanwhile, the selectivities of MEK, 2-methylpropanal and 2-methyl-1-propanol were seen to increase with the increasing space time. Similarly, 2,3-butanedione showed an decreasing trend over catalyst Cu/Y(60) as that observed over Cu/ZSM-5(280). By comparison, Cu/Y(60) exhibited lower reaction rate (0.414 mol g^{-1} h^{-1}) than Cu/ZSM-5(280) under the same reaction conditions. In addition, Cu/Y(60) was seen to present a higher selectivity of heavy products. Note that butene was not formed over Cu/Y(60) at low space times (W/F$_{A0}$<1.14 g h mol^{-1}).

As seen in **Figure 3.11c**, over the catalyst Cu/SiO_2, the predominant product is also 2,3-butanediol, which showed a decreasing selectivity from 78% to 65% when the space time increased from 0.42 to 1.10 g h mol^{-1}. Unlike the results obtained from the catalysts Cu/ZSM-5(280) and Cu/Y(60), 2-methylpropanal and 2-methyl-1-propanol were not observed in the products at the low space time. As reported, 2-methylpropanal can be obtained from dehydration of 2,3-butanediol by a pinacol rearrangement over acid catalysts[34,36]. Hence, without acid sites of the catalysts, the obtained 2,3-butanediol from hydrogenation of acetoin was difficult to convert to 2-methylpropanal, and 2-methyl-1-propanol by subsequent hydrogenation, which is in a good agreement with the result of Cu/SiO_2 shown in **Table 3.3**. As shown in **Table 3.3**, even at high space time ($W/F_{A0}=30$ g h mol^{-1}), the selectivities of 2-methylpropanal and 2-methyl-1-propanol over Cu/SiO_2 are only 1.09% and 4.70%, respectively, both of which are significantly lower than the selectivity of MEK (39.83%, see **Table 3.3**) because MEK can be selectively produced over copper sites of Cu catalysts[91]. Additionally, the selectivity of 2-butanol, which is the intermediate of MEK to butenes, is negligible (<1%) at the low space time (the reason will be discussed later).

In conclusion, as discussed above, it is obvious that conversion of 2,3-butanediol to acetoin is a reversible process. As seen in **Figure 3.9**, at low space time, 2,3-butandiol can readily be converted to acetoin by dehydrogenation over Cu catalysts. With increasing space time (W/F_{A0}), the formed acetoin can react with H_2 to convert to 2,3-butanediol, which can be further convert to MEK, 2-methylpropanal, 2-butanol, 2-methyl-1-propanol, and then butenes as a result.

Table 3.4. Conversion of acetoin to the main products on zeolites[a].

Catalysts	W/F$_{A0}$ (g h mol^{-1})	Conversion (%)	Selectivity (%)					
			MEK	MVK[b]	2,3-butanedione	dimethyl-phenol[c]	aromatics[d]	others[e]
HZSM-5(280)	34.6	34.7	5.60	3.44	2.71	23.16	35.20	29.89
HZSM-5(280)	3.5	9.91	3.56	31.6	8.85	4.28	22.80	28.91
HY(60)	34.6	33.5	2.28	2.08	3.22	35.55	41.60	15.27
HY(60)	3.5	8.67	1.34	8.52	2.98	29.5	33.77	23.89

[a] Reaction conditions: feed rate of acetoin (85%), 3.0 mL/h; H$_2$/acetoin (molar ratio), 5.7:1; temperature, 250 °C; time on stream=40 min.
[b] MVK: methyl vinyl ketone.
[c] Including: 3,4-dimethyl-phenol, 3,5-dimethyl-phenol and 2,3-dimethyl-phenol .
[d] It mainly includes: xylene, 1-ethyl-3-methyl-benzene 1,3,5-trimethyl-benzene, 1,3,5-triethylbenzene and hexamethyl-benzene.
[e] Other products: Including 1,2,3-trimethyl-cyclopentene, 1-(2-methyl-1-cyclopenten-1-yl)-ethanone, 3,4,5-trimethyl-2-cyclopentenone and tetramethylfuran and some unknown products.

In addition, the control experiments of acetoin over the parent zeolites HZSM-5(280) and HY(60) were carried out under the same reaction conditions. **Table 3.4** shows the conversion of acetoin to the main products over HZSM-5(280) and HY(60) at the space time of 3.5 and 34.6 g h mol^{-1}. As seen in **Table 3.4**, the conversion of acetoin over zeolites is about 34% at the space time of 34.6 g h mol^{-1}, and less than 10% at the space time of 3.5 g h mol^{-1}. This indicates that the overall reaction rate of acetoin over zeolite is significantly lower than that over Cu catalyst, since the conversion of acetoin over the corresponding Cu catalyst is more than 60% even at the low space time of 1.14 g h mol^{-1} (see **Figure 3.11a** and **Figure 3.11b**). Additionally, aside from the same products (MEK, 2,3-butanedione, aromatics and other heavy products) observed over Cu catalysts, new products were obtained from the reaction of acetoin over zeolites, such as methyl vinyl ketone (MVK) and dimethyl-phenol (3,4-dimethyl-phenol, 3,5-dimethyl-phenol and 2,3-dimethyl-phenol). As reported by Torresi [91], MVK can be produced by dehydration of 4-hydroxy-2-butanone, which is from dehydrogenation of 1,3-butanediol. Similarly, it is clear that MVK can be formed by the dehydration of acetoin (3-hydroxy-2-butanone) [115]. As for dimethyl-phenol, the reaction mechanism is still unclear. One possible reaction pathway is Robinson annulation reaction between MVK itself or MVK and MEK to form a C8 molecule, because MVK is an excellent Michael addition reagent [116]. Both acid and base catalysts have been extensively used in the Robinson annulation reaction [117–119]. Robinson annulation reaction consists of three consecutive processes: firstly, Michael addition of a carbonyl compound (MVK or MEK) to an α,β-unsaturated ketone (MVK); secondly, an intramolecular aldol condensation reaction; lastly, dehydration [117]. The possible reaction mechanism is described in **Figure B.1** and **Figure B.2** (in **Appendix B**).

As shown in **Table 3.4**, over zeolite HY(60), the selectivity of dimethylphenol is 29.5% even at the low space time of 3.5 g h mol^{-1}, which is probably due to the sufficient space of HY with large channels (0.74 nm) and super cage (1.3 nm) [113,114] for the reactants or intermediates, makes it easier to proceed further reaction to produce the heavy products. However, over the zeolite ZSM-5(280), at the low space time of 3.5 g h mol^{-1}, the selectivity of MVK is more than 30%, while the selectivity of dimethyl-phenol is lower than 5%, which indicates that low space time is not enough for MVK to produce dimethyl-phenol over ZSM-5(280). However, when the space time increased to 34.6 g h mol^{-1}, the selectivity of dimethyl-phenol over ZSM-5(280) significantly increased to 23.16%, while the selectivity of MVK

decreased to 3.44% as a result. However, MVK and dimethyl-phenol were not detected in the previous reactions over Cu catalysts consequently due to the competitive reaction pathways of acetoin over Cu sites and acid sites of zeolite.

3.3.4. Conversion of MEK
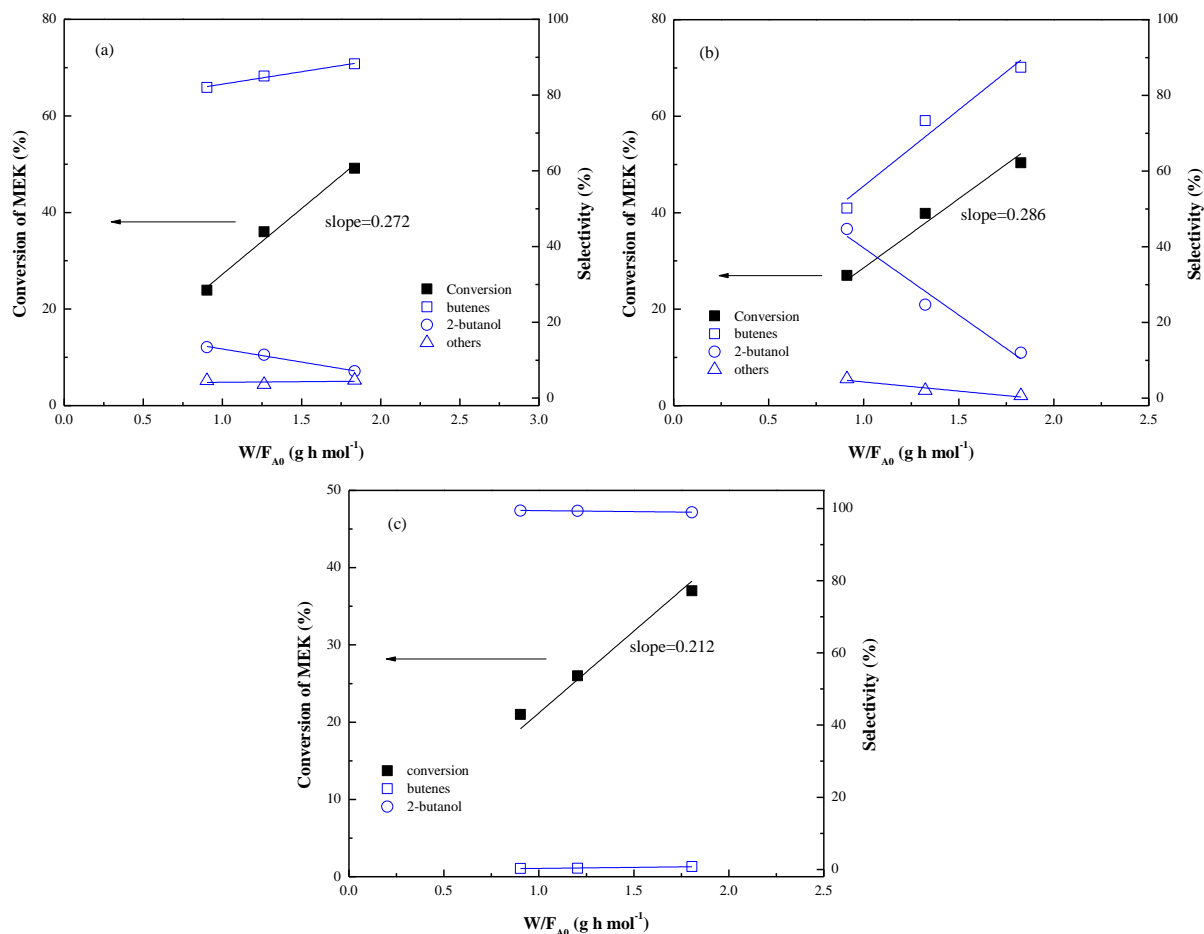
Figure 3.12. Conversion of MEK and selectivities of the main products as a function of space time (W/F$_{A0}$) over different catalysts (a) Cu/ZSM-5(280), (b) Cu/Y(60), (c) Cu/SiO$_2$. Reaction conditions: feed rate of MEK, 3.0 mL/h; H$_2$/MEK (molar ratio), 5:1; temperature, 250 ^{o}C; time on stream=40 min. Other minor product in (a) and (b): C$_3^=$, C$_5^=$−C$_8^=$.

The conversions of MEK together with the selectivities of the main products over different copper catalysts are shown in **Figure 3.12**. It is seen that the conversion of MEK on all

Cu catalysts increased with increasing space time (W/F_{A0}) in the range of 0.9 to 1.8 g h mol^{-1}. The total reaction rate of Cu/ZSM-5(280) (**Figure 3.12a**, 0.272 mol g^{-1} h^{-1}) is almost the same as the one of Cu/Y(60) (**Figure 3.12b**, 0.286 mol g^{-1} h^{-1}), both of which are slightly higher than the reaction rate on Cu/SiO$_2$ (**Figure 3.12c**, 0.212 mol g^{-1} h^{-1}).

As shown in **Figure 3.12c**, the predominant product of conversion of MEK over Cu/SiO$_2$ is 2-butanol with the selectivity of about 100% between the space time of 0.9 to 1.8 g h mol^{-1}, which is formed from direct hydrogenation of MEK. In our previous report [105], 2-butanol is the intermediate in the process of conversion of MEK to butene. However, over Cu/SiO$_2$ catalyst, the butene selectivity was negligible, as shown in **Figure 3.12c**. From **Table 3.2**, we can see the acidity of SiO$_2$ and Cu/SiO$_2$, which is 0 and 0.524 mmol NH$_3$/g$_{cat}$, respectively. This indicates that the addition of copper does not favor the dehydration of 2-butanol to butene. Consequently, 2-butanol becomes the final product due to the lack of acid sites on SiO$_2$. Hence, we can safely draw the conclusion that the dehydration of 2-butanol to butenes can only take place on the acid sites of zeolites.

By comparison, over Cu/ZSM-5(280) catalyst, the dominant products are butenes. As seen in **Figure 3.12a**, the selectivities of butenes increase from 82% to 88% with the increasing space time (W/F_{A0}) from 0.9 to 1.8 g h mol^{-1}, which is accompanied by an increase in the conversion of MEK from 22% to 50%; meanwhile, the selectivity of 2-butanol decreases from 13% to 7% with the increasing space time (W/F_{A0}). Base on the discussion above, we know 2-butanol can be formed readily from the conversion of MEK on the Cu sites of the catalyst, which then convert to butenes by the subsequent dehydration over the adjacent acid sites of the zeolite. **Figure 3.12b** shows the conversion of MEK and the selectivities of the main products over catalyst Cu/Y(60). Similar to the behavior observed over Cu/ZSM-5(280) catalyst, butenes can be seen as the main products over Cu/Y(60) as expected: the selectivity of butenes was almost the same (86%) as that of Cu/ZSM-5(280) at the space time of 1.8 g h mol^{-1}. However, at the space time of 0.9 g h mol^{-1}, Cu/Y(60) was seen to exhibit much lower selectivity of butenes (50%), which was accompanied by an much higher selectivity of 2-butanol (48%). This indicates that dehydration of 2-butanol to butenes occurs more readily over Cu/ZSM-5(280) than over Cu/Y(60).

In contrast, it is seen that the overall reaction rates of MEK are much smaller than the reaction rates of 2,3-butanediol or acetoin over the same catalysts.

Table 3.5. Conversion of MEK over HZSM-5(280) and HY(60)[a].

Catalysts	HZSM-5(280)	HY(60)
W/F_{A0} (g h mol^{-1})	30.1	30.1
Conversion (%)	17.4	18.6
Selectivity (%) hydrocarbons		
$C_2^=$-$C_3^=$	1.8	0.5
$C_4^=$	0.9	3.4
$C_5^=$	32.9	26.7
$C_6^=$	27.1	22.8
$C_7^=$-$C_8^=$	0	0.4
propanoic acid	22.3	17.6
acetic acid	10.1	8.3
2-methylpropanal	0	0.4
aromatics[b]	2.9	11.2
others[c]	2.0	8.7

[a] Reaction conditions: feed rate of MEK, 3.0 mL/h; H_2/MEK (molar ratio), 5:1; temperature, 250 $^{\circ}$C; time on stream=40 min.
[b] Aromatics include: xylene, C_{9+} aromatic hydrocarbons.
[c] Others include: acetone, oxygenated compounds (such as 1-(2-methyl-1-cyclopenten-1-yl)-ethanone, 3,4,5-trimethyl-2-cyclopentenone, tetramethylfurran) and some other unknown products.

In addition, control experiments for the reaction of MEK over the parent zeolites were conducted under the same reaction conditions. **Table 3.5** shows the conversion of MEK to the main products over HZSM-5(280) and HY(60) at the space time of 30.1 g h mol^{-1}. As shown in **Table 3.5**, the conversion of MEK over zeolites are less than 19%, indicating that the reaction of MEK over acid sites of zeolites are significantly slower than the reaction of MEK over the corresponding Cu catalysts (see **Figure 3.12a** and **Figure 3.12b**). However, an interesting point to draw attention is that propanoic acid, acetic acid, together with $C_5^=$ and $C_6^=$ were observed to be the primary products instead of butenes and 2-butanol. This behavior is clearly different from that observed in the conversion of MEK over Cu catalysts mentioned above. The conversion of ketones to carboxylic acids has been reported for reactions over acid catalysts [115,120–123]. As reported, the reaction mechanism involves the high-temperature hydrolytic cleavage of the α,β-unsaturated ketone obtained from aldol condensation of ketones over acid catalyst, which proceeds with the condensation of MEK (carbonyl compound) with an enol, which can be

converted from MEK by the keto-enol tautomerization reaction [124–126]. However, in this process, two different enols, 1-buten-2-ol and 2-buten-2-ol, could be formed by MEK, hence, two different aldol addition products (5-hydroxy-5-methyl-3-heptanone and 4-hydroxy-3,4-dimethylhexan-2-one) were produced accordingly, both of which then underwent dehydration reaction to form α,β-unsaturated ketones (i.e. 5-methyl-4-hepten-3-one or 3,4-dimethylhex-3-en-2-one). The ketones could further undergo hydrolytic cleavage, producing carboxylic acids (propanoic acid and acetic acid) and olefins ($C_5^=$ and $C_6^=$). The reaction pathways are depicted in **Figure 3.13**. In addition to the acids and olefins, aromatics could be formed by acid-catalyzed condensation of ketones as well [8,121,127,128].
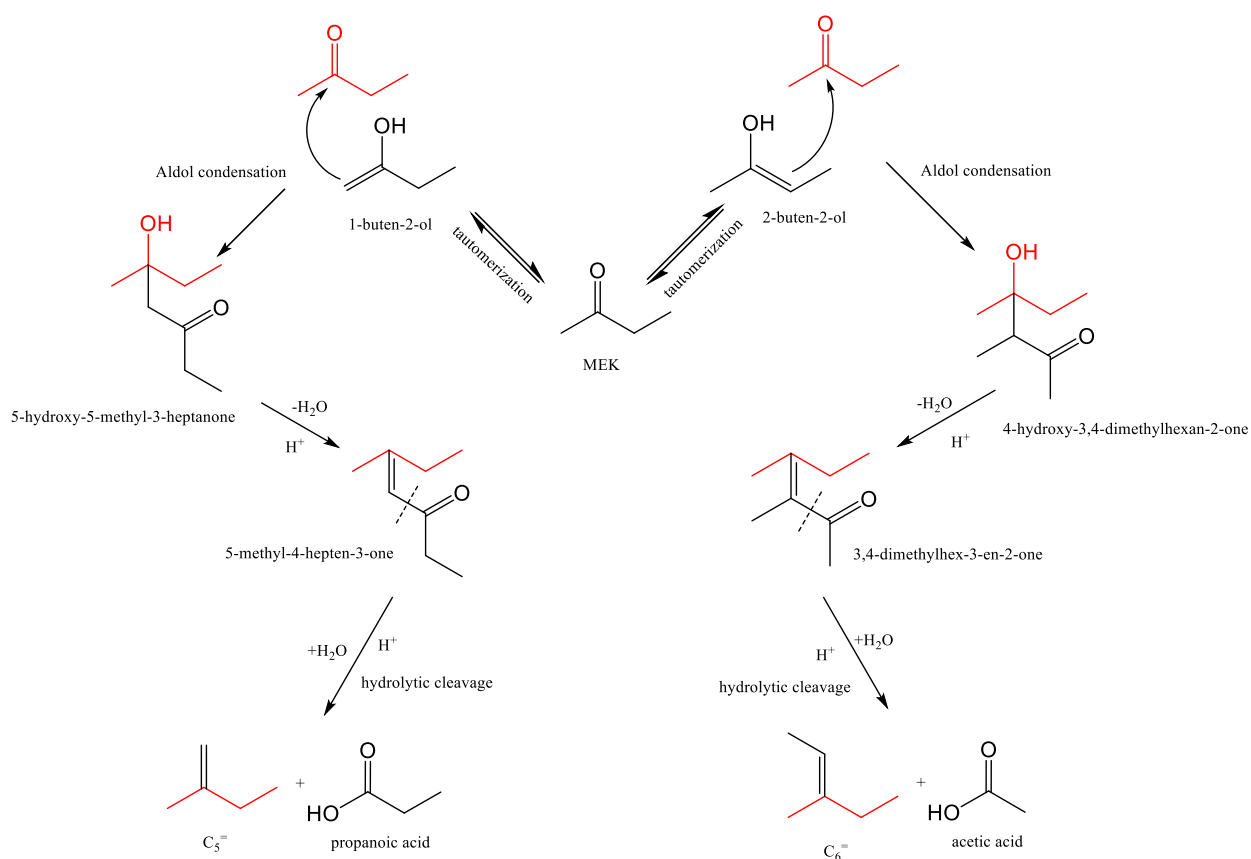
Figure 3.13. Reaction pathways for conversion of MEK over acid catalysts.

81

3.3.5. Conversion of 2-methylpropanal
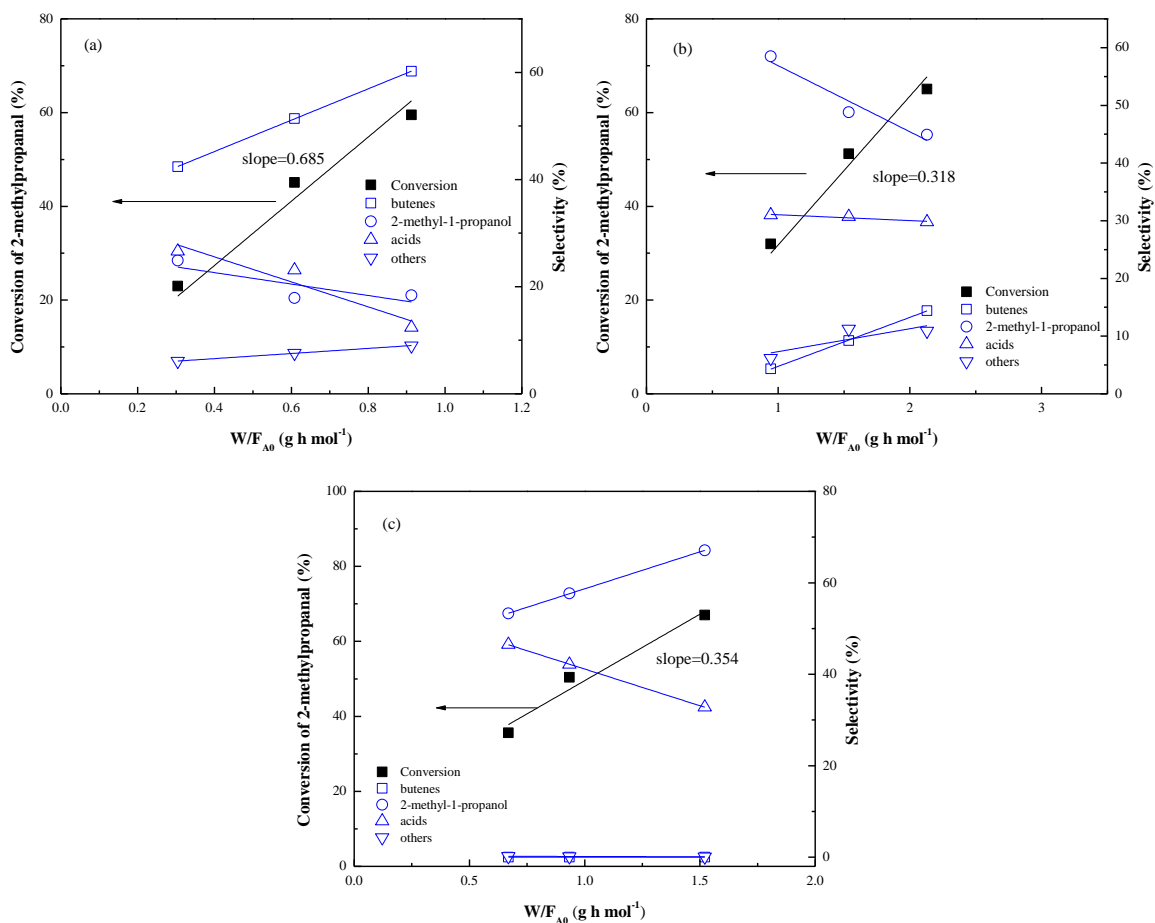
Figure 3.14. Conversion of 2-methylpropanal and selectivities of the main products as a function of space time (W/F$_{A0}$) over different catalysts (a) Cu/ZSM-5(280), (b) Cu/Y(60), (c) Cu/SiO$_2$. Reaction conditions: feed rate of 2-methylpropanal, 3.0 mL/h; H$_2$/2-methylpanal (molar ratio), 5:1; temperature, 250 ^{o}C; time on stream=40 min. Acids include: 2-methyl-propanoic acid, trace amount of propanoic acid and acetic acid. Other minor products include: MEK, acetone, xylene and C$_{9+}$ aromatic hydrocarbons, and trace amount of hydrocarbons (C$_3^=$, C$_5^=$-C$_8^=$), oxygenated compounds (1,2,3-trimethyl-cyclopentene, 1-ethyl-5-methylcyclopentene and 2,3,4-trimethyl-2-cyclopenten-1-one) and other unknown products.

Figure 3.14 shows the conversion of 2-methylpropanal together with the selectivities to the main products over different Cu catalysts as a function of space time (W/F$_{A0}$). It is seen that,

when the conversion is lower than 55%, the total reaction rate of 2-methylpropanal over Cu/ZSM-5(280) (0.685 mol g^{-1} h^{-1}) is about 2 times higher than that on the catalyst Cu/Y(60) and Cu/SiO$_2$, which is 0.318 mol g^{-1} h^{-1} and 0.354 mol g^{-1} h^{-1}, respectively.

As seen in **Figure 3.14a**, the primary products of conversion of 2-methylpropanal over Cu/ZSM-5(280) are butenes, 2-methyl-1-propanol and acids (mainly 2-methyl-propanoic acid, with trace amounts of propanoic acid and acetic acid). As mentioned above, butenes were produced from dehydration of 2-methyl-1-propanol, which could be produced from hydrogenation of 2-methylpropanal. The selectivities of butenes increased from 42% to 60% with the increasing space time from 0.3 to 0.9 g h mol^{-1}, which was accompanied by a decreasing selectivity of 2-methyl-1-propanol from 23% to 19%. Interestingly, the selectivities of acids were significant, decreasing from 26% to 12% when the space time increased from 0.3 to 0.9g h mol^{-1}. This behavior is clearly different from that observed in MEK reaction over Cu catalysts. In the case of MEK reaction, the production of acids were negligible over Cu catalysts; nevertheless, the formation of acids could take place via high-temperature hydrolytic cleavage of the α,β-unsaturated ketone obtained from aldol condensation of ketones over acid sites of zeolite as discussed above. However, as seen in **Figure 3.15**, the self-condensation of 2-methylpropanal [129] cannot produce α,β-unsaturated ketone (aldehyde) due to lack of α-H in the aldol condensation product (3-hydroxy-2,2,4-trimethylpentanal). Such a significant difference indicates that the formation of acids should be from a different pathway other than the aldol condensation. It is reported that disproportionation of aldehyde can produce an acid and an alcohol via Tishchenko reaction over acid catalysts or Cannizzaro reaction over base catalysts [130–132]. In Tishchenko mechanism, an ester is produced in the first step, followed by the subsequent hydrolysis rapidly at the present reaction condition [130,132]. Since zeolites are solid acids, it is possible that the carboxylic acids could be formed in the conversion of 2-methylpropanal over Cu/ZSM-5 or Cu/Y via a Tishchenko-type reaction, which is confirmed by the results of the control experiments conducted over the parent zeolites (see **Table 3.6**). **Table 3.6** showed the conversion of 2-methylpropanal to the main products over HZSM-5(280) and HY(60) at the space time of 30.4 g h mol^{-1}. Acids (mainly 2-methyl-propanoic acid, trace amount of propanoic acid and acetic acid) and butenes were seen to be the primary products; by comparison. 2-methyl-1-propanol was negligible because it was immediately dehydrated to butenes after forming since the reaction of dehydration was extremely fast (will be discussed

later). In addition, the conversion of 2-methylpropanal are 34.5% and 25.3% over HZSM-5(280) and HY(60) at the space time of 30.4 g h mol^{-1}, respectively, which indicates that the reaction rate is considerably slower than the reaction over the corresponding Cu catalyst. Note that, in **Table 3.6**, the selectivity of butenes was much smaller than that of acids. With respect to this, we believed that part of butenes converted to aromatic products or other olefins ($C_2^=$, $C_3^=$, $C_5^=$-$C_8^=$) since aromatization [133,134], oligomerization [19] and cracking reaction [135] of olefins are very easy to occur over the acid sites of zeolites.

Based on the discussion above, 2-methylpropanal can disproportionate into 2-methyl-propanoic acid and 2-methyl-1-propanol via Tishchenko reaction consequently (see **Figure 3.16**), both of which are the primary products in the conversion of 2-methylpropanal over Cu/ZSM-5(280) (see **Figure 3.14a**). This indicates that the formation of 2-methyl-1-propanol could be from either hydrogenation or disproportionation of 2-methylpropanal over Cu/ZSM-5(280) catalyst. Similar behavior was observed over the catalyst Cu/Y(60): 2-methyl-1-propanol and acids (especially 2-methyl-propanoic acid) were produced simultaneously (see **Figure 3.14b**). However, by comparison, the clearly lower activity for the formation of butenes was exhibited in the reaction over Cu/Y(60). As seen in **Figure 3.14b**, the selectivity of butenes increased from 4% to 15% with the increasing space time from 0.94 to 2.1 g h mol^{-1}, which was accompanied by the decreasing selectivity of 2-methyl-1-propanol from 59% to 44%. Such a significant difference with respect to the selectivity of butenes indicates that the intermediate 2-methyl-1-propanol is much harder to dehydrate to butenes over the acid sites of Y-type zeolite than ZSM-5, which probably can be attributed to the different structures of these two zeolites.
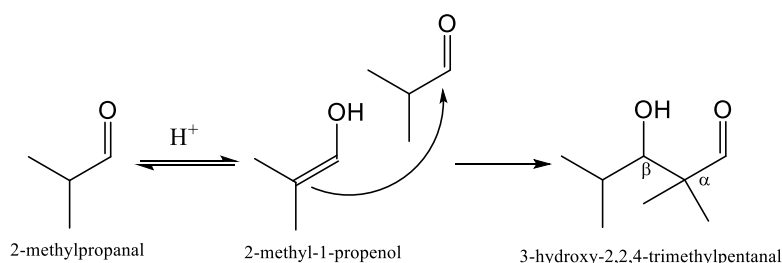
Figure 3.15. Acid-catalyzed self-condensation of 2-methylpropanal.
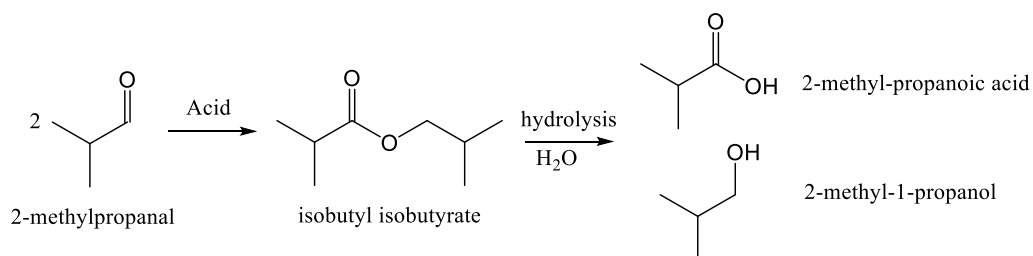
Figure 3.16. Disproportionation of 2-methylpropanal over acid catalyst.

Figure 3.14c shows the catalytic performance of the reduced Cu/SiO_2 in the conversion of 2-methylpropanal to the main products. As shown in **Figure 3.14c**, only 2-methyl-1-propanol and acid (2-methyl-propanoic acid) were seen in the conversion of 2-methylpropanal over Cu/SiO_2. It should be noted that the selectivity of 2-methyl-1-propanol increased over space time, while the acid was seen to decrease with increasing space time. It is apparent that butenes were not produced due to a lack of acid sites for dehydration of 2-methyl-1-propanol, which is similar to that observed on the reaction of MEK over Cu/SiO_2. As SiO_2 is a relatively inert support, it is unlikely for Cu/SiO_2 to catalyze the disproportionation of 2-methylpropanal to 2-methyl-1-propanol and acid via Tishchenko reaction mentioned above. However, some researchers have investigated the reaction of aldehyde over reduced copper catalysts and found that only alcohol and acid were formed. Takeshita et al. [136] and Kawamoto et al. [137] reported that conversion of propionaldehyde over reduced copper (support-free Cu was prepared by precipitation of copper nitrate, followed by reduction at 250 ^{o}C prior to the reaction) can only produce propionic acid and propyl alcohol at 250 ^{o}C, which is similar to the result we present. However, when they used ethanol or the mixture of ethanol and propionaldehyde as reactants to run the reaction under the same conditions, they found a significant amount of esters were formed. They suggested that the esters were formed by a hemiacetal mechanism, in which aldehyde would be the intermediate. Inui et al. held the same opinion and believed that ethanol was first dehydrogenated to acetaldehyde, followed by nucleophilic addition of ethanol to acetaldehyde to form a hemiacetal, which was further dehydrogenated to ethyl acetate [138]. Iwasa et al. [139] investigated the steam reforming of ethanol over reduced Cu/SiO_2 in presence of H_2O; they reported that acetic acid was produced together with the dehydrogenated product

acetaldehyde; meanwhile, the formation of ethyl acetate was significantly retarded by the presence of H_2O. However, when the reaction of acetaldehyde was carried out over the same reduced catalyst Cu/SiO_2 in the presence of H_2O, they noticed that acetic acid was produced at the same level compared to that in the steam reforming of ethanol. They did not mention whether ethanol was produced or not, nevertheless, no ethyl acetate was detected in the effluent. Hence, they suggested that the formation of acetic acid was from the reaction between acetaldehyde and water. Based on the discussion above, it seems that it is complicated for the reaction process of 2-methylpropanal over reduced Cu/SiO_2. Indeed, the acid, 2-methyl-propanoic acid we obtained, could be produced from either the direct reaction between 2-methylpropanal and water (the trace amount in 2-methylpropanal) or the reaction mechanism of hemiacetal, in which 2-methyl-1-propanol acts as an intermediate (see **Figure 3.17**). As seen in **Figure 3.17**, 2-methylpropanal was hydrogenated to 2-methyl-1-propanol in the first step, part of which then attacked 2-methylpropanal by nucleophilic addition to form a hemiacetal (1-isobutoxy-2-methylpropan-1-ol), which was then transformed to the ester (isobutyl isobutyrate) immediately; after that, the formed ester was converted to 2-methyl-propanoic acid and 2-methyl-1-propanol by the subsequent hydrolysis in the presence of trace amount of water in 2-methylpropanal.
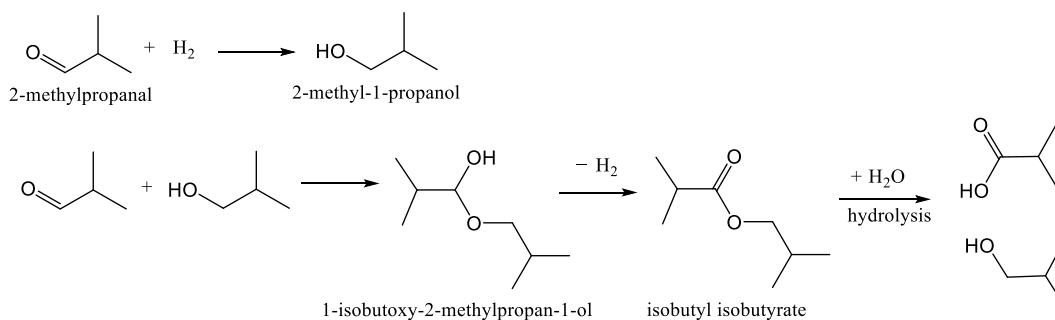
Figure 3.17. Probable reaction pathway of 2-methylpropanal over reduced Cu/SiO_2.

Table 3.6. Conversion of 2-methylpropanal over zeolites[a].

Catalysts	HZSM-5(280)	HY(60)
W/F_{A0} (g h mol^{-1})	30.4	30.4
Conversion (%)	34.5	25.3
Selectivity (%) hydrocarbons		
$C_2^=$-$C_3^=$	7.8	2.7
$C_4^=$	22.6	25.6
$C_5^=$	1.3	0.5
$C_6^=$	0.9	0.5
$C_7^=$-$C_8^=$	0.2	0.7
acids[b]	34.8	48.8
MEK	8.2	6.8
2-methyl-1-propanol	0.3	0.5
aromatics[c]	17.4	9.1
others[d]	6.5	4.8

[a] Reaction conditions: feed rate of 2-methylpropanal, 3.0 mL/h; H_2/2-methylpropanal (molar ratio), 5:1; temperature, 250 ^{o}C; time on stream=40 min.
[b] Acids include: 2-methyl-propanoic acid, trace amount of propanoic acid and acetic acid.
[c] Aromatics include: xylene, C_{9+} aromatic hydrocarbons.
[d] Other minor products include: acetone, oxygenated compound (1,2,3-trimethyl-cyclopentene, 1-ethyl-5-methylcyclopentene and 2,3,4-trimethyl-2-cyclopenten-1-one) and some other unknown products.

3.3.6. Conversion of 2-butanol
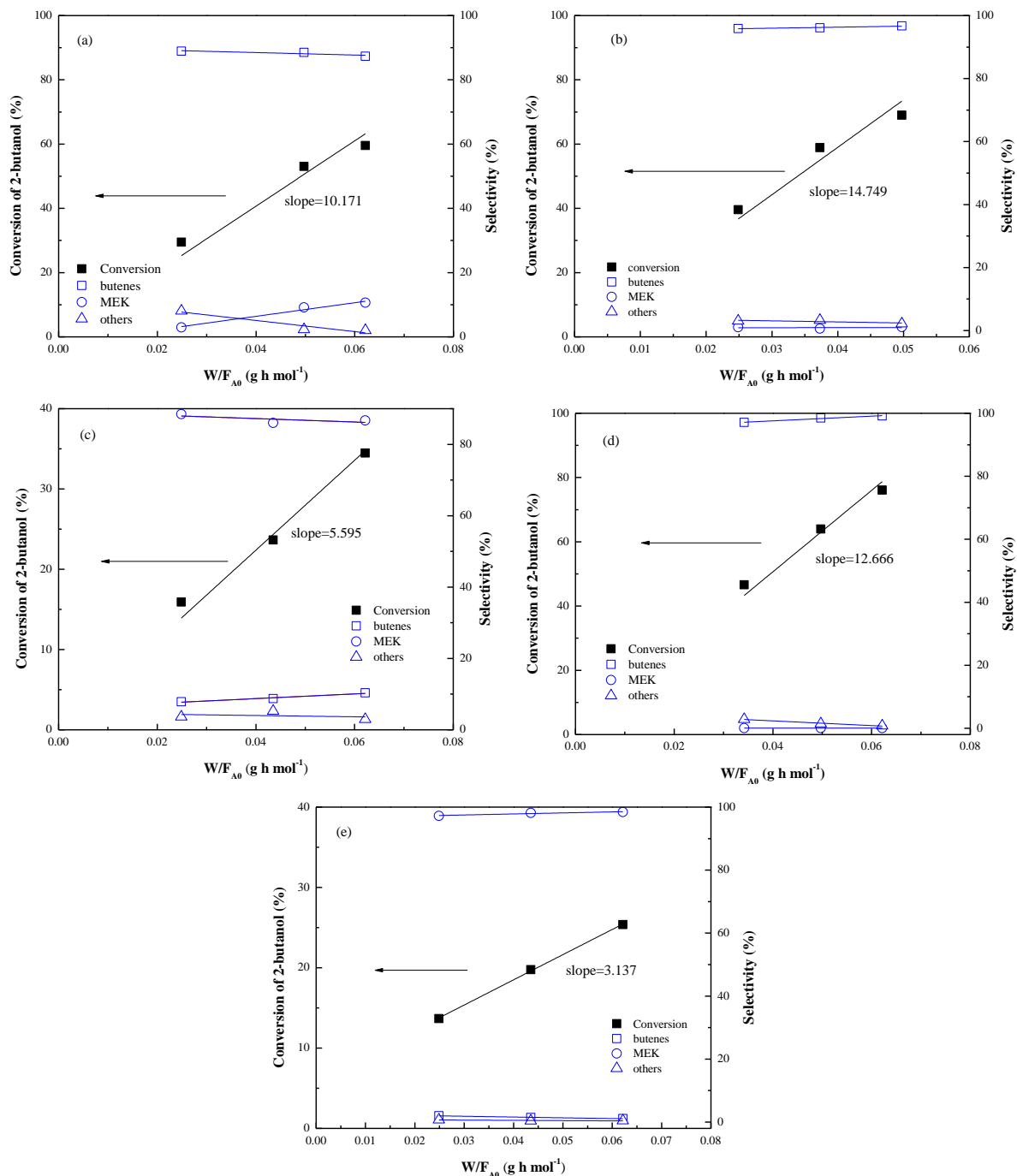
Figure 3.18. Conversion of 2-butanol and selectivities of the main products as a function of space time (W/F$_{A0}$) over different catalysts (a) Cu/ZSM-5(280), (b) HZSM-5(280), (c) Cu/Y(60), (d) HY(60), (e) Cu/SiO$_2$. Reaction conditions: feed rate of 2-butanol, 3.0 mL/h; H$_2$/2-butanol (molar ratio), 5.1:1; temperature, 250 ^{o}C; time on stream=40 min. Other minor products: 2-methyl-1-propanol, 2-methylpropanal, olefins (C$_3^=$ and C$_5^=$) and aromatics.

Figure 3.18 shows the conversion of 2-butanol and the selectivities to the main products over different catalysts as a function of space time. As shown in **Figure 3.18**, the total reaction rate of 2-butanol over each catalyst is more than 10 times higher than that of 2,3-butanediol, acetoin, MEK and 2-methylpropanal over the same catalyst. As displayed in **Figure 3.18a**, we can see the reaction rate of 2-butanol over the catalyst Cu/ZSM-5(280) is 10.171 mol g^{-1} h^{-1} with the conversion increased from 30% to 60% in the range of space time between 0.025 and 0.062 g h mol^{-1}, and the predominant products are butenes, which nearly remain the selectivity of 88%. This indicates that dehydration of 2-butanol occurs readily on the acid sites of zeolite, which is evidenced by the result of reaction of 2-butanol over HZSM-5(280) shown in **Figure 3.18b**. Note that butenes are exclusively produced over HZSM-5(280) with selectivity up to 96%. Only a trace amount of other products (MEK and 2-methyl-1-propanol) are seen in this process, which is similar to that observed over HY(60) shown in **Figure 3.18d**. The reaction rate over HZSM-5(280) is up to 14.749 mol g^{-1} h^{-1}, which is significantly higher than dehydration of 2,3-butanediol over HZSM-5(280) (0.594 mol g^{-1} h^{-1}). In addition, in **Figure 3.18a**, we can see the selectivity of MEK over Cu/ZSM-5 increased slightly from 2.9% to 10.6% with the increasing space time. This implies that 2-butanol undergoes two competitive reaction pathways, namely dehydration and dehydrogenation, over Cu/ZSM-5(280). Obviously, the dehydration process is overwhelmingly favored over dehydrogenation.

Figure 3.18c shows the catalytic performance of Cu/Y(60) in the reaction of 2-butanol. Unlike the results on Cu/ZSM-5(280), MEK becomes the predominant product with a selectivity up to 89% in the range of space time between 0.025 and 0.062 g h mol^{-1}, indicating that dehydrogenation of 2-butanol is the primary process over Cu/Y(60), which is similar to that observed over the control catalyst Cu/SiO$_2$ shown in **Figure 3.18e**. Over Cu/SiO$_2$, it is shown that the selectivity of MEK is up to 98.5% in the space time of 0.025 to 0.062 g h mol^{-1}. It is reasonable that dehydrogenation is the exclusive pathway since only Cu sites play an important role in the reaction of 2-butanol over Cu/SiO$_2$. However, HY(60) presents excellent activity in dehydration of 2-butanol to butenes as mentioned above. Hence, probably the precipitation of copper blocks the acid sites of Y zeolite, which prevents 2-butanol getting access to the acid sites. This could explain the low activity of Cu/Y(60) toward production of butenes. However, as shown in **Table 3.2**, the acidity of Cu/Y(60) (0.722 mmol/g NH$_3$) is higher than that of Cu/SiO$_2$ (0.524 mmol/g NH$_3$), which indicates that most acid sites of HY(60) over Cu/Y(60) could still

play an important role in dehydration of 2-butanol. In view of the low selectivities of butenes over Cu/(5.1) and Cu/Y(500) (shown in **Table 3.3**) by comparison to those of Cu/ZSM-5 catalysts, we suggests that the low activity of Cu/Y(60) toward the production of butenes is probably due to the different structure of zeolite.

3.3.7. Conversion of 2-methyl-1-propanol
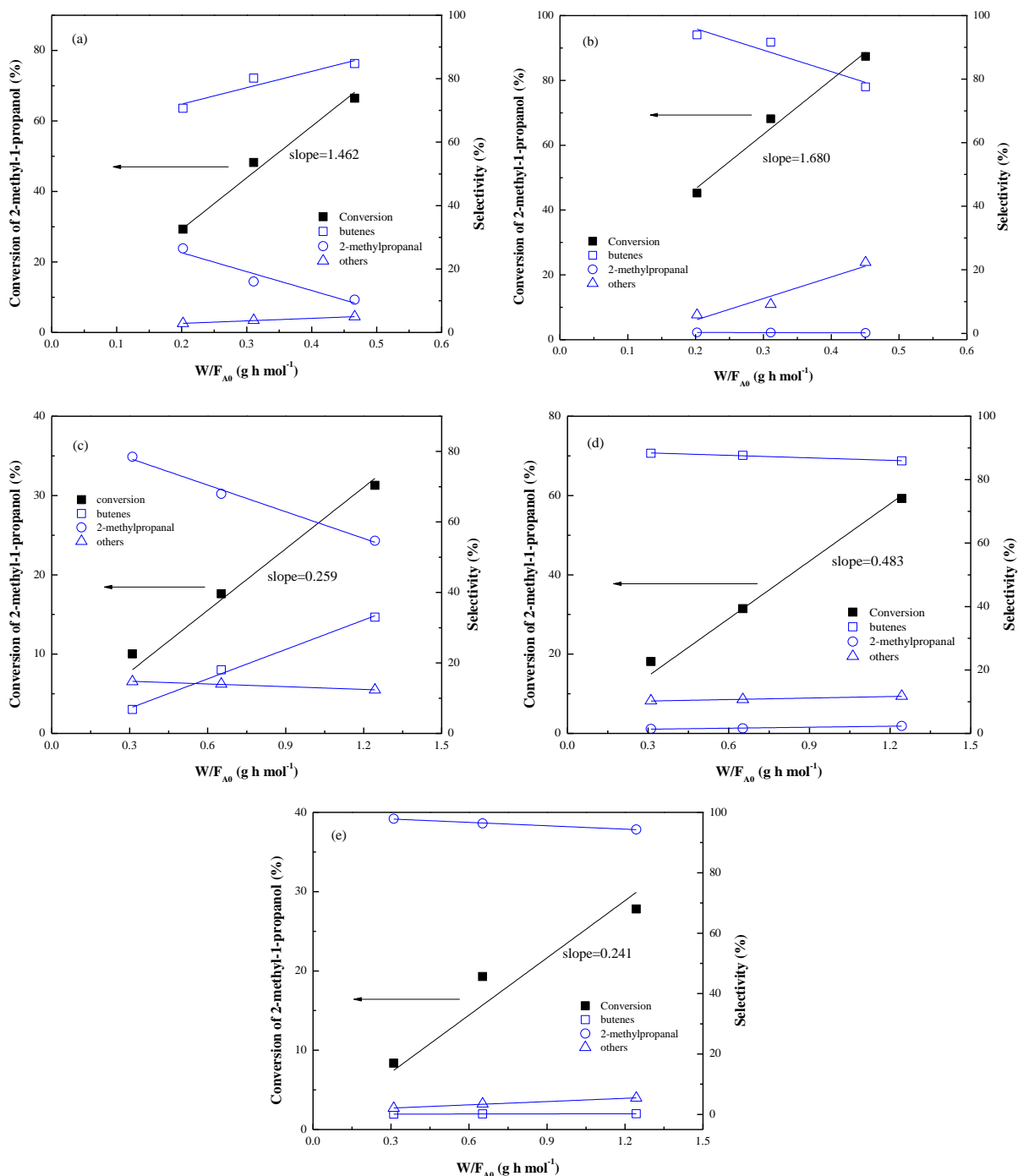
Figure 3.19. Conversion of 2-methyl-1-propanol and selectivities of the main products as a function of space time (W/F$_{A0}$) over different catalysts (a) Cu/ZSM-5(280), (b) HZSM-5(280), (c) Cu/Y(60), (d) HY(60), (e) Cu/SiO$_2$. Reaction conditions: feed rate of 2-methyl-1-propanol, 3.0 mL/h; H$_2$/2-methyl-1-propanol (molar ratio), 5:1; temperature, 250 ^{o}C; time on stream=40 min. Other minor products: olefins (C$_3^=$, C$_5^=$-C$_8^=$), aromatics and other unknown products.

Figure 3.19 shows the conversion of 2-methyl-1-propanol together with the selectivities of the main products over different catalysts as a function of space time. The total reaction rate for 2-methyl-1-propanol was considerably smaller than that of 2-butanol over the same catalyst. As shown in **Figure 3.19a**, the total reaction rate of 2-methyl-1-propanol over the catalyst Cu/ZSM-5(280) is 1.462 mol g^{-1} h^{-1}, and the primary products are butenes and 2-methylpropanal, which are obtained from dehydration and dehydrogenation of 2-methyl-1-propanol, respectively. This indicates that 2-methyl-1-propanol undergoes two main competitive reaction pathways over the bifunctional Cu/ZSM-5(280). As seen, the selectivity of butenes is seen to increase from 70.7% to 84.7% with the increasing space time from 0.20 to 0.46 g h mol^{-1}, which is accompanied by the decreasing selectivity of 2-methylpropanal from 26.5% to 10.3%. In **Figure 3.19b**, we can see the main product of 2-methyl-1-propanol reaction over HZSM-5(280) is butenes, with the selectivity decreased from 94.0% to 77.5% when the space time increased from 0.20 to 0.45 g h mol^{-1}, which was accompanied by the conversion increased from 45.3% to 87.4%. However, the dehydrogenated product, 2-methylpropanal, was almost undetected in the products. Note that the selectivities of the minor products such as olefins ($C_3^=$, $C_5^=$-$C_8^=$) and aromatics increased with increasing space time, which is because aromatization, oligomerization and cracking reaction of butenes are very easy to take place over acid sites of zeolites as discussed above [19,133–135]. **Figure 3.19e** displays the conversion of 2-methyl-1-propanol over the control catalyst Cu/SiO$_2$. As seen, dehydrogenation is the exclusive reaction pathway since only Cu sites play an important role in the reaction of 2-methyl-1-propanol over Cu/SiO$_2$, which is similar to that of 2-butanol mentioned above.

In addition, similar to that observed in the reaction of 2-butanol, 2-methyl-1-propanol conversion over Cu/Y(60) (see **Figure 3.19c**) led to quite substantial numbers of oxygenated product 2-methylpropanal between the space time from 0.31 to 1.24 g h mol^{-1}: selectivity decreased from 78.5% to 54.7%, which is accompanied by the increasing selectivity of butenes from 6.8% to 33.0%. Likewise, as shown in **Figure 3.19d**, butenes were seen to be the primary products in 2-methyl-1-propanol reaction over HY(60) zeolite, which is similar to that observed in 2-butanol conversion over the same zeolite. By comparison, the total reaction rate of 2-methyl-1-propanol over Cu/Y(60) or HY(60) is significantly smaller than that over the catalyst Cu/ZSM-5(280) or HZSM-5(280). Such a significant difference in the catalytic performance of

Y-type and ZSM-5 catalysts in dehydration of 2-methyl-1-propanol as well as 2-butanol further confirm that catalyst structure plays a vital role in dehydration of alcohols, even the conversion of 2,3-butanediol to butenes as a whole.

3.3.8. Kinetic model for 2,3-buanediol conversion to butenes and other products

A kinetic model employing Langmuir-Hinshelwood kinetics was constructed in order to predict 2,3-butanediol chemistry over Cu/ZSM-5 (280). The goal of this model was to predict the trends for all species as shown in **Figure 3.9**. Twenty-one reactions (see **Appendix C**) were included in the final mechanism in order to fit the data. **Table 3.7** shows the Langmuir-Hinshelwood rate laws and kinetic parameters for the main reactions. All the other parameters are shown in **Table C.1** (see **Appendix C**). To obtain the kinetic parameters, the sum of squares of the error between predicted and experimental molar flow rates (or selectivities and conversion) for all species was minimized using the non-linear least square regression in the Excel solver [140,141]. A comparison of the simulated and experimental conversion and selectivities of products is shown in **Figure 3.20**. As seen in this figure, the simulated results from non-linear least square regression were similar to the experimental values, which were evidenced by the R^2 (coefficient of determination) of each species.

Reactions were assumed to occur on two sites (acid and metal sites) with competitive adsorption between all species on those sites. The kinetic measurements above guided the selection of which reactions occurred on which sites. In addition, the kinetic measurements also provided insight into which reactions should be included in the mechanism. However, the kinetic information in those studies was not used in constructing the final model. Instead, fitting the model to the data in **Figure 3.9** was used.

As seen in **Figure 3.9**, the kinetic model fits the experimental data extremely well for all W/F_{A0}. This fact, along with the insight provided by the kinetic measurements described above, allows us to infer several important features about the reaction mechanism for 2,3-BDO reaction in the presence of hydrogen on metal-acid bifunctional catalysts.

First of all, chemistry on the metal sites is generally much faster than that on acid sites. This means that the first step for 2,3-BDO conversion is generally dehydrogenation to acetoin, rather than dehydration to MEK or 2-methylpropanal. This is somewhat surprising, since steady state results for large values of W/F_{A0} previously reported show little acetoin production except

when the catalyst is deactivating [105]. In addition, dehydration of 2,3-BDO to MEK is well known to readily occur on acid sites [16,31,34,35,105]. This research shows that when copper sites are added, those metal sites generally dominate reaction.

Once acetoin is produced, the metal sites can further dehydrogenate acetoin to produce 2,3-butanedione. Indeed, 2,3-butanedione production is shown in **Figure 3.9** for low W/F_{A0} and **Figure 3.11** for the reaction of acetoin over copper-containing catalysts. However, under the conditions in these experiments where high amounts of hydrogen are present, acetoin can be hydrogenated back to 2,3-BDO. This means that the dehydration reaction, although slow, can still proceed. Importantly, dehydration of 2,3-BDO to MEK and 2-methylpropanal appears to be irreversible, or nearly so, shown by the results in **Figures 3.12** and **3.14** and by the large equilibrium constants for those two reactions reported in **Table 3.7** (for MEK, $K_{3P}=1/0.025904383=38.6$ atm; for 2-methylpropanal, K_{4P}, infinity). This means that as the metal sites are catalyzing the reversible dehydrogenation of 2,3-BDO at a fast rate, the acid sites are slowly converting 2,3-BDO to dehydration products. These products increase as the reactants flow through the catalytic bed, and are subsequently converted further to alcohols and hydrocarbons.

Once MEK and 2-methylpropanal are produced, the primary reaction pathway is to hydrogenate them to 2-butanol and 2-methyl-1-propanol, respectively, which are then dehydrated to form butenes. Both the hydrogenation of the ketone/aldehyde and the dehydration of the alcohols appear to be fast reactions. Notably, the kinetics studies for the reaction of MEK and 2-methylpropanal over copper supported on ZSM-5 and HY zeolites both showed significant butene production even at low W/F_{A0}, suggesting that the dehydration of alcohols is fast.

Once butenes are produced, further reactions can still occur, lowering the ultimate selectivity to butenes. The next step appears to be the coupling of two molecules of butene to form C_8 hydrocarbons. As described by the Langmuir-Hinshelwood model, different C_8 species can form. These can be further reacted to form smaller hydrocarbon fragments over acid sites.

Table 3.7. Main reactions and kinetic parameters.

Reaction	Reaction rate	Parameter	value	unit
$BDO(g) \underset{k_{-1}}{\overset{k_1}{\rightleftharpoons}} acetoin(g) + H_2(g)$	$r_{1s} = \dfrac{k_1\left(P_{BDO} - \dfrac{P_{acetoin}P_{H2}}{K_{1P}}\right)}{X^3}$	k_1 $1/K_{1P}$	43.10103544 0.304384698	mol g^{-1} h^{-1} atm^{-1} atm^{-1}
$acetoin(g) \underset{k_{-2}}{\overset{k_2}{\rightleftharpoons}} 2,3\text{-butanedione}(g) + H_2(g)$	$r_{2s} = \dfrac{k_2\left(P_{acetoin} - \dfrac{P_{2,3\text{-butanedione}}P_{H2}}{K_{2P}}\right)}{X^3}$	k_2 $1/K_{2P}$	54.51339314 23.74627538	mol g^{-1} h^{-1} atm^{-1} atm^{-1}
$BDO(g) \underset{k_{-3}}{\overset{k_3}{\rightleftharpoons}} MEK(g) + H_2O(g)$, acid site	$r_{3s} = \dfrac{k_3\left(P_{BDO} - \dfrac{P_{MEK}P_{H2O}}{K_{3P}}\right)}{Y^2}$	k_3 $1/K_{3P}$	82.50865978 0.025904383	mol g^{-1} h^{-1} atm^{-1} atm^{-1}
$BDO(g) \underset{k_{-4}}{\overset{k_4}{\rightleftharpoons}} 2\text{-methylpropanal}(g) + H_2O(g)$	$r_{4s} = \dfrac{k_4\left(P_{BDO} - \dfrac{P_{2\text{-methylpropanal}}P_{H2O}}{K_{4P}}\right)}{Y^2}$	k_4 $1/K_{4P}$	21.98573732 0	mol g^{-1} h^{-1} atm^{-1} atm^{-1}
$MEK(g) + H_2(g) \underset{k_{-5}}{\overset{k_5}{\rightleftharpoons}} 2\text{-butanol}(g)$	$r_{5s} = \dfrac{k_5\left(P_{MEK}P_{H2} - \dfrac{P_{2\text{-butanol}}}{K_{5P}}\right)}{X^3}$	k_5 $1/K_{5P}$	51.78992335 20.13260058	mol g^{-1} h^{-1} atm^{-2} atm
$2\text{-methylpropanal}(g) + H_2(g) \underset{k_{-6}}{\overset{k_6}{\rightleftharpoons}} isobutanol(g)$	$r_{6s} = \dfrac{k_6\left(P_{2\text{-methylpropanal}}P_{H2} - \dfrac{P_{isobutanol}}{K_{6P}}\right)}{X^3}$	k_6 $1/K_{6P}$	10.50697038 0.074095963	mol g^{-1} h^{-1} atm^{-2} atm

$$2\text{-butanol(g)} \underset{k_{-7}}{\overset{k_7}{\rightleftarrows}} 2\text{-butene(g)} + H_2O(g) \qquad r_{7s} = \dfrac{k_7\left(P_{2\text{-butanol}} - \dfrac{P_{2\text{-butene}}P_{H2O}}{K_{7P}}\right)}{Y^2}$$

k_7	112.0947901	mol g^{-1} h^{-1} atm^{-1}
$1/K_{7P}$	0.017217005	atm^{-1}

$$\text{isobutanol(g)} \underset{k_{-8}}{\overset{k_8}{\rightleftarrows}} \text{isobutene(g)} + H_2O(g) \qquad r_{8s} = \dfrac{k_8\left(P_{\text{isobutanol}} - \dfrac{P_{\text{isobutene}}P_{H2O}}{K_{8P}}\right)}{Y^2}$$

k_8	9.546722317	mol g^{-1} h^{-1} atm^{-1}
$1/K_{8P}$	0	atm^{-1}

$$X = 1 + \sqrt{\frac{P_{H2}}{K_{1H}}} + K_{1A}P_{BDO} + \frac{P_{\text{acetoin}}}{K_{1D}} + \frac{P_{2,3\text{-butanedione}}}{K_{2D}} + \frac{P_{2\text{-butanol}}}{K_{5D}} + K_{5A}P_{MEK} + K_{6A}P_{2\text{-methylpropanal}} + \frac{P_{\text{isobutanol}}}{K_{6D}} + K_{N_2}P_{N_2} + K_{2\text{-butene}}P_{2\text{-butene}}$$

$$+ K_{\text{isobutene}}P_{\text{isobutene}} + K_{H_2O}P_{H_2O} + K_{C_{8,1}^=}P_{C_{8,1}^=} + K_{C_{8,2}^=}P_{C_{8,2}^=} + K_{C_{8,3}^=}P_{C_{8,3}^=} + K_{C_3^=}P_{C_3^=} + K_{C_{5,1}^=}P_{C_{5,1}^=} + K_{C_{5,2}^=}P_{C_{5,2}^=} + K_{C_{5,3}^=}P_{C_{5,3}^=} + K_{C_2^=}P_{C_2^=} + K_{C_{6,1}^=}P_{C_{6,1}^=}$$

$$+ K_{C_{6,2}^=}P_{C_{6,2}^=} + K_{C_{6,3}^=}P_{C_{6,3}^=} + K_{C_8H_{10,1}}P_{C_8H_{10,1}} + K_{C_8H_{10,2}}P_{C_8H_{10,2}}$$

$$Y = 1 + \frac{P_{H2O}}{K_{3W}} + K_{3A}P_{BDO} + \frac{P_{MEK}}{K_{3D}} + K_{7A}P_{2\text{-butanol}} + \frac{P_{2\text{-butene}}}{K_{7D}} + \frac{P_{2\text{-methylpropanal}}}{K_{4D}} + K_{8A}P_{\text{isobutanol}} + \frac{P_{\text{isobutene}}}{K_{8D}} + \frac{P_{C_{8,1}^=}}{K_{9D}}$$

$$+ \frac{P_{C_{8,2}^=}}{K_{10D}} + \frac{P_{C_{8,3}^=}}{K_{11D}} + \frac{P_{C_3^=}}{K_{17D}} + \frac{P_{C_{5,1}^=}}{K_{17DE}} + \frac{P_{C_{5,2}^=}}{K_{18DE}} + \frac{P_{C_{5,3}^=}}{K_{19DE}} + \frac{P_{C_2^=}}{K_{20D}} + \frac{P_{C_{6,1}^=}}{K_{20DE}} + \frac{P_{C_{6,2}^=}}{K_{21DE}} + \frac{P_{C_{6,3}^=}}{K_{22DE}} + \frac{P_{C_8H_{10,1}}}{K_{14D}} + \frac{P_{C_8H_{10,,2,1}}}{K_{23D}}$$

$$+ \frac{P_{C_8H_{10,,2,2}}}{K_{24D}} + \frac{P_{C_8H_{10,,2,3}}}{K_{25D}} K_N P_{N_2} + \sqrt{\frac{P_{H2}}{K_{14H}}} + K_{2,3\text{-butanedione}}P_{2,3\text{-butanedione}} + K_{\text{acetoin}}P_{\text{acetoin}}$$

Figure 3.20. A comparison of experimental and simulated conversion and selectivities.

3.4. Conclusions

The kinetic results show that conversion of 2,3-butanediol to acetoin is a reversible process, at low space time, 2,3-butandiol can readily be converted to acetoin by dehydrogenation over Cu catalysts. However, with increasing space time (W/F_{A0}), the formed acetoin can react with H_2 to convert to 2,3-butanediol, which can be further convert to MEK, 2-methylpropanal, 2-butanol, 2-methyl-1-propanol, and then butenes as a result.

The results show that the hydrogenation and dehydrogenation reactions occur on the Cu sites of the catalysts, while the dehydration reactions take place on the acid sites of zeolite. Once MEK and 2-methylpropanal are produced, the primary reaction pathway is to hydrogenate them to 2-butanol and 2-methyl-1-propanol, respectively, which are then dehydrated to form butenes immediately since dehydration process is overwhelmingly favored over dehydrogenation and hydrogenation.

Chapter 4 - Mesoporous catalysts for conversion of 2,3-butanediol to butenes

4.1. Introduction

Over the past few decades, the renewable bio-based chemicals have attracted considerable attention due to the threat of petroleum depletion [4,6]. 2,3-butanediol (2,3-BDO) has significant potential as a platform chemical for production of renewable fuels and chemicals since it can be produced with high productivity via fermentation [9,10,12,14,22] and provides a C_4 building block for further synthesis. Some researchers have investigated dehydration of 2,3-butanediol to 1,3-butanediene and methyl ethyl ketone (MEK) over thoria [17], scandium oxide [38], alumina [37], phosphate catalysts (BP, AlP, TiP, ZrP and NbP) [142] and HZSM-5 [34]. The obtained product 1,3-butadiene can then be dimerized to produce the aromatic intermediate styrene (Diels-Alder reaction) [18], while MEK is widely used as liquid fuel additive or organic solvent as well as a precursor for MEK peroxide [16,143,144]. More recently, the group of Dr. Alexis T. Bell developed novel pathways to catalyze the biomass-derived methyl ketones (including MEK) to produce C_{12}-C_{45} hydrocarbons, which can serve as potential jet fuels (C_{12}-C_{21}) and synthetic lubricants (C_{33+}), by self- and cross-condensation reactions over base catalyst Mg-Al-O or acid catalyst Nb_2O_5 [127,128]. Harvey et al. developed a pathway to selectively convert 2,3-butanediol by acid catalyst Amberlyst-15 to a complex mixture of 2-ethyl-2,4,5-trimethyl-1,3-dioxolanes and 4,5-dimethyl-2-isopropyl dioxolanes, which can be used as a gasoline-range fuel and diesel oxygenate due to an anti-knock index of 90.5, high combustion value, low solubility in water and full miscibility with both gasoline and diesel fuel [33]. Our previous work has shown that bifunctional catalyst Cu/ZSM-5 can convert 2,3-butanediol to butenes with high selecitivty (~70%) [105], herein, in this study we will expand on these results by utilizing mesoporous catalysts in 2,3-butanediol conversion to butenes.

Well-ordered mesoporous siliceous materials have received considerable attention as heterogeneous solid catalysts since the discovery of the novel family of molecular sieves called M41S, especially MCM-41 (space group *p6mm*) and MCM-48 (space group *Ia3d*), due to high surface area, large pore sizes and pore volumes, allowing facile diffusion of large reactants and

products [145–149]. MCM-41 silica possesses one-dimensional ordered arrays of hexagonal channels with uniform mesopore size in the range of 2-10 nm [145,146]. However, MCM-48 is more attractive than MCM-41 for potential applications in catalysis due to its three-dimensional interconnected cubic network, which is more favorable for mass transfer kinetics in contrast to that of the hexagonal MCM-41 material with a one-dimensional channel system prone to diffusion limitations and pore blockage, even though it is more difficult to synthesize [148–150]. Schumacher et al. developed a novel method to prepare MCM-48 and metal-incorporated MCM-48 materials at room temperature, which made it possible to synthesize this kind of material in an easy and fast way [151,152].

Another family of highly ordered mesoporous silica-based materials were synthesized by nonionic triblock copolymers (such as $EO_{20}PO_{70}EO_{20}$) as pore-direct agent in strong acid media, among which SBA-15 was the most popular one [153,154]. SBA-15 has highly ordered hexagonal arrays of mesopores with 1-D channels, indicating a 2-D hexagonal (*p6mm*) mesostructure [153–155] and higher hydrothermal stability than MCM-41 and MCM-48 due to the thicker pore walls (3.1−6.4 nm) [153,154]. However, since it is difficult to introduce heteroatoms (such as Al) to the mesoporous structure of SBA-15 by "direct-synthesis" under strongly acidic conditions, Wu et al. developed a novel method to synthesize the heteroatom substituted SBA-15 by the "pH-adjusting" method to improve the efficiency [155].

More recently, increasing attention has been attracted to zeolite with micro-mesopore hierarchical porosity due to the efficient mass-transport property because the hierarchical zeolite could overcome the diffusion limitations of the micropores [156–162]. The simplest way to introduce mesopores to zeolite is desilication of the zeolite by alkali treatment, leading to an interconnected network of micropores and mesopores. As reported, the framework aluminium would control the process of framework silicon extraction [162], and the mesopore size is controllable by variation of time and temperature of the alkaline treatment and even alkali concentration [158,163,164]. Desilicated zeolites have been investigated in several reactions, including Fischer-Tropsch reaction, 1,3,5-triisopropylbenzene cracking, aromatization and isomerization of 1-hexene, methanol to hydrocarbons and propanal conversion [79,157,158,164,165].

In this study, three different types of mesoporous materials (Al-MCM-48, Al-SBA-15 and mesoporous ZSM-5) were loaded with ~20wt% CuO and tested in the conversion of 2,3-

butanediol to butenes. Our purpose is to investigate the pore size effect on the conversion of 2,3-butanediol to butenes.

4.2. Experimental

4.2.1. Synthesis

All Al-MCM-48 materials were prepared by a room temperature synthesis as reported in the literature [151,152]. Tetraethoxysilane (TEOS, 99.9%, Fisher Scientific) and aluminum isopropoxide (>98.0%, Fisher Scientific) were used as Si and Al sources, respectively, and hexadecyltrimethylammonium bromide (CTAB, >99%, Fisher Scientific) was used as the template. Typically, a 2.4 g aliquot of CTAB (6.6 mmol) and different amount of aluminum isopropoxide (in order to obtain SiO_2/Al_2O_3 molar ratios of 23, 50, 100 and 200) were dissolved in 100 g of deionized water and 50 mL of ethanol (100%, 200 proof, USP, 0.87 mol), and 12 mL of aqueous ammonia (30wt%, certified ACS Plus, 0.20 mol) was added to the surfactant solution. The solution was then stirred (450 rpm) until Al precursor and the template were dissolved and 3.4 g of TEOS (16 mmol) was added at one time. After stirring for 5 h at room temperature, the obtained solid was recovered by filtration, washed with deionized water, and dried in air at ambient temperature. The template was removed by calcination at 550 ^{o}C in air for 6 h with a heating rate of 1 ^{o}C/min. The obtained aluminosilicate materials are designated as Al-MCM-48(n), where n stands for SiO_2/Al_2O_3 ratio. The reference sample MCM-48 was prepared by the same method without adding aluminum isopropoxide.

Al-SBA-15 materials were synthesized by using the pH-adjusting method [155]. TEOS and aluminum isopropoxide were used as Si and Al sources, respectively, and nonionic triblock copolymer surfactant Pluronic P123 ($EO_{20}PO_{70}EO_{20}$, where EO= ethylene oxide, PO= propylene oxide; molecular weight of 5800; BASF Corp.) was utilized as a template. Typically, 4 g of P123 was dissolved in 125 mL of HCl solution (2M). Next, 8.5 g of TEOS and the required amount of aluminum isopropoxide (based on the desired SiO_2/Al_2O_3 molar ratio of 23, 50, 100 or 200) were added, and the resulting mixture was continuously stirred at 40 ^{o}C for 24 h and subsequently hydrothermally treated without stirring at 100 ^{o}C for an additional 48 h and then cooled down to room temperature. The pH was adjusted up to 7.5 by adding aqueous ammonia (30wt%, certified

ACS Plus) dropwise at room temperature and the obtained mixture was finally aged again at 100 ^{o}C for another 48 h. The solid was recovered by filtration, washed with deionized water, and dried in air at ambient temperature. The template was removed by calcination at 550 ^{o}C in air for 6 h with a heating rate of 1 ^{o}C/min. The final aluminosilicate materials are denoted as Al-SBA-15(n), where n stands for the SiO_2/Al_2O_3 ratio in the initial gel. The control sample SBA-15 was prepared by the same method without adding aluminum isopropoxide.

The mesoporous ZSM-5 was prepared by a simple alkaline treatment method reported in the literature [34,44,38,40,43]. 6.6 g of parent ZSM-5 zeolite was vigorously stirred in 200 mL of NaOH solution (0.2 M) at a temperature of 70 ^{o}C for 30 min. The slurry was then quenched immediately, using an ice-water bath. The resultant solid was recovered by filtration, fully washed with deionized water until a neutral pH and finally dried at 100 ^{o}C overnight. After this step, the H-form zeolite was obtained by three consecutive ion-exchanges of the alkaline-treated sample with 1 M NH_4NO_3 solution (10 mL/g) at 80 ^{o}C for 3 h, followed by calcination in air at 550 ^{o}C for 5 h. The obtained sample was named as meso-ZSM-5(n), where n stands for the SiO_2/Al_2O_3 ratio of parent zeolite.

The copper catalysts were prepared by an ammonia evaporation hydrothermal (AEH) method as reported previously [64–66]. To load 20wt% of CuO on the catalysts, 7.6 g of $Cu(NO_3)_2 \cdot 3H_2O$ (99%, Fisher scientific) was dissolved in 40 mL of deionized water at room temperature, followed by adding ammonia hydroxide (28-30wt%, Fisher Scientific) until the pH reached 9.1 to form a dark blue cupric ammine complex $[Cu(NH_3)_4(H_2O)_2]^{2+}$. Next, water was added to make 80 mL of a copper-ammonia complex solution. 10 g of the mesoporous materials described above was added to the solution and then the container was capped to avoid the evaporation of ammonia and stirred for 6 h at room temperature. After that, the container was transferred to an oil bath preheated at 80 ^{o}C to allow for the evaporation of ammonia and the decrease of pH which led to the deposition of copper. When the pH of the suspension decreased to 6-7 or the liquid turned colorless, the evaporation process was terminated. The solid was recovered by filtration, washed, dried at 110 ^{o}C, and calcined in air at 550 ^{o}C for 4 h. Finally, the calcined catalyst was pelletized, crushed and sieved to 40-60 mesh. The content of CuO was determined by the inductively coupled plasma (ICP) method. The copper catalysts were named: Cu/Al-MCM-48(n), Cu/Al-SBA-15(n) and Cu/meso-ZSM-5(n), where n is the SiO_2/Al_2O_3 ratio.

4.2.2. Catalyst characterization

BET surface area and porosity of catalysts were measured using nitrogen physisorption at -196°C on a Quantachrome Autosorb-1 apparatus and analyzed with Autosorb-1 software. Before measurement, the samples were evacuated at 350 ^{o}C for 4 h. The reducibility and the acid property of the calcined catalysts were determined by temperature programmed reduction (H$_2$-TPR) and temperature programmed desorption of ammonia (NH$_3$-TPD), respectively, both of which was carried out in an Altamira AMI-200 system equipped with a thermal conductivity detector. The metallic copper surface area and dispersion were measured by dissociative N$_2$O decomposition method at 90 ^{o}C using the same system as H$_2$-TPR and NH$_3$-TPD. Powder X-ray diffraction (XRD) patterns of the samples were recorded using Rigaku Miniflex II desktop x-ray diffractometer. Scans of two theta angles were obtained from 5° to 90° for all catalysts with a step size of 0.02^o and scan speed of 0.75 ^{o}/min. The XPS analysis of the catalyst was carried out on a PerkinElmer PHI 5400 using achromatic Al Kα radiation (1486.60 eV), and the binding energy (BE) value was referenced to the C1s peak of contaminant carbon at 284.6 eV to correct for the charging on the substrate. The detailed procedure of all characterizations above were reported in the previous study [105].

For the measurement of SAXS (small angle X-ray scattering) of mesoporous materials, a Rigaku three-pinhole S-MAX3000 SAXS camera was used with a microfocus CuKα (λ=1.54 Å) sealed tube source. Samples were encapsulated between two pieces of polyimide tape. The size of the beam at the sample was ~0.4 mm. Pixel-to-angle conversion was determined via scattering from a silver behenate sample.

Solid-state ^{27}Al magic-angle spinning (MAS) NMR (nuclear magnetic resonance) measurement has been performed to analyze the effective incorporation of aluminum into the structure of the mesoporous aluminosilicate material. Typically, approximately 100 mg of each mesoporous aluminosilicate sample was packed into a 4 mm ZrO$_2$ rotor with Kel-F drive cap (Wilmad Labglass). The packed rotor was inserted into a Bruker AVIII 400 MHz solid-state NMR spectrometer with a Bruker HX MAS probe. MAS angle was set using rotor packed with KBr. 27Al NMR acquisition parameters and chemical shift referencing calibrated using Al$_2$O$_3$ standard. Mesoporous aluminosilicate samples were spun at the magic angle at a spin rate equal to 12 kHz. 1D 27Al MAS spectra were recorded with the following acquisition parameters: excitation pulse power, 192 kHz; offset, 0 ppm; sweep width, 400 ppm; acquisition time (aq),

~25 ms; interscan delay, 500 ms; total experiment time, ~10 minutes. To process the data, the raw FID was zero filled to 4k real data points, Fourier transformed without apodization and the resulting spectrum phase corrected for the absorptive Lorentzian line shape.

For transmission electron microscopy (TEM) imaging, a small amount of the support was dispersed in ethanol with a 30 min sonication. A drop of the homogeneous suspension was deposited on a lacey carbon TEM grid and examined by TEM using an FEI Talos TEM at 160 and 200 KV. Morphology of meso-ZSM-5 was characterized using field emission scanning electron microscopy (FESEM) and the content of Al was obtained from energy dispersive spectroscopy (EDS) detector.

4.2.3. Catalytic reaction

The catalytic reactions were performed in a continuous flow fixed-bed reactor made of stainless steel (id=8 mm) under atmospheric pressure. Prior to reaction, the catalyst sample was reduced in the reactor in the H_2/N_2 flow (flow rate of H_2/N_2=1/5) at 300 ^{o}C for 2 h. The H_2 flow of 24 cm^3/min (standard ambient temperature and pressure, SATP) and the N_2 flow of 120 cm^3/min (SATP) were controlled with mass-flow controllers (Brooks). 2,3-butanediol was fed via a micropump (Eldex 1SMP) at 3 mL/h together with a H_2 flow of 67.2 cm^3/min (SATP) and N_2 flow of 15.4 cm^3/min (SATP). The reaction temperature was set at 250 ^{o}C according to the previous report [105]. Product compositions were analyzed by an on-line gas chromatograph (SRI 8610C) equipped with an MXT-1 column (nonpolar phase, 60m, ID 0.25 mm, film thickness 0.25 μm), TCD and FID detectors for the analysis of hydrocarbons and oxygenated chemicals, and quantified by injecting calibration standards to the GC system. The temperature of the tubing from the bottom of the reactor to the inlet of GC was maintained at 230 ^{o}C to avoid the condensation of liquid products. The detailed procedure is described in the earlier report [105]. To confirm the identification of products, GC-MS analyses were also carried out by using an Agilent 7890A GC system equipped with an Agilent 5975C MS detector and HP-1 capillary column. The carbon selectivity and conversion were calculated in the following methods.

$$\text{Carbon selectivity} = \frac{\text{Moles of carbon in specific product}}{\text{Total carbon atoms in identified products}} \times 100\%$$

$$\text{Conversion} = \frac{(\text{moles of 2,3-BDO})_{in} - (\text{moles of 2,3-BDO})_{out}}{(\text{moles of 2,3-BDO})_{in}} \times 100\%$$

The carbon balances were maintained above 90% for all runs in this paper.

4.3. Results and discussion

4.3.1. Characterization of catalysts

4.3.1.1. X-ray diffraction
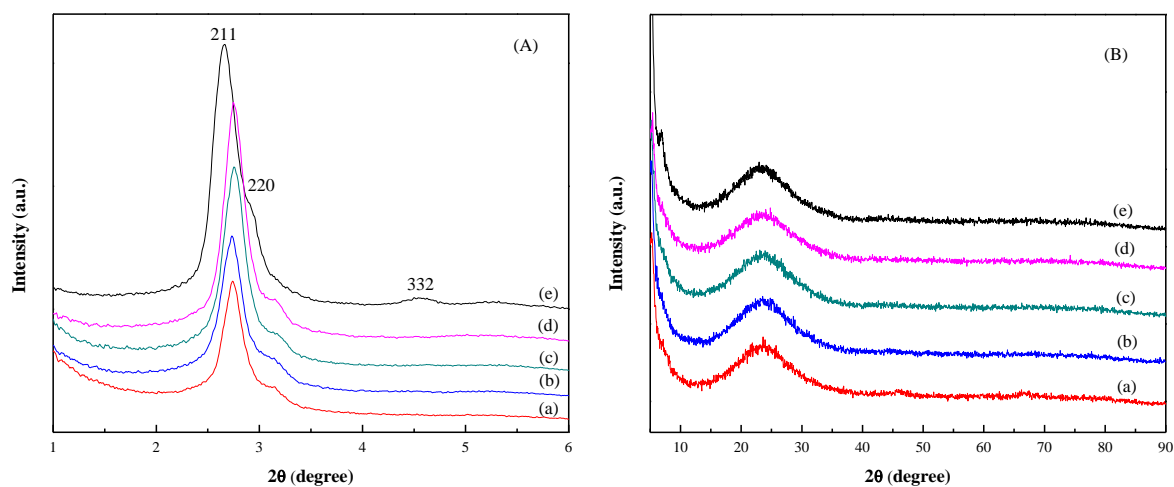
Figure 4.1. (A) Small-angle and (B) wide-angle XRD patterns of calcined mesoporous materials (a)Al-MCM-48(23), (b)Al-MCM-48(50), (c)Al-MCM-48(100), (d)Al-MCM-48(200), (e) purely siliceous MCM-48.
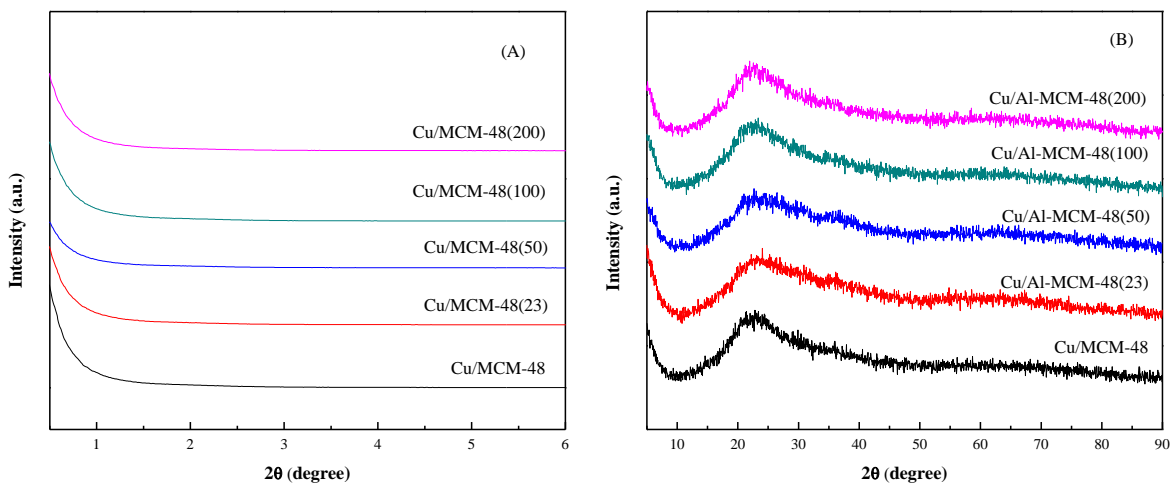
Figure 4.2. (A) Small-angle and (B) wide-angle XRD patterns of calcined Cu/Al-MCM-48 catalysts with different SiO_2/Al_2O_3 ratios.

Figure 4.1A shows the small-angle XRD patterns of the calcined MCM-48 and Al-MCM-48 mesoporous materials with different SiO_2/Al_2O_3 ratios. The patterns exhibit typical diffraction peaks indexed as (211), (220) and (332) corresponding to the *Ia3d* space group (cubic pore structure) [148,151,168,169]. The (220) reflection was found to exist as a shoulder peak rather than a distinct peak. The repetition distance of the pores (d spacing) was obtained by the Bragg's Law using the position of (211) diffraction peak (shown in **Table 4.1**). The lattice parameter *a* of the cubic unit cell was obtained by the formula $a = d_{hkl} (h^2+k^2+l^2)^{1/2}$ [149,170]. The pore wall thickness was calculated according to the formula $\varepsilon = (a/3.092) - (D/2)$, where *D* is the pore diameter from N_2 adsorption-desorption (shown in **Table 4.1**) [52,149,170].

As shown, the (211) and (220) peaks shifted to a slightly higher 2θ angle from 2.67^o to 2.94 ^{o} and 2.76^o to 3.16^o, respectively, after the introduction of Al as compared to the purely siliceous MCM-48. In addition, the intensity of (211) peak was observed to decrease with increasing content of Al, namely, the decreasing SiO_2/Al_2O_3 ratio from 200 to 23. The peak of (332) was seen to disappear after the introduction of Al. All these facts indicate that the substitution of Si by Al leads to the deterioration of the ordered pore structures and the contraction of the unit cell [169]. As shown in **Table 4.1,** the lattice parameter *a* decreased slightly from 8.1 nm for purely siliceous MCM-48 to 7.9 nm for aluminosilicate MCM-48.

Figure 4.1B shows the wide-angle XRD patterns of calcined Al-MCM-48. As seen, the broad diffraction peak at 2θ of 22° was exhibited, which was the characteristic of amorphous silica since the pore wall of MCM-48 was amorphous [55,147,169,171].

 Figure 4.2A shows the small-angle XRD patterns of calcined Cu/Al-MCM-48 catalysts. As seen, no peaks were observed in the low angle region, presumably resulting from the deposition of Cu in the mesopores, destroying the ordered pore structures as a result. No obvious diffraction peaks corresponding to CuO can be seen in the wide-angle XRD patterns shown in **Figure 4.2B**, indicating that all copper species were well dispersed on the support.
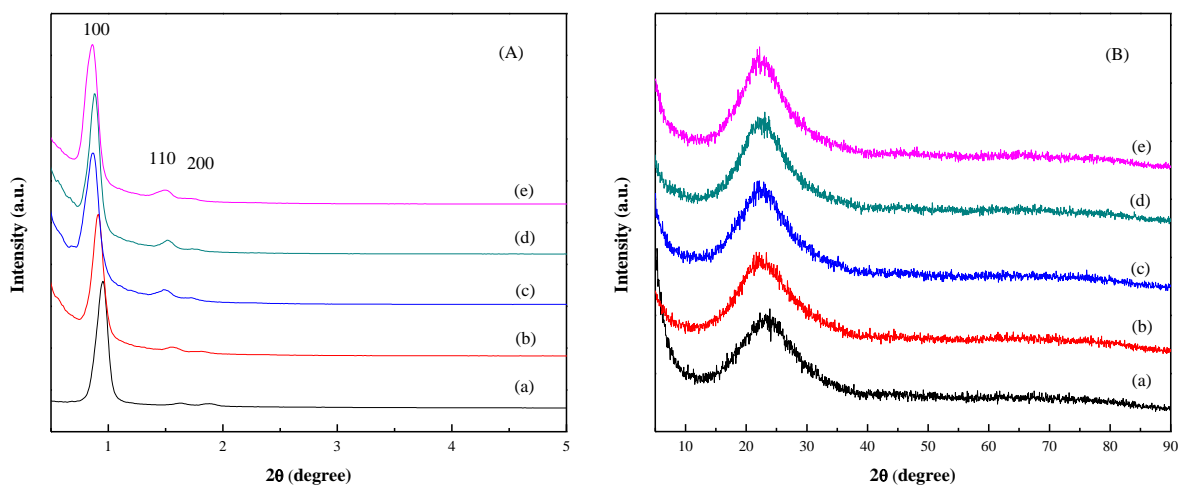
Figure 4.3. (A) Small-angle and (B) wide-angle XRD patterns of calcined mesoporous materials (a)purely siliceous SBA-15, (b)Al-SBA-15(23), (c) Al-SBA-15(50), (d) Al-SBA-15(100), (e) Al-SBA-15(200).
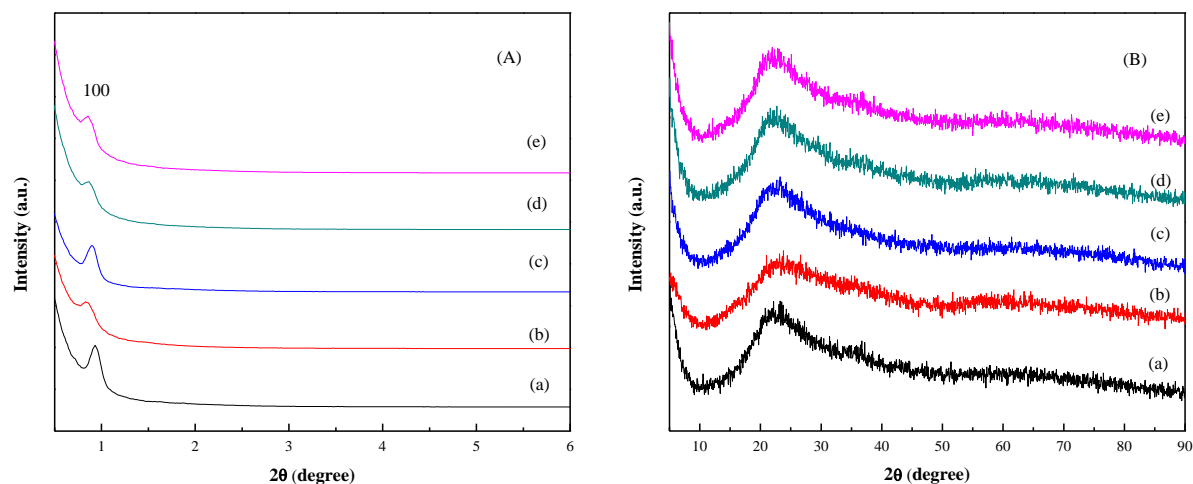
Figure 4.4. (A) Small-angle and (B) wide-angle XRD patterns of calcined Cu/Al-SBA-15 catalysts with different Al contents: (a) Cu/SBA-15, (b) Cu/Al-SBA-15(23), (c) Cu/Al-SBA-15(50), (d) Cu/Al-SBA-15(100), (e) Cu/Al-SBA-15(200).

The small-angle powder XRD patterns of calcined SBA-15 and Al-SBA-15 mesoporous materials with different SiO_2/Al_2O_3 ratios are shown in **Figure 4.3A**. It is shown that the XRD patterns with three typical diffraction peaks at approximately $2\theta=0.9^{o}$, 1.5^{o} and 1.8^{o} are observed for all samples, which can be indexed as (100), (110) and (200) reflection, respectively, corresponding to 2D hexagonal mesostructured with *p6mm* space group [153–155]. Unlike the mesoporous Al-MCM-48, the peak intensity of Al-SBA-15 with different Al contents is similar, which is because the pH-adjusting method allows a large amount of Al to be incorporated while retaining a highly ordered mesostructured [155]. The d-spacing was obtained by the Bragg's Law using the position of (100) diffraction peak (shown in **Table 4.2**). The lattice parameter *a* of the hexagonal unit cell was obtained by the formula $a = 2d_{100}/\sqrt{3}$ [154,172–176], where d_{100} represents the d-spacing value of (100) diffraction peak of XRD. The pore wall thickness was calculated according to the formula $\varepsilon = a - D$, where *a* is the unit cell and *D* represents the pore diameter from N_2 adsorption-desorption (shown in **Table 4.2**) [154,175–177]. As shown in **Table 4.2**, the d_{100} spacing and the unit cell parameter (*a*) of all the obtained Al-SBA-15 materials are larger than the ones of the purely siliceous SBA-15 (d_{100}=9.2 nm, *a* =10.7 nm), which is caused by the longer Al−O bond (1.75 Å) than the Si-O bond (1.60 Å) [155,175]. However, the d_{100} spacing and the unit cell parameter (*a*) of Al-SBA-15 material with the highest

content of Al (SiO$_2$/Al$_2$O$_3$=23) in this paper is 9.7 nm and 11.2 nm, respectively, both of which are smaller than the ones of the other Al-SBA-15 materials with SiO$_2$/Al$_2$O$_3$ ratios of 50, 100 and 200 (shown in **Table 4.2**), which is in accordance to the reports [155,173].

        Figure 4.4A shows the small-angle XRD patterns of calcined Cu/SBA-15 and Cu/Al-SBA-15 catalysts with different SiO$_2$/Al$_2$O$_3$ ratios. Compared with the parent supports, it is noted that Cu/(Al)-SBA-15 catalysts show much weaker d_{100} intensity, indicating the partial destruction of the ordered pore structure of SBA-15 after introduction of Cu. It is probably due to the dissolution of Si when the Cu/(Al)-SBA-15 catalysts were prepared by ammonia evaporation hydrothermal (AEH) method in this paper, which is similar to the reports that the catalysts were prepared by the homogeneous deposition precipitation (HDP) method [178,179]. In addition, no diffraction peaks corresponding to CuO can be seen in the wide-angle XRD patterns shown in **Figure 4.4B**, indicating that all copper species were well dispersed on the support.
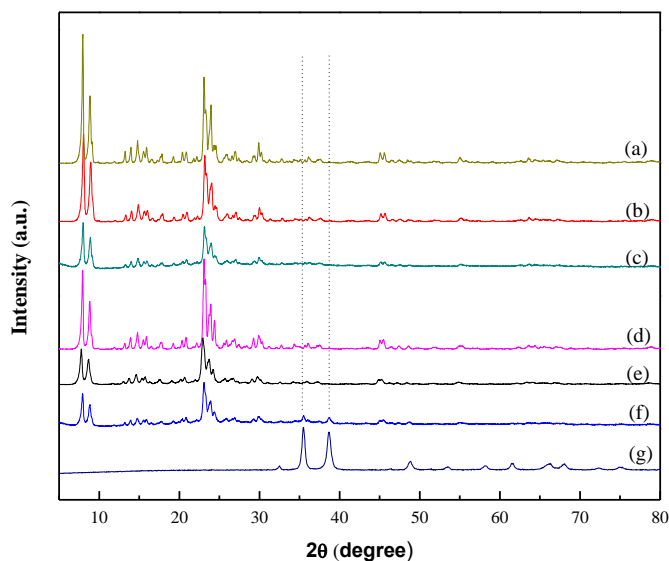
Figure 4.5. XRD patterns of meso-ZSM-5 and Cu/meso-ZSM-5 catalysts. (a)HZSM-5(280), (b)meso-HZSM-5(280), (c)Cu/meso-ZSM-5(280), (d)HZSM-5(50), (e)meso-ZSM-5(50), (f)Cu/meso-ZSM-5(50), (g)CuO.

XRD was carried out to investigate the possible structural changes in alkaline-treated ZSM-5 zeolites. **Figure 4.5** shows the XRD patterns of the original ZSM-5, meso-ZSM-5 and the corresponding Cu/meso-ZSM-5 catalysts. As shown, although a slight decrease in the intensity of the main peaks was noticed on the zeolites after alkaline treatment, by comparison to the original ZSM-5 zeolites, all the characteristic peaks of ZSM-5 were observed on meso-ZSM-5(50) and meso-ZSM-5(280), indicating that alkali-treated ZSM-5 zeolites maintain their crystallinity. The decrease of the peak intensity is due to the partial desilication from the framework without complete destruction of the lattice [167], which is evidenced by the preserved microporosity in the alkaline-treated ZSM-5 zeolites as measured with N_2 adsorption-desorption (shown later).

In addition, two characteristic peaks related to CuO (35.7^o and 38.55^o) were only observed on Cu/meso-ZSM-5(50), indicating that the bulk CuO existed on the alkaline-treated ZSM-5(50). As shown in **Table 4.3**, the partial desilication of ZSM-5(50) resulted in the slight increase of the acidity, which increased from 0.746 to 0.774 mmol NH_3/g_{cat} after alkaline treatment. Sano et al. investigated the effect of the framework aluminum on the dissolution process of ZSM-5 zeolite and found out that the dissolution rate was dependent largely upon the amount of Al on the framework of the zeolite [180]. Groen et al. reported that the tetrahedrally coordinated Al on the zeolite can regulate the process of Si dissociation and the formation of mesopores, which is because the negatively charged AlO_4^- tetrahedral could hinder the hydrolysis of the Si-O-Al bond in the presence of alkaline (OH^-) in comparison with the relatively easy cleavage of the Si-O-Si bond without the presence of neighbouring Al [162]. In other words, Al is more difficult to extract by alkalinity than Si in the framework of the zeolite. Consequently, zeolite ZSM-5 normally shows a lower SiO_2/Al_2O_3 ratio after alkaline treatment (partial desilication) compared to the original zeolite, which is evidenced by the EDS results of HZSM-5(280) and meso-ZSM-5(280) (shown in **Table D.1**): the SiO_2/Al_2O_3 ratio decreased from 284.8 to 186 after alkaline treatment. Hence, the partial desilication of ZSM-5(50) probably results in a higher content of Al (lower SiO_2/Al_2O_3 ratio) in part of the structure, leading to the existence of bulk CuO on the meso-ZSM-5(50), which is similar to the catalyst Cu/ZSM-5(23) in our previous report since low SiO_2/Al_2O_3 (or high acidity) is not favorable for the dispersion of Cu [105].

4.3.1.2. H$_2$-TPR
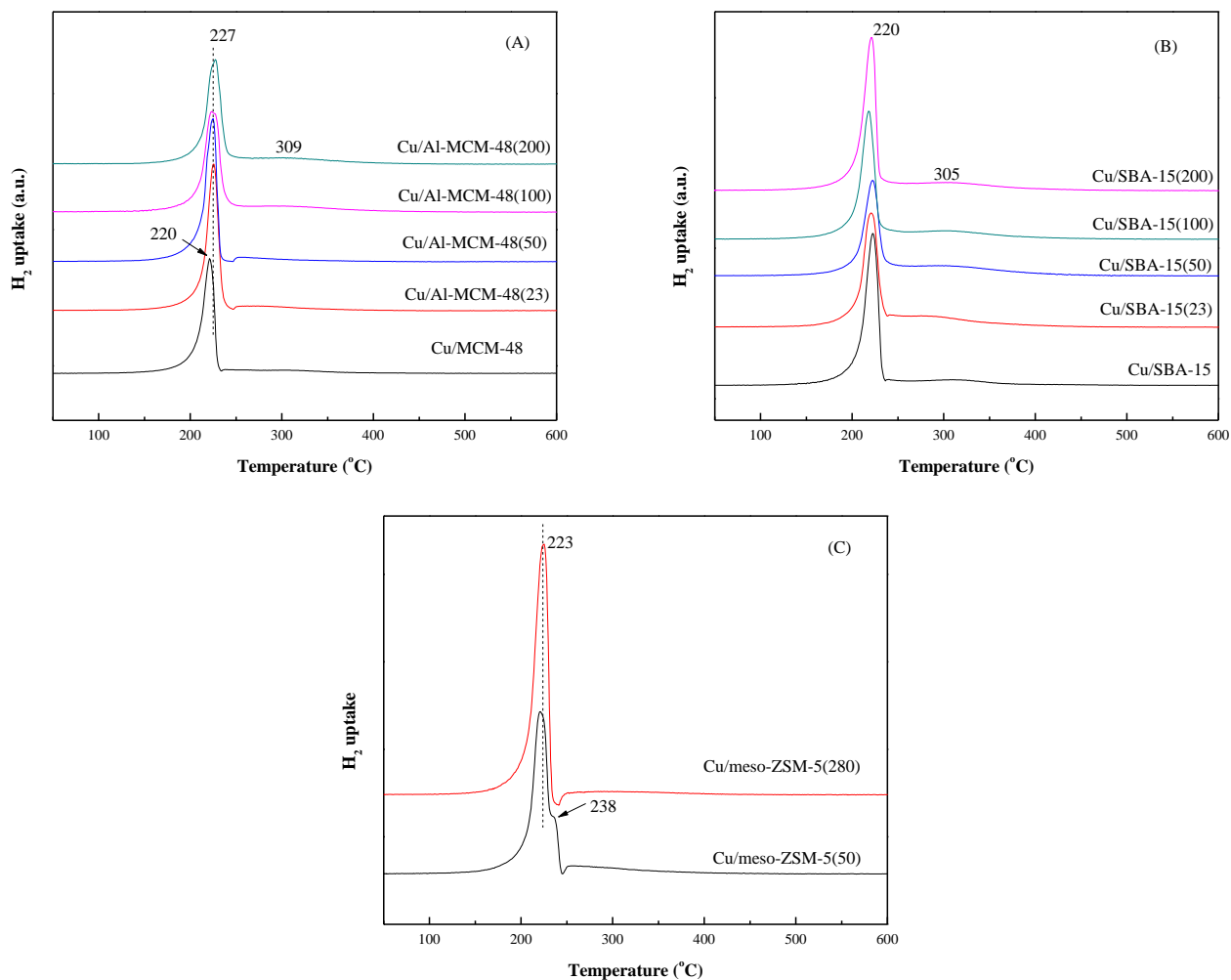
Figure 4.6. H$_2$-TPR profiles of the calcined (A) Cu/Al-MCM-48 with various Al contents; (B) Cu/Al-SBA-15 with various Al contents; (C) Cu/meso-ZSM-5(50) and Cu/meso-ZSM-5(280).

In order to investigate the reducibility of Cu on the mesoporous supports, H$_2$-TPR was performed. **Figure 4.6** shows the H$_2$-TPR profiles of copper loaded on various mesoporous supports. As shown, all catalysts except Cu/meso-ZSM-5(50) showed a sharp reduction peak at low temperature region (around 220-227 ^{o}C), which is assigned to the well dispersed CuO on the supports, and a small but broad reduction peak at around 305 ^{o}C, which is ascribed to the reduction of bulk CuO according to our previous work [105]. Li et al. suggested that the

reduction peak at low temperature was ascribable to the collective contribution of the reduction of copper phyllosilicate and well-dispersed CuO species[181]. By comparison, the latter reduction peak is considerably smaller than the former one, indicating that most of the Cu species are well dispersed on the surface and the amount of bulk CuO is negligible, which is in accordance with the XRD results since no obvious diffraction peaks corresponding to CuO can be observed in the wide-angle XRD patterns. As seen, apart from the sharp reduction peak at low temperature (220 $^{\circ}$C), Cu/meso-ZSM-5(50) displayed an additional shoulder reduction peak at 238 $^{\circ}$C. Since the characteristic peaks related to CuO (35.7° and 38.55°) were observed on Cu/meso-ZSM-5(50) as discussed above, we suggested that this shoulder peak should be assigned to the reduction of the bulk CuO.

4.3.1.3. N$_2$ adsorption
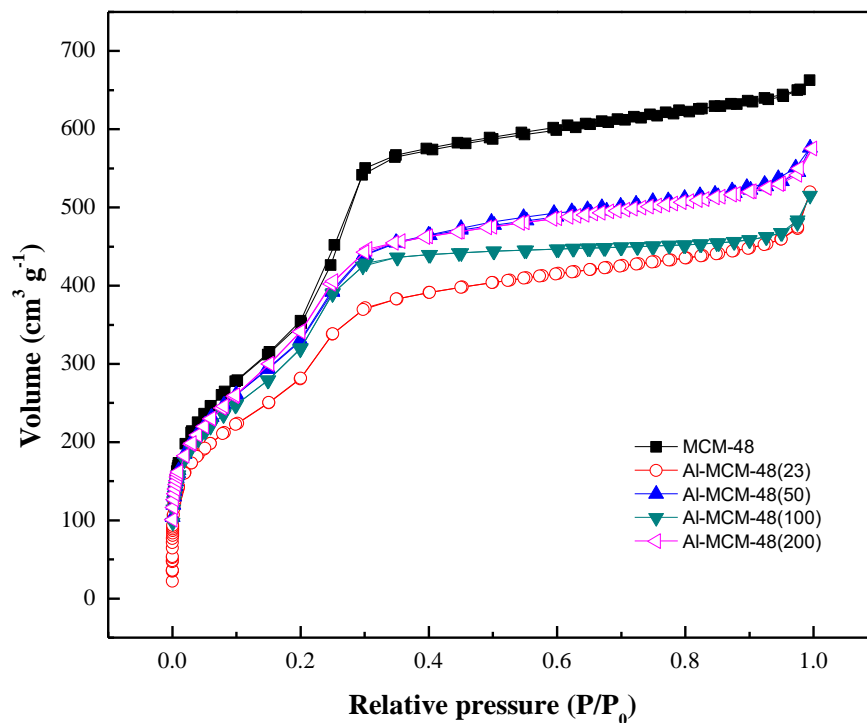
Figure 4.7. Nitrogen adsorption-desorption isotherm and the pore size distributions for calcined MCM-48 and Al-MCM-48 with different SiO$_2$/Al$_2$O$_3$.

The N$_2$ adsorption-desorption isotherms at -196 ^{o}C for all calcined aluminosilicate MCM-48 (and siliceous MCM-48) are shown in **Figure 4.7**. The textural properties of the prepared MCM-48 catalysts are shown in **Table 4.1**. As seen in **Figure 4.7**, all samples exhibit a typical reversible type IV adsorption isotherm as defined by IUPAC [182]. No hysteresis appears between the adsorption branch and the desorption branch. At relative pressures, P/P$_0$ between 0.2 and 0.35, a sharp increase due to capillary condensation within the uniform mesopores was observed on siliceous MCM-48, which is characteristic of the cubic MCM-48 mesoporous materials. The sharpness of the capillary condensation step reflects the uniform pore size in the material [149,183]. As seen, these steps of all the aluminosilicate MCM-48 are not as sharp as the siliceous MCM-48, indicating that mesopores with smaller size exist on the aluminosilicate MCM-48 materials, which is evidenced by the pore size distributions shown in **Figure 4.8**.
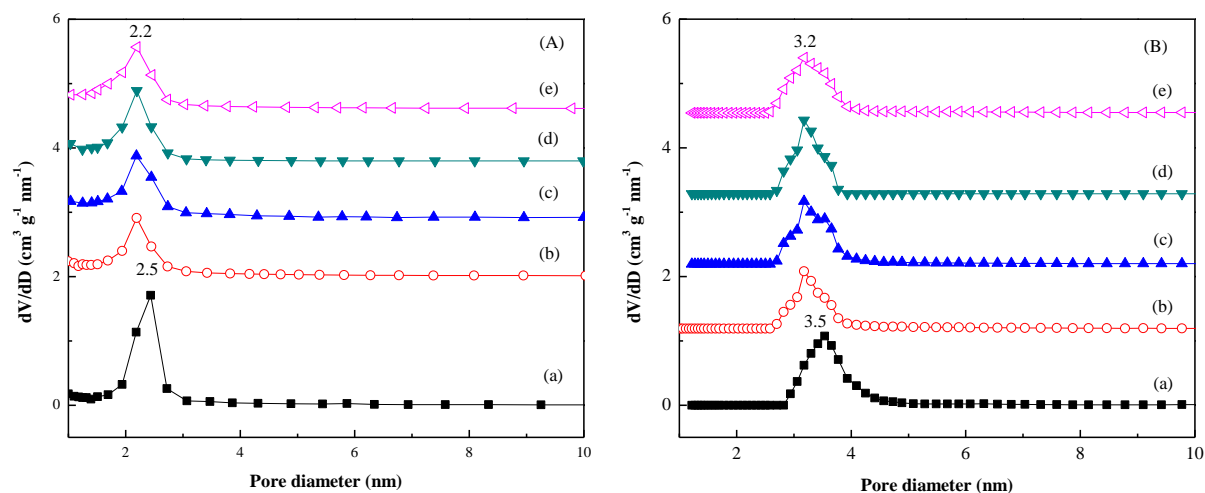
Figure 4.8. Pore size distributions of calcined mesoporous materials obtained from nitrogen adsorption branch of the isotherm using (A) BJH method, (B) NLDFT method. (a) MCM-48, (b) Al-MCM-48(23), (c) Al-MCM-48(50), (d) Al-MCM-48(100), (e) Al-MCM-48(200).

Figure 4.8 shows the pore size distribution of MCM-48 and aluminosilicate MCM-48. The most commonly used methods for determination of pore size distribution include the Barret-Joyner-Halenda (BJH) method and Horvath-Kawazoe (HK) methods. The BJH method is based on the Kelvin equation for the hemispherical meniscus, is widely used for pore size distribution

over the mesopores and part of the macropore range [34,35], while the HK method is for slit-shaped pores [186]. However, the accuracy of these methods are limited, especially in the nanometer range of pore sizes, typical for M41S (MCM-41, MCM-48, MCM-50, et al.) and other nanoporous materials [149,187–189]. Hence, a new model based on the nonlocal density functional theory (NLDFT) method was developed and widely used for the adsorption and capillary condensation in cylindrical pores [149,190–192], which could provide more accurate estimation of the porous structure in mesoporous materials. For comparison, the pore size distributions were calculated from the adsorption branch of the isotherm by using BJH method and NLDFT method for all mesoporous materials (see **Figure 4.8** and **Table 4.1).**

As shown in **Figure 4.8**, all [Al]-MCM-48 materials exhibit a remarkably narrow pore size distribution with a pore size of about 2.2-2.5 nm and 3.2-3.5 nm (see **Table 4.1**), from BJH method and NLDFT method, respectively. It should be noted that the pore sizes of the aluminosilicate MCM-48 materials are smaller than the siliceous MCM-48 calculated by each method, which is probably due to the contraction of the unit cell as discussed above.

Figure 4.9. Pore size distributions of calcined copper catalysts obtained from nitrogen adsorption branch of the isotherm using (A) BJH method, (B) NLDFT method. (a) Cu/MCM-48, (b) Cu/Al-MCM-48(23), (c) Cu/Al-MCM-48(50), (d) Cu/Al-MCM-48(100), (e) Cu/Al-MCM-48(200).

Figure 4.9 shows the pore size distribution of Cu/MCM-48 and Cu/Al-MCM-48(n) catalysts calculated by both BJH and NLDFT methods. As shown, all Cu catalysts exhibited a broader pore size distribution compared to the initial mesoporous supports, indicating that the pores with non-uniform size existed on the surface of the [Al]-MCM-48 supports (shown in Table 3.1, D_{BJH} is from the mean pore diameter), which probably resulted from the deposition of Cu in the mesopores, destroying the ordered pore structures as a result. This is in good agreement with the XRD results shown in **Figure 4.2**.

The BET surface area was calculated from the linear part of BET plot in the relative pressure range of 0.05-0.3. By comparison, the surface area was also calculated from NLDFT method. As seen in **Table 4.1**, the siliceous MCM-48 has high surface area, which is 1305 and 1007 m^2/g, from BJH and NLDFT, respectively, and large pore volume (up to 1 cm^3/g) from both methods. In addition, a decrease in surface area and pore volume was observed after introduction of Al in the materials. Modification of the mesoporous materials (MCM-48 and Al-MCM-48) with copper resulted in a significant loss of their initial surface area and total pore volume (see **Table 4.1**).

Table 4.1. Textural properties of the prepared MCM-48 catalysts.

Sample	Loading[a] (%)	Surface area		Pore diameter		Pore volume		d_{211}[d] (nm)	a[e] (nm)	ε[f] (nm)
		S_{BET}[b] (m²/g)	S_{DFT}[c] (m²/g)	D_{BJH}[b] (nm)	D_{DFT}[c] (nm)	V_{total}[b] (cm³/g)	V_{DFT}[c] (cm³/g)			
MCM-48	–	1305	1007	3.2	3.5	1.028	0.962	3.3	8.1	0.9
Al-MCM-48(23)	–	1050	776	3.1	3.2	0.806	0.728	3.2	7.9	1.0
Al-MCM-48(50)	–	1226	871	2.9	3.2	0.893	0.820	3.2	7.9	1.0
Al-MCM-48(100)	–	1120	826	2.9	3.2	0.800	0.726	3.2	7.9	0.9
Al-MCM-48(200)	–	1221	879	2.9	3.2	0.892	0.815	3.2	7.9	1.0
CuO/MCM-48	20.5	363	304	2.8	4.3	0.709	0.665	–	–	–
CuO/Al-MCM-48(23)	22.3	351	298	2.9	4.3	0.696	0.635	–	–	–
CuO/Al-MCM-48(50)	22.1	338	277	2.8	4.1	0.588	0.532	–	–	–
CuO/Al-MCM-48(100)	19.4	322	263	2.8	4.3	0.683	0.619	–	–	–
CuO/Al-MCM-48(200)	19.0	298	253	2.8	4.3	0.652	0.598	–	–	–

[a] Copper loading (CuO) was measured by ICP method.

[b] The Brunauer-Emmett-Teller (BET) area (S_{BET}) was calculated from the linear part of BET plot in the relative pressure range of 0.05-0.3. Pore diameter (D_{BJH}) was calculated from adsorption branch of the isotherm using the BJH method. Pore volume (V_{total}) is the total pore volume at relative pressure of 0.995.

[c] Surface area (S_{DFT}), pore diameter (D_{DFT}) and pore volume (V_{DFT}) were obtained by DFT method using the kernel of NLDFT equilibrium capillary condensation isotherm of N_2 at -196°C on silica.

[d] d_{211} spacing is the interplanar spacing, obtained by Bragg's Law.

[e] Lattice parameter of the unit cell (a) was calculated as $6^{1/2}d_{211}$.

[f] The wall thickness (ε) = (a/3.092)-(D_{DFT}/2).
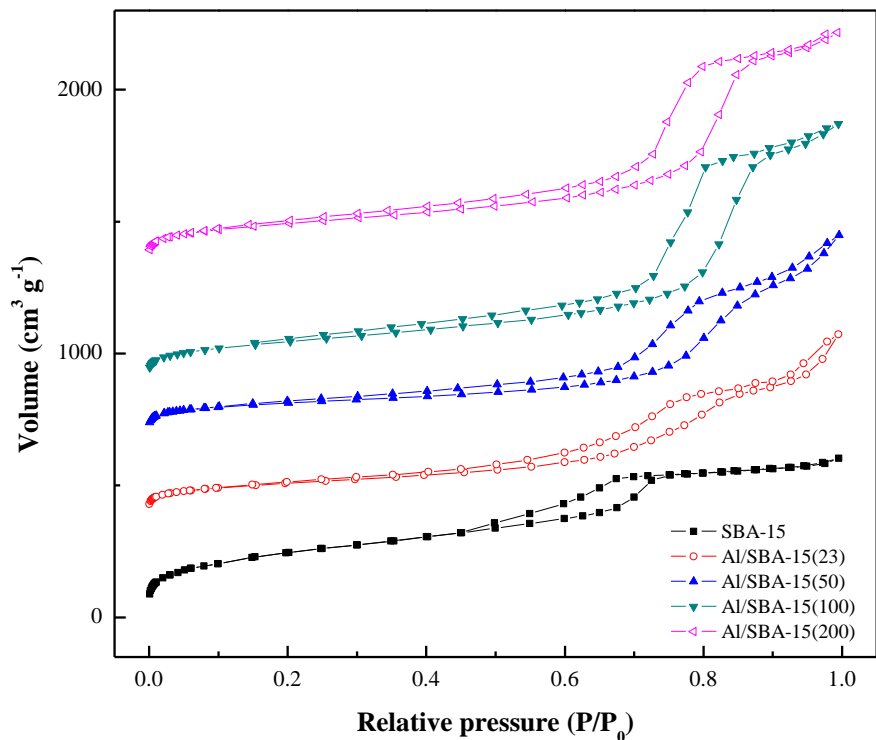
Figure 4.10. Nitrogen adsorption-desorption isotherm and the pore size distributions for calcined SBA-15 and Al-SBA-15 with different SiO_2/Al_2O_3.

The N_2 adsorption-desorption isotherms at -196 ^{o}C for all calcined aluminosilicate Al-SBA-15 materials together with purely siliceous SBA-15 are shown in **Figure 4.10** and the pore size distribution was calculated by applying the BJH method and the NLDFT method from the adsorption branch of the isotherm (see **Figure 4.11**). The textural properties are reported in **Table 4.2**.

As shown in **Figure 4.10**, all materials present typical type IV isotherms as defined by IUPAC [182] and displayed a broad H1 type hysteresis loop, indicating the presence of uniform cylindrical mesopores, which is evidenced by the results shown in **Figure 4.11** that all mesoporous materials display a relatively narrow pore size distribution. In **Figure 4.10**, siliceous SBA-15 exhibits a capillary condensation step at relative pressure P/P_0 ranging from 0.5 to 0.7, which is accompanied by the pore size at around 7.3 nm and 7.0 nm calculated from BJH and NLDFT method, respectively (shown in **Figure 4.11**). The surface area is around 800 $m^2 g^{-1}$, the total pore volume is approximately 0.9 $cm^3 g^{-1}$, and the micropore volume is 0.102 $cm^3 g^{-1}$,

117

which is calculated by the t-plot method. The micropore includes the intrawall pores within the silica matrix and the surface pores as well [190]. As shown in **Figure 4.10**, it is noted that the starting point of hysteresis shifts to the higher P/P_0 indicating an increase of pore size compared to siliceous SBA-15 for all aluminosilicate SBA-15 materials, which is evidenced by the pore size distribution shown in **Figure 4.11** and data shown in **Table 4.2**. It is in accordance with the unit cell expansion (shown in **Table 4.2**) when Al is incorporated into the framework of siliceous SBA-15 due to the longer Al-O bond (1.75 Å) [155,175]. In addition, a significant decrease of surface area and micropore volume was observed on all aluminosilicate SBA-15 materials compared to the siliceous SBA-15 (see **Table 4.2**), which is due to the incorporation of Al species into the pore wall and the micropores as well [175]. Bhange et al. suggested that location of Al in the channels of SBA-15 could be divided into two parts: one is in the pore walls of SBA-15, where Si^{4+} ions are substituted by Al^{3+} ions and the other is in the "microporous corona" region, where the silanol groups interact with Al^{3+} during preparation process [174]. With regard to the corona region, Impéror-Clerc et al. suggested that it is from the partial embedding of the PEO chains of the surfactant (P123) in the silica matrix, and it can turn to micropores upon calcination [193]. Moreover, the increase of total pore volume was observed on all aluminosilicate SBA-15 in contrast to the siliceous SBA-15, which is probably due to the longer Al-O bond (1.75 Å) than the Si-O bond (1.60 Å) when Al is incorporated into the framework of siliceous SBA-15. Furthermore, it is seen that SBA-15 and all Al-SBA-15 materials (see **Table 4.2**) have thicker walls than those of MCM-48 and Al-MCM-48 materials (about 1 nm, see **Table 4.1**), which could make them more thermally and hydrothermally stable as a result [194].

Figure 4.12 shows the pore size distribution of Cu/SBA-15 and Cu/Al-SBA-15(n) catalysts calculated by both BJH and NLDFT methods. As shown, all Cu catalysts exhibited a broader pore size distribution compared to the parent mesoporous supports, which is similar to copper loaded MCM-48 type catalysts (**Figure 4.9**), indicating that the pores with non-uniform size existed on the surface of Cu/[Al]-SBA-15 catalysts (see **Table 4.2**). In addition, a decreased surface area and pore volume was observed after introduction of copper compared to the parent mesoporous Al-SBA-15 materials (see **Table 4.2**). All of these mentioned above are probably due to the dissolution of the silica pore wall of the mesoporous materials for the formation of copper phyllosilicate [178]. It was reported that the appearance of the pores with the size around 3 nm was attributed to the presence of copper phyllosilicate (see **Figure 4.12A**, pore size

distribution from BJH method) [178]. Furthermore, it is noted that the introduction of copper leads to the disappearance of the micropores on Cu/SBA-15 and all Cu/Al-SBA-15(n) catalysts, which is obviously due to the deposition of CuO blocking the micropores on the wall.
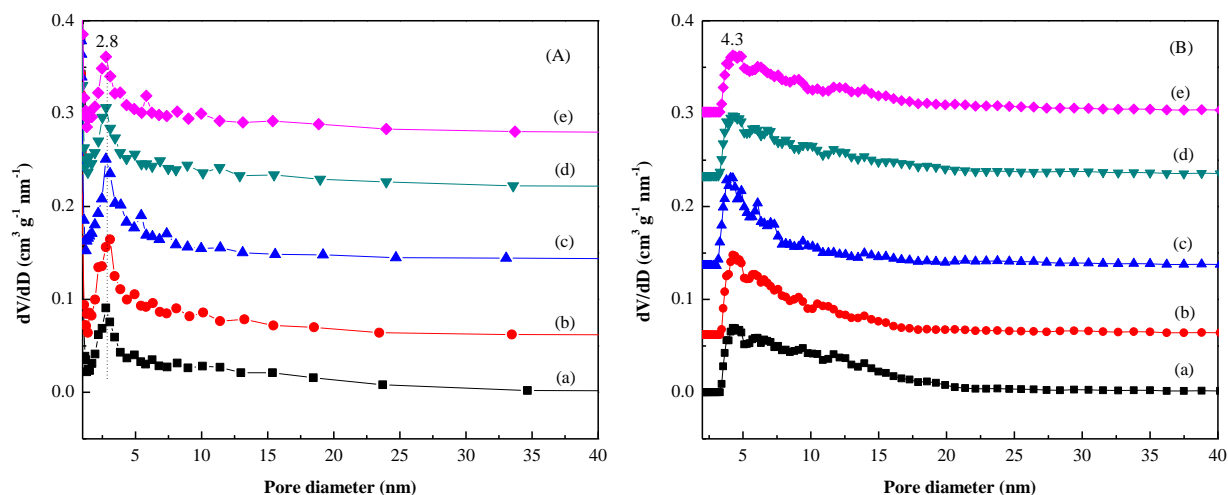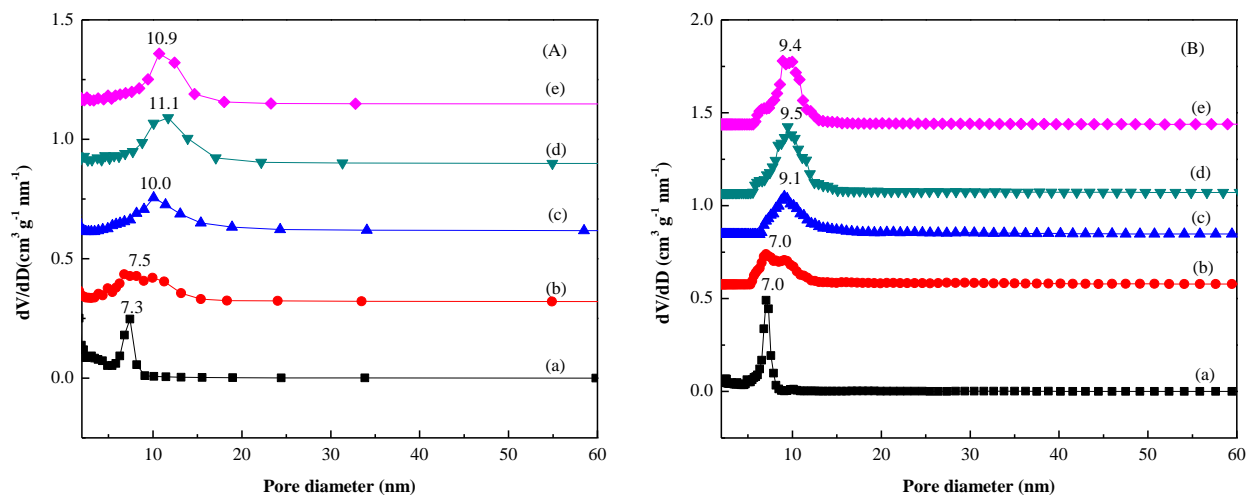

Figure 4.11. Pore size distributions of calcined mesoporous materials obtained from nitrogen adsorption branch of the isotherm using (A) BJH method, (B) NLDFT method. (a) SBA-15, (b) Al-SBA-15(23), (c) Al-SBA-15(50), (d) Al-SBA-15(100), (e) Al-SBA-15(200).
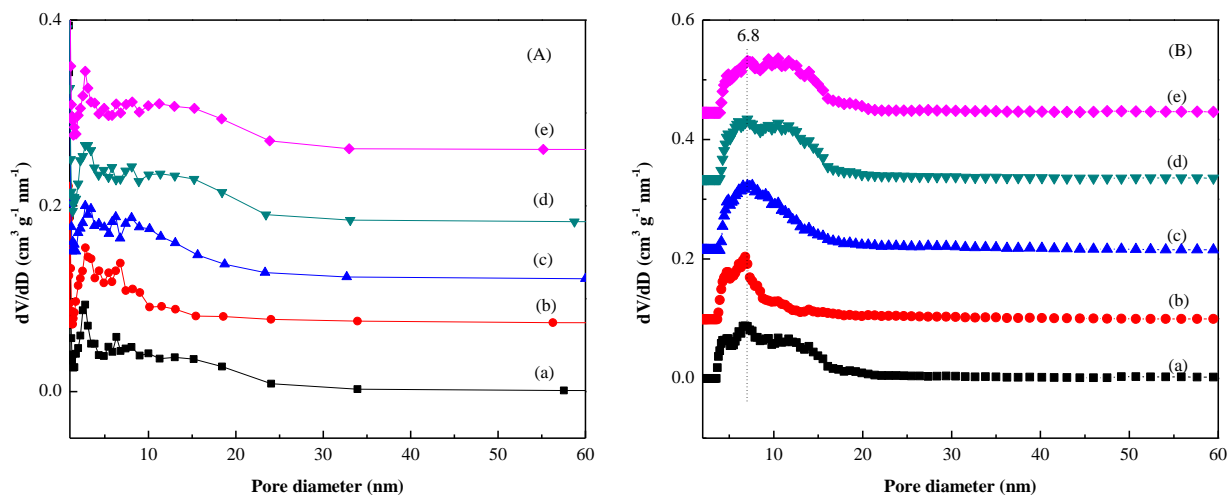
Figure 4.12. Pore size distributions of calcined copper catalysts obtained from nitrogen adsorption branch of the isotherm using (A) BJH method, (B) NLDFT method. (a) Cu/SBA-15, (b) Cu/Al-SBA-15(23), (c) Cu/Al-SBA-15(50), (d) Cu/Al-SBA-15(100), (e) Cu/Al-SBA-15(200).
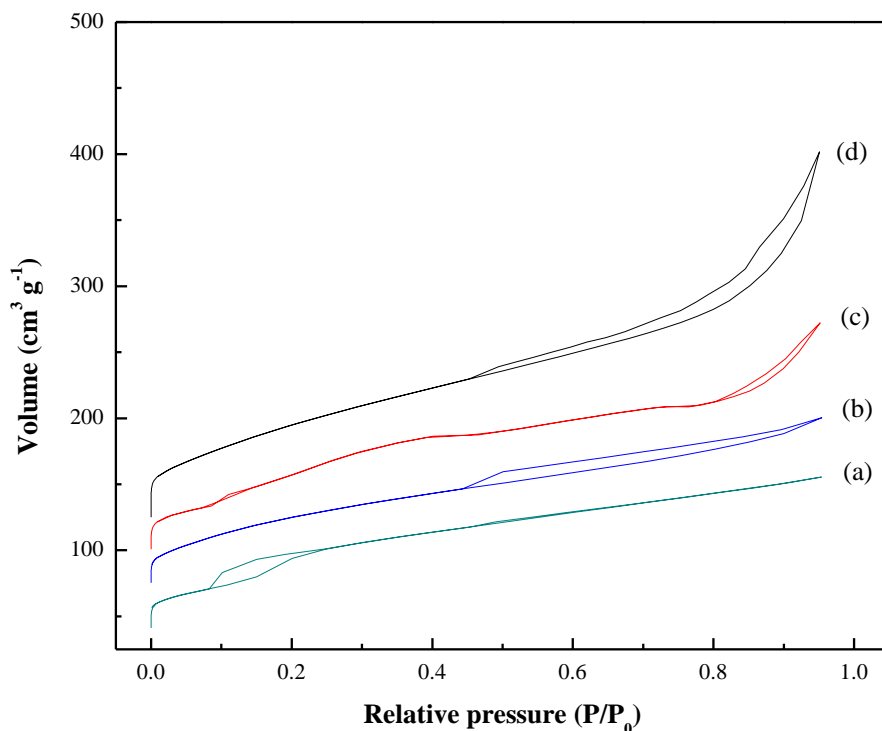
Figure 4.13. Nitrogen adsorption-desorption isotherms for calcined zeolites (a) HZSM-5(280), (b) HZSM-5(50), (c) meso-HZSM-5(280) and (d) meso-HZSM-5(50).

Table 4.2. Textural properties of the prepared SBA-15 catalysts.

Sample	Loading[a] (%)	Surface area		Pore diameter		Pore volume			d_{100}[e] (nm)	a[f] (nm)	ε[g] (nm)
		S_{BET}[b] (m²/g)	S_{DFT}[c] (m²/g)	D_{BJH}[b] (nm)	D_{DFT}[c] (nm)	V_{total}[b] (cm³/g)	V_{DFT}[c] (cm³/g)	V_{micro}[d] (cm³/g)			
SBA-15	–	802	790	7.3	7.0	0.935	0.864	0.102	9.2	10.7	3.7
Al-SBA-15(23)	–	422	361	7.5	7.0	1.170	0.951	0.004	9.7	11.2	4.2
Al-SBA-15(50)	–	455	419	10.0	9.1	1.308	1.217	0.037	10.2	11.8	2.7
Al-SBA-15(100)	–	526	514	11.1	9.5	1.505	1.443	0.041	10.0	11.6	2.1
Al-SBA-15(200)	–	521	493	10.9	9.4	1.340	1.290	0.050	10.2	11.8	2.4
CuO/SBA-15	21.2	439	386	8.9	6.8	1.001	0.922	0	–	–	–
CuO/Al-SBA-15(23)	20.7	347	302	7.6	6.8	0.666	0.630	0	–	–	–
CuO/Al-SBA-15(50)	18.2	446	395	8.6	7.6	0.961	0.920	0	–	–	–
CuO/Al-SBA-15(100)	19.8	477	430	9.1	7.0	1.082	1.028	0	–	–	–
CuO/Al-SBA-15(200)	20.9	440	396	9.5	10.5	1.043	0.989	0	–	–	–

[a] Copper loading (CuO) was measured by ICP method.

[b] The Brunauer-Emmett-Teller (BET) area (S_{BET}) was calculated from the linear part of BET plot in the relative pressure range of 0.05-0.3. Pore diameter (D_{BJH}) was calculated from adsorption branch of the isotherm using the BJH method. Pore volume (V_{total}) is the total pore volume at relative pressure of 0.995.

[c] Surface area (S_{DFT}), pore diameter (D_{DFT}) and pore volume (V_{DFT}) were obtained by DFT method using the kernel of NLDFT equilibrium capillary condensation isotherm of N_2 at -196°C on silica.

[d] Micropore volume (V_{micro}) was obtained by t-plot method.

[e] d_{100} spacing was obtained by Bragg's Law.

[f] Lattice parameter of the unit cell (a) was calculated by $a = 2d_{100}/\sqrt{3}$

[g] The wall thickness (ε) = $a - D_{DFT}$.
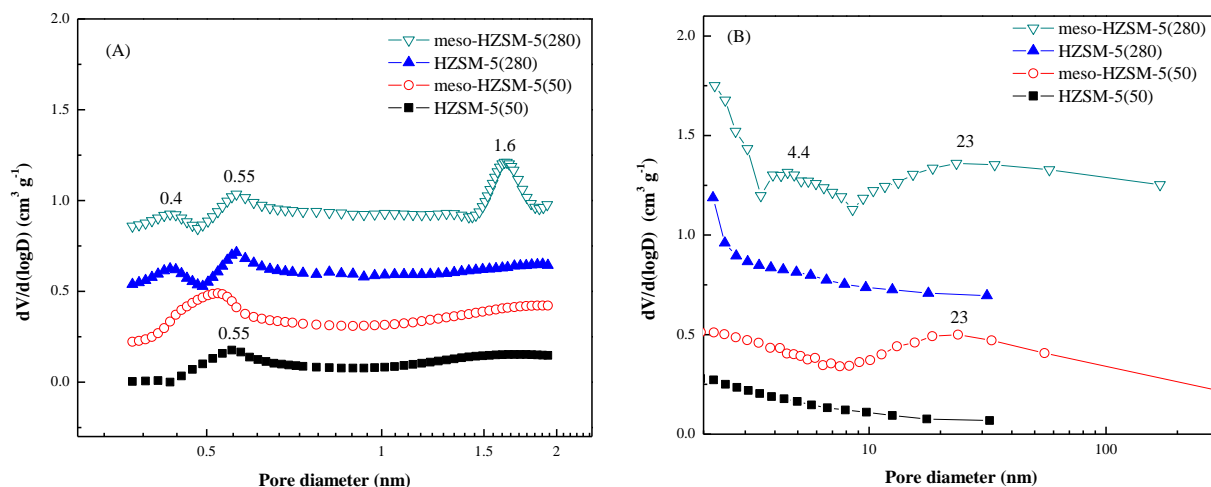
Figure 4.14. Pore size distribution derived from the nitrogen adsorption-desorption isotherms using the HK (A) and the BJH (B) methods for the meso-ZSM-5 prepared by NaOH treatment of the conventional ZSM-5.

Figure 4.13 shows the N_2 adsorption-desorption isotherms of the desilicated and parent HZSM-5 zeolites. The results from the N_2 sorption are summarized in **Table 4.3**. As seen in **Figure 4.13**, the N_2 isotherm of meso-ZSM-5(50) (alkaline-treated) displayed a similar uptake at low relative pressure compared to the parent zeolite HZSM-5(50). However, the significant increasing adsorption in the range $P/P_0>0.8$ and a larger hysteresis loop were observed over meso-HZSM-5(50) (**Figure 4.13d**), indicating the development of larger mesopores. As shown in **Table 4.3**, the mesopore area and volume of meso-ZSM-5(50) increased from 115 to 199 m^2 g^{-1} and 0.150 to 0.343 cm^3 g^{-1}, respectively, after alkaline treatment of HZSM-5(50); meanwhile, the micropore area and volume decreased from 333 to 235 $m^2 g^{-1}$ and 0.169 to 0.137 cm^3 g^{-1}, respectively. As for the zeolite HZSM-5(280), it is seen that the appearance of hysteresis loop in the desorption branch in the range $P/P_0>0.8$ after being treated by NaOH, indicating the enhancement of the mesopores, which is evidenced by the results shown in **Table 4.3**. The mesopore area and volume of meso-ZSM-5(280) increased from 105 to 148 $m^2 g^{-1}$ and 0.121 to 0.223 cm^3 g^{-1}, respectively, after being treated by NaOH, while the micropore area and volume decreased from 332 to 266 $m^2 g^{-1}$ and 0.180 to 0.153 cm^3 g^{-1}, respectively. It is noted that a small hysteresis loop was observed in N_2 isotherm of HZSM-5(280) in the relative pressure of 0.1-0.2, which was not suggested to be attributed to pore filling into supermicropores or small

mesopores, but was usually associated with the phenomenon of phase transition of adsorbed nitrogen [147]. Kyriakou et al.[195] investigated the nature of the hysteresis loop at low pressure observed in the nitrogen adsorption isotherms of some MFI zeolites with different counterions, NH^{4+}, Ca^{2+}, and Cu^{2+} by diffuse reflectance infrared Fourier transform (DRIFTS) and the results showed that the position of the hysteresis loop at low pressure was influenced by the presence of defects in the crystals, which represented strong adsorption to nitrogen, hence, a great quantity of such defects would require higher concentration of adsorbed nitrogen for aggregating away from the wall of zeolite, which gave rise to the observed hysteresis loop at low relative pressure.

As we know, the most commonly used methods for determination of pore size distribution include the Barret-Joyner-Halenda (BJH) method and Horvath-Kawazoe (HK) methods. The BJH method is based on the Kelvin equation for the hemispherical meniscus, is widely used for pore size distribution over the mesopores and part of the macropore range [34,35], while the HK method is for slit-shaped micropores [158,186]. The pore size distributions derived from the N_2 adsorption-desorption isotherms calculated by HK and BJH methods for the micropores and mesopores, respectively, are shown in **Figure 4.14**. As seen in **Figure 4.14**, apart from the micropores with diameters of ~0.55 nm (**Figure 4.14A**), which is typical for ZSM-5 zeolite, mesopores with pore sizes of ~23 nm also appeared in both meso-ZSM-5 zeolites (**Figure 4.14B**). Micropores with a size of ~1.6 nm and mesopores with a size of ~4.4 nm were observed on meso-HZSM-5(280). Based on the discussion above, we conclude that the alkaline treatment of ZSM-5 zeolite can result in the introduction of connected intracrystalline mesopores, while maintain the intrinsic structure (micropores) of the zeolite.

As for the copper catalysts, Cu/meso-ZSM-5(50) and Cu/meso-ZSM-5(280), the mesopore area and volume were observed to increase significantly, which was accompanied by the decrease of micropore area and volume accordingly (as shown in **Table 4.3**). Obviously, it is caused by the deposition of the copper species in the micropores of zeolite, reducing the micropore area and volume as a result.

Table 4.3. Surface area and pore volume of catalysts and supports.

Sample	Surface area			Pore volume		
	S_{BET} (m^2g^{-1})	S_{micro} (m^2g^{-1})	$S_{external}$ (m^2g^{-1})	V_{total}[a] (cm^3g^{-1})	V_{micro} (cm^3g^{-1})	V_{meso} (cm^3g^{-1})
HZSM-5(50)	447	333	115	0.319	0.169	0.150
HZSM-5(280)	437	332	105	0.301	0.180	0.121
meso-ZSM-5(50)	434	235	199	0.480	0.137	0.343
meso-ZSM-5(280)	414	266	148	0.376	0.153	0.223
20%CuO/meso-ZSM-5(50)	424	159	265	0.536	0.101	0.435
20%CuO/meso-ZSM-5(280)	428	149	279	0.493	0.105	0.388

[a] Pore volume was evaluated by single point volume at a relative pressure of 0.95.

4.3.1.4. TEM

Transmission electron microscopy (TEM) experiments were performed to investigate the morphology characteristics of the mesoporous samples. As shown in **Figure 4.15**, TEM images revealed a visualization of the pore structure of calcined mesoporous materials MCM-48, Al-MCM-48(100) and catalyst Cu/Al-MCM-48(100). The micrographs in **Figure 4.15A** and **Figure 4.15C** show part of a spherical particle of calcined MCM-48 and Al-MCM-48(100), respectively, in the direction of the pore axis; while **Figure 4.15B** and **Figure 4.15C** display the pore structure in the direction perpendicular to the pore axis. It can be seen that both MCM-48 and Al-MCM-48(100) possess well-ordered wormhole-like pore structures throughout the particle with uniform pore size, which is consistent with the results reported in the literatures [149,152,196,197]. From the TEM micrographs, an approximate pore channel diameter of 3 nm and pore wall thickness of 1 nm can be obtained, which are very close to the results obtained from N_2 sorption and XRD. TEM images of Cu/Al-MCM-48(100) presented in **Figure 4.15E** and **Figure 4.15F** demonstrated that Al-MCM-48(100) was covered by highly dispersed CuO. From **Figure 4.15E**, we can see dark zones over and inside the mesoporous structure (channel), corresponding to CuO nanoparticles. In **Figure 4.15F**, we can see small CuO particles (dark dotlike objects) deposited outside the mesopores of Al-MCM-48(100), leading to pore clogging, which is in agreement with XRD results discussed above. The size of CuO particle was estimated to be about 3 nm (see **Figure 4.15F**).
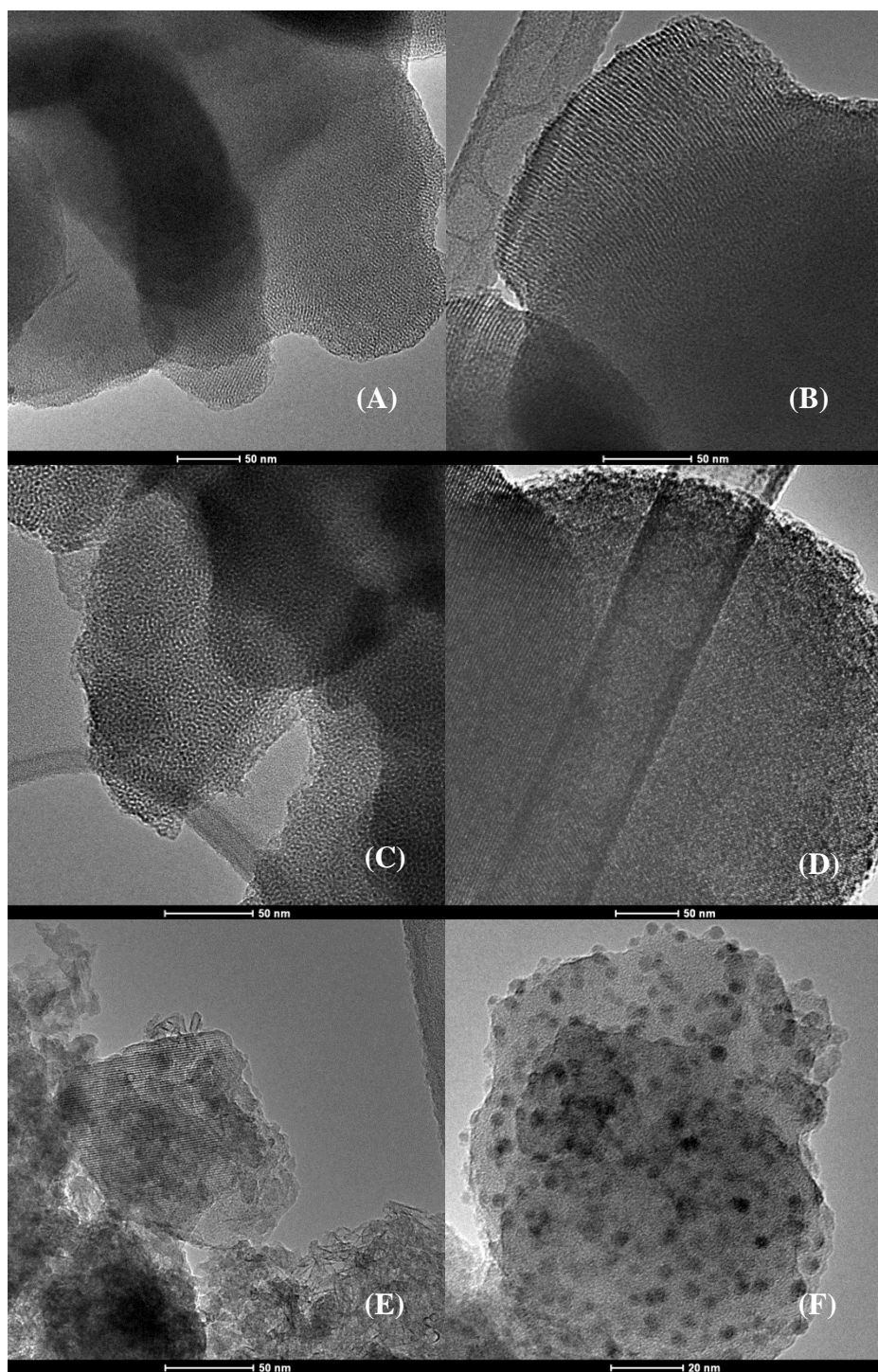
Figure 4.15. TEM images of (A),(B) MCM-48; (C),(D) Al-MCM-48(100); (E),(F) Cu/Al-MCM-48(100).
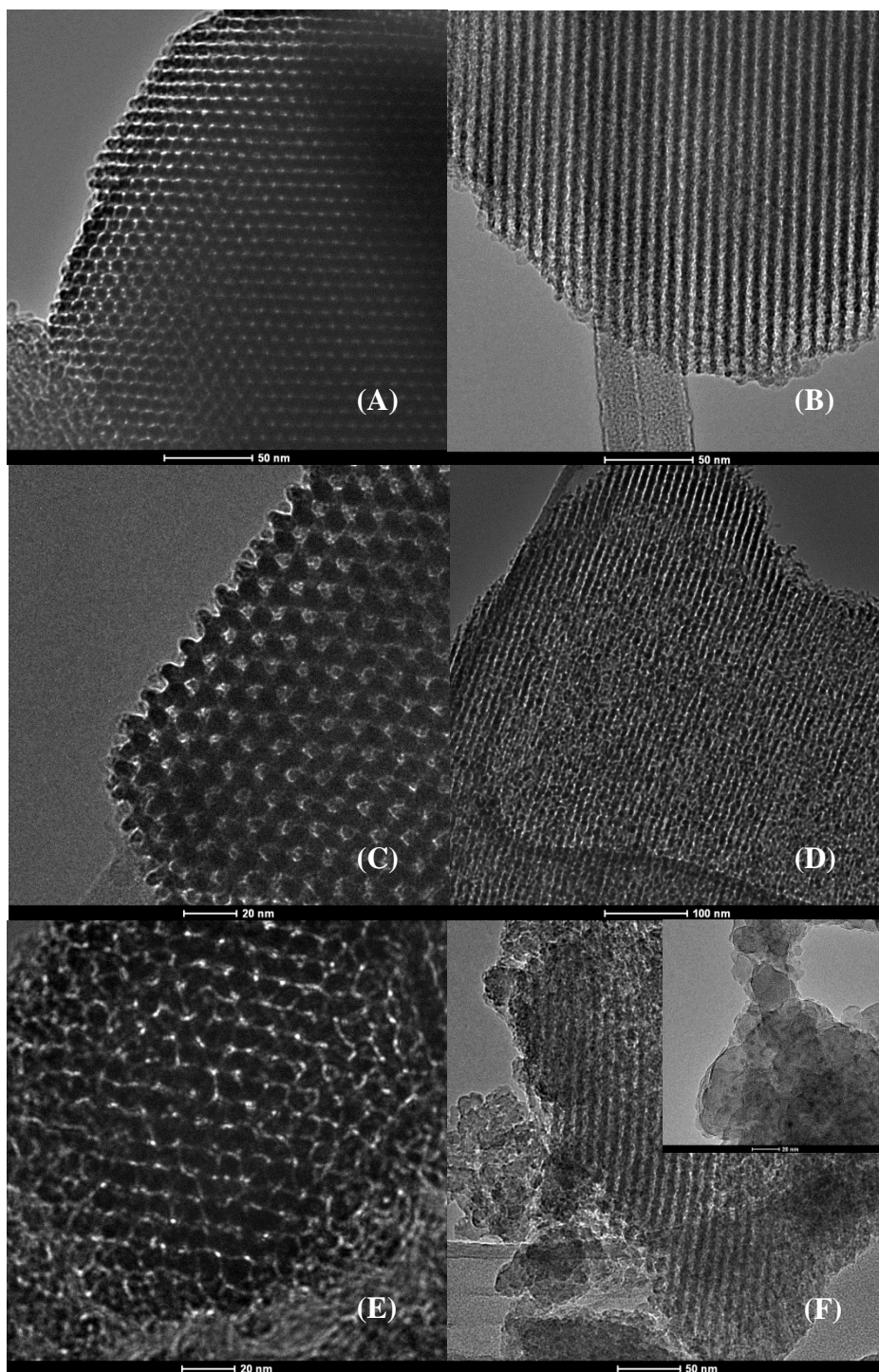
Figure 4.16. TEM images of (A),(B) SBA-15; (C),(D) Al-SBA-15(50); (E),(F) Cu/Al-SBA-15(50): (A),(C),(E) in the direction of the pore axis and (B),(D),(F) in the direction perpendicular to the pore axis, respectively.

Transmission electron microscopy (TEM) images (**Figures 4.16A** and **B**) of calcined mesoporous material SBA-15 exhibit highly ordered hexagonal arrays of mesopores with 1-D channels, indicating a 2-D hexagonal (*p6mm*) mesostructure, which is in agreement with the literature [153,154]. For SBA-15, the distance between two consecutive centers of hexagonal pores estimated from the TEM image is ca. 10 nm, the average thickness of the wall is ca. 3 nm and pore diameter is around 7 nm, which are consistent with the results from the N_2 sorption.

TEM images (**Figures 4.16C** and **D**) of the Al-SBA-15(50) material also show well-ordered 2-D hexagonal mesostructures, which are in agreement with results of the small-angle XRD pattern. In addition, the pore diameter and pore wall thickness are estimated to be ca. 9 nm and 3 nm, respectively, which are consistent with the results calculated from the small-angle XRD and N_2 sorption. However, the defects are observed in the channels since the pore walls are not as smooth as those of purely siliceous SBA-15, indicating partial destruction of the ordered structure, which could be attributed to framework defects of aluminosilicate due to the incorporation of Al species into the pore walls [175], which is in accordance with the discussion above about the small-angle XRD and N_2 sorption.

TEM images of Cu/Al-SBA-15(50) are shown in **Figures 4.16E** and **F**. As seen, the typical mesoporous structure of SBA-15 has been well preserved. However, partial destruction of the ordered structure can be seen in the TEM images (**Figures 4.16E** and **F**), which is similar to Al-SBA-15(50). In addition, as seen in the inset of **Figure 4.16F**, the copper particles were uniformly distributed on the support with the size of ca. 3 nm.

4.3.1.5. ^{27}Al MAS solid state NMR
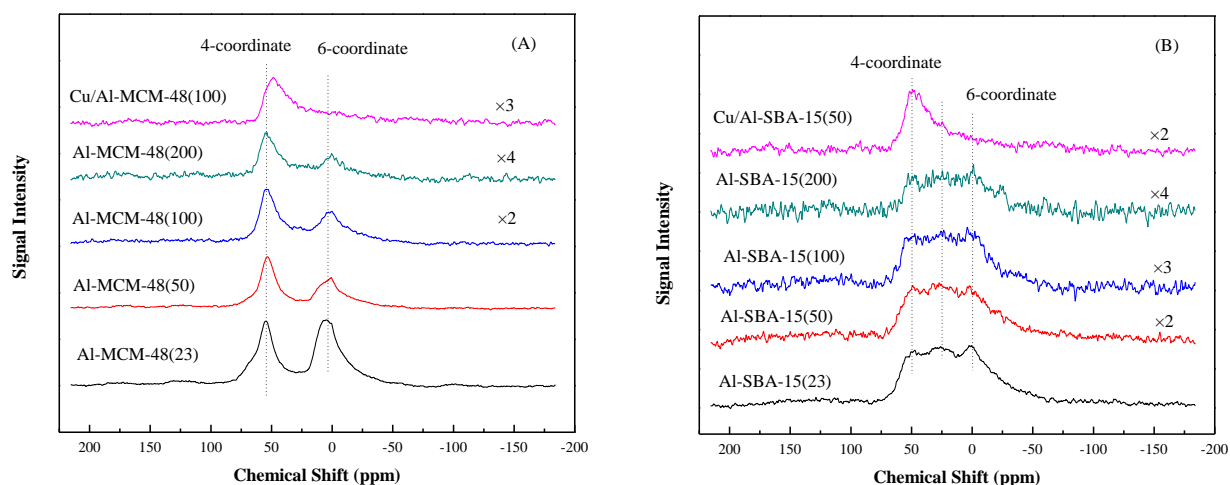
Figure 4.17. ^{27}**Al MAS NMR spectra for (A) calcined Al-MCM-48 samples with Si/Al$_2$O$_3$ ratios of 23, 50, 100, 200, and Cu/Al-MCM-48(100), (B) calcined Al-SBA-15 samples with Si/Al$_2$O$_3$ ratios of 23, 50, 100, 200, and Cu/Al-SBA-15(50).**

Solid-state ^{27}Al MAS NMR spectra were measured on the mesoporous materials Al-MCM-48 and Al-SBA-15 with various Si/Al$_2$O$_3$ ratios to determine the coordination environment of aluminum species in the mesoporous framework. The ^{27}Al MAS NMR spectra of Al-MCM-48 samples after calcination are shown in **Figure 4.17A**. As seen, two resonance signals were observed. The NMR peak centered at ca. 52 ppm can be assigned to the 4-coordinate Al species (tetrahedral AlO$_4$ structural unit), indicating that the Al atoms are tetrahedrally coordinated and incorporated into the framework of the aluminosilicate material, while the peak at 0 ppm is ascribe to the 6-coordinate nonframework Al species (octahedral AlO$_6$ structural unit), suggesting that Al species may be located on the surface of the material [152,155,169,198–200]. The results indicated that under our synthesis conditions, only a part of the Al species are incorporated into the mesoporous framework. For better comparison, the peaks of Al-MCM-48(100) and Al-MCM-48(200) were multiplied by 2 and 4, respectively, to get comparative signal intensity of 4-coordinate peaks. As seen, the relative intensity of the 6-coordinate Al decreases with decreasing Al content, indicating that the proportion of nonframework aluminum atoms decreases as well.

Figure 4.17B illustrates the ^{27}Al MAS NMR spectra of Al-SBA-15 materials with various Si/Al_2O_3 and copper catalyst Cu/Al-SBA-15(50). As shown, apart from the peaks at 52 ppm and 0 ppm corresponding to tetrahedral Al and octahedral Al species, respectively, a new peak at ca. 30 ppm can be observed to be overlapped with the other two peaks mentioned above on the Al-SBA-15 materials. As reported, the peak in the range of 20-50 ppm can be assigned to pentacoordinated aluminum [200–203]. This indicates that not all Al species can be readily incorporated into the framework of SBA-15 under our synthesis conditions, which is similar to the results reported in the literature [200,203]. Li et al. suggested that the Al atoms can be transferred from tetrahedral sites in the mesoporous walls to the octahedral and pentahedral sites when Al-SBA-15 was calcined to remove the template, especially when the material was treated by steam at high temperature [200].

Interestingly, on the ^{27}Al MAS NMR spectra of copper catalysts (Cu/Al-MCM-48(100) in **Figure 4.17A**, and Cu/Al-SBA-15(50) in **Figure 4.17B**), the peak for octahedral aluminum (0 ppm) was not detected, which was present in the corresponding mesoporous support. It is similar to Yue's report that non-framework aluminum (including octahedral and pentahedral Al) was eliminated when Al-SBA-15 material was washed by NH_4Cl solution [203]. It should be noted that when our copper catalysts were synthesized by the ammonia evaporation hydrothermal (AEH) method, there were a bunch of ammonia in the solution since copper was introduced to the mesoporous materials as cupric ammine complex $[Cu(NH_3)_4(H_2O)_2]^{2+}$, hence, 6-coordinated and 5-coordinated Al species were removed as a result. In addition, Klimova et al. demonstrated that the aluminum species can be transformed from octahedrally to tetrahedrally coordinated Al by means of the adsorption of ammonia when they investigated the reversible transformation of tetrahedral-octahedral framework aluminum in zeolite Y [204].

4.3.1.6. NH₃-TPD
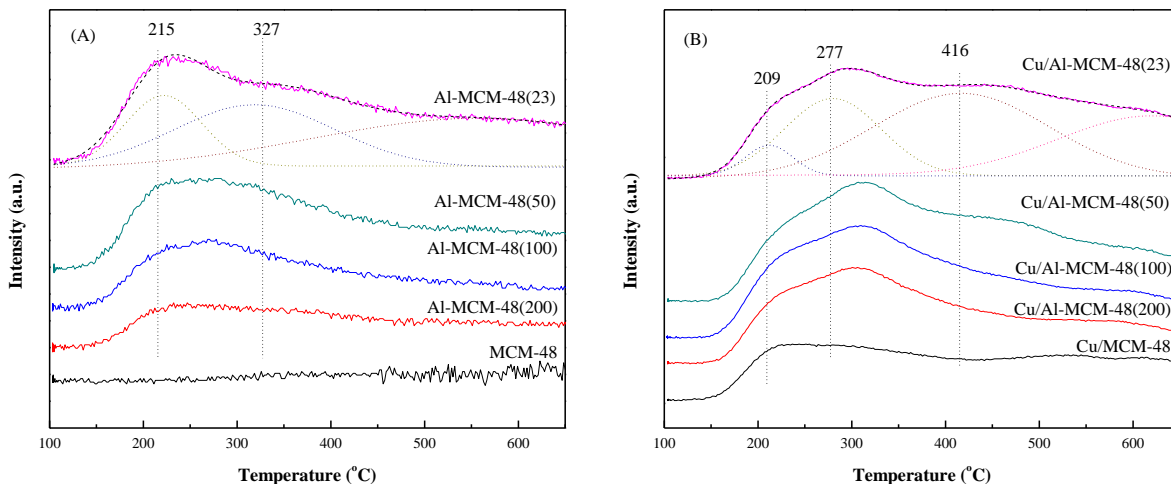
Figure 4.18. NH₃-TPD profiles of (A) calcined MCM-48 and Al-MCM-48 with different SiO₂/Al₂O₃ ratios and (B) reduced Cu/MCM-48 and Cu/Al-MCM-48 with different SiO₂/Al₂O₃ ratios.
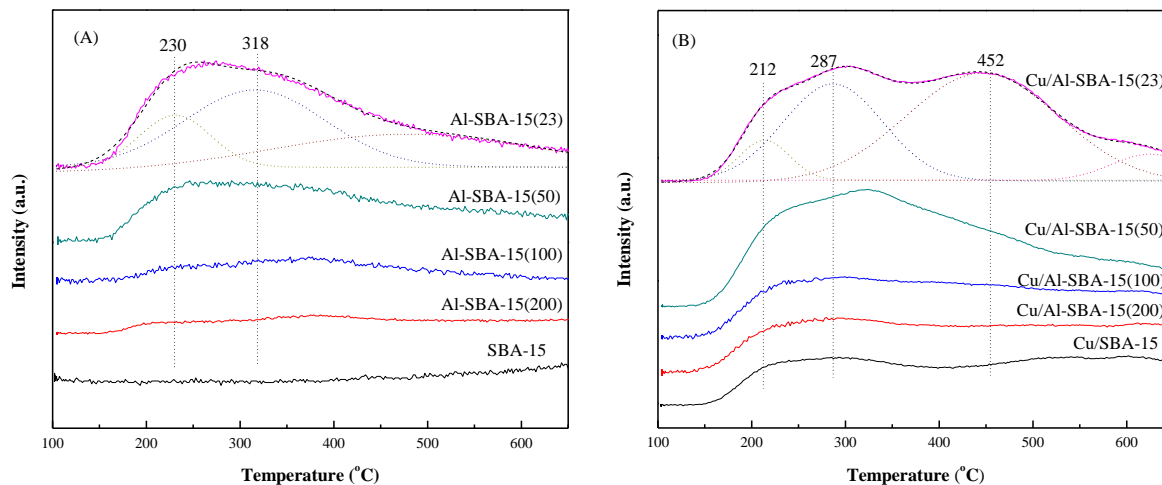
Figure 4.19. NH₃-TPD profiles of (A) calcined SBA-15 and Al-SBA-15 with different SiO₂/Al₂O₃ ratios, and (B) reduced Cu/SBA-15 and Cu/Al-SBA-15 with different SiO₂/Al₂O₃ ratios.
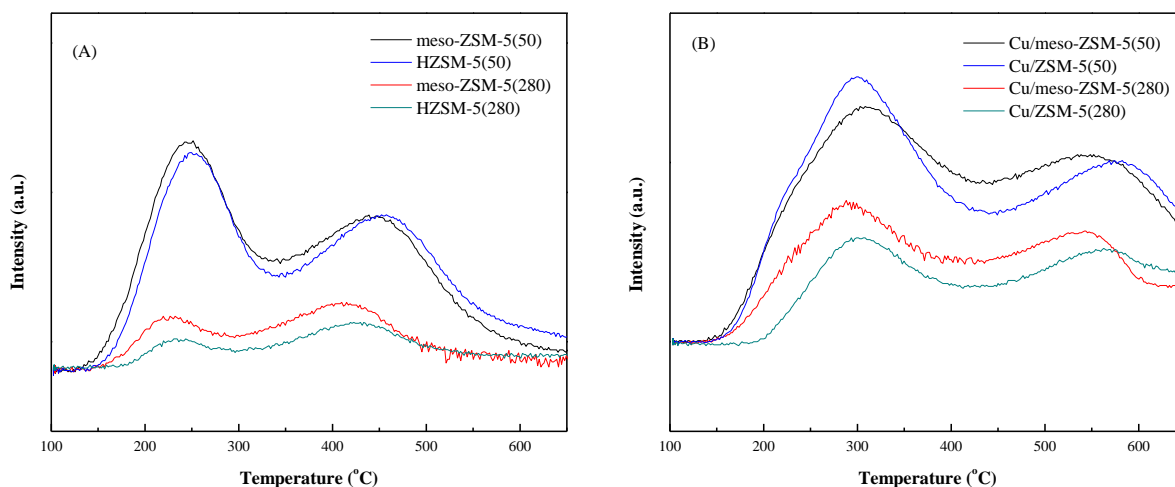
Figure 4.20. NH₃-TPD profiles of (A) meso-ZSM-5 and the parent zeolite HZSM-5, (B) reduced Cu/meso-ZSM-5 catalysts and the corresponding reference catalysts Cu/ZSM-5.

The acidity of the mesoporous materials and the corresponding reduced copper catalysts was determined by NH_3-TPD (shown in **Figures 4.18**, **4.19**, **4.20**), and the amount of ammonia uptake was given in **Tables 4.4**, **4.5**, **4.6**. As shown in **Figures 4.18A** and **4.19A**, the purely siliceous MCM-48 and SBA-15 were observed to be relatively inert since no obvious desorption peak of NH_3 could be observed, which is similar to the conventional SiO_2 we discussed in **Chapter 3**. However, it could be seen that the incorporation of aluminum into the mesoporous materials MCM-48 and SBA-15 resulted in the acidic properties of the materials (see **Figures 4.18A** and **4.19A**, **Tables 4.4** and **4.5**). As seen, the NH_3-TPD profiles of Al-MCM-48 and Al-SBA-15 with different SiO_2/Al_2O_3 ratios show broad peaks centered at about 200 to 260 °C with long tails extending up to 650 °C, indicating a wide distribution of acid sites varying from weak to strong. Deconvolution of desorption profiles results in three distinct peaks: the first peak (centered at around 215 °C and 230 °C for Al-MCM-48 and Al-SBA-15, respectively) can be attributed to the weak Brönsted acid sites, and the moderate Brönsted acid sites due to Al^{3+} in the framework; the second peak (centered at ca. 327 °C and 318 °C for Al-MCM-48 and Al-SBA-15, respectively) can ascribe to the contribution of strong Brönsted acid sites of Al^{3+} in the framework; the broad peak at ca. 550 °C is attributed to the strong Lewis acid sites of non-framework aluminum species [205–207]. As seen, Al-MCM-48(23) possess a broad and large

131

peak at high temperature (550 ^{o}C), which is in good agreement with the ^{27}Al-NMR result that a lot of non-framework Al was observed in Al-MCM-48(23) material. In addition, from **Figures 4.18A** and **4.19A**, we can see that the ammonia uptake of the aluminosilicate materials increases with increasing content of aluminium (see **Tables 4.4** and **4.5**), especially in the low temperatures (200-400 ^{o}C) corresponding to the weak-strong Brönsted acid sites.

Table 4.4. Copper dispersion and ammonia uptake of MCM-48 catalysts.

Sample	NH$_3$ uptake (mmol /g$_{cat}$)	Cu area[a] (m^2/g$_{Cu}$)	Dispersion[a]
20%CuO/MCM-48	0.657	92.5	0.14
20%CuO/Al-MCM-48(23)	0.872	42.8	0.06
20%CuO/Al-MCM-48(50)	0.808	42.3	0.06
20%CuO/Al-MCM-48(100)	0.714	54.3	0.08
20%CuO/Al-MCM-48(200)	0.694	63.4	0.09
MCM-48	0.000	−	−
Al-MCM-48(23)	0.155	−	−
Al-MCM-48(50)	0.133	−	−
Al-MCM-48(100)	0.089	−	−
Al-MCM-48(200)	0.049	−	−

[a] Cu dispersion and Cu area were determined by dissociative N$_2$O adsorption method at 90 ^{o}C.

Table 4.5. Copper dispersion and ammonia uptake of SBA-15 catalysts.

Sample	NH$_3$ uptake (mmol /g$_{cat}$)	Cu area[a] (m^2/g$_{Cu}$)	Dispersion[a]
20%CuO/SBA-15	0.772	87.8	0.13
20%CuO/Al-SBA-15(23)	1.076	66.5	0.10
20%CuO/Al-SBA-15(50)	0.996	84.8	0.13
20%CuO/Al-SBA-15(100)	0.803	83.5	0.12
20%CuO/Al-SBA-15(200)	0.756	80.2	0.12
SBA-15	0.000	−	−
Al-SBA-15(23)	0.190	−	−
Al-SBA-15(50)	0.115	−	−
Al-SBA-15(100)	0.053	−	−
Al-SBA-15(200)	0.035	−	−

[a] Cu dispersion and Cu area were determined by dissociative N$_2$O adsorption method at 90 ^{o}C.

Figures 4.18B and **4.19B** display the NH_3-TPD profiles of reduced Cu/[Al]-MCM-48 and Cu/[Al]-SBA-15 catalysts. By comparison to the purely siliceous MCM-48 and SBA-15, the corresponding reduced copper catalysts (Cu/MCM-48 and Cu/SBA-15) show a broad NH_3 desorption peak with a long tail in the temperature range of 100 to 650 $^{\circ}$C, which indicates that the reduced copper catalysts show a wide distribution of acid sites varying from weak to strong. The peak at low temperature (ca. 210 $^{\circ}$C) can be attributed to adsorption of NH_3 at the weak acid sites related to Cu species [208], while the peak at high temperature (400-500 $^{\circ}$C) can be ascribed to NH_3 adsorbed on the medium acid sites created by copper species, which is probably from the formation of copper phyllosilicate phase [209]. In addition, the peak above 600 $^{\circ}$C is probably due to due to the formation of N_2, which is from oxidization of NH_3 over unreduced Cu^{2+} species [80]. As depicted in **Figures 4.18B** and **4.19B**, with increasing content of Al, the peak at ca. 287 $^{\circ}$C increased accordingly, which can be attributed to the combination of NH_3 desorption from both Lewis acid sites of aluminosilicate materials copper sites on the surface. Interestingly, an obvious peak at 400-450 $^{\circ}$C was observed on both Cu/Al-MCM-48 and Cu/Al-SBA-15 with the highest content of Al (SiO_2/Al_2O_3=23), which can be probably ascribable to NH_3 adsorbed on Cu species that binds to the non-framework aluminium of the aluminosilicate materials.

Table 4.6. Copper loading, copper dispersion and ammonia uptake of meso-ZSM-5 catalysts.

Sample	CuO loading (%)	NH_3 uptake (mmol /g_{cat})	Cu area[a] (m^2/g_{Cu})	Dispersion[a]
HZSM-5(50)	−	0.746	−	−
HZSM-5(280)	−	0.145	−	−
meso-ZSM-5(50)	−	0.774	−	−
meso-ZSM-5(280)	−	0.231	−	−
20%CuO/ZSM-5(50)[b]	18.3	1.144	50.5	0.07
20%CuO/ZSM-5(280)[b]	19.2	0.487	209.7	0.22
20%CuO/meso-ZSM-5(50)	18.8	1.153	55.5	0.08
20%CuO/meso-ZSM-5(280)	19.5	0.652	74.5	0.11

[a]Cu dispersion and Cu area were determined by dissociative N_2O adsorption method at 90 $^{\circ}$C.
[b] reproduced from chapter 3.

Figure 4.20 shows the NH_3-TPD profiles of meso-ZSM-5 zeolites and the corresponding reduced copper catalysts. The amount of ammonia uptake is summarized in **Table 4.6**. As shown in **Figure 4.20A**, the NH_3-TPD profiles of all parent zeolite HZSM-5 zeolites before and after NaOH treatment exhibited two distinct desorption peaks centering at around 250 and 450 $^{\circ}$C, which are the characteristic peaks of zeolite with MFI structure [79]. The peak at low temperature is assigned to ammonia weakly held or physically adsorbed on the Lewis acid sites of the zeolite, whereas the peak at high temperature is ascribable to the desorption of ammonia strongly adsorbed on and/or interacting with the dislodged Al, and decomposition of NH^{4+} on the Brönsted acid sites [81–84,105]. By comparison, apart from the slight shift of desorption peaks to lower temperature, no obvious changes can be observed on the NH_3 desorption profiles of ZSM-5(50) and ZSM-5(280) before and after NaOH treatment. As shown in **Table 4.6**, the acidity of ZSM-5(50) and ZSM-5(280) increased slightly from 0.746 and 0.145 mmol /g_{cat} to 0.774 and 0.231 mmol /g_{cat}, respectively, upon alkaline-treatment. Similar to the parent supports, no significant changes of NH_3-TPD profiles can be seen on the copper catalysts (**Figure 4.20B**). Two distinct peaks centered at ca. 300 and 550 $^{\circ}$C were exhibited on all reduced Cu catalysts. The peak at low temperature is ascribable to the combination of NH_3 desorption from both Lewis acid sites of zeolites and copper sites on the surface, while the high temperature peak is probably due to NH_3 adsorbed on Cu that only binds to one Al[86]. As shown in **Table 4.6**, the total acid concentration of Cu/ZSM-5(50) and Cu/ZSM-5(280) increased slightly from 1.144 and 0.487 mmol /g_{cat} to 1.153 and 0.652 mmol /g_{cat}, respectively, by comparison to copper loaded on NaOH-treated ZSM-5(50) and ZSM-5(280).

4.3.2. Reaction of 2,3-butanediol over mesoporous catalysts

Table 4.7. Conversion of 2,3-butanediol to the main products on reduced mesoporous Cu catalysts in 10 min and 190 min (shown in parentheses).[a]

Catalysts	Conversion (%)	Selectivity (%)						
		Butenes	MEK	2-MPA[b]	IBA[c]	2-Butanol	Acetoin	Others[d]
Cu/MCM-48	97.2	1.6	45.0	3.0	10.1	9.6	17.6	13.1
	(93.4)	(0.9)	(49.4)	(1.5)	(5.8)	(10.9)	(22.2)	(9.3)
Cu/Al-MCM-48(23)	100.0	55.0	17.9	2.4	7.2	1.1	0.0	16.4
	(100.0)	(22.5)	(31.1)	(3.8)	(14.2)	(6.4)	(1.9)	(20.1)
Cu/Al-MCM-48(50)	100.0	66.9	18.8	2.1	1.3	0.4	0.0	10.5
	(100.0)	(33.8)	(25.0)	(4.5)	(16.0)	(3.0)	(0.1)	(17.6)
Cu/Al-MCM-48(100)	100.0	72.6	10.1	1.7	0.4	0.4	0.0	14.8
	(100.0)	(41.0)	(19.8)	(4.4)	(13.3)	(2.2)	(0.2)	(19.1)
Cu/Al-MCM-48(200)	100.0	52.6	17.7	1.8	6.9	1.2	0.0	19.8
	(100.0)	(23.8)	(27.8)	(4.7)	(13.9)	(6.2)	(2.7)	(20.9)
Cu/SBA-15	97.4	2.2	49.5	2.6	10.5	12.8	9.7	12.7
	(94.5)	(1.2)	(49.9)	(1.7)	(7.2)	(13.7)	(14.8)	(11.5)
Cu/Al-SBA-15(23)	100.0	66.4	17.5	0.0	0.3	0.5	0.0	15.3
	(100.0)	(51.5)	(32.4)	(0.8)	(1.5)	(1.4)	(0.2)	(12.2)
Cu/Al-SBA-15(50)	100.0	76.6	4.3	0.0	0.2	0.0	0.0	18.9
	(100.0)	(58.5)	(23.7)	(0.9)	(1.9)	(0.9)	(0.0)	(14.1)
Cu/Al-SBA-15(100)	100.0	69.9	7.0	0.2	0.7	0.4	0.0	21.8
	(100.0)	(44.0)	(20.2)	(5.1)	(13.9)	(2.1)	(0.1)	(14.6)
Cu/Al-SBA-15(200)	100.0	69.6	5.5	0.6	1.6	0.4	0.0	22.3
	(100.0)	(42.2)	(22.2)	(4.0)	(12.2)	(3.3)	(0.1)	(16.0)
Cu/meso-ZSM-5(50)	100.0	21.2	11.9	0.0	0.0	0.0	0.0	66.9
	(100.0)	(42.4)	(38.6)	(1.7)	(0.0)	(0.0)	(0.0)	(17.3)
Cu/meso-ZSM-5(280)	100.0	40.3	1.7	0.0	0.0	0.0	0.0	58.0
	(100.0)	(69.6)	(11.0)	(0.0)	(0.0)	(0.0)	(0.0)	(19.4)

[a] Reaction condition: feed rate of 2,3-butanediol, 3.0 mL/h; catalyst weight, 1.0g; H_2/2,3-butanediol (molar ratio), 5:1; temperature, 250 °C, space time W/F_{A0}=30 g h mol^{-1}.
[b] 2-MPA: 2-methylpropanal.
[c] IBA: 2-methyl-1-propanol.
[d] Other products: Including propylene, $C_5^=$~$C_8^=$, aromatics, and other oxygenated compounds (1-acetyl-2-methyl-1-cyclopentene, 1-ethyl-5-methylcyclopentene, tetramethylfuran, etc).

Experiments were carried out over reduced mesoporous copper catalysts in the presence of hydrogen (H_2: 67.2 cm^3 min^{-1}, SATP; N_2: 15.4 cm^3 min^{-1}, SATP) at 250 °C. The reaction condition was as follows: feed rate of 2,3-butanediol of 3.0 mL h^{-1}, hydrogen to 2,3-butanediol molar ratio of 5. The detailed reaction procedures are described in the earlier report [105]. As discussed previously[105], the main products of 2,3-butanediol conversion over reduced

Cu/ZSM-5 catalysts consist of olefins ($C_3^=$–$C_8^=$), MEK, 2-methylpropanal, 2-butanol, 2-methyl-1-propanol and 3-hydroxy-2-butanone, and some other minor products, such as aromatics and oxygenated compounds. In this study, to investigate the pore size effect of the catalysts on conversion of 2,3-butanediol, we only focus on the discussion of the main products. The conversion of 2,3-butanediol and selectivities of the main products taken at 10 min and 190 min are shown in **Table 4.7**. The selectivities of the major products as a function of time on stream are shown in **Figures D.2**, **D.3**, **D.4** and **D.5** (see **Appendix D**).

As shown in **Table 4.7**, the conversion of 2,3-butanediol over all mesoporous catalysts under this reaction condition was almost 100% except Cu/MCM-48 and Cu/SBA-15, which is in accordance to the results of the previous report about the Cu/ZSM-5 catalysts [105]. As for Cu/MCM-48 and Cu/SBA-15, the conversion of 2,3-butanediol was 97.2% and 97.4% in 10 min, and 93.4% and 94.5% in 190 min, respectively.

As seen in **Figure D.2A**, with regard to the MCM-48 series of catalysts, the selectivities of butenes (the summation of 1-butene, cis-2-butene, trans-2-butene and isobutene) over all Cu/Al-MCM-48 catalysts with various SiO_2/Al_2O_3 ratios exhibited the similar trend, decreasing gradually with time on stream, which is probably due to deactivation caused by coking [105]. The catalyst Cu/Al-MCM-48(100) with moderate acidity (0.714 mmol /g_{cat} NH_3, see **Table 4.4**) was observed to have the highest butenes selectivity, which decreased from 72.6% during the first initial 10 min to 41% at 190 min (**Table 4.7**), and the lowest selectivity of MEK, increasing slightly from 10.1% at 10 min to 19.8% at 190 min. However, the catalysts with highest acidity (Cu/Al-MCM-48(23)) and lowest acidity (Cu/Al-MCM-48(200)) were found to show the similar selectivity of butenes, decreasing from 55% and 52.6% in the initial 10 min to 22.5% and 23.8% at 190 min (**Table 4.7**), respectively. The catalytic performance is similar to the catalyst Cu/ZSM-5 discussed in **Chapter 3** (**Table 3.3**): moderate acidity of zeolite is beneficial for the conversion of 2,3-butanediol and production of butenes as well.

As for the SBA-15 series of catalysts shown in **Table 4.7** (**Figure D.3**), Cu/Al-SBA-15(50) showed the best catalytic performance toward the production of butenes; the selectivity of butenes was up to 76.6% at the initial 10 min and 58.5% at 190 min of stream, both of which were higher than the corresponding results of Cu/Al-MCM-48(100). Meanwhile, it is seen that Cu/Al-SBA-15(50) shows the lowest selectivity of MEK, which is 4.3% and 23.7% at 10 min and 190 min, respectively. As shown in **Table 4.7**, similar to the MCM-48 series of catalysts,

Cu/Al-SBA-15 with higher acidity (SiO_2/Al_2O_3=23) and lower acidity (SiO_2/Al_2O_3=100 and 200) show lower selectivities of butenes and higher selectivity to MEK by comparison to Cu/Al-SBA-15(50).

As shown in **Figures D.2B and D.3B**, the reference catalysts Cu/MCM-48 and Cu/SBA-15 exhibited the highest selectivity of MEK, which remained approximately 45% and 49%, respectively, in 190 min of reaction. As reported by Torresi, dehydration of diols will occur on Cu/SiO$_2$ catalyst since Cu is a Lewis acid [91]. Hence, MEK (and 2-methylpropanal) can be formed via dehydration of 2,3-butanediol over Cu sites on the surface of the catalyst. According to our previous study [105], MEK is the intermediate product in the production of butenes from 2,3-butanediol; MEK is converted to 2-butanol by hydrogenation over Cu sites, which then is converted to butenes by the subsequent dehydration reaction over the acid sites of the zeolite (aluminosilicate in this study). As mentioned above, the catalysts Cu/Al-MCM-48(100) and Cu/Al-SBA-15(50) showed the lowest selectivity of MEK among its corresponding series of catalysts, which was because most of the obtained MEK in the reaction of 2,3-butanediol over Cu/Al-MCM-48(100) and Cu/Al-SBA-15(50) converted to 2-butanol and butenes, resulting in the lowest selectivity of MEK consequently.

According to the previous report [105], 2-methyl-1-propanol and 2-butanol were produced via hydrogenation of the intermediate products, 2-methylpropanal and MEK, respectively. As shown in **Table 4.7**, Cu/MCM-48 and Cu/SBA-15 exhibit high selectivities of 2-methyl-1-propanol (10.1% and 10.5%, respectively) and 2-butanol (9.6% and 12.8%, respectively) in the initial 10 min. Meanwhile, we can see that the reference catalysts Cu/MCM-48 and Cu/SBA-15 were not favorable to produce butenes, the selectivities of which were 1.6% and 2.2% at 10 min, 0.9% and 1.2% at 190 min (see **Table 4.7**), respectively, which can be attributed to the deficiency of acid sites for the dehydration reaction of 2-methyl-1-propanol and 2-butanol. However, over Cu/Al-MCM-48(100) and Cu/Al-SBA-15(50), the selectivites of alcohols (2-methyl-1-propanol and 2-butanol) were nearly 0% (see **Table 4.7**) at the initial 10 min, because all of them were converted to butenes via subsequent dehydration reaction immediately once they were formed by hydrogenation reactions.

In addition, as seen in **Figures D.2** and **D.3**, Cu/Al-SBA-15(50) displays higher catalytic stability than Cu/Al-MCM-48(100) based on the selectivities of butenes, which is probably due to the thicker pore wall (~3 nm, see **Table 4.2**) leading to greater hydrothermal stability [153]. It

should be noted that a considerable amount of acetoin (3-hydroxy-2-butanone) can be produced over Cu/MCM-48 and Cu/SBA-15 catalysts (see **Table 4.7**), which were from dehydrogenation of 2,3-butanediol over Cu sites of catalysts [36,105].

For the mesoporous ZSM-5 series of catalysts, as shown in **Table 4.7**, the selectivity of butenes is 21.2% and 40.3% at the initial 10 min for meso-Cu/ZSM-5(50) and meso-Cu/ZSM-5(280), respectively. However, as shown in **Figures D.4** and **D.5**, the selectivity of butenes increased significantly with increasing time on stream, which then tended to be relatively stable after 100 min of stream. In addition, the selectivities of MEK were seen to increase over time, increasing from 11.9% at the initial 10 min to 38.6% at 190 min, from 1.7% at 10 min to 11.0% at 190 min, for meso-Cu/ZSM-5(50) and Cu/meso-ZSM-5(280), respectively. Interestingly, as shown in **Figures D.4** and **D.5**, both mesoporous Cu/ZSM-5 catalysts showed perfect catalytic activities toward the production of olefins ($C_3^=$, $C_5^=-C_8^=$) at the initial 10 min of reaction, especially the catalyst meso-Cu/ZSM-5(280) with lower acidity (0.652 mmol NH_3/g_{cat}, see **Table 4.6**). In addition, it is seen that the catalyst Cu/meso-ZSM-5(280) presents the higher selectivity of butenes than Cu/meso-ZSM-5(50).
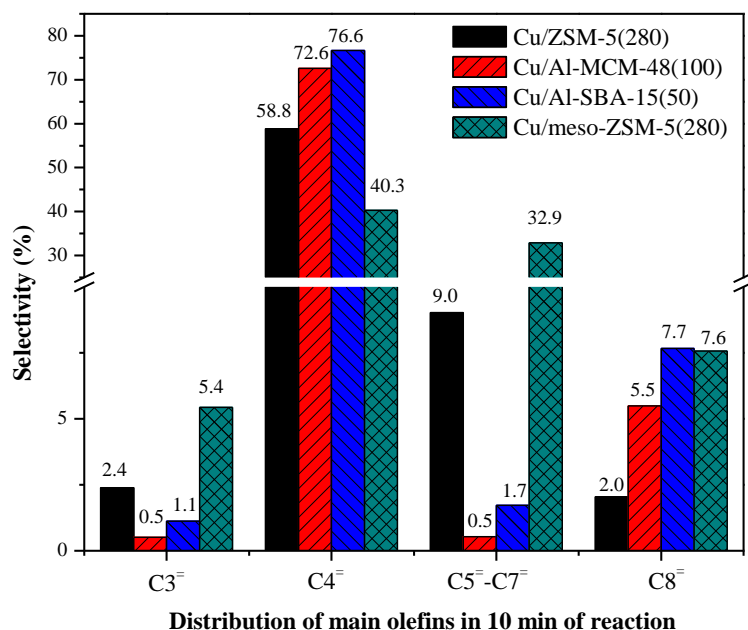
Figure 4.21. Distribution of olefins in the initial 10 min over Cu/ZSM-5(280), Cu/Al-MCM-48(100), Cu/Al-SBA-15(50) and Cu/meso-ZSM-5(280).

Figure 4.21 shows the comparison of the distribution of olefins in the initial 10 min of reaction over the optimal mesoporous catalyst in each series (MCM-48, SBA-15 and meso-ZSM-5), and the regular Cu/ZSM-5(280) (data are reproduced from ref. [105]) as well. As seen, Cu/Al-MCM-48(100) and Cu/Al-SBA-15(50) exhibited high selectivity of butenes, 72.6% and 76.6%, respectively, in the initial 10 min of reaction, both of which were higher than that of Cu/meso-ZSM-5(280) (40.3%) and regular Cu/ZSM-5(280) (58.8%). This is probably attributed to the well-ordered mesoporous structure of Al-MCM-48(100) and Al-SBA-15(50) with pore size of 3.2 and 9.1 nm, respectively (see **Table 4.2**). According to the previous study [105], cracking and oligomerization reactions will take place simultaneously over Cu/ZSM-5 catalysts especially at the beginning of the reaction when 2,3-butanediol was used as reactant; the formed $C_4^=$ will oligomerize to produce $C_8^=$ (and $C_{12}^=$, which is not detected), which then is converted to the smaller olefins $C_2^=$, $C_3^=$ and $C_{5+}^=$ by subsequent cracking reactions. As shown in **Figure 4.21**, the selectivities of cracking products ($C_3^=$: 2.4%, $C_5^=-C_7^=$: 9.0%) are higher than $C_8^=$ (2.0%) from oligomerization of butenes, indicating cracking reaction occurs readily over Cu/ZSM-5(280) especially in the beginning of reaction, which results in the lower selectivity of $C_8^=$ consequently. By comparison, as shown in **Figures D.6** and **D.7**, all Cu/Al-MCM-48 and Cu/Al-SBA-15 catalysts exhibit much higher selectivity to $C_8^=$ than the cracking products, indicating that cracking reactions of heavy olefins (especially $C_8^=$) are not favorable over the mesoporous catalysts Cu/Al-MCM-48 and Cu/Al-SBA-15. Suzuki et al. [210] investigated the catalytic performance of mesoporous ZSM-5, regular ZSM-5 (microporous) and mesoporous aluminosilicate material Al-MCM-41 in the catalytic cracking of octane and found that the turnover frequency (TOF) of Al-MCM-41 in octane cracking was much smaller (one tenth) than that of regular HZSM-5 catalyst, which is similar to our result. In addition, from pore size distribution derived from the nitrogen adsorption-desorption, we can see that both micropores (diameters of ~0.55 nm, see **Figure 4.14A**) and mesopores (pore sizes of ~23 nm, see **Figure 4.14B**) exist on the meso-ZSM-5(280), which indicates that meso-ZSM-5(280) should have the property similar to the usual HZSM-5 and the mesoporous materials (Al-MCM-48 and Al-SBA-15) as well, which is evidenced by the results shown in **Figure 4.21**: Cu/meso-ZSM-5(280) exhibits high selectivities of cracking products ($C_3^=$: 5.4%, $C_5^=-C_7^=$:32.9%) and $C_8^=$ (7.6%). Furthermore, it is observed that the selectivity of $C_8^=$ over Cu/meso-ZSM-5(280) is close to the one of Cu/Al-SBA-15(50) (7.7%). However, from **Figure 4.21**, we can see that, over Cu/Al-

SBA-15(50), most of $C_8^=$ from oligomerization of $C_4^=$ was converted to light olefins. Hence, the oligomerization reaction occurs more readily over the mesoporous copper catalyst with larger mesopores (meso-ZSM-4(280), 23 nm, see **Figure 4.14B**), since it can provide sufficient space for intermediate products (butenes) to proceed further reaction to produce $C_8^=$ as a result. Therefore, it is safe to conclude that the mesopores are favorable for the oligomerization reaction, while the micropores are beneficial for the cracking reaction.
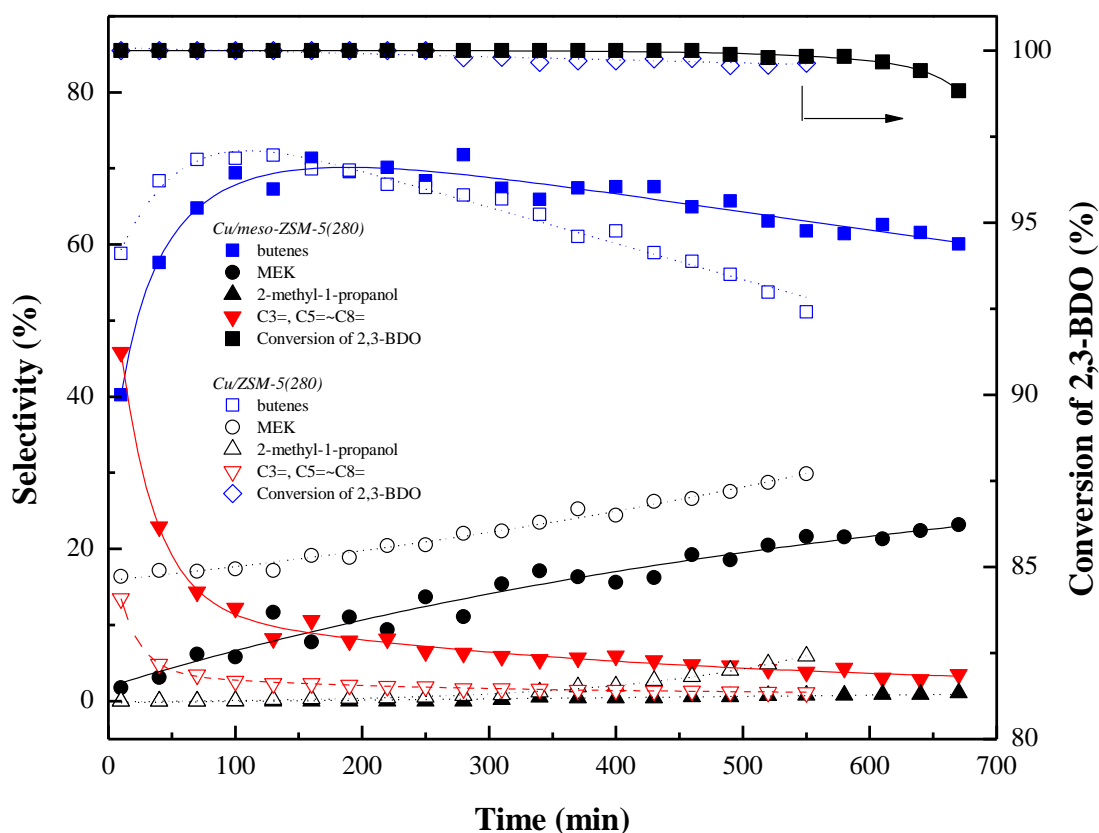
Figure 4.22. Catalytic results as a function of time on stream for the conversion of 2,3-butanediol over reduced 20%Cu/meso-ZSM-5(280) (solid symbols), and 20%Cu/ZSM-5(280) (open symbols). Reaction conditions: feed rate of 2,3-butanediol, 3.0 mL/h; catalyst weight, 1.0g; H_2/2,3-BDO, 5:1; temperature, 250°C.

140

Figure 4.22 shows the catalytic performance as a function of time on stream for the conversion of 2,3-butanediol over reduced Cu/meso-ZSM-5(280). By comparison to the results of Cu/ZSM-5(280) (data are reproduced from ref. [105]), it is seen that Cu/meso-ZSM-5(280) exhibits much better activity and stability. As seen, both catalysts show excellent conversion of 2,3-butanediol. Over Cu/meso-ZSM-5(280), conversion of 2,3-butanediol starts to decline from 100% at 490 min of reaction to 98.8% at 670 min of stream, which is better than the catalyst Cu/ZSM-5(280). Over Cu/ZSM-5(280), the conversion starts to decrease from 100% at 250 min to 99.6% at 550 min of stream. In addition, the selectivities of MEK over both catalysts are seen to increase over time; however, Cu/meso-ZSM-5(280) is seen to show much lower selectivity of MEK than Cu/ZSM-5(280), which increases from 1.7% at the initial 10 min to 23.2% at 670 min of stream. Meanwhile, the selectivities of products from cracking and oligomerization reaction ($C_3^=$ and $C_5^=-C_8^=$) over Cu/meso-ZSM-5(280) are much higher than Cu/ZSM-5(280) especially in the initial 100 min, which is because the mesopores are beneficial for the oligomerization as discussed above. More importantly, it can be seen that Cu/meso-ZSM-5(280) shows the higher stability based on the selectivities of butenes, which increase significantly from 40.3% during the initial 10 min to 71.3% at 160 min and then start to decline gradually to 61.0% at 670 min of reaction, which is better than the catalyst Cu/ZSM-5(280), the selectivities of butenes drop from 71.4% at 130 min to 51.2% in 550 min of reaction. The enhancement of activity and stability (catalytic lifetime) in the conversion of 2,3-butanediol is attributed to the introduction of mesopores to the catalyst. As reported [164], alkaline-treated HZSM-5 could improve the stability of the catalyst for propanal conversion as well as suppression of coke due to a reduction in microporosity and a shortened diffusion path length. Zhou et al. [211] demonstrated that mesoporous ZSM-5 can greatly enhance catalytic activity for cracking of triisopropylbenzene and esterification reactions due to the diminished coke formation by the shortening of the diffusion length in the microporous networks. Sun et al. [212] suggested that the improved catalytic activity of mesoporous ZSM-5 in the reaction of methanol to propylene was due to the enlarged pore size and pore volume, improving the diffusion property of catalyst, which slowed down the deactivation caused by coking. Hence, the higher the proportion of the mesopores in ZSM-5, the longer is the catalytic lifetime.

4.4. Conclusions

Three different types of mesoporous materials (Al-MCM-48, Al-SBA-15 and meso-ZSM-5) were loaded with ~20wt% CuO and investigated in the conversion of 2,3-butanediol to butenes. The results showed that the existence of mesopores on the catalysts (Al-MCM-48 and Al-SBA-15 types) could decrease the selectivities of products from cracking reactions, especially $C_3^=$ and $C_5^=-C_7^=$ by comparison with the catalyst with ~20wt% CuO loaded on the regular HZSM-5(280); meanwhile, the selectivity of $C_8^=$ from oligomerization of butenes was found to increase with increasing pore size of the catalysts. With respect to Cu/meso-ZSM-5(280) catalyst, it can be seen that the catalyst has performance with similarities to both Cu/ZSM-5(280) catalyst and mesoporous copper catalysts (Cu/Al-MCM-48 and Cu/Al-SBA-15) since both micropores (diameter of ~0.55 nm) and mesopores (pore size of ~23 nm) exist on meso-ZSM-5(280). Hence, Cu/meso-ZSM-5(280) displayed high activity for both cracking reactions ($C_3^=$ and $C_5^=-C_7^=$) and oligomerization ($C_8^=$). In addition, Cu/meso-ZSM-5(280) showed excellent catalytic stability; the selectivity of butenes dropped from 71.3% to 61.0% at 670 min of reaction, which is much better than the catalyst with Cu loaded on conventional HZSM-5(280), where selectivity of butenes dropped from 71.4% to 51.2% in 550 min of reaction. This is probably because the introduction of mesopores to the catalysts could reduce the microporosity and shorten the diffusion path length, and improve the diffusion properties of the catalyst which could slow down deactivation caused by coking.

Chapter 5 - Conversion of 2,3-butanediol over different metal-based catalysts

5.1. Introduction

Copper is well known as a hydrogenation catalyst. Brands et al. [56] investigated a series of Cu/SiO_2 catalysts promoted with several metals in the hydrogenation reaction of methyl acetate, and the results showed that Cu-containing catalysts have high activity for vapor-phase hydrogenation reaction, particularly the selective hydrogenation of C−O bonds; however, copper catalysts are relatively inactive for hydrogenolysis of C−C bonds. They found that Ni, Co and Mo promoted catalysts showed high activity in hydrogenolysis of C−C bonds, especially the Ni-promoted catalyst, which exhibited high methane formation (up to 70%), which was due to C-C cleavage.

Vasiliadou et al.[59] investigated the hydrogenolysis of glycerol to propylene glycol over highly dispersed Cu/SiO_2 catalysts. Their results showed that Cu selectively converted glycerol to propylene glycol with selectivity of 92−97% via consecutive dehydration-hydrogenation reactions with a conversion up to 50% at 240 ^{o}C. They demonstrated that the weak activity of Cu in C−C bond cleavage limited the formation of ethylene glycol. Sato et al.[60] reported that reduced Cu catalyst could effectively catalyze the dehydration of glycerol to hydroxyacetone in N_2, and the hydrogenation of hydroxyacetone followed by hydrogenolysis in H_2 to form ethylene glycol, acetaldehyde and ethanol.

Sitthisa et al.[58] investigated the hydrodeoxygenation of furfural over Cu, Pd and Ni supported on SiO_2, and found that the Cu catalyst mainly produced furfuryl alcohol via hydrogenation of the carbonyl group (C=O) due to the weak interaction of Cu with C=C. However, Pd/SiO_2 catalyst catalyzed the hydrodeoxygenation of furfural to produce a large amount of furan by decarbonylation, which is more favorable than hydrogenation over Pd catalysts. Ni/SiO_2 was beneficial for the formation of ring opening products such as butanal, butanol and butane. They suggested that the different product distribution was due to the strength of interaction of the furan ring with the metal surface and the type of intermediates on the surface that each metal can stabilize.

As different metal has different catalytic performance in the reaction, in this study, conversion of 2,3-butanediol over different metal-based catalysts (Ni, Pd, Pt and Rh) were conducted under the same reaction conditions to investigate the catalytic performance of different metal in the process of reaction. 5%Cu/ZSM-5 catalyst was used as a reference.

5.2. Experimental

5.2.1. Synthesis

Ni catalysts were prepared by the ammonia evaporation method which is similar to the method we used to prepare the Cu/ZSM-5 catalysts [105]. Typically, the required amount of $Ni(NO_3)_2 \cdot 6H_2O$ (99%, Fisher scientific) was dissolved in 40 mL of deionized water at room temperature, followed by adding ammonia hydroxide (28-30wt%, Fisher Scientific) until the pH reached 10.0 to form a dark blue complex $[Ni(NH_3)_6]^{2+}$, and then water was added to make 80 mL of a nickel-ammonia complex solution. 10 g of zeolite HZSM-5(280) (CBV 28014, SiO_2/Al_2O_3=280, Zeolyst International) was added to the solution and then the container was capped to avoid the evaporation of ammonia and stirred for 6 h at room temperature. After that, the container was moved to an oil batch preheated at 80 ^{o}C to allow for the evaporation of ammonia and the decrease of pH and deposition of nickel, consequently. When the pH value of the suspension decreased to 7.5, the evaporation process was terminated. Then the solid was recovered by filtration, washed, dried at 110 ^{o}C, and calcined in air at 550 ^{o}C for 4 h. Finally, the calcined catalyst was pelletized, crushed and sieved to 40-60 mesh.

Pt, Pd and Rh catalysts were prepared by an impregnation method [130,213–215], and the metal precursors were chloroplatinic acid hexahydrate ($H_2PtCl_6 \cdot xH_2O$, 37.5% Pt, certified ACS grade, Fisher Chemical), palladium nitrate hydrate ($Pd(NO_3)_2 \cdot xH_2O$, Sigma-Aldrich) and rhodium (III) nitrate dihydrate ($Rh(NO_3)_3 \cdot 2H_2O$, 31.83% Rh, Alfa Aesar), respectively. Typically, 5 g of zeolite HZSM-5(280) (CBV 28014, SiO_2/Al_2O_3=280, Zeolyst International) was impregnated in 5 mL solution containing the calculated amount of H_2PtCl_6, $Pd(NO_3)_2$ and $Rh(NO_3)_3$, respectively, for 4 h to give approximately 1wt% and 5wt% metal loading. Then the catalysts were dried in air at 100 ^{o}C for 12 h and calcined in air at 550 ^{o}C with a heating rate of 1 ^{o}C/min (Pt catalysts were calcined at 350 ^{o}C with a heating rate of 0.5 ^{o}C/min) for 4 h. Finally,

the calcined catalyst was pelletized, crushed and sieved to 40-60 mesh. The content of metal (shown in **Table 5.1**) was determined by inductively coupled plasma (ICP) method.

5.2.2. Catalyst characterization

BET surface area and porosity of catalysts were measured using nitrogen physisorption at -196°C on a Quantachrome Autosorb-1 apparatus and analyzed with Autosorb-1 software. Before measurement, the samples were evacuated at 350 ^{o}C for 4 h. Powder X-ray diffraction (XRD) patterns of the samples were recorded using Rigaku Miniflex II desktop x-ray diffractometer. Scans of two theta angles were obtained from 5° to 90° for all catalysts with a step size of 0.02^{o} and scan speed of 0.75 ^{o}/min. The XPS analysis of the catalyst was carried out on a PerkinElmer PHI 5400 using achromatic Al Kα radiation (1486.60 eV), and the binding energy (BE) value was referenced to the C1s peak of contaminant carbon at 284.6 eV to correct for the charging on the substrate.

The surface area and dispersion of Ni, Pt and Rh were determined by H_2 pulse chemisorption using the same equipment as NH_3-TPD. Before adsorption measurement, the catalysts were pretreated by reduction in H_2/Ar flow (10v/v%, 40 mL/min) for 2 h at 300 ^{o}C, 500 ^{o}C and 700 ^{o}C for Pt [215], Ni [216] and Rh [214] catalysts, respectively, and then pretreated in a highly pure Ar flow to remove the adsorbed H_2, followed by cooling down to 30 ^{o}C. Next, H_2 pulse chemisorption was performed at 30 ^{o}C using Ar as carrier gas, and 20 doses (0.5 mL each pulse) of 10% H_2/Ar were subsequently introduced by a 6-port injection valve until the saturated coverage was achieved. The effluent gas was detected with a thermal conductivity detector (TCD). The dispersion of metal was calculated on the basis of the amount of chemisorbed hydrogen with a surface stoichiometry H/metal$_{surface}$=1 [215–217]. Pd surface area and dispersion was determined by CO pulse chemisorption [218,219]. The Pd catalysts were pretreated by reduction in H_2/Ar flow (10v/v%, 40 mL/min) at 400 ^{o}C for 2 h, then cooled down to 30 ^{o}C. CO pulse chemisorption was conducted at 30 ^{o}C using Ar as carrier gas, and 20 pulses (0.5 mL each pulse) of 20v/v% CO/Ar were subsequently injected until the saturated coverage was achieved. The uptake of CO was detected with a thermal conductivity detector (TCD). The dispersion of Pd was calculated on the basis of the amount of chemisorbed CO with a surface stoichiometry CO/Pd$_{surface}$=1 [219].

5.2.3. Catalytic reaction

The catalytic reactions were performed in a continuous flow fixed-bed reactor made of stainless steel (id=8 mm) under atmospheric pressure. Prior to reaction, Ni, Pt, Rh and Pd catalysts were reduced in the reactor in the H_2/N_2 flow (flow rate of H_2/N_2=1/5) at 500 $^{\circ}$C, 300 $^{\circ}$C, 700 $^{\circ}$C and 400 $^{\circ}$C, respectively, for 2 h. The detailed reaction condition is described in the earlier report [105]. The carbon selectivity and conversion were calculated in the following methods.

$$\text{Carbon selectivity} = \frac{\text{Moles of carbon in specific product}}{\text{Total carbon atoms in identified products}} \times 100\%$$

$$\text{Conversion} = \frac{(\text{moles of 2,3-BDO})_{in} - (\text{moles of 2,3-BDO})_{out}}{(\text{moles of 2,3-BDO})_{in}} \times 100\%$$

The carbon balances were maintained above 90% for all runs in this paper.

5.3. Results and discussion

5.3.1. Characterization of catalysts

5.3.1.1. X-ray diffraction

Figures 5.1−5.4 show the XRD patterns of the calcined Ni/ZSM-5(280), Pt/ZSM-5(280), Rh/ZSM-5(280) and Pd/ZSM-5(280) catalysts with various metal loadings, respectively. As seen, a slight decrease in the intensity of the main peaks was noticed after introduction of metal. All the characteristic peaks of the parent HZSM-5(280) were observed in the catalysts, indicating that the introduction of metal (Ni, Pt, Rh and Pd) did not destroy the structure of the parent zeolite. It is noted that over the catalysts with higher loadings, the characteristic peaks related to the metal oxide can be observed. As seen, two broad peaks at around 37.23° and 62.83° were observed over 10%Ni/ZSM-5(280) and 15%Ni/ZSM-5(280) catalysts (see **Figure 5.1**), which can be attributed to (111) and (220) crystal planes of the cubic NiO (JCPDS card no. 73-1523) [220]. For 5%Pt/ZSM-5(280), compared to the parent HZSM-5(280), two new sharp peaks at around 12.8° and 35° can be observed (**Figure 5.2**). The former peak could be attributed to PtCl$_4$

(JCPDS no. 30-0886) or $PtCl_2$ (JCPDS no. 46-0902), while the later one could be ascribed to $PtCl_2$ (JCPDS no. 46-0902) or PtO (JCPDS no. 27-1331) or PtO_2 (JCPDS no. 21-1283). As reported, the Pt precursor $H_2PtCl_6\cdot6H_2O$ could decompose into $PtCl_2$ at the temperature about $300-350\,^{o}C$, which could further decompose to Pt metal at the temperature about $375\,^{o}C$ [221–223]. Hence, various Pt species including $PtCl_4$, $PtCl_2$, PtO, PtO_2 and Pt could exist on the surface of the calcined Pt/ZSM-5 catalyst. However, it is difficult to determine which Pt species exists on the surface of the catalyst from XRD. Hence, additional measurement will be performed on XPS, which will be discussed later. In addition, for the calcined Rh/ZSM-5(280) catalysts (**Figure 5.3**), two characteristic peaks at 35.2^{o} and 53.7^{o} corresponding to (110) and (116) crystal planes of Rh_2O_3 (JCPDS no. 76-0148) can be seen over Rh/ZSM-5(280) with 5% Rh loading. In **Figure 5.4**, compared to the parent HZSM-5(280), three peaks centered at around 33.8^{o}, 60.22^{o} and 71.46^{o} corresponding to the (101), (103) and (202) reflections of PdO (JCPDS no. 41-1107) can be observed on 5%Pd/ZSM-5(280). This indicates that the metals (Ni, Pt, Rh and Pd) have better dispersion over the catalysts with lower loadings, which is evidenced by the dispersion results shown in **Table 5.1**. As shown, the dispersion of metal decreased with increasing loadings, especially for the catalysts Pt/ZSM-5(280), Rh/ZSM-5(280) and Pd/ZSM-5(280), the dispersion decreased from 32.7% to 6.1%, 28.7% to 7.1%, and 22.5% to 5.3, respectively, when the nominal loadings of metal increased from 1% to 5%.
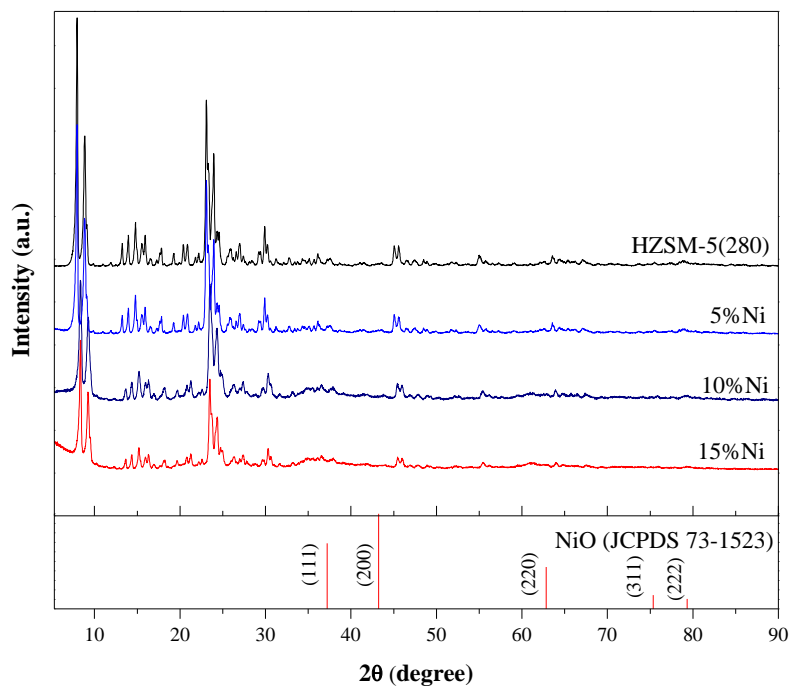
Figure 5.1. XRD patterns of the calcined Ni/ZSM-5(280) catalysts with various Ni loadings.
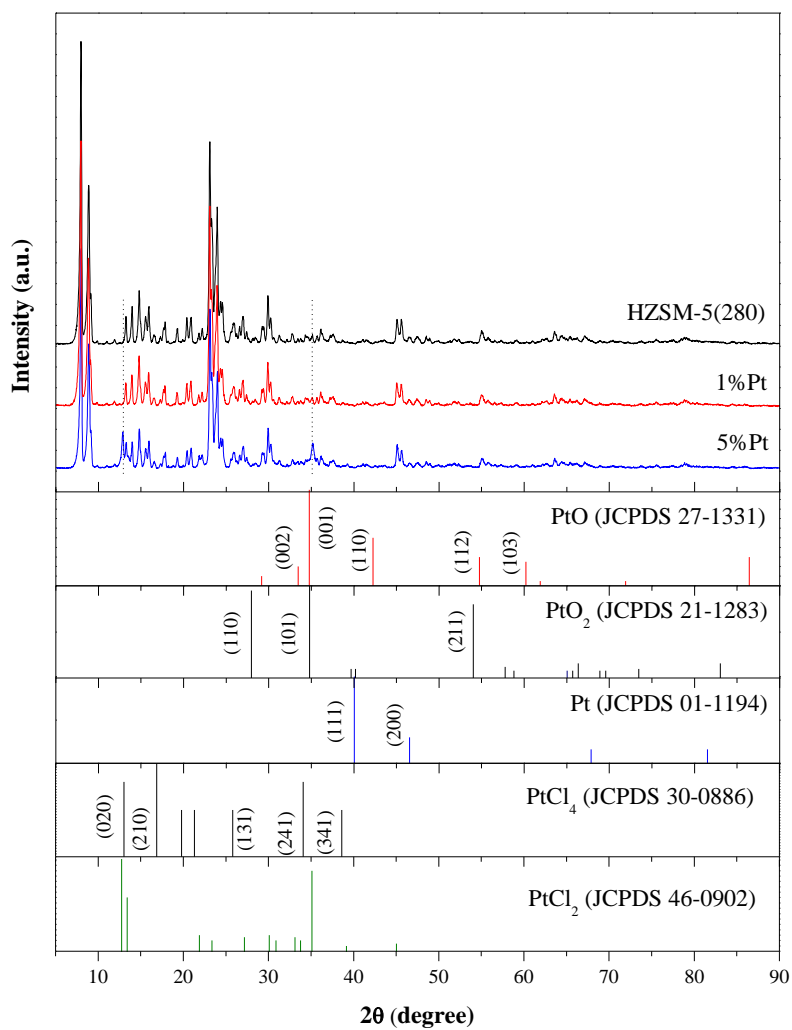
Figure 5.2. XRD patterns of the calcined Pt/ZSM-5(280) catalysts with various Pt loadings.
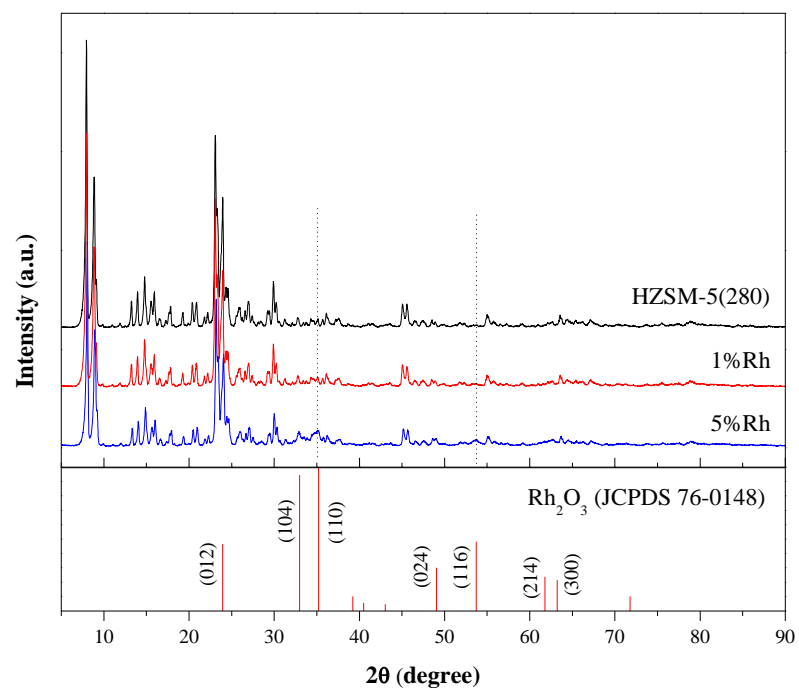
Figure 5.3. XRD patterns of the calcined Rh/ZSM-5(280) catalysts with various Rh loadings.
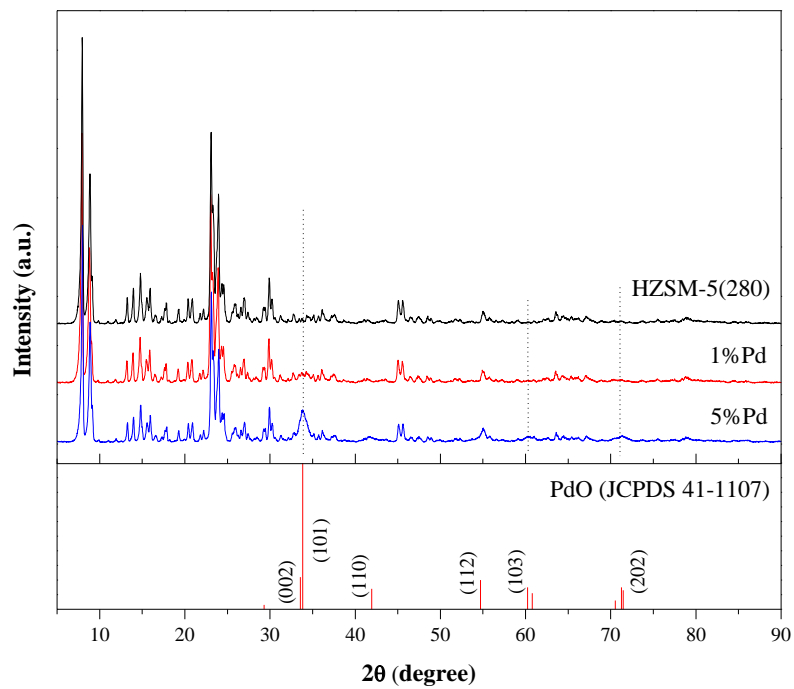
Figure 5.4. XRD patterns of the calcined Rd/ZSM-5(280) catalysts with various Rd loadings.

5.3.1.2. XPS
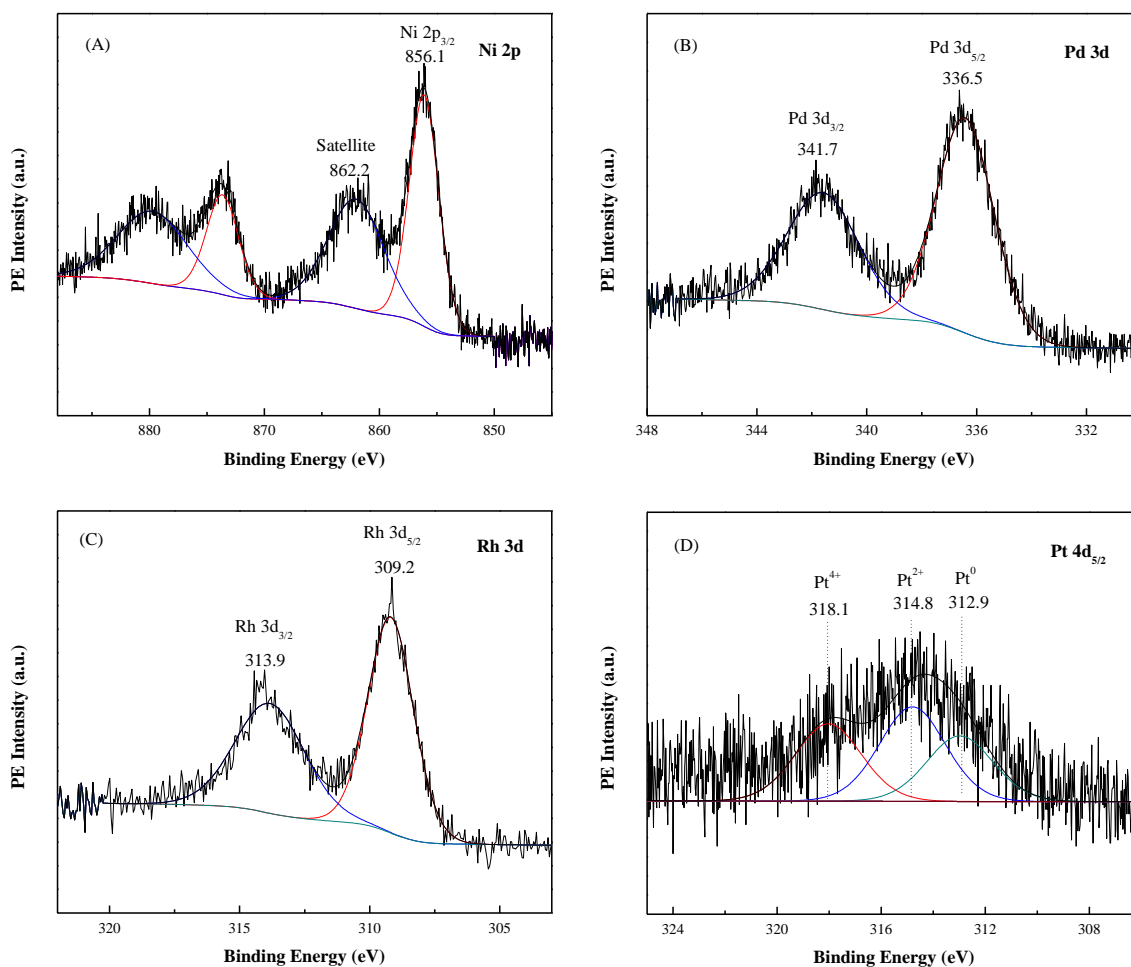
Figure 5.5. XPS spectra of (A) Ni 2p of calcined 15%Ni/ZSM-5(280); (B) Pd 3d of calcined 5%Pd/ZSM-5(280); (C) Rh 3d of calcined 5%Rh/ZSM-5(280); (D) Pt 4d$_{5/2}$ of calcined 5%Pt/ZSM-5(280). Spectra were curve fitted by the software CasaXPS.

XPS analysis was applied to determine the oxidation states of metals (Ni, Pd, Rh and Pt) on the catalysts. The Ni 2p photoelectron spectrum of the calcined Ni/ZSM-5(280) is shown in **Figure 5.5A**. As seen, the symmetric peak of Ni 2p$_{3/2}$ is centered around 856.1 eV, which is accompanied by a satellite peak at 862.2 eV. Typically, the peak at 856.1 eV is assigned to the free NiO or Ni^{2+} of NiO in an octahedral site [224,225]. **Figure 5.5B** displays the XPS spectrum of Pd 3d of the calcined 5%Pd/ZSM-5(280). As seen, two separated peaks with the binding energy of 336.5 eV and 341.7 eV can be observed, which could be assigned to Pd3d$_{5/2}$ and

Pd3d$_{3/2}$ of bulk PdO, respectively [213]. This indicates that PdO is the main species exists on the calcined Pd/ZSM-5(280) catalysts prepared by impregnation method, which is in good agreement with the XRD result showed in **Figure 5.4**. The Rh 3d XPS spectrum of calcined Rh/ZSM-5(280) is presented in **Figure 5.5C**. The peak of Rh$_{3d5/2}$ is observed at around 309.2 eV, which is accompanied by Rh$_{3d3/2}$ peak at about 313.9 eV. This indicates that the oxidation state of Rh on the catalyst is +3, and Rh$_2$O$_3$ is the main species on the calcined Rh/ZSM-5(280) [226], which is in accordance with the result of XRD (**Figure 5.3**).

Figure **5.5D** shows the XPS spectrum of the calcined Pt/ZSM-5(280) catalyst prepared by impregnation method. As reported, the most intense photoemission lines of Pt are those arising from the Pt 4f levels, but it is difficult to analyze the Pt 4f lines because this energy region around 70-80 eV is overlapped by the presence of a strong Al 2p peak [227–229]. Consequently, the energy region of the less intense Pt 4d peak was analyzed instead. As seen, the broad Pt 4d$_{5/2}$ can be deconvoluted into three components with binding energies of 318.1 eV, 314.8 eV and 312.9 eV. As reported, the peak centered at 318.1 eV can be attributed to Pt^{4+} (or PtO$_2$) species created in the calcination process, while the peaks at 314.8 eV and 312.9 eV can be ascribed to Pt^{2+} (or PtO) and Pt^0 species, both of which are created from decomposition of PtCl$_4$ during calcination [227–229]. However, the characteristic diffraction peaks related to the metallic Pt was not observed in XRD pattern of Pt/ZSM-5(280) (**Figure 5.2**), which is probably due to well-dispersed of the small size of the Pt crystals on the surface of catalyst.

5.3.1.3. N$_2$ adsorption

Table 5.1. Textural properties and metal dispersions of the calcined catalysts.

Catalyst	Metal loading[a] (%)	Dispersion[b] (%)	Surface area			Pore volume		
			S_{BET}[c] (m^2g^{-1})	S_{micro}[d] (m^2g^{-1})	$S_{external}$[e] (m^2g^{-1})	V_{total}[f] (cm^3g^{-1})	V_{micro}[d] (cm^3g^{-1})	V_{meso}[g] (cm^3g^{-1})
HZSM-5(280)[h]	–	–	437	332	105	0.301	0.180	0.121
5%Ni/ZSM-5(280)	3.9	5.1	402	252	150	0.323	0.140	0.183
10%Ni/ZSM-5(280)	10.1	4.0	423	235	188	0.407	0.140	0.267
15%Ni/ZSM-5(280)	14.1	3.4	427	225	202	0.371	0.122	0.249
1%Pt/ZSM-5(280)	0.7	32.7	409	316	93	0.264	0.160	0.104
5%Pt/ZSM-5(280)	4.1	6.1	379	286	93	0.246	0.144	0.102
1%Rh/ZSM-5(280)	0.8	28.7	407	314	93	0.269	0.165	0.104
5%Rh/ZSM-5(280)	4.3	7.1	403	307	96	0.333	0.206	0.127
1%Pd/ZSM-5(280)	0.8	22.5	397	277	120	0.292	0.134	0.158
5%Pd/ZSM-5(280)	4.2	5.3	384	248	136	0.248	0.117	0.131

[a] Metal loading was measured by ICP method. Rh content was calculated by H$_2$-TPR using CuO as a reference, by considering the complete reduction of Rh^{3+} to Rh^0.
[b] Dispersion of Ni, Pt and Rh were obtained by H$_2$-chemisorption. Dispersion of Pd was obtained by CO-chemisorption.
[c] The Brunauer-Emmett-Teller (BET) surface area (S_{BET}) was calculated from the linear part of BET plot from 0.007 to 0.03.
[d] The micropore area (S_{micro}) and volume (V_{micro}) were obtained by the t-plot method.
[e] The external surface area $S_{external}=S_{BET}-S_{micro}$.
[f] The total pore volume (V_{total}) was evaluated by single point pore volume at a relative pressure of 0.95.
[g] The mesopore volume $V_{meso}=V_{total}-V_{micro}$.
[h] The data of HZSM-5(280) were reproduced from ref.[105].

The structural properties of catalysts with different metals can be derived from the results of N$_2$ adsorption-desorption measurement at −196°C. The surface area and pore volume are summarized in **Table 5.1**. As seen, the introduction of Ni into zeolite HZSM-5(280) leads to the decrease of total surface area (S_{BET}) and pore volume (V_{total}), and micropore surface area (S_{micro}) and volume (V_{micro}), and the increase of the external surface area ($S_{external}$) and volume (V_{meso}), which is assumed to be caused by Ni deposition in the micropores of the zeolite. With the increasing Ni loadings from 5% to 15%, the micropore surface area decreases from 252 to 225 m^{2}g^{-1}, while the external surface area increases from 150 to 202 m^{2}g^{-1}. The increase of the external surface area is probably attributed to the agglomeration of NiO particles on the surface. For Pd catalysts, the addition of Pd results in the decrease of micropore surface area and volume, and the increase of the external surface area and volume, which is similar to Ni catalysts. However, for the Pt/ZSM-5(280) and Rh/ZSM-5(280) catalysts, it is seen that the addition of

metal leads to the decrease of both micropore and external (mesopore) area at the same time. This is probably due to the deposition of Pt and Rh in the mesopores of zeolite.

5.3.2. Reaction of 2,3-butanediol over different metal based catalysts

Experiments were carried out over the reduced catalysts in the presence of hydrogen (H_2: 67.2 cm^3 min^{-1}, SATP; N_2: 15.4 cm^3 min^{-1}, SATP) at 250 ^{o}C. The reaction condition was as follows: feed rate of 2,3-butanediol of 3.0 mL h^{-1}, hydrogen to 2,3-butanediol molar ratio of 5. The detailed reaction procedures are described in the earlier report[105]. In the previous study[105], conversion of 2,3-butanediol over Cu/ZSM-5(280) catalysts in the presence of H_2 can produce a significant amount of unsaturated hydrocarbons, such as propylene, butenes, and $C_5^=-C_8^=$, and negligible amount of saturated hydrocarbons, such as isobutane and butane. For better understanding the catalytic performance of different metal-based catalysts, 4.8%Cu/ZSM-5(280) was used as a reference, which was reproduced from previous report (shown in **Table 5.2**). It should be noted that the conversion of all catalysts under the reaction conditions are nearly 100%.

As seen in **Table 5.2**, the major product is $C_4^=$ over 4.8%Cu/ZSM-5(280), and the selectivity is 50.8% and 60.88% in 40 min and 190 min, respectively. The other minor unsaturated hydrocarbons are ethylene (0.22% in 40 min, 0.23% in 190 min), propylene (2.80% in 40 min, 1.15% in 190 min), $C_5^=$ (6.55% in 40 min, 1.70% in 190 min) and $C_6^=-C_8^=$ (5.59% in 40 min, 1.82% in 190 min). From the previous study [105], we know the selectivities of the products from cracking and oligomerization will decrease with increasing time on stream, leading to the increase of $C_4^=$ selectivity, which is due to the deactivation of the catalyst.

Over 5%Ni/ZSM-5(280) catalysts, it is seen that the majority of hydrocarbons are saturated ones. As seen, the selectivities of butane (C_4) and isobutane (i-C_4) are 22.75% and 7.37%, respectively, in the initial 40 min, which then decrease to 14.89% and 3.18%, respectively, in 190 min of reaction. It is obvious that both butane and isobutane could be produced by further hydrogenation of the butenes (including isobutene, 1-butene and 2-butene) since Ni is a good catalyst for hydrogenation of olefins or aromatics [216,224,230]. Interestingly, with increasing time on stream, the selectivity of butenes increases from 10.64% at 40 min to 19.31% at 190 min. This is probably due to the deactivation of catalyst, decreasing the catalytic activity of Ni for further hydrogenation of butenes to butane (or isobutane). Apart from the

saturated C_4, it is seen that conversion of 2,3-butanediol over 5%Ni/ZSM-5(280) catalyst produce plenty of saturated hydrocarbons such as methane (5.15% in 40 min), ethane (2.08% in 40 min), propane (7.31% in 40 min), C_5 (2.41% in 40 min) and C_6–C_8 (5.17% in 40 min) alkanes. This is because hydrocracking of high alkanes over Ni catalysts could produce light alkanes and the molecular hydrogen associated with an active site is believed to be involved in the C−C bond rupture [231–234]. As seen, the selectivities of cracking products decrease over time, which is due to the deactivation of catalyst. In addition, with the increasing Ni loadings from 5% to 15%, the selectivity of $C_4^=$ decrease from 10.64% to 6.92% in the initial 40 min of stream, which is accompanied by the increasing selectivity of methane (5.15% to 8.49%), propane (7.31% to 8.79%) and butane (22.75% to 27.78%), and decreasing selectivity of C_5 (2.41% to 1.11%) and C_6-C_8 (5.17% to 2.81%), indicating that Ni is the active site for the hydrogenation of olefins and cracking of heavy alkanes. In addition, Ni is believed to serve the same role as Cu in the process of conversion of 2,3-butanediol to butenes over Cu/ZSM-5 catalyst, which includies hydrogenation of MEK and 2-methylpropanal to 2-butanol and 2-methyl-1-propanol, respectively.

In **Table 5.2**, it is seen that the selectivity of butene over Pd/ZSM-5(280) catalysts are 0% at the initial 40 min even over the catalyst with only 1% of Pd loading. Probably butenes were converted to butane or isobutane once they were formed over Pd catalyst since Pd is good for hydrogenation of alkenes and alkynes [235–238], which is evidenced by the formation of C_4 with the selectivity of 10.19% and 10.5% over 1%Pd/ZSM-5(280) and 5%Pd/ZSM-5(280), respectively, at the initial 40 min. In addition, the alkanes such as ethane, propane, C_5 and C_6-C_8 are also observed over Pd catalysts. However, methane was not detected, indicating that the formation of propane would be from the cracking of C_{5+} alkanes, but not from the cracking of butane, which implied that the hydrocracking ability of Pd is not as good as Ni. Interestingly, conversion of 2,3-butanediol over Pd catalysts can selectively produce xylene, with the selectivity of 17.22% and 12.38% over 1%Pd/ZSM-5(280) and 5%Pd/ZSM-5(280), respectively, at the initial 40 min. As reported, aromatization, oligomerization and cracking reaction of butenes are very easy to take place over acid sites of zeolite [133,134]. In addition, it is reported that Pd catalysts can transform n-butane to aromatic hydrocarbons [239]. By taking into account of both acid and metal (Pd) functions of Pd/ZSM-5, we can see that aromatization of butene or

156

butane occurs readily over the catalyst. However, the mechanism for selective production of xylene is not clear.

Similar to Ni and Pd catalysts, it is shown that Pt/ZSM-5(280) catalyzes the production of alkanes, such as ethane, propane, isobutane, butane and C_5-C_8, all of which are from hydrogenation, cracking and oligomerization of butenes formed over Pt catalysts, since Pt catalysts are good for hydrogenation of olefins [240–242] and cracking reactions of long-chain alkanes [243,244]. As seen, the selectivity of butenes is only 1.61% and 2.29% over 1%Pt/ZSM-5(280) and 5%Pt/ZSM-5(280), respectively, at 40 min of reaction. Interestingly, most of the aromatic products from conversion of 2,3-butanediol over Pt/ZSM-5(280) catalysts is 5-ethyl-1,2,3,4-tetrahydro-naphthalene. The reaction mechanism is not clear.

With respect to Rh catalysts, the formation of methane was observed over 1%Rh/ZSM-5(280) and 5%Rh/ZSM-5(280) catalysts, with the selectivity of 1.77% and 3.18%, respectively, at the initial 40 min. In addition, over 1%Rh/ZSM-5(280), the selectivity of butenes is 4.89% at 40 min, which is decreased to 1.9% at the same reaction time when Rh loading increases to 5%, indicating that addition of Rh is favorable for the hydrogenation of butene. It seems that the selectivity of butene increases over time, which is due to the deactivation of the catalyst. Additionally, significant amount of alkanes like ethane, propane, isobutane, butane, C_5 and C_6–C_8 were observed over Rh catalysts.

When compared various metal-based ZSM-5(280) catalysts with similar amount of metal (Cu, Ni, Pd, Pt and Rh) loading (5%), it is obvious that Cu/ZSM-5 is favorable for the production of the unsaturated hydrocarbons, especially butene, with the selectivity up to 50.8% at 40 min, which is accompanied by small amount of ethylene, propylene, and $C_{5+}^=$. It should be noted that, over Cu catalyst, the selectivity of saturated hydrocarbon such as isobutane is negligible. This indicates that Cu is not favorable for hydrogenation of butenes from dehydration of alcohols (2-butanol and 2-methyl-1-propanol), but it favors the hydrogenation of carbonyl group (C=O) to form the hydroxyl group (−OH), from which butenes are formed by dehydration over acid sites of zeolite. However, over the other metal-based catalysts, the saturated hydrocarbons become the main products. Over 5%Pd/ZSM-5(280), olefins, especially butenes, were not observed even at 190 min of reaction, indicating that Pd is favorable for further hydrogenation of butenes and other unsaturated hydrocarbons ($C_2^=$, $C_3^=$, $C_5^=$–$C_8^=$) from oligomerization and cracking reactions of butenes, to produce saturated hydrocarbons such as isobutane and butane, and some other

saturated hydrocarbons such as ethane, propane, and C_5-C_8. In contrast, butenes can be observed over the other metal (Ni, Pt and Rh) loaded catalysts. In particular, over 5%Ni/ZSM-5(280), the selectivity of butenes is 10.64% at 40 min. However, it seems that Ni catalyst favors the formation of methane (5.15%), which is from hydrocracking of heavy hydrocarbons. Hence, Ni is a good catalyst for hydrogenation of olefins and cracking of heavy hydrocarbons. Similar to Ni catalyst, methane and some other saturated hydrocarbons such as ethane, propane, C_4 and C_5, are also observed over 5%Rh/ZSM-5(280) catalyst, indicating that Rh is favorable for hydrogenation of olefins and hydrocracking reactions of heavy hydrocarbons. However, it is seen that the selectivity of MEK over 5%Rh/ZSM-5(280) is 54.93% at 40 min, which is much higher than the other catalysts, indicating that Rh is not favorable for the hydrogenation of carbonyl group (C=O) of MEK, even though Rh is good for hydrogenation of olefins. As for 5%Pt/ZSM-5(280) catalyst, the catalytic performance is similar to Pd/ZSM-5(280). However, it seems that Pt favors the production of heavy aromatics, while the Pd catalyst is favorable for the formation of xylene.

5.4. Conclusions

Conversion of 2,3-butanediol over different metal-based catalysts were investigated under the same reaction conditions. The results show that Cu is not favorable for hydrogenation of butenes from dehydration of alcohols (2-butanol and 2-methyl-1-propanol), but it favors the hydrogenation of carbonyl group (C=O) to form hydroxyl group (−OH), from which butenes are formed by dehydration over acid sites of the zeolite. A Pd catalyst is active in further hydrogenating butenes and other unsaturated hydrocarbons ($C_2^=$, $C_3^=$, $C_5^=$−$C_8^=$) from oligomerization and cracking reactions of butenes. Both Ni and Rh catalysts are good for hydrogenation of olefins and cracking of heavy hydrocarbons; however, Rh is not as good as Ni for the hydrogenation of carbonyl group (C=O) of MEK. In addition, the results show that Pt favors the formation of heavy aromatics such as 5-ethyl-1,2,3,4-tetrahydro-naphthalene, while Pd is favorable for the production of xylene.

Table 5.2. Carbon selectivity of the products (%) on different reduced metals loaded on ZSM-5(280) in 40 min and 190 min (shown in parentheses). [a]

	4.8%Cu/Z	5%Ni/Z	10%Ni/Z	15%Ni/Z	1%Pd/Z	5%Pd/Z	1%Pt/Z	5%Pt/Z	1%Rh/Z	5%Rh/Z
Methane CH$_4$	0	5.15	7.25	8.49	0	0	0	0	1.77	3.18
	(0)	(4.92)	(5.54)	(7.26)	(0)	(0)	(0)	(0)	(1.2)	(1.45)
Ethylene C2$^=$	0.22	0	0	0	0	0	0	0	0	0
	(0.23)	(0)	(0)	(0)	(0)	(0)	(0)	(0)	(0)	(0)
Ethane C2	0	2.08	2.04	1.86	0.13	0.56	0.25	0.22	1.82	2.5
	(0)	(1.48)	(1.18)	(1.12)	(0.15)	(0.16)	(0.14)	(0.15)	(1.13)	(1.14)
propane C3	2.80^b	7.31	8.16	8.79	8	10.38	8.95	10.95	9.08	13.07
	(1.15)^b	(5.37)	(4.98)	(5.61)	(7.21)	(9.36)	(9.25)	(9.78)	(10.29)	(8.41)
isobutane i-C4	0.17	7.37	7.89	7.38	0.4	0.42	3.71	2.83	0.13	0.22
	(0.10)	(3.18)	(1.66)	(2.19)	(0.3)	(0.41)	(1.85)	(2.05)	(0.09)	(0.08)
butane C4	0	22.75	24.15	27.78	10.19	10.5	14.52	15.05	7.64	7.71
	(0)	(14.89)	(10.65)	(14.73)	(11.71)	(10.42)	(11.31)	(11.84)	(6.01)	(4.66)
butene C4$^=$	50.80	10.64	8.49	6.92	0	0	1.61	2.29	4.89	1.9
	(60.88)	(19.31)	(21.29)	(17.73)	(1.1)	(0)	(2.6)	(2.86)	(8.42)	(4.96)
C5	6.55^b	2.41	1.8	1.11	3.75	2.07	3.21	2.77	7.47	2.25
	(1.70)^b	(0.73)	(0.51)	(0.45)	(4.1)	(0.73)	(0.5)	(0.75)	(3.82)	(0.14)
C6-C8	5.59^b	5.17	2.89	2.81	8.62	8.37	7.76	6.28	8.62	2.37
	(1.82)^b	(1.66)	(1.18)	(0.61)	(7.29)	(8.51)	(2.17)	(3.13)	(4.85)	(2.06)
2-methylpropanal	0	0	0	0	1.1	0	0.2	0.61	0.32	0.31
	(0.07)	(0.05)	(0.32)	(0.19)	(5.12)	(0.66)	(3.46)	(2.82)	(2.99)	(5.33)
MEK	20.01	29.19	28.14	27.27	35.11	36.28	39.92	42.27	42.85	54.93
	(24.94)	(38.07)	(38.8)	(37.93)	(36.69)	(37.9)	(51.35)	(51.87)	(43.43)	(50.0)
2-methyl-1-propanol	0	0.44	0	0	0	0	0.41	0	0	0.44
	(0)	(0.38)	(0.57)	(0.59)	(0.97)	(0)	(0.44)	(0)	(1.58)	(1.09)

3-hydroxy-2-butanone	0.40 (0)	0 (0)	0 (0)	0 (0)	0 (0)	0 (0)	0 (4.98)	0 (3.22)	0 (0.58)	0 (14.64)
aromatics	1.84 (1.23)	1.53 (5.07)	1.28 (6.39)	1.53 (5.1)	17.22[c] (17.71)[c]	12.38[c] (15.93)[c]	6.94[d] (8.3)[d]	7.22[d] (6.74)[d]	7.42 (4.75)	2.66 (3.26)
others	11.62 (7.88)	5.96 (4.89)	7.60 (6.93)	5.97 (6.49)	15.48 (7.65)	19.04 (15.93)	12.52 (3.65)	9.51 (4.79)	7.99 (10.86)	8.46 (2.81)

[a]Reaction condition: feed rate of 2,3-butanediol, 3.0 mL/h; catalyst weight, 1.0g; H_2/2,3-butanediol (molar ratio), 5:1; temperature, 250 ^{o}C.

[b]For Cu/ZSM-5(280) catalyst, only $C3^{=}$, $C5^{=}$ and $C6^{=}-C8^{=}$ unsaturated hydrocarbons were detected.

[c]Most of the aromatic products from Pd/ZSM-5(280) catalysts are xylene.

[d]Most of the aromatic products from Pt/ZSM-5(280) are 5-ethyl-1,2,3,4-tetrahydro-naphthalene.

Chapter 6 - Future work

DFT simulation will be performed to model to the dehydration reaction of 2,3-BDO catalyzed by using bifunctional catalysts (Cu/ZSM-5 and Cu/Y) to explain the confinement effect to the reaction. Since the structure of ZSM-5 and Y are very large, the cluster model will be introduced. It will be significant to look at how the Cu site and the confinement would anticipate in the reaction mechanism first; then the calculations will be performed based on brönsted acid site (proton site) plus the confinement. Since the bifunctional catalysts were employed in the reaction, the combined of these two active sites and the confinement will be introduced into the calculations to further understand the reactions on the molecular level. The potential energy surfaces will be plotted in order to look at the thermodynamic effect, and the transition state and energy barrier of each reaction step can be calculated in order to compare the simulation results with the experiment results.

Deactivation of zeolite-based catalyst is mainly due to the formation of coke, which is a non-desorbed product that prevents access to the acid sites of catalysts. It is important to know the change of acid sites after reaction. I will use NH_3 as probe molecules to detect the acid sites by in situ FTIR. For in situ reaction, about 0.03 g of catalyst powder is placed into the ceramic cup of a commercial gas cell with a ZnSe window. Prior to reaction, the catalyst is heated to 300 ºC to get rid of adsorbed species with flowing Ar for 30 min. Then the catalyst is reduced with $10\%H_2/Ar$ at 300 ºC for 30 min followed by cooling down to 250 ºC. Then 2,3-BDO can be fed as vapor into the gas cell through a saturator using $10\%H_2/Ar$ as a carrier gas. After 2 hours, the reaction will be stopped followed by Ar evacuation at 250 ºC for 30 min. Then NH_3 gas is introduced into the gas cell at 250 ºC for 10 min followed by Ar purge for 30 min. IR spectra of ammonia adsorbed on catalysts can present the Brönsted and Lewis acid sites in the catalyst post reaction. And then the fresh catalyst sample is placed into the gas cell to collect IR spectra of ammonia adsorbed on fresh reduced catalyst at 250 ºC, which can describe Brönsted and Lewis acid sites in the catalyst before reaction. By comparing these spectra, we can understand the change of acid sites during the reaction.

References

[1]   D. Liu, E. Chen, Integrated catalytic process for biomass conversion and upgrading to C_{12} furoin and alkane fuel, ACS Catal. 4 (2014) 1302–1310.

[2]   Y. Cheng, G.W. Huber, Chemistry of furan conversion into aromatics and olefins over HZSM-5: A model biomass conversion reaction, ACS Catal. 1 (2011) 611–628. doi:10.1021/cs200103j.

[3]   P. Azadi, R. Carrasquillo-Flores, Y.J. Pagán-Torres, E.I. Gürbüz, R. Farnood, J.A. Dumesic, Catalytic conversion of biomass using solvents derived from lignin, Green Chem. 14 (2012) 1573–1576. doi:10.1039/c2gc35203f.

[4]   G.W. Huber, S. Iborra, A. Corma, Synthesis of transportation fuels from biomass: chemistry, catalysts, and engineering, Chem. Rev. 106 (2006) 4044–4098. doi:10.1021/cr068360d.

[5]   J.C. Serrano-Ruiz, J.A. Dumesic, Catalytic routes for the conversion of biomass into liquid hydrocarbon transportation fuels, Energy Environ. Sci. 4 (2011) 83. doi:10.1039/c0ee00436g.

[6]   G.W. Huber, J.N. Chheda, C.J. Barrett, J.A. Dumesic, Production of liquid alkanes by aqueous-phase processing of biomass-derived carbohydrates, Science. 308 (2005) 1446–1450. doi:10.1126/science.1111166.

[7]   J.N. Chheda, J.A. Dumesic, An overview of dehydration, aldol-condensation and hydrogenation processes for production of liquid alkanes from biomass-derived carbohydrates, Catal. Today. 123 (2007) 59–70. doi:10.1016/j.cattod.2006.12.006.

[8]   R.M. West, E.L. Kunkes, D.A. Simonetti, J.A. Dumesic, Catalytic conversion of biomass-derived carbohydrates to fuels and chemicals by formation and upgrading of mono-functional hydrocarbon intermediates, Catal. Today. 147 (2009) 115–125. doi:10.1016/j.cattod.2009.02.004.

[9]   X.-J. Ji, H. Huang, J. Du, J.-G. Zhu, L.-J. Ren, N. Hu, et al., Enhanced 2,3-butanediol production by Klebsiella oxytoca using a two-stage agitation speed control strategy, Bioresour. Technol. 100 (2009) 3410–3414. doi:10.1016/j.biortech.2009.02.031.

[10]   X.-J. Ji, H. Huang, P.-K. Ouyang, Microbial 2,3-butanediol production: a state-of-the-art review, Biotechnol. Adv. 29 (2011) 351–364. doi:10.1016/j.biotechadv.2011.01.007.

[11]   X.-J. Ji, H. Huang, J. Du, J.-G. Zhu, L.-J. Ren, S. Li, et al., Development of an industrial medium for economical 2,3-butanediol production through co-fermentation of glucose and xylose by Klebsiella oxytoca, Bioresour. Technol. 100 (2009) 5214–5218. doi:10.1016/j.biortech.2009.05.036.

[12]   P. Perego, A. Converti, A. Del Borghi, P. Canepa, 2,3-Butanediol production by

Enterobacter aerogenes: selection of the optimal conditions and application to food industry residues, Bioprocess Eng. 23 (2000) 613–620. doi:10.1007/s004490000210.

[13]   P. Perego, A. Converti, M. Del Borghi, Effects of temperature, inoculum size and starch hydrolyzate concentration on butanediol production by Bacillus licheniformis, Bioresour. Technol. 89 (2003) 125–131. doi:10.1016/S0960-8524(03)00063-4.

[14]   B.C. Saha, R.J. Bothast, Production of 2,3-butanediol by newly isolated Enterobacter cloacae, Appl. Microbiol. Biotechnol. 52 (1999) 321–326. http://www.ncbi.nlm.nih.gov/pubmed/10531643.

[15]   L. Ge, X. Wu, J. Chen, J. Wu, A new method for industrial production of 2,3-butanediol, J. Biomater. Nanobiotechnol. 2 (2011) 335–336. doi:10.1007/s002530000486.

[16]   A. V. Tran, R.P. Chambers, The dehydration of fermentative 2,3-butanediol into methyl ethyl ketone, Biotechnol. Bioeng. 27 (1987) 343–351.

[17]   M.E. Winfield, The catalytic dehydration of 2,3-butanediol to butadiene II. adsorption equilibria, Aust. J. Chem. 3 (1950) 290–305.

[18]   B.O. Palsson, S. Fathi-Afshar, D.F. Rudd, E.N. Lightfoot, Biomass as a source of chemical feedstocks: an economic evaluation, Science. 213 (1981) 513–517. doi:10.1126/science.213.4507.513.

[19]   A. Coelho, G. Caeiro, M.A.N.D.A. Lemos, F. Lemos, F.R. Ribeiro, 1-Butene oligomerization over ZSM-5 zeolite: Part 1 – Effect of reaction conditions, Fuel. 111 (2013) 449–460. doi:10.1016/j.fuel.2013.03.066.

[20]   M.E. Wright, B.G. Harvey, R.L. Quintana, Highly efficient zirconium-catalyzed batch conversion of 1-butene : a new route to jet fuels, Energy & Fuels. 22 (2008) 3299–3302. doi:10.1021/ef800380b.

[21]   J.Q. Bond, A.A. Upadhye, H. Olcay, G.A. Tompsett, J. Jae, R. Xing, et al., Production of renewable jet fuel range alkanes and commodity chemicals from integrated catalytic processing of biomass, Energy Environ. Sci. 7 (2014) 1500–1523. doi:10.1039/c3ee43846e.

[22]   A. Multer, N. Mcgraw, K. Hohn, P. Vadlani, Production of methyl ethyl ketone from biomass using a hybrid biochemical/catalytic approach, Ind. Eng. Chem. Res. 52 (2013) 56–60.

[23]   N. Jansen, M.C. Flickinger, G.T. Tsao, Production of 2,3-butanediol from D-xylose by Klebsiella oxytoca ATCC 8724, Biotechnol. Bioeng. XXVI (1984) 362–369.

[24]   B. Schiel-Bengelsdorf, J. Montoya, S. Linder, P. Dürre, Butanol fermentation, Environ. Technol. 34 (2013) 1691–1710. doi:10.1080/09593330.2013.827746.

[25]   N. Qureshi, T.C. Ezeji, J. Ebener, B.S. Dien, M.A. Cotta, H.P. Blaschek, Butanol

production by Clostridium beijerinckii. Part I: Use of acid and enzyme hydrolyzed corn fiber, Bioresour. Technol. 99 (2008) 5915–5922. doi:10.1016/j.biortech.2007.09.087.

[26]   N. Qureshi, B.C. Saha, M.A. Cotta, Butanol production from wheat straw hydrolysate using Clostridium beijerinckii, Bioprocess Biosyst. Eng. 30 (2007) 419–427. doi:10.1007/s00449-007-0137-9.

[27]   J. Yu, T. Zhang, J. Zhong, X. Zhang, T. Tan, Biorefinery of sweet sorghum stem, Biotechnol. Adv. 30 (2012) 811–816. doi:10.1016/j.biotechadv.2012.01.014.

[28]   C. Lu, J. Zhao, S.T. Yang, D. Wei, Fed-batch fermentation for n-butanol production from cassava bagasse hydrolysate in a fibrous bed bioreactor with continuous gas stripping, Bioresour. Technol. 104 (2012) 380–387. doi:10.1016/j.biortech.2011.10.089.

[29]   M. Winfield, The catalytic dehydration of 2,3-butanediol to butadiene: II. Adsorption equilibria, Aust. J. Sci. Res. Ser. A Phys. Sci. 3 (1949) 290–305.

[30]   R.R. Emerson, M.C. Fllckinger, G.T. Tsao, Kinetics of dehydration of aqueous 2, 3-butanediol to methyl ethyl ketone, Ind. Eng. Chem. Prod. Res. Dev. 21 (1982) 473–477.

[31]   A.N. Bourns, R.V. V. Nicholls, The catalytic action of aluminium silicates I. the dehydration of 2,3-butanediol and 2-butanone over activated Morden bentonite, Can. J. Res. 25 (1946) 80–89.

[32]   I. Bucsi, A. Molnar, M. Bartok, G.A. Olah, Transformation of 1,2-diols over perfluorinated resinsulfonic acid (nafion-H), Tetrahedron. 50 (1994) 8195–8202.

[33]   B.G. Harvey, W.W. Merriman, R.L. Quintana, Renewable gasoline, solvents, and fuel additives from 2,3-butanediol, ChemSusChem. (2016) 1814–1819. doi:10.1002/cssc.201600225.

[34]   W. Zhang, D. Yu, X. Ji, H. Huang, Efficient dehydration of bio-based 2,3-butanediol to butanone over boric acid modified HZSM-5 zeolites, Green Chem. 14 (2012) 3441–3450. doi:10.1039/c2gc36324k.

[35]   J. Lee, J.B. Grutzner, W.E. Walters, W.N. Delgass, The conversion of 2,3-butanediol to methyl ethyl ketone over zeolites, Stud. Surf. Sci. Catal. 130 (2000) 2603–2608.

[36]   H. Duan, D. Sun, Y. Yamada, S. Sato, Dehydration of 2,3-butanediol into 3-buten-2-ol catalyzed by ZrO_2, Catal. Commun. 48 (2014) 1–4. doi:10.1016/j.catcom.2014.01.018.

[37]   X. Liu, V. Fabos, S. Taylor, D. Knight, K. Whiston, G.J. Hutchings, One-step production of 1,3-butadiene from 2,3-butanediol dehydration, Chem. - A Eur. J. 101407 (2016) 1–6. doi:10.1002/chem.201602390.

[38]   H. Duan, Y. Yamada, S. Sato, Efficient production of 1,3-butadiene in the catalytic dehydration of 2,3-butanediol, Appl. Catal. A Gen. 491 (2015) 163–169.

[39]   S. Sato, R. Takahashi, T. Sodesawa, A. Igarashi, H. Inoue, Catalytic reaction of 1,3-butanediol over rare earth oxides, Appl. Catal. A Gen. 328 (2007) 109–116. doi:10.1016/j.apcata.2007.05.033.

[40]   H. Gotoh, Y. Yamada, S. Sato, Dehydration of 1,3-butanediol over rare earth oxides, Appl. Catal. A Gen. 377 (2010) 92–98. doi:10.1016/j.apcata.2010.01.025.

[41]   N. Yamamoto, S. Sato, R. Takahashi, K. Inui, Synthesis of homoallyl alcohol from 1,4-butanediol over ZrO_2 catalyst, Catal. Commun. 6 (2005) 480–484. doi:10.1016/j.catcom.2005.04.011.

[42]   S. Sato, R. Takahashi, H. Fukuda, K. Inui, Dehydrogenation of 1,3-butanediol over Cu-based catalyst, J. Mol. Catal. A Chem. 272 (2007) 164–168. doi:10.1016/j.molcata.2007.03.034.

[43]   A. Dyer, An introduction to zeolite molecular sieves, John Wiley & Sons, 1988.

[44]   R. Szostak, Molecular sieves: principles of synthesis and identification, Van Nostrand Reinhold Catalysis Series, New York, 1989.

[45]   A. Corma, S. Zones, Zeolites and catalysis: synthesis, reactions and applications, Wiley-VCH Verlag GmbH & Co. KGaA, Weinheim, Germany, 2010. doi:10.1002/9783527630295.

[46]   J.S. Woertink, P.J. Smeets, M.H. Groothaert, M. A. Vance, B.F. Sels, R. A. Schoonheydt, et al., A $[Cu_2O]^{2+}$ core in Cu-ZSM-5, the active site in the oxidation of methane to methanol, Proc. Natl. Acad. Sci. U. S. A. 106 (2009) 18908–18913. doi:10.1073/pnas.0910461106.

[47]   J. Cejka, H. van Bekkum, A. Corma, F. Schuth, Introduction to zeolite science and practice 3rd revised edition, Elsevier, Amsterdam, 2007.

[48]   J.N. Kondo, R. Nishitani, E. Yoda, T. Yokoi, T. Tatsumi, K. Domen, A comparative IR characterization of acidic sites on HY zeolite by pyridine and CO probes with silica-alumina and γ-alumina references., Phys. Chem. Chem. Phys. 12 (2010) 11576–11586. doi:10.1039/c0cp00203h.

[49]   J.S. Beck, K.D. Schmitt, J.B. Higgins, J.L. Schlenkert, A new family of mesoporous molecular sieves prepared with liquid crystal templates, J. Am. Chem. Soc. 114 (1992) 10834–10843.

[50]   S. Kawi, S.-C. Shen, Effects of structural and non-structural Al species on the stability of MCM-41 materials in boiling water, Mater. Lett. 42 (2000) 108–112.

[51]   Z. Zhang, Y. Han, L. Zhu, R. Wang, Y. Yu, S. Qiu, et al., Strongly acidic and high-temperature hydrothermally stable mesoporous aluminosilicates with ordered hexagonal structure, Angew. Chemie. 113 (2001) 1298–1302. doi:10.1002/1521-3757(20010401)113:7<1298::AID-ANGE1298>3.0.CO;2-H.

[52] K. Zhang, E.-H. Yuan, L.-L. Xu, Q.-S. Xue, C. Luo, B. Albela, et al., Preparation of high-quality MCM-48 mesoporous silica and the mode of action of the template, Eur. J. Inorg. Chem. 2012 (2012) 4183–4189. doi:10.1002/ejic.201200316.

[53] D. Zhao, P. Yang, N. Melosh, J. Feng, B.F. Chmelka, G.D. Stucky, Continuous mesoporous silica films with highly ordered large pore structures, Adv. Mater. 10 (1998) 1380–1385. doi:10.1002/(SICI)1521-4095(199811)10:16<1380::AID-ADMA1380>3.0.CO;2-8.

[54] Y. Li, W. Zhang, L. Zhang, Q. Yang, Z. Wei, Z. Feng, et al., Direct synthesis of Al-SBA-15 mesoporous materials via hydrolysis-controlled approach, J. Phys. Chem. B. 108 (2004) 9739–9744.

[55] L.T. Gibson, Mesosilica materials and organic pollutant adsorption: part A removal from air, Chem. Soc. Rev. 43 (2014) 5163–5172. doi:10.1039/c3cs60096c.

[56] D.S. Brands, E.K. Poels, A. Bliek, Ester hydrogenolysis over promoted Cu/SiO$_2$ catalysts, Appl. Catal. A Gen. 184 (1999) 279–289.

[57] L. Guo, J. Zhou, J. Mao, X. Guo, S. Zhang, Supported Cu catalysts for the selective hydrogenolysis of glycerol to propanediols, Appl. Catal. A Gen. 367 (2009) 93–98. doi:10.1016/j.apcata.2009.07.040.

[58] S. Sitthisa, D.E. Resasco, Hydrodeoxygenation of furfural over supported metal catalysts: a comparative study of Cu, Pd and Ni, Catal. Letters. 141 (2011) 784–791. doi:10.1007/s10562-011-0581-7.

[59] E.S. Vasiliadou, T.M. Eggenhuisen, P. Munnik, P.E. De Jongh, K.P. De Jong, A.A. Lemonidou, Synthesis and performance of highly dispersed Cu/SiO$_2$ catalysts for the hydrogenolysis of glycerol, Appl. Catal. B Environ. 145 (2014) 108–119.

[60] S. Sato, M. Akiyama, R. Takahashi, T. Hara, K. Inui, M. Yokota, Vapor-phase reaction of polyols over copper catalysts, Appl. Catal. A Gen. 347 (2008) 186–191. doi:10.1016/j.apcata.2008.06.013.

[61] M. Iwamoto, H. Yahiro, Y. Torikai, T. Yoshioka, N. Mizuno, Novel preparation method of highly copper ion-exchanged ZSM-5 zeolites and their catalytic activities for NO decomposition, Chem. Lett. (1990) 1967–1970.

[62] M. Schreier, S. Teren, L. Belcher, J.R. Regalbuto, J.T. Miller, The nature of "overexchanged" copper and platinum on zeolites, Nanotechnology. 16 (2005) S582–S591. doi:10.1088/0957-4484/16/7/036.

[63] Y.-Y. Zhu, S.-R. Wang, L.-J. Zhu, X.-L. Ge, X.-B. Li, Z.-Y. Luo, The influence of copper particle dispersion in Cu/SiO$_2$ catalysts on the hydrogenation synthesis of ethylene glycol, Catal. Letters. 135 (2010) 275–281. doi:10.1007/s10562-010-0298-z.

[64] J. Gong, H. Yue, Y. Zhao, S. Zhao, L. Zhao, J. Lv, et al., Synthesis of ethanol via syngas

on Cu/SiO$_2$ catalysts with balanced Cu^0-Cu$^+$ sites, J. Am. Chem. Soc. 134 (2012) 13922–13925. doi:10.1021/ja3034153.

[65]   S. Zhao, H. Yue, Y. Zhao, B. Wang, Y. Geng, J. Lv, et al., Chemoselective synthesis of ethanol via hydrogenation of dimethyl oxalate on Cu/SiO$_2$: Enhanced stability with boron dopant, J. Catal. 297 (2013) 142–150. doi:10.1016/j.jcat.2012.10.004.

[66]   L. Chen, P. Guo, M. Qiao, S. Yan, H. Li, W. Shen, et al., Cu/SiO$_2$ catalysts prepared by the ammonia-evaporation method: Texture, structure, and catalytic performance in hydrogenation of dimethyl oxalate to ethylene glycol, J. Catal. 257 (2008) 172–180. doi:10.1016/j.jcat.2008.04.021.

[67]   H. Zhang, Y. Cheng, T.P. Vispute, R. Xiao, G.W. Huber, R. Xiao, et al., Catalytic conversion of biomass-derived feedstocks into olefins and aromatics with ZSM-5: the hydrogen to carbon effective ratio, Energy Environ. Sci. 4 (2011) 2297–2307. doi:10.1039/c1ee01230d.

[68]   Z. Xiao, S. Jin, X. Wang, W. Li, J. Wang, C. Liang, Preparation, structure and catalytic properties of magnetically separable Cu–Fe catalysts for glycerol hydrogenolysis, J. Mater. Chem. 22 (2012) 16598–16605. doi:10.1039/c2jm32869k.

[69]   A. Gervasini, Characterization of the textural properties of metal loaded ZSM-5 zeolites, Appl. Catal. A Gen. 180 (1999) 71–82. doi:10.1016/S0926-860X(98)00333-0.

[70]   C.C. Chusuei, M.A. Brookshier, D.W. Goodman, Correlation of relative X-ray photoelectron spectroscopy shake-up intensity with CuO particle size, Langmuir. 15 (1999) 2806–2808.

[71]   C.J.G. Van Der Grift, A.F.H. Wielers, B.P.J. Joghi, J. Van Beijnum, M. De Boer, M. Versluijs-Helder, et al., Effect of the reduction treatment on the structure and reactivity of silica-supported copper particles, J. Catal. 131 (1991) 178–189. doi:10.1016/0021-9517(91)90334-Z.

[72]   J.J. Bravo-Suárez, B. Subramaniam, R. V. Chaudhari, Ultraviolet-visible spectroscopy and temperature-programmed techniques as tools for structural characterization of Cu in CuMgAlO$_x$ mixed metal oxides, J. Phys. Chem. C. 116 (2012) 18207–18221. doi:10.1021/jp303631v.

[73]   S.J. Jong, A.R. Pradhan, J.F. Wu, T.C. Tsai, S.B. Liu, On the regeneration of coked H-ZSM-5 catalysts, J. Catal. 174 (1998) 210–218. ISI:000072715600012.

[74]   L. Martins, R.P.S. Peguin, M.S. Batista, Identification of extra-framework species on Fe/ZSM-5 and Cu/ZSM-5 catalysts typical microporous molecular sieves with zeolitic structure, Mater. Res. 5 (2002) 321–327.

[75]   A. Sultana, T. Nanba, M. Haneda, M. Sasaki, H. Hamada, Influence of co-cations on the formation of Cu$^+$ species in Cu/ZSM-5 and its effect on selective catalytic reduction of NO$_x$ with NH$_3$, Appl. Catal. B Environ. 101 (2010) 61–67.

doi:10.1016/j.apcatb.2010.09.007.

[76]   Y. Zhang, I.J. Drake, A.T. Bell, Characterization of Cu-ZSM-5 prepared by solid-state ion exchange of H-ZSM-5 with CuCl, Chem. Mater. 18 (2006) 2347–2356.

[77]   M.K. Neylon, C.L. Marshall, A.J. Kropf, In situ EXAFS analysis of the temperature-programmed reduction of Cu-ZSM-5, J. Am. Chem. Soc. 124 (2002) 5457–5465. http://www.ncbi.nlm.nih.gov/pubmed/11996587.

[78]   Z. Huang, F. Cui, J. Xue, J. Zuo, J. Chen, C. Xia, Cu/SiO_2 catalysts prepared by hom- and heterogeneous deposition–precipitation methods: Texture, structure, and catalytic performance in the hydrogenolysis of glycerol to 1,2-propanediol, Catal. Today. 183 (2012) 42–51. doi:10.1016/j.cattod.2011.08.038.

[79]   Y. Li, S. Liu, Z. Zhang, S. Xie, X. Zhu, L. Xu, Aromatization and isomerization of 1-hexene over alkali-treated HZSM-5 zeolites: Improved reaction stability, Appl. Catal. A Gen. 338 (2008) 100–113. doi:10.1016/j.apcata.2007.12.026.

[80]   T. Nanba, S. Masukawa, A. Ogata, J. Uchisawa, A. Obuchi, Active sites of Cu-ZSM-5 for the decomposition of acrylonitrile, Appl. Catal. B Environ. 61 (2005) 288–296. doi:10.1016/j.apcatb.2005.05.013.

[81]   K. Kubo, H. Iida, S. Namba, A. Igarashi, Ultra-high steaming stability of Cu-ZSM-5 zeolite as naphtha cracking catalyst to produce light olefin, Catal. Commun. 29 (2012) 162–165. doi:10.1016/j.catcom.2012.10.004.

[82]   D. Jin, Z. Hou, L. Zhang, X. Zheng, Selective synthesis of para–para′-dimethyldiphenylmethane over H-beta zeolite, Catal. Today. 131 (2008) 378–384. doi:10.1016/j.cattod.2007.10.049.

[83]   F. Lonyi, J. Valyon, On the interpretation of the NH_3-TPD patterns of H-ZSM-5 and H-mordenite, Microporous Mesoporous Mater. 47 (2001) 293–301.

[84]   M. Niwa, S. Nishikawa, N. Katada, IRMS–TPD of ammonia for characterization of acid site in β-zeolite, Microporous Mesoporous Mater. 82 (2005) 105–112. doi:10.1016/j.micromeso.2005.03.002.

[85]   E.-Y. Choi, I.-S. Nam, Y.G. Kim, TPD study of mordenite-type zeolites for selective catalytic reduction of NO by NH_3, J. Catal. 161 (1996) 597–604.

[86]   O. Mihai, C.R. Widyastuti, S. Andonova, K. Kamasamudram, J. Li, S.Y. Joshi, et al., The effect of Cu-loading on different reactions involved in NH_3-SCR over Cu-BEA catalysts, J. Catal. 311 (2014) 170–181. doi:10.1016/j.jcat.2013.11.016.

[87]   A. Gervasini, M. Manzoli, G. Martra, A. Ponti, N. Ravasio, L. Sordelli, et al., Dependence of copper species on the nature of the support for dispersed CuO catalysts, J. Phys. Chem. B. 110 (2006) 7851–7861. doi:10.1021/jp056604c.

[88] S. Contarini, L. Kevan, X-ray photoelectron spectroscopic study of copper-exchanged X- and Y-type sodium zeolites: resolution of two cupric ion components and dependence on dehydration and x-irradiation, J. Phys. Chem. 90 (1986) 1630–1632. doi:10.1021/j100399a035.

[89] J. Morales, A. Barranco, A. Caballero, J.P. Holgado, A.R. Gonza, Interface effects for Cu, CuO, and Cu_2O deposited on SiO_2 and ZrO_2. XPS determination of the valence state of copper in Cu/SiO_2 and Cu/ZrO_2 catalysts, J. Phys. Chem. B. 106 (2002) 6921–6929.

[90] K. Maiti, O. Knauff, K. Ruck, M.S. Golden, G. Krabbes, J. Fink, et al., Cu-O network-dependent core-hole screening in low-dimensional cuprate systems : A high-resolution X-ray photoemission study, 57 (1998) 138–141.

[91] P.A. Torresi, V.K. Díez, P.J. Luggren, J.I. Di Cosimo, Conversion of diols by dehydrogenation and dehydration reactions on silica-supported copper catalysts, Appl. Catal. A Gen. 458 (2013) 119–129. doi:10.1016/j.apcata.2013.03.031.

[92] B. Wang, G. Manos, A novel thermogravimetric method for coke precursor characterisation, J. Catal. 250 (2007) 121–127. doi:10.1016/j.jcat.2007.05.018.

[93] H.S. Cerqueira, G. Caeiro, L. Costa, F. Ramôa Ribeiro, Deactivation of FCC catalysts, J. Mol. Catal. A Chem. 292 (2008) 1–13. doi:10.1016/j.molcata.2008.06.014.

[94] Y. Zhang, N. Zheng, K. Wang, S. Zhang, J. Wu, Effect of copper nanoparticles dispersion on catalytic performance of Cu/SiO_2 catalyst for hydrogenation of dimethyl oxalate to ethylene glycol, J. Nanomater. 2013 (2013) 1–6.

[95] C. Bearez, F. Chevalier, M. Guisnet, Mechanism of butane transformation on H mordenite I, kinetic study, React. Kinet. Catal. Lett. 22 (1983) 405–409.

[96] G. Caeiro, R.H. Carvalho, X. Wang, M.A.N.D.A. Lemos, F. Lemos, M. Guisnet, et al., Activation of C_2–C_4 alkanes over acid and bifunctional zeolite catalysts, J. Mol. Catal. A Chem. 255 (2006) 131–158. doi:10.1016/j.molcata.2006.03.068.

[97] M.J. Wulfers, F.C. Jentoft, Identification of carbonaceous deposits formed on H-mordenite during alkane isomerization, J. Catal. 307 (2013) 204–213. doi:10.1016/j.jcat.2013.07.011.

[98] H. Zhang, S. Shao, R. Xiao, D. Shen, J. Zeng, Characterization of coke deposition in the catalytic fast pyrolysis of biomass derivates, Energy and Fuels. 28 (2014) 52–57. doi:10.1021/ef401458y.

[99] S.K. Sahoo, S.S. Ray, I.D. Singh, Structural characterization of coke on spent hydroprocessing catalysts used for processing of vacuum gas oils, Appl. Catal. A Gen. 278 (2004) 83–91. doi:10.1016/j.apcata.2004.09.028.

[100] I. V. Kozhevnikov, S. Holmes, M.R.H. Siddiqui, Coking and regeneration of $H_3PW_{12}O_{40}/SiO_2$ catalysts, Appl. Catal. A Gen. 214 (2001) 47–58. doi:10.1016/S0926-

860X(01)00469-0.

[101] C.-J. Jia, Y. Liu, W. Schmidt, A.-H. Lu, F. Schüth, Small-sized HZSM-5 zeolite as highly active catalyst for gas phase dehydration of glycerol to acrolein, J. Catal. 269 (2010) 71–79. doi:10.1016/j.jcat.2009.10.017.

[102] M. Guisnet, P. Magnoux, Organic chemistry of coke formation, Appl. Catal. A Gen. 212 (2001) 83–96. doi:10.1016/S0926-860X(00)00845-0.

[103] D.P. Serrano, J. Aguado, J.M. Rodríguez, A. Peral, Catalytic cracking of polyethylene over nanocrystalline HZSM-5: Catalyst deactivation and regeneration study, J. Anal. Appl. Pyrolysis. 79 (2007) 456–464. doi:10.1016/j.jaap.2006.11.013.

[104] Y. Kissin, Chemical mechanisms of catalytic cracking over solid acidic catalysts: alkanes and alkenes, Catal Rev. 43 (2001) 85–146.

[105] Q. Zheng, M.D. Wales, M.G. Heidlage, M. Rezac, H. Wang, S.H. Bossmann, et al., Conversion of 2,3-butanediol to butenes over bifunctional catalysts in a single reactor, J. Catal. 330 (2015) 222–237. doi:10.1016/j.jcat.2015.07.004.

[106] H. Liu, Z. Huang, C. Xia, Y. Jia, J. Chen, H. Liu, Selective hydrogenolysis of xylitol to ethylene glycol and propylene glycol over silica dispersed copper catalysts prepared by a precipitation-gel method, ChemCatChem. 6 (2014) 2918–2928. doi:10.1002/cctc.201402141.

[107] R. Dimitrijevic, W. Lutz, A. Ritzmann, Hydrothermal stability of zeolites: Determination of extra-framework species of H-Y faujasite-type steamed zeolite, J. Phys. Chem. Solids. 67 (2006) 1741–1748. doi:10.1016/j.jpcs.2006.03.014.

[108] W. Lutz, Zeolite Y: synthesis, modification, and properties—A case revisited, Adv. Mater. Sci. Eng. 2014 (2014). doi:10.1155/2014/724248.

[109] W. Lutz, H. Toufar, R. Kurzhals, M. Suckow, Investigation and modeling of the hydrothermal stability of technically relevant zeolites, Adsorption. 11 (2005) 405–413. doi:10.1007/s10450-005-5406-9.

[110] H.G. Karge, V. Dondur, J. Weitkamp, Investigation of the distribution of acidity strength in zeolites by temperature-programmed desorption of probe molecules. 2. dealuminated Y-type zeolites, J. Phys. Chem. 95 (1991) 283–288. doi:10.1021/j100154a053.

[111] V.S. Marakatti, A.B. Halgeri, Metal ion-exchanged zeolites as highly active solid acid catalysts for the green synthesis of glycerol carbonate from glycerol, RSC Adv. 5 (2015) 14286–14293. doi:10.1039/C4CY00596A.

[112] W. Alharbi, E.F. Kozhevnikova, I. V. Kozhevnikov, E. Epelde, A.T. Aguayo, M. Olazar, et al., Dehydration of methanol to dimethyl ether over heteropoly acid catalysts: the relationship between reaction rate and catalyst acid strength, ACS Catal. 5 (2015) 10599–10607. doi:10.1021/acscatal.5b01911.

[113] Y. Gu, N. Cui, Q. Yu, C. Li, Q. Cui, Study on the influence of channel structure properties in the dehydration of glycerol to acrolein over H-zeolite catalysts, Appl. Catal. A Gen. 429–430 (2012) 9–16. doi:10.1016/j.apcata.2012.03.030.

[114] B. Katryniok, S. Paul, F. Dumeignil, Recent developments in the field of catalytic dehydration of glycerol to acrolein, ACS Catal. 3 (2013) 1819–1834. doi:10.1021/cs400354p.

[115] S.H. McAllister, J. Bailey, WM. A., C.M. Bouton, The catalyzed cleavage of diacetone alcohol and other ketols and unsaturated ketones, J. Am. Chem. Soc. 62 (1940) 3210–3215. doi:10.1021/ja01868a090.

[116] R.S.E. Conn, A.V. Lovell, S. Karady, L.M. Weinstock, Chiral Michael addition: methyl vinyl ketone addition catalyzed by Cinchona alkaloid derivatives, J. Org. Chem. 51 (1986) 4710–4711. doi:10.1021/jo00374a039.

[117] T. Akiyama, T. Katoh, K. Mori, Enantioselective robinson-type annulation reaction catalyzed by chiral phosphoric acids, Angew. Chemie - Int. Ed. 48 (2009) 4226–4228. doi:10.1002/anie.200901127.

[118] C.H. Heathcock, J.E. Ellis, J.E. Mcmurr, A. Coppolino, Acid-catalyzed robinson annelations, Tetrahedron Lett. (1971) 4995–4996.

[119] M.E. Jung, A review of annulation, Tetrahedron. 32 (1976) 3–31.

[120] A. de Klerk, Effect of oxygenates on the oligomerization of Fischer-Tropsch olefins over amorphous silica-alumina, Energy and Fuels. 21 (2007) 625–632. doi:10.1021/ef060485y.

[121] A. de Klerk, R.J.J. Nel, R. Schwarzer, Oxygenate conversion over solid phosphoric acid, Ind. Eng. Chem. Res. 46 (2007) 2377–2382. doi:10.1021/ie061522b.

[122] R.A.L. Baylon, J. Sun, K.J. Martin, P. Venkitasubramanian, Y. Wang, Beyond ketonization : selective conversion of carboxylic acids to olefins over balanced Lewis acid-base pairs, Chem. Commun. 52 (2016) 4975–4978. doi:10.1039/c5cc10528e.

[123] T. Tago, H. Konno, Y. Nakasaka, T. Masuda, Size-controlled synthesis of nano-zeolites and their application to light olefin synthesis, Catal. Surv. from Asia. 16 (2012) 148–163. doi:10.1007/s10563-012-9141-4.

[124] F. Lin, Y.H. Chin, Mechanism of intra- and inter-molecular C=C bond formation of propanal on Brønsted acid sites contained within MFI zeolites, J. Catal. 311 (2014) 244–256. doi:10.1016/j.jcat.2013.11.018.

[125] J. Tendam, U. Hanefeld, Renewable chemicals: Dehydroxylation of glycerol and polyols, ChemSusChem. 4 (2011) 1017–1034. doi:10.1002/cssc.201100162.

[126] T.Q. Hoang, X. Zhu, T. Sooknoi, D.E. Resasco, R.G. Mallinson, A comparison of the reactivities of propanal and propylene on HZSM-5, J. Catal. 271 (2010) 201–208.

doi:10.1016/j.jcat.2010.01.017.

[127] E.R. Sacia, M. Balakrishnan, M.H. Deaner, K.A. Goulas, F.D. Toste, A.T. Bell, Highly selective condensation of biomass-derived methyl ketones as a source of aviation fuel, ChemSusChem. 8 (2015) 1726–1736. doi:10.1002/cssc.201500002.

[128] M. Balakrishnan, E.R. Sacia, S. Sreekumar, A.A. Gokhale, C.D. Scown, F.D. Toste, et al., Novel pathways for fuels and lubricants from biomass optimized using life-cycle greenhouse gas assessment, Proc. Natl. Acad. Sci. 112 (2015) E3969–E3969. doi:10.1073/pnas.1511659112.

[129] O. Loog, U. Mäeorg, Selfcondensation of 2-methylpropanal with homochiral BINOL catalysts as a model asymmetric aldol - Tishchenko reaction, Tetrahedron Asymmetry. 10 (1999) 2411–2415. doi:10.1016/S0957-4166(99)00219-0.

[130] B. Peng, C. Zhao, I. Mejia-Centeno, G.A. Fuentes, A. Jentys, J.A. Lercher, Comparison of kinetics and reaction pathways for hydrodeoxygenation of C_3 alcohols on Pt/Al_2O_3, Catal. Today. 183 (2012) 3–9. doi:10.1016/j.cattod.2011.10.022.

[131] Z. He, X. Wang, Hydrodeoxygenation of model compounds and catalytic systems for pyrolysis bio-oils upgrading, Catal. Sustain. Energy, Versita. 1 (2012) 28–52. doi:10.2478/cse-2012-0004.

[132] A. Wawrzetz, B. Peng, A. Hrabar, A. Jentys, A.A. Lemonidou, J.A. Lercher, Towards understanding the bifunctional hydrodeoxygenation and aqueous phase reforming of glycerol, J. Catal. 269 (2010) 411–420. doi:10.1016/j.jcat.2009.11.027.

[133] Y. Ono, H. Kitagawa, Y. Sendoda, Transformation of but-1-ene into aromatic hydrocarbons over ZSM-5 zeolites, J. Chem. Soc. Faraday Trans. 1 Phys. Chem. Condens. Phases. 83 (1987) 2913–2923. doi:10.1039/F19878302913.

[134] V.R. Choudhary, D. Panjala, S. Banerjee, Aromatization of propene and n-butene over H-galloaluminosilicate (ZSM-5 type) zeolite, Appl. Catal. A Gen. 231 (2002) 243–251. doi:10.1016/S0926-860X(02)00061-3.

[135] X. Zhu, S. Liu, Y. Song, S. Xie, L. Xu, Catalytic cracking of 1-butene to propene and ethene on MCM-22 zeolite, Appl. Catal. A Gen. 290 (2005) 191–199. doi:10.1007/s11144-010-0188-9.

[136] K. Takeshita, K. Kawamoto, Reduced copper catalyzed conversion of primary alcohols into esters and ketones., Bull Chem Soc Jpn. 51 (1978) 2622–2627. doi:10.1246/bcsj.51.2622.

[137] K. Kawamoto, Y. Nishimura, The catalytic reaction of alcohols with reduced copper, Bull. Chem. Soc. Jpn. 44 (1971) 819–825.

[138] K. Inui, T. Kurabayashi, S. Sato, Direct synthesis of ethyl acetate from ethanol carried out under pressure, J. Catal. 212 (2002) 207–215. doi:10.1006/jcat.2002.3769.

[139] N. Iwasa, N. Takezawa, Reforming of ethanol-dehydrogenation to ethyl acetate and steam reforming to acetic acid over copper-based catalysts, Bull. Chem. Soc. Jpn. 64 (1991) 2619–2623.

[140] P. Ciambelli, V. Palma, A. Ruggiero, Low temperature catalytic steam reforming of ethanol. 2. Preliminary kinetic investigation of Pt/CeO_2 catalysts, Appl. Catal. B Environ. 96 (2010) 190–197. doi:10.1016/j.apcatb.2010.02.019.

[141] C. Chen, G. Chen, F. Yang, H. Wang, J. Han, Q. Ge, et al., Vapor phase hydrodeoxygenation and hydrogenation of m-cresol on silica supported Ni, Pd and Pt catalysts, Chem. Eng. Sci. 135 (2015) 145–154. doi:10.1016/j.ces.2015.04.054.

[142] M.A. Nikitina, I.I. Ivanova, Conversion of 2,3-butanediol over phosphate catalysts, ChemCatChem. 8 (2016) 1346–1353. doi:10.1002/cctc.201501399.

[143] Z. Liu, W. Huo, H. Ma, K. Qiao, Development and commercial application of methyl-ethyl-ketone production technology, Chinese J. Chem. Eng. 14 (2006) 676–684. doi:10.1016/S1004-9541(06)60134-1.

[144] F.L. Norman, Fuel additive containing lithium alkylaromatic sulfonate and peroxides, US 6858047 B1, 2005.

[145] C.T. Kresge, M.E. Leonowicz, W.J. Roth, J.C. Vartuli, J.S. Beck, Ordered mesoporous molecular sieves synthesized by a liquid-crystal template mechanism, Nature. 359 (1992) 710–712. doi:10.1038/359710a0.

[146] A. Corma, From microporous to mesoporous molecular sieve materials and their use in catalysis, Chem. Rev. 97 (1997) 2373–2420. http://www.ncbi.nlm.nih.gov/pubmed/11848903.

[147] Y. Tao, H. Kanoh, L. Abrams, K. Kaneko, Mesopore-modified zeolites: preparation, characterization, and applications., Chem. Rev. 106 (2006) 896–910. doi:10.1021/cr040204o.

[148] A. Sayari, Novel synthesis of high-quality MCM-48 silica, J. Am. Chem. Soc. 122 (2000) 6504–6505. doi:10.1021/ja0005946.

[149] K. Schumacher, P.I. Ravikovitch, A. Du Chesne, A. V. Neimark, K.K. Unger, Characterization of MCM-48 materials, Langmuir. 16 (2000) 4648–4654. doi:10.1021/la991595i.

[150] S. Kim, J. Ida, V. V. Guliants, J.Y.S. Lin, Tailoring pore properties of MCM-48 silica for selective adsorption of CO_2, J. Phys. Chem. B. 109 (2005) 6287–6293. doi:10.1021/jp045634x.

[151] K. Schumacher, M. Grun, K.K. Unger, Novel synthesis of spherical MCM-48, Microporous Mesoporous Mater. 27 (1999) 201–206.

[152] K. Schumacher, C.D.F. Von Hohenesche, K.K. Unger, R. Ulrich, A. Du Chesne, U. Wiesner, et al., The synthesis of spherical mesoporous molecular sieves MCM-48 with heteroatoms incorporated into the silica framework, Adv. Mater. 11 (1999) 1194–1198.

[153] D. Zhao, J. Feng, Q. Huo, N. Melosh, G.H. Fredrickson, B.F. Chmelka, et al., Triblock copolymer syntheses of mesoporous silica with periodic 50 to 300 angstrom pores, Science 279 (1998) 548–552.

[154] D. Zhao, Q. Huo, J. Feng, B.F. Chmelka, G.D. Stucky, Nonionic triblock and star diblock copolymer and oligomeric surfactant syntheses of highly ordered, hydrothermally stable, mesoporous silica structures, J. Am. Chem. Soc. 120 (1998) 6024–6036.

[155] S. Wu, Y. Han, Y.C. Zou, J.W. Song, L. Zhao, Y. Di, et al., Synthesis of heteroatom substituted SBA-15 by the "pH-adjusting" method, Chem. Mater. 16 (2004) 486–492. doi:10.1021/cm0343857.

[156] S. van Donk, A.H. Janssen, J.H. Bitter, K.P. de Jong, Generation, characterization, and impact of mesopores in zeolite catalysts, Catal. Rev. 45 (2003) 297–319. doi:10.1081/CR-120023908.

[157] U. Olsbye, S. Svelle, M. Bjrgen, P. Beato, T.V.W. Janssens, F. Joensen, et al., Conversion of methanol to hydrocarbons: How zeolite cavity and pore size controls product selectivity, Angew. Chemie - Int. Ed. 51 (2012) 5810–5831. doi:10.1002/anie.201103657.

[158] J. Kang, K. Cheng, L. Zhang, Q. Zhang, J. Ding, W. Hua, et al., Mesoporous zeolite-supported ruthenium nanoparticles as highly selective Fischer-Tropsch catalysts for the production of C_5-C_{11} isoparaffins, Angew. Chemie - Int. Ed. 50 (2011) 5200–5203. doi:10.1002/anie.201101095.

[159] X. Peng, K. Cheng, J. Kang, B. Gu, X. Yu, Q. Zhang, et al., Impact of hydrogenolysis on the selectivity of the Fischer-Tropsch synthesis: diesel fuel production over mesoporous zeolite-Y-supported cobalt fanoparticles, Angew. Chemie - Int. Ed. 54 (2015) 4553–4556. doi:10.1002/anie.201411708.

[160] J.C. Groen, W. Zhu, S. Brouwer, S.J. Huynink, F. Kapteijn, J.A. Moulijn, et al., Direct demonstration of enhanced diffusion in mesoporous ZSM-5 zeolite obtained via controlled desilication, J. Am. Chem. Soc. 129 (2007) 355–360. doi:10.1021/ja065737o.

[161] D. Verboekend, J. Pérez-Ramírez, Design of hierarchical zeolite catalysts by desilication, Catal. Sci. Technol. 1 (2011) 879–890. doi:10.1039/c1cy00150g.

[162] J.C. Groen, L.A.A. Peffer, J.A. Moulijn, J. Perez-Ramirez, Mechanism of hierarchical porosity development in MFI zeolites by desilication: The role of aluminium as a pore-directing agent, Chem. - A Eur. J. 11 (2005) 4983–4994. doi:10.1002/chem.200500045.

[163] J.C. Groen, T. Bach, U. Ziese, A.M. Paulaime-Van Donk, K.P. De Jong, J.A. Moulijn, et al., Creation of hollow zeolite architectures by controlled desilication of A1-zoned ZSM-5 crystals, J. Am. Chem. Soc. 127 (2005) 10792–10793. doi:10.1021/ja052592x.

[164] X. Zhu, L.L. Lobban, R.G. Mallinson, D.E. Resasco, Tailoring the mesopore structure of HZSM-5 to control product distribution in the conversion of propanal, J. Catal. 271 (2010) 88–98. doi:10.1016/j.jcat.2010.02.004.

[165] Q. Lei, T. Zhao, F. Li, L. Zhang, Y. Wang, Catalytic cracking of large molecules over hierarchical zeolites, Chem. Commun. (Camb). (2006) 1769–1771. doi:10.1039/b600547k.

[166] J.C. Groen, J. a. Moulijn, J. Perez-Ramirez, Desilication: on the controlled generation of mesoporosity in MFI zeolites, J. Mater. Chem. 16 (2006) 2121–2131. doi:10.1039/b517510k.

[167] J.C. Groen, L.A.A. Peffer, J.A. Moulijn, J. Perez-Ramirez, Mesoporosity development in ZSM-5 zeolite upon optimized desilication conditions in alkaline medium, Colloids Surfaces A Physicochem. Eng. Asp. 241 (2004) 53–58. doi:10.1016/j.colsurfa.2004.04.012.

[168] Q. Huo, D.I. Margolese, G.D. Stucky, Surfactant control of phases in thes synthesis of mesoporous silica-nased materials, Chem. Mater. 4756 (1996) 1147–1160. doi:10.1021/cm960137h.

[169] A.A. Romero, M.D. Alba, J. Klinowski, Aluminosilicate mesoporous molecular sieve MCM-48, J. Phys. Chem. B. 102 (1998) 123–128. doi:10.1021/jp971469s.

[170] J.M. Campelo, D.L. Luna, R. Luque, J.M. Marinas, A.A. Romero, J.J. Calvino, et al., Synthesis of acidic Al-MCM-48: influence of the Si/Al ratio, degree of the surfactant hydroxyl exchange, and post-treatment in NHF solution, J. Catal. 230 (2005) 327–338. doi:10.1016/j.jcat.2004.12.004.

[171] P. Van Der Voort, C. Vercaemst, D. Schaubroeck, F. Verpoort, Ordered mesoporous materials at the beginning of the third millennium: new strategies to create hybrid and non-siliceous variants, Phys. Chem. Chem. Phys. 10 (2007) 347–360. doi:10.1039/b707388g.

[172] M.S. Morey, S. O'Brien, S. Schwarz, G.D. Stucky, Hydrothermal and postsynthesis surface modification of cubic, MCM-48, and ultralarge pore SBA-15 mesoporous silica with titanium, Chem. Mater. 12 (2000) 898–911. doi:10.1021/cm9901663.

[173] G. Muthu Kumaran, S. Garg, K. Soni, M. Kumar, J.K. Gupta, L.D. Sharma, et al., Synthesis and characterization of acidic properties of Al-SBA-15 materials with varying Si/Al ratios, Microporous Mesoporous Mater. 114 (2008) 103–109. doi:10.1016/j.micromeso.2007.12.021.

[174] P. Bhange, D.S. Bhange, S. Pradhan, V. Ramaswamy, Direct synthesis of well-ordered mesoporous Al-SBA-15 and its correlation with the catalytic activity, Appl. Catal. A Gen. 400 (2011) 176–184. doi:10.1016/j.apcata.2011.04.031.

[175] Q. Li, Z. Wu, B. Tu, S.S. Park, C.-S. Ha, D. Zhao, Highly hydrothermal stability of

ordered mesoporous aluminosilicates Al-SBA-15 with high Si/Al ratio, Microporous Mesoporous Mater. 135 (2010) 95–104. doi:10.1016/j.micromeso.2010.06.016.

[176] W. Li, S. Huang, S. Liu, M. Coppens, Influence of the Al source and synthesis of ordered Al-SBA-15 hexagonal particles with nanostairs and terraces, Langmuir. 21 (2005) 2078–2085.

[177] Y. Han, S. Wu, Y. Sun, D. Li, F.S. Xiao, J. Liu, et al., Hydrothermally stable ordered hexagonal mesoporous aluminosilicates assembled from a triblock copolymer and preformed aluminosilicate precursors in strongly acidic media, Chem. Mater. 14 (2002) 1144–1148. doi:10.1021/cm010633s.

[178] L.-F. Chen, P.-J. Guo, L.-J. Zhu, M.-H. Qiao, W. Shen, H.-L. Xu, et al., Preparation of Cu/SBA-15 catalysts by different methods for the hydrogenolysis of dimethyl maleate to 1,4-butanediol, Appl. Catal. A Gen. 356 (2009) 129–136. doi:10.1016/j.apcata.2008.12.029.

[179] S. Wang, W. Guo, H. Wang, L. Zhu, S. Yin, K. Qiu, Effect of Cu/SBA-15 catalyst preparation method on methyl acetate hydrogenation for ethanol production, New J. Chem. (2014) 2792–2800. doi:10.1039/c4nj00134f.

[180] T. Sano, Y. Nakajima, Z.B. Wang, Y. Kawakami, K. Soga, A. Iwasaki, Effect of framework aluminum on the dissolution process of ZSM-5 zeolite crystal, Microporous Mater. 12 (1997) 71–77. doi:10.1016/S0927-6513(97)00058-8.

[181] F. Li, L. Wang, X. Han, P. He, Y. Cao, H. Li, Influence of support on the performance of copper catalysts for the effective hydrogenation of ethylene carbonate to synthesize ethylene glycol and methanol, RSC Adv. 6 (2016) 45894–45906. doi:10.1039/C6RA06464G.

[182] S. Brunauer, L.S. Deming, W.E. Deming, E. Teller, On a theory of the van der Waals adsorption of gases, J. Am. Chem. Soc. 62 (1940) 1723–1732. doi:10.1021/ja01864a025.

[183] J. Xu, Z. Luan, M. Hartmann, L. Kevan, Synthesis and characterization of Mn-containing cubic mesoporous MCM-48 and AlMCM-48 molecular sieves, Chem. Mater. (1999) 2928–2936.

[184] X. Du, E. Wu, Porosity of microporous zeolites A, X and ZSM-5 studied by small angle X-ray scattering and nitrogen adsorption, J. Phys. Chem. Solids. 68 (2007) 1692–1699. doi:10.1016/j.jpcs.2007.04.013.

[185] E.P. Barrett, L.G. Joyner, P.P. Halenda, The determination of pore volume and area distributions in porous substances. I. computations from nitrogen isotherms, J. Am. Chem. Soc. 73 (1951) 373–380. doi:10.1021/ja01145a126.

[186] G. Horvath, K. Kawazoe, Method for the calculation of effectiv pore size distribution in molecular sieve carbon, J. Chem. Eng. Japan. 16 (1983) 470–475. doi:10.1252/jcej.16.470.

[187] P.I. Ravikovitch, S.C.O. Domhnaill, A.V. Neimark, F. Schueth, K.K. Unger, Capillary hysteresis in nanopores: theoretical and experimental studies of nitrogen adsorption on MCM-41, Langmuir. 11 (1995) 4765–4772. doi:10.1021/la00012a030.

[188] P.I. Ravikovitch, D. Wei, W.T. Chueh, G.L. Haller, A.V. Neimark, Evaluation of pore structure parameters of MCM-41 catalyst supports and catalysts by means of nitrogen and argon adsorption, J. Phys. Chem. B. 101 (1997) 3671–3679. http://metalib.lib.ic.ac.uk:9003/sfx_local?id=doi:10.1021/jp9625321.

[189] M.W. Maddox, J.P. Olivier, K.E. Gubbins, Characterization of MCM-41 using molecular simulation: heterogeneity effects, Langmuir. 13 (1997) 1737–1745. doi:10.1021/la961068o.

[190] P.I. Ravikovitch, A. V. Neimark, Characterization of micro- and mesoporosity in SBA-15 materials from adsorption data by the NLDFT method, J. Phys. Chem. B. 105 (2001) 6817–6823. doi:10.1021/jp010621u.

[191] T.W. Kim, F. Kleitz, B. Paul, R. Ryoo, MCM-48-like large mesoporous silicas with tailored pore structure: Facile synthesis domain in a ternary triblock copolymer-butanol-water system, J. Am. Chem. Soc. 127 (2005) 7601–7610. doi:10.1021/ja042601m.

[192] M. Luisa Ojeda, J. Marcos Esparza, A. Campero, S. Cordero, I. Kornhauser, F. Rojas, On comparing BJH and NLDFT pore-size distributions determined from N_2 sorption on SBA-15 substrata, Phys. Chem. Chem. Phys. 5 (2003) 1859–1866. doi:10.1039/b300821e.

[193] M. Imperor-Clerc, P. Davidson, A. Davidson, Existence of a microporous corona around the mesopores of silica-based SBA-15 materials templated by triblock copolymers, J. Am. Chem. Soc. 122 (2000) 11925–11933. doi:10.1021/ja002245h.

[194] A. Crosman, W.F. Hoelderich, Enantioselective hydrogenation over immobilized rhodium diphosphine complexes on mesostructured materials, Catal. Today. 121 (2007) 130–139. doi:10.1016/j.cattod.2006.11.023.

[195] G. Kyriakou, C. Theocharis, The anomalous sorptive behaviour of ZSM-5 and Silicalite-I: observation of low pressure hysteresis in nitrogen adsorption, Stud. Surf. Sci. Catal. 144 (2002) 709–716.

[196] O. Collart, P. Cool, P. Van Der Voort, V. Meynen, E.F. Vansant, K. Houthoofd, et al., Aluminum incorporation into MCM-48 toward the creation of bronsted acidity, J. Phys. Chem. B. 108 (2004) 13905–13912. doi:10.1021/jp049837x.

[197] J.M. Campelo, D. Luna, R. Luque, J.M. Marinas, A.A. Romero, J.J. Calvino, et al., Synthesis of acidic Al-MCM-48: Influence of the Si/Al ratio, degree of the surfactant hydroxyl exchange, and post-treatment in NH_4F solution, J. Catal. 230 (2005) 327–338. doi:10.1016/j.jcat.2004.12.004.

[198] T. Klimova, J. Reyes, O. Gutierrez, L. Lizama, Novel bifunctional NiMo/Al-SBA-15 catalysts for deep hydrodesulfurization: Effect of support Si/Al ratio, Appl. Catal. A Gen.

335 (2008) 159–171. doi:10.1016/j.apcata.2007.11.008.

[199] G.A. Eimer, L.B. Pierella, G.A. Monti, O.A. Anunziata, Synthesis and characterization of Al-MCM-41 and Al-MCM-48 mesoporous materials, Catal. Letters. 78 (2002) 65–75. doi:10.1023/A:1014924332500.

[200] Y. Li, D. Pan, C. Yu, Y. Fan, X. Bao, Synthesis and hydrodesulfurization properties of NiW catalyst supported on high-aluminum-content, highly ordered, and hydrothermally stable Al-SBA-15, J. Catal. 286 (2012) 124–136. doi:10.1016/j.jcat.2011.10.023.

[201] D. Kang, J. Zang, E.R. Wright, A.L. Mccanna, C.W. Jones, S. Nair, Dehydration, dehydroxylation, and rehydroxylation of single-walled aluminosilicate nanotubes, ACS Nano. 4 (2015) 4897–4907.

[202] W.P. Zhang, D. Ma, X.W. Han, X.M. Liu, X.H. Bao, X.W. Guo, et al., Methane dehydro-aromatization over Mo/HZSM-5 in the absence of oxygen: A multinuclear solid-state NMR study of the interaction between supported Mo species and HZSM-5 zeolite with different crystal sizes, J. Catal. 188 (1999) 393–402. doi:10.1006/jcat.1999.2670.

[203] Y. Yue, A. Gédéon, J.-L. Bonardet, J.-B. D'Espinose, J. Fraissard, N. Melosh, Direct synthesis of AlSBA mesoporous molecular sieves: characterization and catalytic activities, Chem. Commun. (1999) 1967–1968. doi:10.1039/a904467a.

[204] B.H. Wouters, T.H. Chen, P.J. Grobet, Reversible tetrahedral-octahedral framework aluminum transformation in zeolite Y, J. Am. Chem. Soc. 120 (1998) 11419–11425. doi:10.1021/ja982082l.

[205] H. Kosslick, G. Lischke, B. Parlitz, W. Storek, R. Fricke, Acidity and active sites of Al-MCM-41, Appl. Catal. A Gen. 184 (1999) 49–60. doi:10.1016/S0926-860X(99)00078-2.

[206] A. Sakthivel, S.E. Dapurkar, N.M. Gupta, S.K. Kulshreshtha, P. Selvam, The influence of aluminium sources on the acidic behaviour as well as on the catalytic activity of mesoporous H-AlMCM-41 molecular sieves, Microporous Mesoporous Mater. 65 (2003) 177–187. doi:10.1016/j.micromeso.2003.08.004.

[207] S.K. Badamali, A. Sakthivel, P. Selvam, Tertiary butylation of phenol over mesoporous H–FeMCM-41, Catal. Letters. 65 (2000) 153–157.

[208] P.N. Panahi, A. Niaei, D. Salari, S.M. Mousavi, G. Delahay, Ultrasound-assistant preparation of Cu-SAPO-34 nanocatalyst for selective catalytic reduction of NO by NH_3, J. Environ. Sci. (China). 35 (2015) 135–143. doi:10.1016/j.jes.2015.01.032.

[209] F. Dong, G. Ding, H. Zheng, X. Xiang, L. Chen, Y. Zhu, et al., Highly dispersed Cu nanoparticles as an efficient catalyst for the synthesis of the biofuel 2-methylfuran, Catal. Sci. Technol. 6 (2016) 767–779. doi:10.1039/C5CY00857C.

[210] K. Suzuki, Y. Aoyagi, N. Katada, M. Choi, R. Ryoo, M. Niwa, Acidity and catalytic activity of mesoporous ZSM-5 in comparison with zeolite ZSM-5, Al-MCM-41 and silica-

alumina, Catal. Today. 132 (2008) 38–45. doi:10.1016/j.cattod.2007.12.010.

[211] J. Zhou, Z. Hua, Z. Liu, W. Wu, Y. Zhu, J. Shi, Direct synthetic strategy of mesoporous ZSM-5 zeolites by using conventional block copolymer templates and the improved catalytic properties, ACS Catal. 1 (2011) 287–291. doi:10.1021/cs1000976.

[212] C. Sun, J. Du, J. Liu, Y. Yang, N. Ren, W. Shen, et al., A facile route to synthesize endurable mesopore containing ZSM-5 catalyst for methanol to propylene reaction, Chem. Commun. 46 (2010) 2671–2673. doi:10.1039/b925850g.

[213] Y. Bi, G. Lu, Catalytic CO oxidation over palladium supported NaZSM-5 catalysts, Appl. Catal. B Environ. 41 (2003) 279–286. doi:10.1016/S0926-3373(02)00166-2.

[214] J. Wei, E. Iglesia, Structural requirements and reaction pathways in methane activation and chemical conversion catalyzed by rhodium, J. Catal. 225 (2004) 116–127. doi:10.1016/j.jcat.2003.09.030.

[215] L. Nie, D.E. Resasco, Kinetics and mechanism of m-cresol hydrodeoxygenation on a Pt/SiO$_2$ catalyst, J. Catal. 317 (2014) 22–29. doi:10.1016/j.jcat.2014.05.024.

[216] A. Masalska, Ni-loaded catalyst containing ZSM-5 zeolite for toluene hydrogenation, Appl. Catal. A Gen. 294 (2005) 260–272. doi:10.1016/j.apcata.2005.07.039.

[217] M.Y. Kim, K. Lee, M. Choi, Cooperative effects of secondary mesoporosity and acid site location in Pt/SAPO-11 on n-dodecane hydroisomerization selectivity, J. Catal. 319 (2014) 232–238. doi:10.1016/j.jcat.2014.09.001.

[218] J.A.Z. Pieterse, R.W. Van Den Brink, S. Booneveld, F.A. De Bruijn, Influence of zeolite structure on the activity and durability of Co-Pd-zeolite catalysts in the reduction of NOx with methane, Appl. Catal. B Environ. 46 (2003) 239–250. doi:10.1016/S0926-3373(03)00213-3.

[219] V. Naydenov, L. Tosheva, J. Sterte, Palladium-containing zeolite beta macrostructures prepared by resin macrotemplating, Chem. Mater. 14 (2002) 4881–4885. doi:10.1021/cm0211507.

[220] J. Zhang, J. Tu, D. Zhou, H. Tang, L. Li, X. Wang, et al., Hierarchical SnO$_2$@NiO core/shell nanoflake arrays as energy-saving electrochromic materials, J. Mater. Chem. C. 2 (2014) 10409–10417. doi:10.1039/C4TC02204A.

[221] A.E. Schweizer, G.T. Kerr, Thermal decomposition of hexachloroplatinic acid, Inorg. Chem. 17 (1978) 2326–2327.

[222] M.Y. Smirnova, O. V Kikhtyanin, M.Y. Smirnov, A. V Kalinkin, A.I. Titkov, A.B. Ayupov, et al., Effect of calcination temperature on the properties of Pt/SAPO-31 catalyst in one-stage transformation of sunflower oil to green diesel, Appl. Catal. A Gen. 505 (2015) 524–531. doi:10.1016/j.apcata.2015.06.019.

[223] K. Scholz (nee Böhme), J. Scholz, A. James McQuillan, G. Wagner, O. Klepel, Partially embedded highly dispersed Pt nanoparticles in mesoporous carbon with enhanced leaching stability, Carbon 48 (2010) 1788–1798.

[224] S.R. Kirumakki, B.G. Shpeizer, G.V. Sagar, K.V.R. Chary, A. Clearfield, Hydrogenation of naphthalene over $NiO/SiO_2-Al_2O_3$ catalysts: structure-activity correlation, J. Catal. 242 (2006) 319–331. doi:10.1016/j.jcat.2006.06.014.

[225] G. Poncelet, M.A. Centeno, R. Molina, Characterization of reduced α-alumina-supported nickel catalysts by spectroscopic and chemisorption measurements, Appl. Catal. A Gen. 288 (2005) 232–242. doi:10.1016/j.apcata.2005.04.052.

[226] J. Du, W. Kuang, H. Xu, W. Shen, D. Zhao, The influence of precursors on Rh/SBA-15 catalysts for N_2O decomposition, Appl. Catal. B Environ. 84 (2008) 490–496. doi:10.1016/j.apcatb.2008.05.004.

[227] J.C. Serrano-Ruiz, G.W. Huber, M.A. Sánchez-Castillo, J.A. Dumesic, F. Rodríguez-Reinoso, A. Sepúlveda-Escribano, Effect of Sn addition to $Pt/CeO_2-Al_2O_3$ and Pt/Al_2O_3 catalysts: An XPS, [119]Sn Mossbauer and microcalorimetry study, J. Catal. 241 (2006) 378–388. doi:10.1016/j.jcat.2006.05.005.

[228] R.M. Navarro, M.C. Álvarez-Galván, M.C. Sánchez-Sánchez, F. Rosa, J.L.G. Fierro, Production of hydrogen by oxidative reforming of ethanol over Pt catalysts supported on Al_2O_3 modified with Ce and La, Appl. Catal. B Environ. 55 (2005) 229–241. doi:10.1016/j.apcatb.2004.09.002.

[229] B.A. Riguetto, S. Damyanova, G. Gouliev, C.M.P. Marques, L. Petrov, J.M. Bueno, Surface behavior of alumina-supported Pt catalysts modified with cerium as revealed by X-ray diffraction , X-ray photoelectron spectroscopy, and fourier transform infrared spectroscopy of CO adsorption, J. Phys. Chem. B. 108 (2004) 5349–5358. doi:10.1021/jp031167s.

[230] J.J. Brunet, P. Gallois, P. Caubere, Activation of reducing agents. Sodium hydride containing complex reducing agents. 12. New convenient, highly active, and selective nickel hydrogenation catalysts, J. Org. Chem. 45 (1980) 1937–1945. doi:10.1021/jo01298a036.

[231] V.M. Akhmedov, S.H. Al-Khowaiter, E. Akhmedov, A. Sadikhov, Low temperature hydrocracking of hydrocarbons on Ni-supported catalysts, Appl. Catal. A Gen. 181 (1999) 51–61.

[232] E. Kikuchi, Y. Morita, Hydrogenolysis of n-pentane on nickel catalyst, J. Catal. 15 (1969) 217–223. doi:10.1016/0021.

[233] K.I. Alhumaizi, V.M. Akhmedov, S.M. Al-Zahrani, S.H. Al-Khowaiter, Low temperature hydrocracking of n-heptane over Ni-supported catalysts: Study of global kinetics, Appl. Catal. A Gen. 219 (2001) 131–140. doi:10.1016/S0926-860X(01)00675-5.

[234] A. Lugstein, A. Jentys, H. Vinek, Hydroisomerization and cracking of n-octane and C_8 isomers on Ni-containing zeolites, Appl. Catal. A Gen. 176 (1999) 119–128.

[235] R.A.W. Johnstone, J.Y. Liu, L. Lu, D. Whittaker, Hydrogenation of alkenes over palladium and platinum metals supported on a variety of metal(IV) phosphates, J. Mol. Catal. A Chem. 191 (2003) 289–294. doi:10.1016/S1381-1169(02)00212-1.

[236] D. Teschner, Z. Révay, J. Borsodi, M. Hävecker, A. Knop-Gericke, R. Schlögl, et al., Understanding palladium hydrogenation catalysts: When the nature of the reactive molecule controls the nature of the catalyst active phase, Angew. Chemie - Int. Ed. 47 (2008) 9274–9278. doi:10.1002/anie.200802134.

[237] S.D. Jackson, G.J. Kelly, S.R. Watson, R. Gulickx, Cycloalkene hydrogenation over palladium catalysts, Appl. Catal. A Gen. 187 (1999) 161–168. doi:10.1016/S0926-860X(99)00204-5.

[238] J.P. Boitiaux, J. Cosyns, S. Vasudevan, Hydrogenation of highly unsaturated hydrocarbons over highly dispersed palladium catalyst: Part I: behaviour of small metal particles, Appl. Catal. 6 (1983) 41–51. doi:10.1016/0166.

[239] N. Kumar, R. Byggningsbacka, M. Korpi, L.E. Lindfors, T. Salmi, Synthesis and characterization of Pd-MCM-22 and Pt-SAPO-11 catalysts for transformation of n-butane to aromatic hydrocarbons, Appl. Catal. A Gen. 227 (2002) 97–103. doi:10.1016/S0926-860X(01)00926-7.

[240] H. Chen, H. Yang, Y. Briker, C. Fairbridge, O. Omotoso, L. Ding, et al., Effect of hydrogen spillover on the hydrogenation of 1-hexene over diluted carbon molecular sieve supported Pt catalyst, Catal. Today. 125 (2007) 256–262. doi:10.1016/j.cattod.2007.01.024.

[241] G.C. Bond, J.J. Phillipson, P.B. Wells, J.M. Winterbottom, Hydrogenation of olefins part 1.-hydrogenation of ethylene, propylene and the n-butenes over alumina-supported platinum and iridium, Trans. Faraday Soc. 60 (1964) 1847–1864.

[242] F. Zaera, On the mechanism for the hydrogenation of olefins on transition-metal surfaces: The chemistry of ethylene on Pt(111), Langmuir. 12 (1996) 88–94. doi:10.1021/la9407020.

[243] A. Soualah, J.L. Lemberton, L. Pinard, M. Chater, P. Magnoux, K. Moljord, Hydroisomerization of long-chain n-alkanes on bifunctional Pt/zeolite catalysts: Effect of the zeolite structure on the product selectivity and on the reaction mechanism, Appl. Catal. A Gen. 336 (2008) 23–28. doi:10.1016/j.apcata.2007.09.038.

[244] J.M. Campelo, A.F. Lee, R. Luque, D. Luna, J.M. Marinas, A.A. Romero, Preparation of highly active and dispersed platinum nanoparticles on mesoporous Al-MCM-48 and their activity in the hydroisomerisation of n-octane, Chem. - A Eur. J. 14 (2008) 5988–5995. doi:10.1002/chem.200800182.

Appendix A - Supporting information for Chapter 2
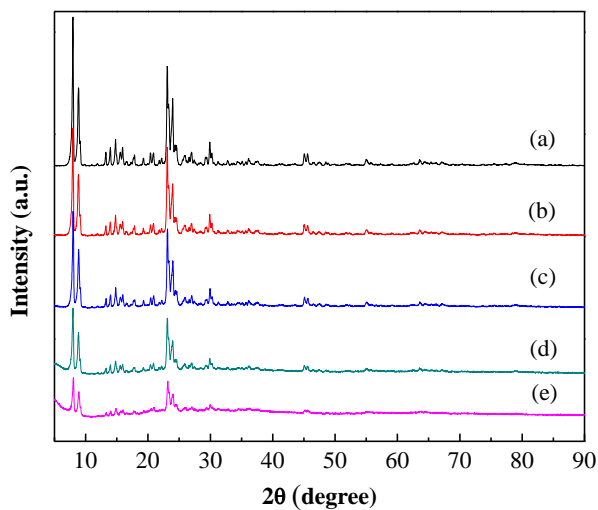
Figure A.1. XRD patterns of the calcined catalysts with different Cu loading on zeolite HZSM-5(280). (a) HZSM-5(280), (b) 6.0%CuO/ZSM-5(280),(c) 9.2%CuO/ZSM-5(280),(d) 19.2% CuO/ZSM-5(280), (e) 29.1%CuO/ZSM-5(280).
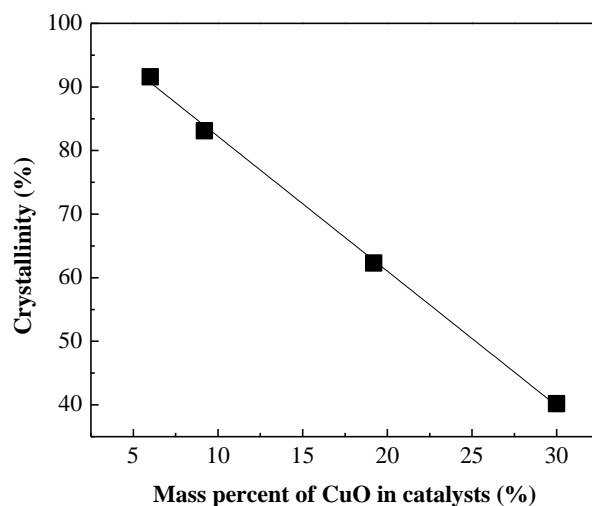
Figure A.2. Relative crystallinity of Cu/ZSM-5 (280) versus mass percent of CuO

Figure A.1 displays the XRD patterns of the calcined catalysts with different copper loadings on zeolite HZSM-5(280). All the characteristic peaks of parent HZSM-5 were observed in Cu/ZSM-5 catalysts. However, a slight decrease in the intensity of main peaks was noticed after introduction of copper compared to the parent HZSM-5, which indicates Cu species enter the channels of HZSM-5 zeolite. In addition, no CuO (35.7º and 38.55º) or Cu_2O (36.4º, 42.3º and 61.3º) peaks were observed, which indicates that copper was highly dispersed in zeolite channel. The relative crystallinity of Cu/ZSM-5 can be calculated based on the intensity of the peaks of angle 2θ=22-25º in XRD pattern and the parent HZSM-5 was assumed to be 100% crystalline. From **Figure A.2** we can see, with increasing addition of Cu, the relative crystallinity of catalysts decreased linearly, which dropped from 93% to 40% when the content of CuO increased from 6.0% to 29.1%.
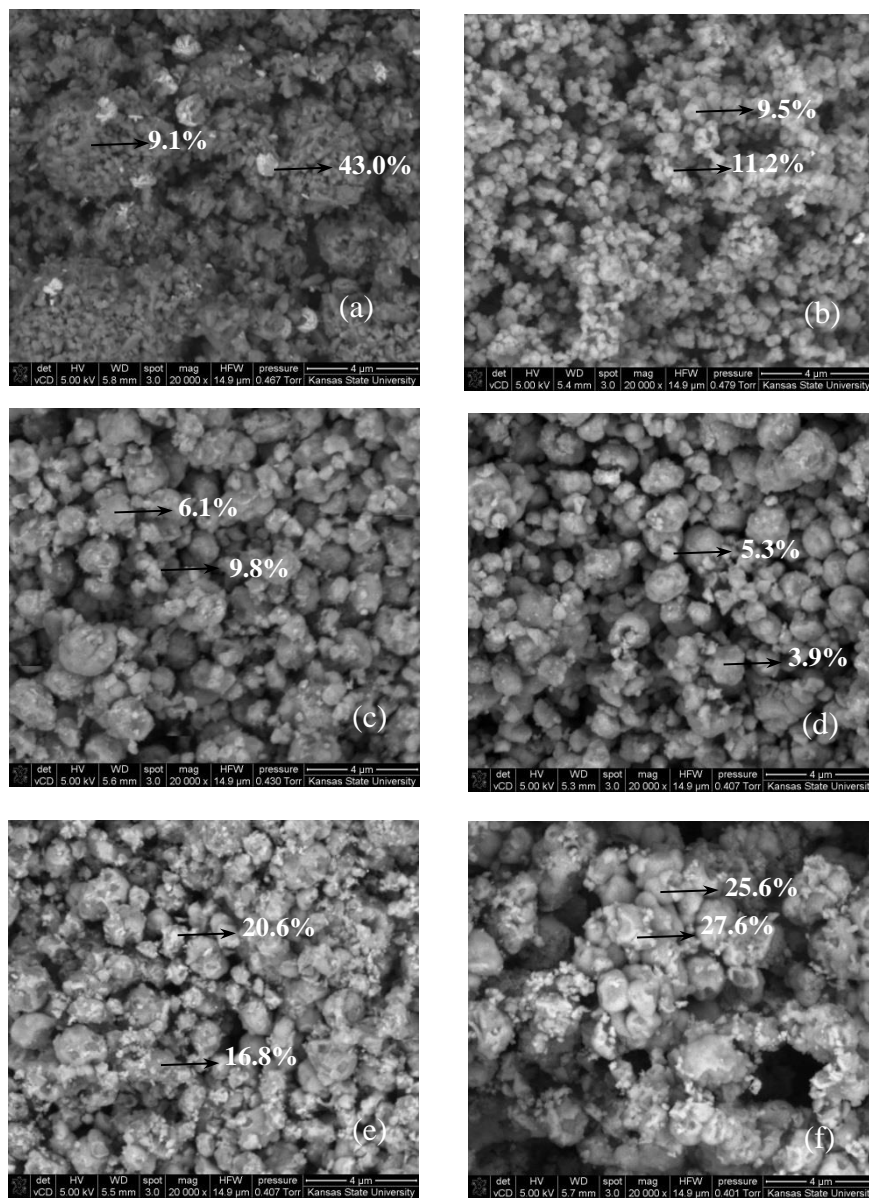
Figure A.3. SEM images of CuO/ZSM-5 catalysts. (a) 9.5%CuO/ZSM-5(23), (b) 9.7%CuO/ZSM-5(50), (c) 9.2%CuO/ZSM-5(280), (d) 6.0%CuO/ZSM-5(280), (e) 19.2%CuO/ZSM-5(280), (f) 29.1%CuO/ZSM-5(280).

The morphology of catalysts was characterized using scanning electron microscopy (SEM, see **Figure A.3**). The data on **Figure A.3** are the contents of CuO obtained from EDS detector. The SEM images indicated the copper species were well distributed on zeolites by the ion-exchange method in the copper-ammonia complex solution, except for 9.5%CuO/ZSM-5(23)

(**Figure A.3a**). As seen in this figure, some big bright copper clusters were observed on the surface with the size of 0.5 µm-1.0µm, and the weight percent of CuO in these clusters was estimated at ~ 43% obtained by EDS detector, which is consistent with the XRD results and the reduction peak at high temperature observed in TPR that indicated the presence of CuO. The color of seven other copper catalysts prepared on HZSM-5(23) (not shown in this paper) by the same method are as black as 9.5%CuO/ZSM-5(23), which is probably due the reaction of copper ammonia complex with the acid sites (the acidity is 1.167 mmol NH_3/g_{cat}) leading to the precipitation of CuO on the surface. However, the color of all catalysts prepared on zeolites HZSM-5(50) and HZSM-5(280) are green. It should be noted that the percent of copper in the bright spots are only marginally higher than the dark spots in SEM images for HZSM-5(50) and HZSM-5(280) (**Figure A.3b-S3f**).
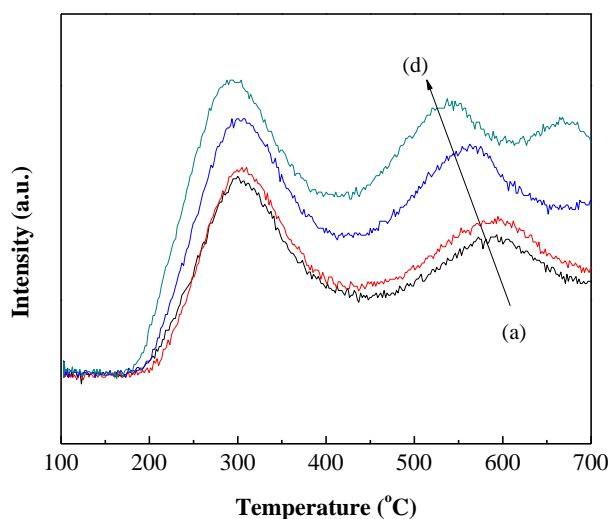
Figure A.4. NH_3-TPD profiles of reduced Cu/ZSM-5(280) catalysts with different CuO loadings (a) 6.0%, (b) 9.2%, (c) 19.2%, (d) 29.1%.

Figure A.4 displays the NH_3-TPD profiles of reduced Cu/ZSM-5(280) catalysts with various CuO loadings. As is shown, the temperatures of NH_3 desorption peaks of 6.0%CuO/ZSM-5(280) and 9.2%CuO/ZSM-5(280) remained unchanged. However, the high temperature peak exhibited a slight shift from 600 to 550 ℃ when the content of CuO was increased from 9.2% to 29.1%. An additional peak at 680 ℃ was observed on the profile of high

copper loading catalyst 29.1%CuO/ZSM-5(280). The reason is still unclear, but part of it is probably due to the formation of N_2, which is from oxidization of NH_3 over unreduced Cu^{2+} species or from the strong acid sites of catalysts caused by high loading of CuO.
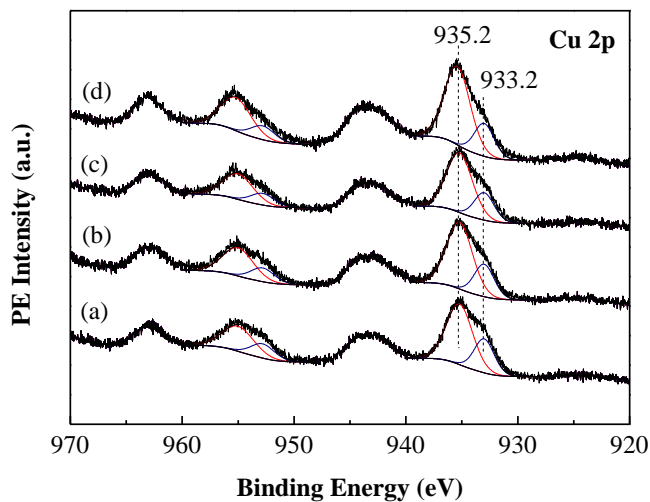
Figure A.5. XPS spectra of the calcined Cu/ZSM-5(280) with various Cu loadings. (a) 6.0%, (b) 9.2%, (c) 19.2%, (d) 29.1%. Spectra were curve fitted by the software CasaXPS.
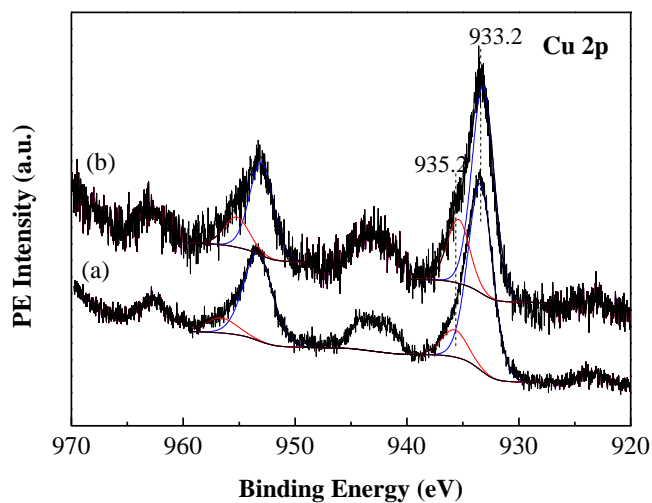
Figure A.6. XPS spectra of (a) catalyst 18.6% CuO/ZSM-5(23). (b) 9.5%CuO/ZSM-5(23). Spectra were curve fitted by the software CasaXPS.
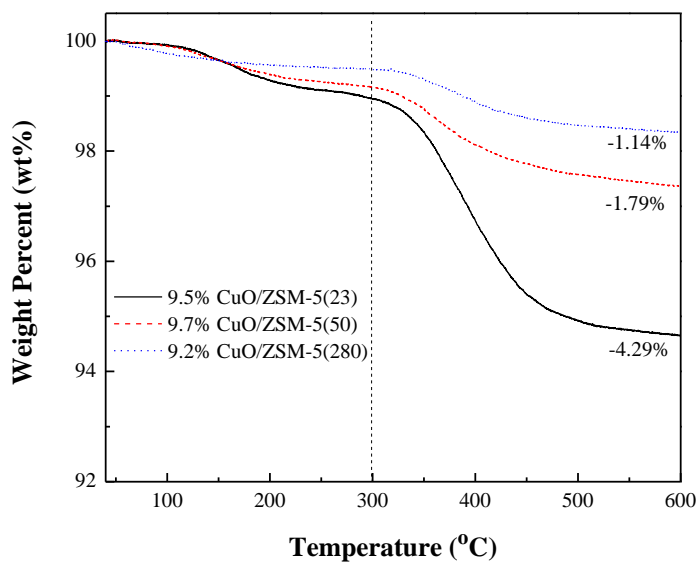
Figure A.7. Thermogravimetric profile of catalysts after 40 min of reaction. Reaction conditions: feed rate of 2,3-butanediol, 3.0 mL/hour; catalyst weight, 1.0 g; H$_2$/2,3-butanediol (molar ratio), 5:1; temperature: 250 ºC.
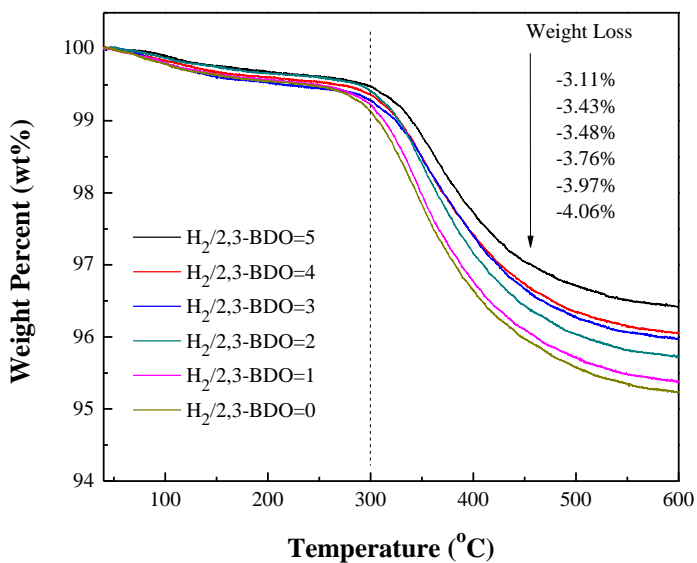
Figure A.8. Thermogravimetric profile of catalyst 19.2wt%CuO/ZSM-5(280) after 280 min of reaction at different hydrogen to 2,3-BDO ratios. Reaction conditions: feed rate of 2,3-butanediol, 3.0 mL/hour; catalyst weight, 1.0 g; temperature: 250 ºC.
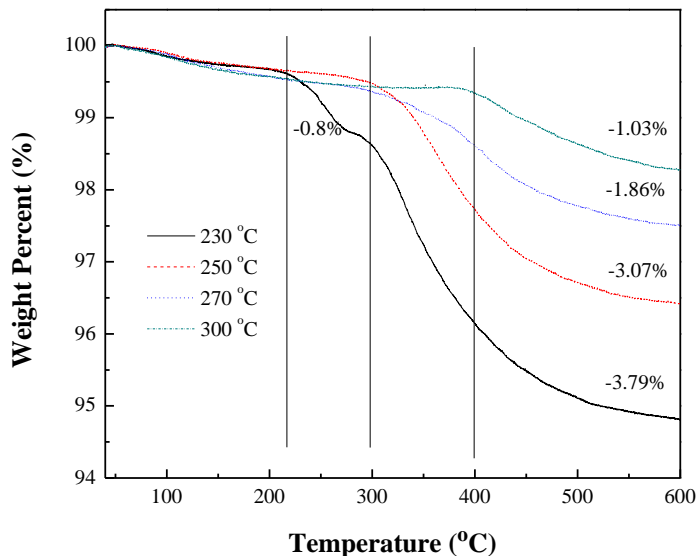
Figure A.9. Thermogravimetric profile of catalyst 19.2wt%CuO/ZSM-5(280) after 310 min of reaction at different temperature. Reaction conditions: feed rate of 2,3-butanediol, 3.0 mL/hour; catalyst weight, 1.0 g; H_2/2,3-butanediol (molar ratio), 5:1.
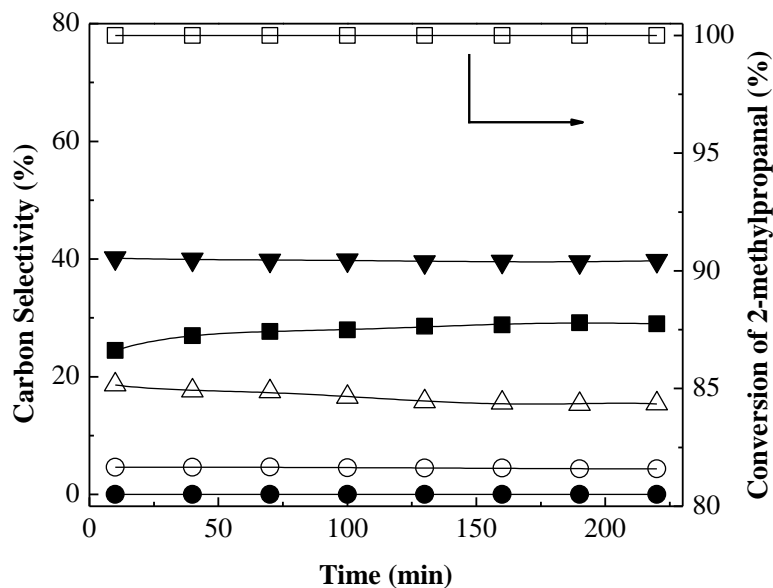
Figure A.10. Catalytic results for the conversion of 2-methylpropanal over reduced catalyst 19.2%CuO/ZSM-5(280) with time on stream. Selectivity to products: (■)butene, (○)propylene, (△)pentene, (▼)$C_6^=-C_8^=$, (●)2-methyl-1-propanol, (□)conversion of 2-methylpropanal. Reaction conditions: feed rate of 2-methylpropanal, 3.0 mL/hour; catalyst weight, 1.0 g; H_2/2-methylpropanal (molar ratio)=5.

Table A.1. H$_2$ consumption summarized from TPR.

sample	H$_2$ uptake (mmol/g$_{cat}$)[a]	H$_2$/Cu (mol/mol)
9.5%CuO/ZSM-5(23)	1.373	1.15
9.7%CuO/ZSM-5(50)	1.459	1.196
6.0%CuO/ZSM-5(280)	0.874	1.158
9.2%CuO/ZSM-5(280)	1.255	1.085
19.2%CuO/ZSM-5(280)	2.478	1.027
29.1%CuO/ZSM-5(280)	4.225	1.155

[a] H$_2$ consumption was calibrated by 0.03g of pure CuO and Cu$_2$O.

Table A.2. Conversion of 2,3-butanediol (%) and carbon selectivity of the products (%) on reduced catalysts CuO/ZSM-5(280) with different CuO loadings in 40 min and 310 min (shown in parentheses)[a].

	CuO content			
	6.0%	9.2%	19.2%	29.1%
ethylene (C_2H_4)	0.22 (0.16)	0.21 (0.14)	0.15 (0.10)	0.16 (0.09)
propylene (C_3H_6)	2.80 (0.75)	1.90 (0.72)	1.07 (0.55)	1.19 (0.52)
isobutane and butane (C_4H_{10})	0.17 (0.07)	0.18 (0.10)	0.14 (0.08)	0.20 (0.09)
butenes (C_4H_8)	50.80 (56.52)	58.65 (62.30)	68.38 (65.97)	61.36 (53.27)
C_5 olefins (C_5H_{10})	6.55 (0.98)	3.74 (0.71)	1.80 (0.48)	1.58 (0.50)
C_6 olefins (C_6H_{12})	3.53 (0.62)	2.10 (0.11)	0.80 (0.07)	0.60 (0.07)
C_7 olefins (C_7H_{14})	0.84 (0.19)	0.38 (0.18)	0.30 (0.01)	0.24 (0.12)
C_8 olefins (C_8H_{16})	1.22 (0.51)	1.24 (0.67)	0.88 (0.52)	1.20 (0.60)
MEK (C_4H_8O)	20.01 (30.17)	19.06 (24.58)	17.16 (22.37)	17.26 (18.28)
2-methylpropanal (C_4H_8O)	0 (0.20)	0 (0.24)	0 (0.30)	0.54 (2.46)
2-methyl-1-propanol ($C_4H_{10}O$)	0 (0.49)	0 (0.63)	0 (0.83)	2.11 (8.29)
2,3-butanedione ($C_4H_6O_2$)	0.43 (0.05)	0.14 (0.01)	0.05 (0.01)	0.05 (0.04)
3-hydroxy-2-butanone ($C_4H_8O_2$)	0.40 (0)	0.22 (0)	0.04 (0)	0.10 (1.14)
2-butanol ($C_4H_{10}O$)	0.87 (0.52)	0.57 (0.22)	0.34 (0.22)	0.28 (0.68)
2-ethyl-2,4,5-trimethyl-1,3-dioxolane ($C_8H_{16}O_2$)	0.22 (0)	0.15 (0)	0 (0)	0.05 (0.12)
ethylbenzene (C_8H_{10})	0.55 (0.53)	0.55 (0.59)	0.38 (0.57)	0.63 (0.79)
p-xylene (C_8H_{10})	0.88 (0.39)	0.72 (0.42)	0.33 (0.38)	0.72 (0.60)
tetramethylfuran ($C_8H_{12}O$)	0.72 (3.08)	0.98 (3.69)	0.92 (3.84)	3.06 (6.36)
1-ethyl-3-methyl-benzene (C_9H_{12})	0.20 (0.09)	0.19 (0.07)	0.12 (0.04)	0 (0)
1,3,5-trimethyl-benzene (C_9H_{12})	0.21 (0.10)	0.19 (0.08)	0.16 (0.06)	0.17 (0.07)
conversion of 2,3-butanediol	100 (99.68)	100 (99.69)	100 (99.80)	100 (99.45)

[a] Reaction conditions: feed rate of 2,3-butanediol, 3.0 mL/hour; catalyst weight, 1.0 g; H_2/2,3-butanediol (mol ratio),5:1; temperature, 250 ºC.

Table A.3. Conversion of 2,3-butanediol (%) and carbon selectivity of the products (%) on 19.2%CuO/ZSM-5(280) at different hydrogen to 2,3-butanediol ratios in 40 min and 280 min (shown in parentheses)[a].

	H$_2$/2,3-BDO molar ratio					
	0	1	2	3	4	5
ethylene (C$_2$H$_4$)	0.03 (0)	0 (0)	0.12 (0.03)	0.19 (0.08)	0.19 (0.08)	0.15 (0.10)
propylene (C$_3$H$_6$)	0.12 (0.04)	0.31 (0.06)	0.59 (0.20)	1.05 (0.46)	1.17 (0.47)	1.07 (0.55)
isobutane and butane (C$_4$H$_{10}$)	0 (0)	0 (0)	0.07 (0.05)	0.12 (0.07)	0.15 (0.07)	0.14 (0.08)
butenes (C$_4$H$_8$)	6.91 (2.50)	25.34 (5.53)	40.04 (20.61)	51.54 (40.48)	55.21 (43.02)	68.38 (66.47)
C$_5$ olefins (C$_5$H$_{10}$)	0.09 (0)	0.25 (0.05)	0.68 (0.18)	1.55 (0.45)	1.75 (0.45)	1.80 (0.49)
C$_6$ olefins (C$_6$H$_{12}$)	0.07 (0)	0 (0)	0.10 (0.06)	0.43 (0.04)	0.56 (0.05)	0.80 (0.07)
C$_7$ olefins (C$_7$H$_{14}$)	0 (0)	0 (0.05)	0.24 (0.06)	0.42 (0.19)	0.35 (0.16)	0.30 (0.01)
C$_8$ olefins (C$_8$H$_{16}$)	0.58 (0.29)	0 (0)	1.23 (0.48)	0.22 (0)	1.14 (0.42)	0.88 (0.54)
MEK (C$_4$H$_8$O)	28.22 (19.30)	27.78 (21.55)	33.68 (29.26)	28.24 (25.50)	24.86 (26.20)	17.16 (22.01)
2-methylpropanal (C$_4$H$_8$O)	13.15 (8.69)	10.12 (10.35)	4.16 (7.91)	1.00 (5.01)	0.55 (3.45)	0 (0.26)
2-methyl-1-propanol (C$_4$H$_{10}$O)	2.83 (2.62)	5.01 (6.85)	3.18 (8.34)	1.43 (7.23)	1.28 (7.35)	0 (0.73)
2,3-butanedione (C$_4$H$_6$O$_2$)	10.69 (14.02)	2.65 (7.30)	0.16 (1.99)	0.06 (0.24)	0.08 (0.14)	0.05 (0.01)
3-hydroxy-2-butanone (C$_4$H$_8$O$_2$)	25.71 (43.45)	12.22 (32.16)	2.47 (18.10)	0.50 (5.23)	0.05 (3.87)	0.04 (0)
2-butanol (C$_4$H$_{10}$O)	0 (0.43)	0.42 (0.83)	0 (0.74)	0.48 (0.67)	0.43 (0.66)	0.34 (0.19)
2-ethyl-2,4,5-trimethyl-1,3-dioxolane (C$_8$H$_{16}$O$_2$)	0 (0)	0.99 (0)	0.06 (1.03)	0.04 (0.56)	0.02 (0.36)	0 (0)
ethylbenzene (C$_8$H$_{10}$)	0.43 (0.36)	0 (0.63)	0.94 (0.84)	0.84 (0.94)	0.69 (0.88)	0.38 (0.56)
p-xylene (C$_8$H$_{10}$)	0.92 (0.78)	0.76 (1.63)	0.96 (0.36)	0.84 (0.57)	0.75 (0.67)	0.33 (0.37)
tetramethylfuran (C$_8$H$_{12}$O)	3.94 (3.55)	7.56 (7.51)	4.36 (5.94)	3.00 (6.66)	2.77 (6.44)	0.92 (3.89)
1-ethyl-3-methyl-benzene (C$_9$H$_{12}$)	0.08 (0.11)	0.14 (0.20)	0.13 (0.06)	0.16 (0.03)	0.13 (0.03)	0.12 (0.04)
1,3,5-trimethyl-benzene (C$_9$H$_{12}$)	0.18 (0.47)	0.23 (0.79)	0.29 (0.13)	0.12 (0.19)	0 (0.15)	0.16 (0.06)
conversion of 2,3-butanediol	99.17 (97.92)	99.11(95.76)	99.55 (98.10)	100 (99.11)	100 (99.47)	100 (99.80)

[a]Reaction conditions: feed rate of 2,3-butanediol, 3.0 mL/hour; catalyst: 19.2wt%CuO/ZSM-5(280); catalyst weight, 1.0 g; temperature: 250 ºC.

Table A.4. Conversion of 2,3-butanediol (%) and carbon selectivity of the products (%) on reduced 19.2%CuO/ZSM-5(280) at different temperatures in 40 min and 310 min (shown in parentheses)[a].

	Temperature (ºC)			
	230	250	270	300
ethylene (C_2H_4)	0.08 (0)	0.15 (0.10)	0.23 (0.28)	0.41 (0.50)
propylene (C_3H_6)	0.55 (0.06)	1.07 (0.55)	5.99 (3.54)	8.60 (5.57)
isobutane and butane (C_4H_{10})	0.09 (0.03)	0.14 (0.08)	0.47 (0.27)	1.35 (0.18)
butenes (C_4H_8)	52.98 (12.16)	68.38 (65.97)	43.58 (62.08)	31.76 (41.78)
C_5 olefins (C_5H_{10})	0.54 (0.04)	1.80 (0.48)	15.38 (5.90)	21.71 (9.48)
C_6 olefins (C_6H_{12})	0.34 (0)	0.80 (0.07)	7.99 (2.85)	9.14 (3.10)
C_7 olefins (C_7H_{14})	0.14 (0.11)	0.30 (0.01)	1.67 (0.61)	2.11 (0.62)
C_8 olefins (C_8H_{16})	0.60 (0.20)	0.88 (0.52)	3.52 (1.36)	2.61 (1.56)
MEK (C_4H_8O)	30.97 (31.16)	17.16 (22.37)	3.38 (9.83)	1.80 (25.71)
2-methylpropanal (C_4H_8O)	0.82 (3.31)	0 (0.30)	0 (0)	0 (0.53)
2-methyl-1-propanol ($C_4H_{10}O$)	3.03 (11.20)	0 (0.83)	0 (0)	0 (0)
2,3-butanedione ($C_4H_6O_2$)	0 (0.26)	0.05 (0.01)	1.46 (0.27)	2.17 (0.52)
3-hydroxy-2-butanone ($C_4H_8O_2$)	0 (16.97)	0.04 (0)	1.10 (0.39)	1.21 (0.93)
2-butanol ($C_4H_{10}O$)	0.45 (2.82)	0.34 (0.22)	1.31 (0.36)	1.36 (0.88)
2-ethyl-2,4,5-trimethyl-1,3-dioxolane ($C_8H_{16}O_2$)	0 (2.48)	0 (0)	0.52 (0)	0.41 (0)
ethylbenzene (C_8H_{10})	0.43 (1.72)	0.38 (0.57)	0.56 (0.43)	0.78 (1.03)
p-xylene (C_8H_{10})	0.53 (0.44)	0.33 (0.38)	1.22 (0.61)	2.25 (1.51)
tetramethylfuran ($C_8H_{12}O$)	4.39 (10.70)	0.92 (3.84)	0.38 (0.64)	0.29 (0.57)
1-ethyl-3-methyl-benzene (C_9H_{12})	0.03 (1.48)	0.12 (0.04)	0.26 (0.26)	0.92 (0.72)
1,3,5-trimethyl-benzene (C_9H_{12})	0.08 (0.09)	0.16 (0.06)	0.25 (0.22)	0.41 (0.47)
conversion of 2,3-butanediol	100 (93.11)	100 (99.80)	100 (99.11)	100 (99.07)

[a]Reaction conditions: feed rate of 2,3-butanediol, 3.0 mL/hour; catalyst: 19.2wt%CuO/ZSM-5(280); catalyst weight, 1.0 g; H_2/2,3-BDO (molar ratio)=5.

Appendix B - Supporting information for Chapter 3
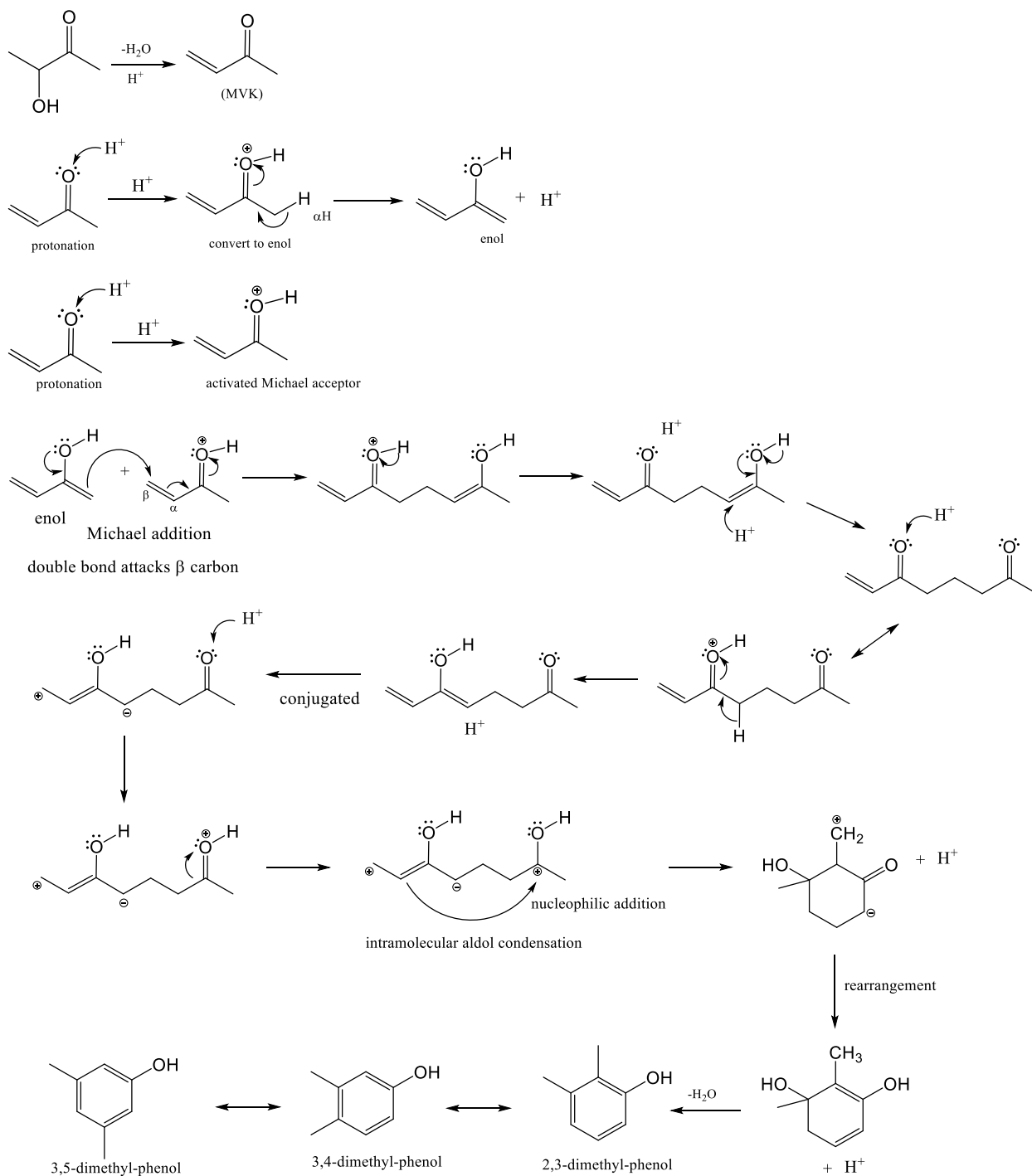
Figure B.1. The Robinson annulation mechanism for the formation of dimethyl-phenol (from MVK).
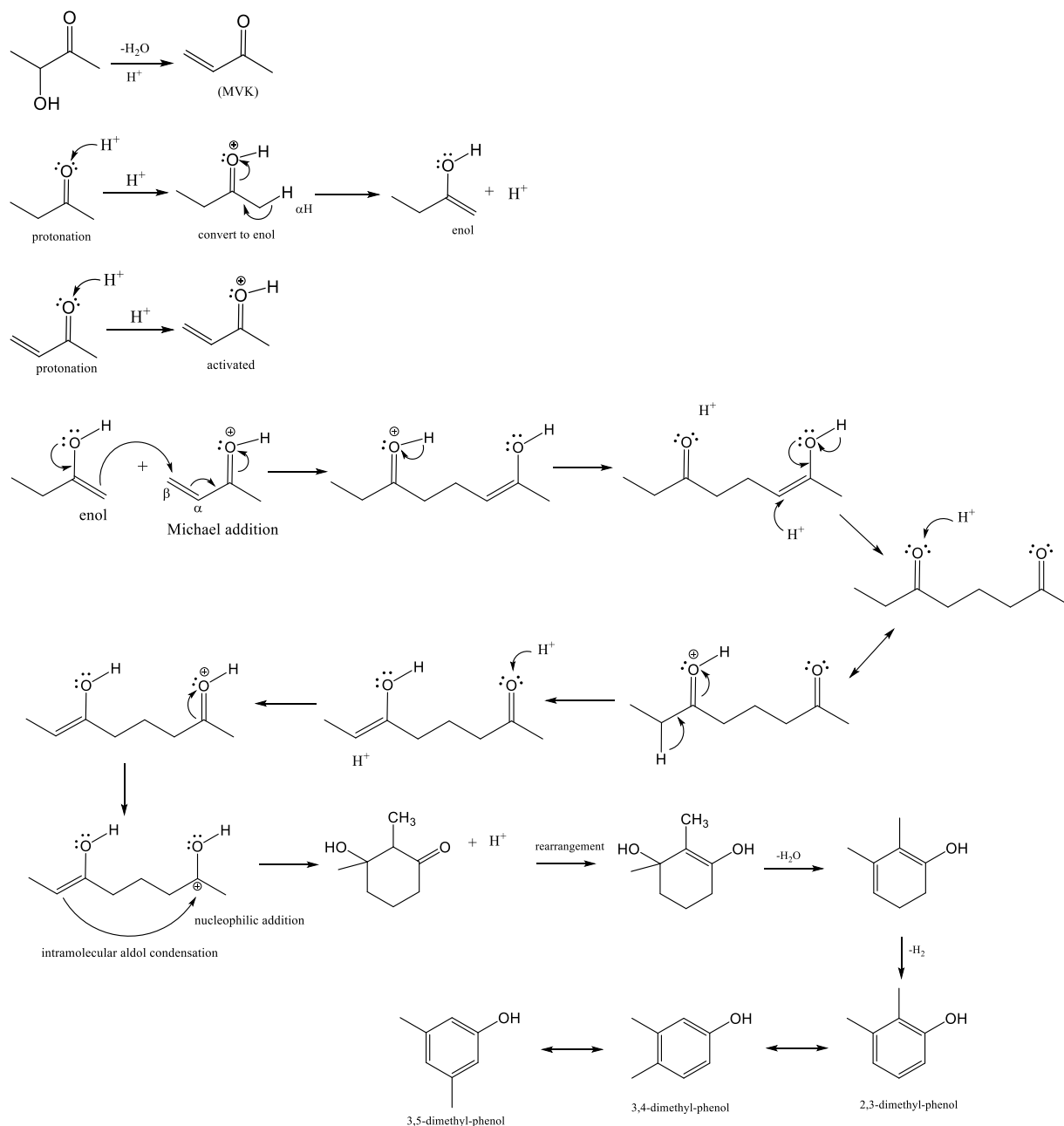
Figure B.2. The Robinson annulation mechanism for the formation of dimethyl-phenol (from MEK).

In the Robinson annulation reaction, the carbonyl compound (MVK or MEK) is protonated by acid (H$^+$) to form an enol, which then attacks the β carbon of an α,β-unsaturated ketone (MVK) to form the keto alcohol, which is then followed by the intramolecular aldol condensation and dehydration (dehydrogenation) to produce the dimethylphenol.

Appendix C - Kinetic model

We assumed all surface reactions are rate-limiting and we treated each step as an elementary reaction.

Reaction 1: $\quad$ BDO(g) $\underset{k_{-1}}{\overset{k_1}{\rightleftharpoons}}$ acetoin(g) + H_2(g) $\qquad$ on Cu Sites

Adsorption: $\quad$ BDO(g) + * $\underset{k_{-1A}}{\overset{k_{1A}}{\rightleftharpoons}}$ BDO*
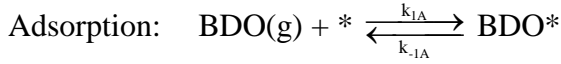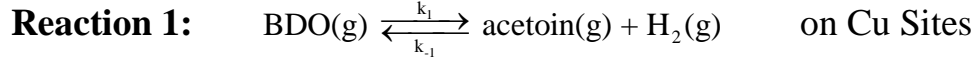
$$r_{1A} = k_{1A}\left(P_{BDO}C_V - \frac{C_{BDO*}}{K_{1A}}\right), \; K_{1A} = \frac{k_{1A}}{k_{-1A}}, \; P_{BDO}C_V = \frac{C_{BDO*}}{K_{1A}}, \; C_{BDO*} = K_{1A}P_{BDO}C_V$$
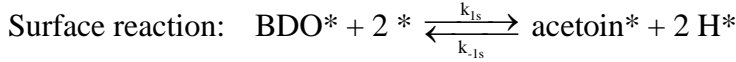
Surface reaction: $\quad$ BDO* + 2 * $\underset{k_{-1s}}{\overset{k_{1s}}{\rightleftharpoons}}$ acetoin* + 2 H*

$$r_{1s} = k_{1s}\left(C_{BDO*}C_V^2 - \frac{C_{acetoin*}C_{H*}^2}{K_{1s}}\right), \; K_{1s} = \frac{k_{1s}}{k_{-1s}},$$

Desorption of H_2: $\quad$ 2 H* $\underset{k_{-1H}}{\overset{k_{1H}}{\rightleftharpoons}}$ H_2(g) + 2 *

$$r_{1H} = k_{1H}\left(C_{H*}^2 - \frac{P_{H2}C_V^2}{K_{1H}}\right), \; K_{1H} = \frac{k_{1H}}{k_{-1H}}, \; C_{H*}^2 = \frac{P_{H2}C_V^2}{K_{1H}}, \; C_{H*} = \sqrt{\frac{P_{H2}}{K_{1H}}}C_V$$

Desorption of acetoin: $\quad$ acetoin* $\underset{k_{-1D}}{\overset{k_{1D}}{\rightleftharpoons}}$ acetoin(g) + *
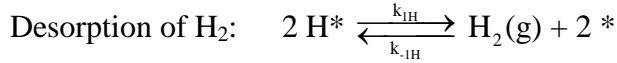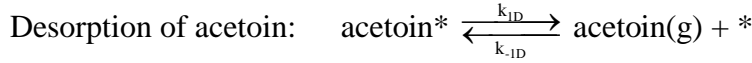
$$r_{1D} = k_{1D}\left(C_{acetoin*} - \frac{P_{acetoin}C_V}{K_{1D}}\right), \; K_{1D} = \frac{k_{1D}}{k_{-1D}}, \; C_{acetoin*} = \frac{P_{acetoin}C_V}{K_{1D}}$$

$$r_{1s} = k_{1s}\left(C_{BDO*}C_V^2 - \frac{C_{acetoin*}C_{H*}^2}{K_{1s}}\right) = k_{1s}\left(K_{1A}P_{BDO}C_VC_V^2 - \frac{\dfrac{P_{acetoin}C_V}{K_{1D}}\dfrac{P_{H2}C_V^2}{K_{1H}}}{K_{1s}}\right)$$

$$= k_{1s}\left(K_{1A}P_{BDO} - \frac{P_{acetoin}P_{H2}}{K_{1D}K_{1H}K_{1s}}\right)C_V^3$$

$$C_t = C_V + C_{H*} + C_{BDO*} + C_{acetoin*} + \cdots$$

$$C_t = C_V + \sqrt{\frac{P_{H2}}{K_{1H}}}C_V + K_{1A}P_{BDO}C_V + \frac{P_{acetoin}C_V}{K_{1D}} + \cdots$$

$$C_V = \frac{C_t}{1 + \sqrt{\dfrac{P_{H2}}{K_{1H}}} + K_{1A}P_{BDO} + \dfrac{P_{acetoin}}{K_{1D}} + \cdots}$$

$$C_V = \frac{C_t(Cu)}{1 + \sqrt{\dfrac{P_{H2}}{K_{1H}}} + K_{1A}P_{BDO} + \dfrac{P_{acetoin}}{K_{1D}} + \dfrac{P_{2,3\text{-butanedione}}}{K_{2D}} + \dfrac{P_{2\text{-butanol}}}{K_{5D}} + \dfrac{P_{MEK}}{K_{3D}} + \dfrac{P_{2\text{-methylpropanal}}}{K_{4D}} + \dfrac{P_{isobutanol}}{K_{6D}}}$$

$$r_{1s} = k_{1s}\left(K_{1A}P_{BDO} - \frac{P_{acetoin}P_{H2}}{K_{1D}K_{1H}K_{1s}}\right)C_V^3 = k_{1s}\left(K_{1A}P_{BDO} - \frac{P_{acetoin}P_{H2}}{K_{1D}K_{1H}K_{1s}}\right)\left(\frac{C_t}{1 + \sqrt{\dfrac{P_{H2}}{K_{1H}}} + K_{1A}P_{BDO} + \dfrac{P_{acetoin}}{K_{1D}} + \cdots}\right)^3$$

$$= \frac{k_{1s}K_{1A}C_t^3\left(P_{BDO} - \dfrac{P_{acetoin}P_{H2}}{K_{1D}K_{1H}K_{1s}K_{1A}}\right)}{\left(1 + \sqrt{\dfrac{P_{H2}}{K_{1H}}} + K_{1A}P_{BDO} + \dfrac{P_{acetoin}}{K_{1D}} + \cdots\right)^3} = \frac{k_1\left(P_{BDO} - \dfrac{P_{acetoin}P_{H2}}{K_{1P}}\right)}{\left(1 + \sqrt{\dfrac{P_{H2}}{K_{1H}}} + K_{1A}P_{BDO} + \dfrac{P_{acetoin}}{K_{1D}} + \cdots\right)^3}$$

$$k_1 = k_{1s}K_{1A}C_t^3, \quad K_{1P} = K_{1D}K_{1H}K_{1s}K_{1A}$$

Reaction 2: acetoin(g) $\underset{k_{-2}}{\overset{k_2}{\rightleftharpoons}}$ 2,3-butanedione(g)+H$_2$(g) $\qquad$ on Cu sites

Adsorption: acetoin(g) + * $\underset{k_{-2A}}{\overset{k_{2A}}{\rightleftharpoons}}$ acetoin*
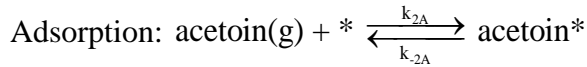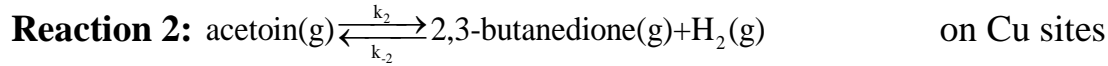
$$r_{2A} = k_{2A}\left(P_{acetoin}C_V - \frac{C_{acetoin*}}{K_{2A}}\right), \quad K_{2A} = \frac{1}{K_{1D}}, \quad C_{acetoin*} = K_{2A}P_{acetoin}C_V$$

Surface reaction: acetoin* + 2 * $\underset{k_{-2s}}{\overset{k_{2s}}{\rightleftharpoons}}$ 2,3-butanedione* + 2 H*

$$r_{2s} = k_{2s}\left(C_{acetoin*}C_V^2 - \frac{C_{2,3\text{-butanedione*}}C_{H*}^2}{K_{2s}}\right)$$

Desorption of 2,3-butanedione: 2,3-butanedione* $\underset{k_{-2D}}{\overset{k_{2D}}{\rightleftharpoons}}$ 2,3-butanedione(g) + *
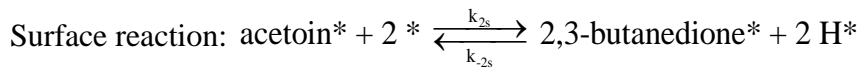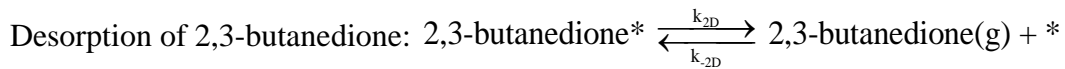
$$r_{2D} = k_{2D}\left(C_{2,3\text{-butanedione*}} - \frac{P_{2,3\text{-butanedione}}C_V}{K_{2D}}\right), \quad C_{2,3\text{-butanedione*}} = \frac{P_{2,3\text{-butanedione}}C_V}{K_{2D}}$$

Desorption of H_2: $2\,H^* \underset{k_{-1H}}{\overset{k_{1H}}{\rightleftharpoons}} H_2(g) + 2\,^*$

$$r_{1H} = k_{1H}\left(C_{H^*}^2 - \frac{P_{H2}C_V^2}{K_{1H}}\right),\ \ K_{1H} = \frac{k_{1H}}{k_{-1H}},\ C_{H^*}^2 = \frac{P_{H2}C_V^2}{K_{1H}},\ C_{H^*} = \sqrt{\frac{P_{H2}}{K_{1H}}}C_V$$

$$r_{2s} = k_{2s}\left(C_{acetoin^*}C_V^2 - \frac{C_{2,3\text{-butanedione}^*}C_{H^*}^2}{K_{2s}}\right) = k_{2s}\left(K_{2A}P_{acetoin}C_V^3 - \frac{\dfrac{P_{2,3\text{-butanedione}}C_V}{K_{2D}}\dfrac{P_{H2}C_V^2}{K_{1H}}}{K_{2s}}\right)$$

$$= k_{2s}K_{2A}\left(P_{acetoin} - \frac{P_{2,3\text{-butanedione}}P_{H2}}{K_{2D}K_{1H}K_{2s}K_{2A}}\right)C_V^3$$

$$C_t = C_V + C_{H^*} + C_{2,3\text{-butanedione}^*} + C_{acetoin^*} + \cdots$$

$$C_t = C_V + \sqrt{\frac{P_{H2}}{K_{1H}}}C_V + \frac{P_{2,3\text{-butanedione}}C_V}{K_{2D}} + K_{2A}P_{acetoin}C_V + \cdots$$

$$C_V = \frac{C_t}{1 + \sqrt{\dfrac{P_{H2}}{K_{1H}}} + \dfrac{P_{2,3\text{-butanedione}}}{K_{2D}} + K_{2A}P_{acetoin} + \cdots}$$

$$r_{2s} = k_{2s}K_{2A}\left(P_{acetoin} - \frac{P_{2,3\text{-butanedione}}P_{H2}}{K_{2D}K_{1H}K_{2s}K_{2A}}\right)C_V^3$$

$$= k_{2s}K_{2A}\left(P_{acetoin} - \frac{P_{2,3\text{-butanedione}}P_{H2}}{K_{2D}K_{1H}K_{2s}K_{2A}}\right)\left(\frac{C_t}{1 + \sqrt{\frac{P_{H2}}{K_{1H}}} + \frac{P_{2,3\text{-butanedione}}}{K_{2D}} + K_{2A}P_{acetoin} + \cdots}\right)^3$$

$$= \frac{k_{2s}K_{2A}C_t^3\left(P_{acetoin} - \frac{P_{2,3\text{-butanedione}}P_{H2}}{K_{2D}K_{1H}K_{2s}K_{2A}}\right)}{\left(1 + \sqrt{\frac{P_{H2}}{K_{1H}}} + \frac{P_{2,3\text{-butanedione}}}{K_{2D}} + K_{2A}P_{acetoin} + \cdots\right)^3}$$

$$= \frac{k_2\left(P_{acetoin} - \frac{P_{2,3\text{-butanedione}}P_{H2}}{K_{2P}}\right)}{\left(1 + \sqrt{\frac{P_{H2}}{K_{1H}}} + \frac{P_{2,3\text{-butanedione}}}{K_{2D}} + K_{2A}P_{acetoin} + \cdots\right)^3}$$

$$k_2 = k_{2s}K_{2A}C_t^3 , \quad K_{2P} = K_{2D}K_{1H}K_{2s}K_{2A}, \quad K_{2A} = \frac{1}{K_{1D}}$$

Reaction 3: $BDO(g) \underset{k_{-3}}{\overset{k_3}{\rightleftharpoons}} MEK(g) + H_2O(g)$, on acid sites of HZSM-5
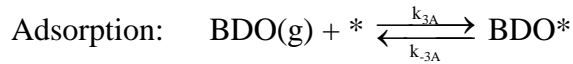
Adsorption: $BDO(g) + * \underset{k_{-3A}}{\overset{k_{3A}}{\rightleftharpoons}} BDO*$

$$r_{3A} = k_{3A}\left(P_{BDO}C_V - \frac{C_{BDO*}}{K_{3A}}\right), \quad K_{3A} = \frac{k_{3A}}{k_{-3A}}, \quad P_{BDO}C_V = \frac{C_{BDO*}}{K_{3A}}, \quad C_{BDO*} = K_{3A}P_{BDO}C_V$$

Surface reaction: $BDO* + * \underset{k_{-3s}}{\overset{k_{3s}}{\rightleftharpoons}} MEK* + H_2O*$

$$r_{3s} = k_{3s}\left(C_{BDO*}C_V - \frac{C_{MEK*}C_{H2O*}}{K_{3s}}\right)$$

Desorption of H₂O: $H_2O* \underset{k_{-3W}}{\overset{k_{3W}}{\rightleftharpoons}} H_2O(g) + *$
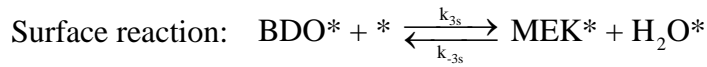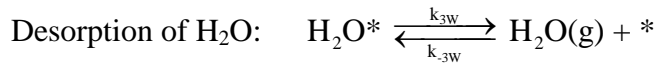
$$r_{3W} = k_{3W}\left(C_{H2O^*} - \frac{P_{H2O}C_V}{K_{3W}}\right), \ K_{3W} = \frac{k_{3W}}{k_{-3W}}, \ C_{H2O^*} = \frac{P_{H2O}C_V}{K_{3W}}$$

Desorption of MEK: $\quad MEK^* \ \underset{k_{-3D}}{\overset{k_{3D}}{\rightleftharpoons}} \ MEK + *$

$$r_{3D} = k_{3D}\left(C_{MEK^*} - \frac{P_{MEK}C_V}{K_{3D}}\right), \ K_{3D} = \frac{k_{3D}}{k_{-3D}}, \ C_{MEK^*} = \frac{P_{MEK}C_V}{K_{3D}}$$

$$r_{3s} = k_{3s}\left(C_{BDO^*}C_V - \frac{C_{MEK^*}C_{H2O^*}}{K_{3s}}\right) = k_{3s}\left(K_{3A}P_{BDO}C_V^2 - \frac{\dfrac{P_{MEK}C_V}{K_{3D}}\dfrac{P_{H2O}C_V}{K_{3W}}}{K_{3s}}\right)$$

$$= k_{3s}K_{3A}\left(P_{BDO} - \frac{P_{MEK}P_{H2O}}{K_{3D}K_{3W}K_{3s}K_{3A}}\right)C_V^2$$

$$C_t = C_V + C_{H2O^*} + C_{BDO^*} + C_{MEK^*} + \cdots$$

$$C_t = C_V + \frac{P_{H2O}C_V}{K_{3W}} + K_{3A}P_{BDO}C_V + \frac{P_{MEK}C_V}{K_{3D}} + \cdots$$

$$C_V = \frac{C_t}{1 + \dfrac{P_{H2O}}{K_{3W}} + K_{3A}P_{BDO} + \dfrac{P_{MEK}}{K_{3D}} + \cdots}$$

$$r_{3s} = k_{3s}K_{3A}\left(P_{BDO} - \frac{P_{MEK}P_{H2O}}{K_{3D}K_{3W}K_{3s}K_{3A}}\right)C_V^2$$

$$= k_{3s}K_{3A}\left(P_{BDO} - \frac{P_{MEK}P_{H2O}}{K_{3D}K_{3W}K_{3s}K_{3A}}\right)\left(\frac{C_t}{1 + \dfrac{P_{H2O}}{K_{3W}} + K_{3A}P_{BDO} + \dfrac{P_{MEK}}{K_{3D}} + \cdots}\right)^2$$

$$= \frac{k_{3s}K_{3A}C_t^2\left(P_{BDO} - \dfrac{P_{MEK}P_{H2O}}{K_{3D}K_{3W}K_{3s}K_{3A}}\right)}{\left(1 + \dfrac{P_{H2O}}{K_{3W}} + K_{3A}P_{BDO} + \dfrac{P_{MEK}}{K_{3D}} + \cdots\right)^2} = \frac{k_3\left(P_{BDO} - \dfrac{P_{MEK}P_{H2O}}{K_{3P}}\right)}{\left(1 + \dfrac{P_{H2O}}{K_{3W}} + K_{3A}P_{BDO} + \dfrac{P_{MEK}}{K_{3D}} + \cdots\right)^2}$$

$$k_3 = k_{3s}K_{3A}C_t^2, \ K_{3P} = K_{3D}K_{3W}K_{3s}K_{3A}$$

Reaction 4: $BDO(g) \xrightleftharpoons[k_{-4}]{k_4}$ 2-methylpropanal(g) + $H_2O(g)$ on acid sites of HZSM-5
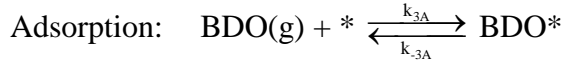
Adsorption: $BDO(g) + * \xrightleftharpoons[k_{-3A}]{k_{3A}} BDO*$
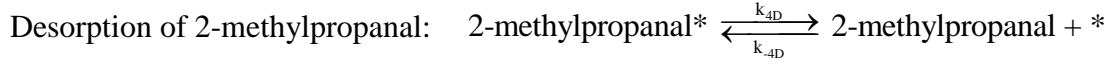
$$r_{3A} = k_{3A}\left(P_{BDO}C_V - \frac{C_{BDO*}}{K_{3A}}\right), \; K_{3A} = \frac{k_{3A}}{k_{-3A}}, \; P_{BDO}C_V = \frac{C_{BDO*}}{K_{3A}}, \; C_{BDO*} = K_{3A}P_{BDO}C_V$$

Surface reaction: $BDO* + * \xrightleftharpoons[k_{-4s}]{k_{4s}}$ 2-methylpropanal* + H_2O*

$$r_{4s} = k_{4s}\left(C_{BDO*}C_V - \frac{C_{\text{2-methylpropanal}*}C_{H2O*}}{K_{4s}}\right)$$

Desorption of H_2O: $H_2O* \xrightleftharpoons[k_{-3W}]{k_{3W}} H_2O(g) + *$

$$r_{3W} = k_{3W}\left(C_{H2O*} - \frac{P_{H2O}C_V}{K_{3W}}\right), \; K_{3W} = \frac{k_{3W}}{k_{-3W}}, C_{H2O*} = \frac{P_{H2O}C_V}{K_{3W}}$$

Desorption of 2-methylpropanal: 2-methylpropanal* $\xrightleftharpoons[k_{-4D}]{k_{4D}}$ 2-methylpropanal + *
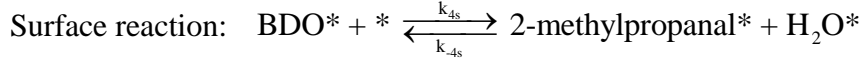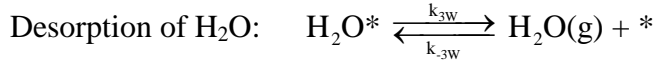
$$r_{4D} = k_{4D}\left(C_{\text{2-methylpropanal}*} - \frac{P_{\text{2-methylpropanal}}C_V}{K_{4D}}\right), \; K_{4D} = \frac{k_{4D}}{k_{-4D}}, \; C_{\text{2-methylpropanal}*} = \frac{P_{\text{2-methylpropanal}}C_V}{K_{4D}}$$

$$r_{4s} = k_{4s}\left(C_{BDO*}C_V - \frac{C_{\text{2-methylpropanal}*}C_{H2O*}}{K_{4s}}\right) = k_{4s}\left(K_{3A}P_{BDO}C_V^2 - \frac{\frac{P_{\text{2-methylpropanal}}C_V}{K_{4D}}\frac{P_{H2O}C_V}{K_{3W}}}{K_{4s}}\right)$$

$$= k_{4s}K_{3A}\left(P_{BDO} - \frac{P_{\text{2-methylpropanal}}P_{H2O}}{K_{4D}K_{3W}K_{3A}K_{4s}}\right)C_V^2$$

$$C_t = C_V + C_{H2O*} + C_{BDO*} + C_{\text{2-methylpropanal}*} + \cdots = C_V + \frac{P_{H2O}C_V}{K_{3W}} + K_{3A}P_{BDO}C_V + \frac{P_{\text{2-methylpropanal}}C_V}{K_{4D}} + \cdots$$

$$C_V = \frac{C_t}{1 + \frac{P_{H2O}}{K_{3W}} + K_{3A}P_{BDO} + \frac{P_{\text{2-methylpropanal}}}{K_{4D}} + \cdots}$$

$$r_{4s} = k_{4s}K_{3A}\left(P_{BDO} - \frac{P_{\text{2-methylpropanal}}P_{H2O}}{K_{4D}K_{3W}K_{3A}K_{4s}}\right)\left(\frac{C_t}{1 + \frac{P_{H2O}}{K_{3W}} + K_{3A}P_{BDO} + \frac{P_{\text{2-methylpropanal}}}{K_{4D}} + \cdots}\right)^2$$

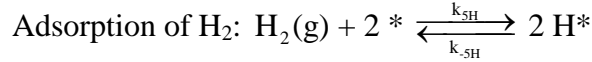$$= \frac{k_{4s}K_{3A}C_t^2\left(P_{BDO} - \frac{P_{\text{2-methylpropanal}}P_{H2O}}{K_{4D}K_{3W}K_{3A}K_{4s}}\right)}{\left(1 + \frac{P_{H2O}}{K_{3W}} + K_{3A}P_{BDO} + \frac{P_{\text{2-methylpropanal}}}{K_{4D}} + \cdots\right)^2} = \frac{k_4\left(P_{BDO} - \frac{P_{\text{2-methylpropanal}}P_{H2O}}{K_{4P}}\right)}{\left(1 + \frac{P_{H2O}}{K_{3W}} + K_{3A}P_{BDO} + \frac{P_{\text{2-methylpropanal}}}{K_{4D}} + \cdots\right)^2}$$

$$k_4 = k_{4s}K_{3A}C_t^2, \quad K_{4P} = K_{4D}K_{3W}K_{3A}K_{4s}$$

Reaction 5: $MEK(g) + H_2(g) \xrightarrow[k_{-5}]{k_5} \text{2-butanol}(g)$ on Cu sites

Adsorption: $MEK(g) + * \xrightarrow[k_{-5A}]{k_{5A}} MEK*$
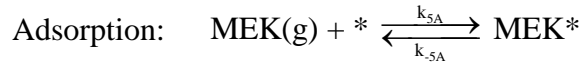
$$r_{5A} = k_{5A}\left(P_{MEK}C_V - \frac{C_{MEK*}}{K_{5A}}\right), \quad P_{MEK}C_V = \frac{C_{MEK*}}{K_{5A}}, \quad C_{MEK*} = K_{5A}P_{MEK}C_V,$$

Adsorption of H_2: $H_2(g) + 2* \xrightarrow[k_{-5H}]{k_{5H}} 2H*$

$$r_{5H} = k_{5H}\left(P_{H2}C_V^2 - \frac{C_{H*}^2}{K_{5H}}\right), \quad P_{H2}C_V^2 = \frac{C_{H*}^2}{K_{5H}}, \quad C_{H*}^2 = K_{5H}P_{H2}C_V^2, \quad K_{5H} = \frac{1}{K_{1H}}$$

Surface reaction: $MEK* + 2H* \xrightarrow[k_{-5s}]{k_{5s}} \text{2-butanol}* + 2*$

$$r_{5s} = k_{5s}\left(C_{MEK*}C_{H*}^2 - \frac{C_{\text{2-butanol}*}C_V^2}{K_{5s}}\right)$$

Desorption of 2-butanol: $\text{2-butanol}* \xrightarrow[k_{-5D}]{k_{5D}} \text{2-butanol} + *$
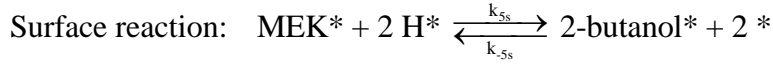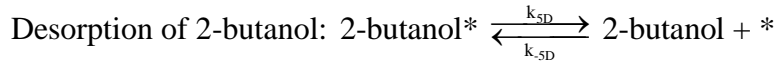
$$r_{5D} = k_{5D}\left(C_{\text{2-butanol}*} - \frac{P_{\text{2-butanol}}C_V}{K_{5D}}\right), \quad C_{\text{2-butanol}*} = \frac{P_{\text{2-butanol}}C_V}{K_{5D}}$$

$$r_{5s} = k_{5s}\left(C_{MEK^*}C_{H^*}^2 - \frac{C_{2\text{-butanol}^*}C_V^2}{K_{5s}} \right) = k_{5s}\left(K_{5A}P_{MEK}C_V \times K_{5H}P_{H2}C_V^2 - \frac{\dfrac{P_{2\text{-butanol}}}{K_{5D}}C_V^3}{K_{5s}} \right)$$

$$= k_{5s}K_{5A}K_{5H}\left(P_{MEK}P_{H2} - \frac{P_{2\text{-butanol}}}{K_{5D}K_{5s}K_{5A}K_{5H}} \right)C_V^3$$

$$C_t = C_V + C_{H^*} + C_{2\text{-butanol}^*} + C_{MEK^*} + \cdots$$

$$C_t = C_V + \sqrt{K_{5H}P_{H2}}C_V + \frac{P_{2\text{-butanol}}C_V}{K_{5D}} + K_{5A}P_{MEK}C_V + \cdots$$

$$C_V = \frac{C_t}{1 + \sqrt{K_{5H}P_{H2}} + \dfrac{P_{2\text{-butanol}}}{K_{5D}} + K_{5A}P_{MEK} + \cdots}$$

$$r_{5s} = k_{5s}K_{5A}K_{5H}\left(P_{MEK}P_{H2} - \frac{P_{2\text{-butanol}}}{K_{5D}K_{5s}K_{5A}K_{5H}} \right)\left(\frac{C_t}{1 + \sqrt{K_{5H}P_{H2}} + \dfrac{P_{2\text{-butanol}}}{K_{5D}} + K_{5A}P_{MEK} + \cdots} \right)^3$$

$$r_{5s} = k_{5s}K_{5A}K_{5H}C_t^3 \frac{\left(P_{MEK}P_{H2} - \dfrac{P_{2\text{-butanol}}}{K_{5D}K_{5s}K_{5A}K_{5H}} \right)}{\left(1 + \sqrt{K_{5H}P_{H2}} + \dfrac{P_{2\text{-butanol}}}{K_{5D}} + K_{5A}P_{MEK} + \cdots \right)^3} = \frac{k_5\left(P_{MEK}P_{H2} - \dfrac{P_{2\text{-butanol}}}{K_{5P}} \right)}{\left(1 + \sqrt{K_{5H}P_{H2}} + \dfrac{P_{2\text{-butanol}}}{K_{5D}} + K_{5A}P_{MEK} + \cdots \right)^3}$$

$$k_5 = k_{5s}K_{5A}K_{5H}C_t^3, \quad K_{5P} = K_{5D}K_{5s}K_{5A}K_{5H}, \quad K_{5H} = \frac{1}{K_{1H}}.$$

$$k_5 = \frac{k_{5s}K_{5A}C_t^3}{K_{1H}}, \quad K_{5P} = \frac{K_{5D}K_{5s}K_{5A}}{K_{1H}},$$

$$r_{5s} = \frac{k_5\left(P_{MEK}P_{H2} - \dfrac{P_{2\text{-butanol}}}{K_{5P}} \right)}{\left(1 + \sqrt{\dfrac{P_{H2}}{K_{1H}}} + \dfrac{P_{2\text{-butanol}}}{K_{5D}} + K_{5A}P_{MEK} + \cdots \right)^3}$$

Reaction 6: 2-methylpropanal(g) + H_2(g) $\xrightleftharpoons[k_{-6}]{k_6}$ isobutanol(g)   on Cu sites

Adsorption: 2-methylpropanal(g) + * $\xrightleftharpoons[k_{-6A}]{k_{6A}}$ 2-methylpropanal*

$$r_{6A} = k_{6A}\left(P_{\text{2-methylpropanal}}C_V - \frac{C_{\text{2-methylpropanal*}}}{K_{6A}}\right), \quad P_{\text{2-methylpropanal}}C_V = \frac{C_{\text{2-methylpropanal*}}}{K_{6A}},$$

$$C_{\text{2-methylpropanal*}} = K_{6A}P_{\text{2-methylpropanal}}C_V$$

Adsorption of H_2: H_2(g) + 2 * $\xrightleftharpoons[k_{-5H}]{k_{5H}}$ 2 H*

$$r_{5H} = k_{5H}\left(P_{H2}C_V^2 - \frac{C_{H*}^2}{K_{5H}}\right), \quad P_{H2}C_V^2 = \frac{C_{H*}^2}{K_{5H}}, \quad C_{H*}^2 = K_{5H}P_{H2}C_V^2, \quad K_{5H} = \frac{1}{K_{1H}}$$

Surface reaction: 2-methylpropanal* + 2 H* $\xrightleftharpoons[k_{-6s}]{k_{6s}}$ isobutanol* + 2 *

$$r_{6s} = k_{6s}\left(C_{\text{2-methylpropanal*}}C_{H*}^2 - \frac{C_{\text{isobutanol*}}C_V^2}{K_{6s}}\right)$$

Desorption of isobutanol: isobutanol* $\xrightleftharpoons[k_{-6D}]{k_{6D}}$ isobutanol(g) + *

$$r_{6D} = k_{6D}\left(C_{\text{isobutanol*}} - \frac{P_{\text{isobutanol}}C_V}{K_{6D}}\right), \quad C_{\text{isobutanol*}} = \frac{P_{\text{isobutanol}}C_V}{K_{6D}}$$

$$r_{6s} = k_{6s}\left(C_{\text{2-methylpropanal*}}C_{H*}^2 - \frac{C_{\text{isobutanol*}}C_V^2}{K_{6s}}\right) = k_{6s}\left(K_{6A}P_{\text{2-methylpropanal}}K_{5H}P_{H2}C_V^3 - \frac{\frac{P_{\text{isobutanol}}C_V^3}{K_{6D}}}{K_{6s}}\right)$$

$$= k_{6s}K_{6A}K_{5H}\left(P_{\text{2-methylpropanal}}P_{H2} - \frac{P_{\text{isobutanol}}}{K_{6D}K_{6s}K_{6A}K_{5H}}\right)C_V^3$$

$$C_t = C_V + C_{H*} + C_{\text{2-methylpropanal*}} + C_{\text{isobutanol*}} + \cdots$$

$$= C_V + \sqrt{K_{5H}P_{H2}}C_V + K_{6A}P_{\text{2-methylpropanal}}C_V + \frac{P_{\text{isobutanol}}C_V}{K_{6D}} + \cdots$$

$$C_V = \cfrac{C_t}{1+\sqrt{K_{5H}P_{H2}} + K_{6A}P_{\text{2-methylpropanal}} + \cfrac{P_{\text{isobutanol}}}{K_{6D}} + \cdots}$$

$$r_{6s} = k_{6s}K_{6A}K_{5H}\left(P_{\text{2-methylpropanal}}P_{H2} - \frac{P_{\text{isobutanol}}}{K_{6D}K_{6s}K_{6A}K_{5H}}\right)C_V^3$$
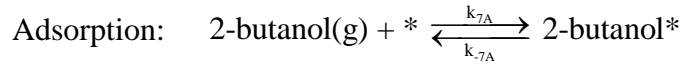
$$= k_{6s}K_{6A}K_{5H}\left(P_{\text{2-methylpropanal}}P_{H2} - \frac{P_{\text{isobutanol}}}{K_{6D}K_{6s}K_{6A}K_{5H}}\right)\left(\cfrac{C_t}{1+\sqrt{K_{5H}P_{H2}} + K_{6A}P_{\text{2-methylpropanal}} + \cfrac{P_{\text{isobutanol}}}{K_{6D}} + \cdots}\right)^3$$

$$= \cfrac{k_{6s}K_{6A}K_{5H}C_t^3\left(P_{\text{2-methylpropanal}}P_{H2} - \cfrac{P_{\text{isobutanol}}}{K_{6D}K_{6s}K_{6A}K_{5H}}\right)}{\left(1+\sqrt{K_{5H}P_{H2}} + K_{6A}P_{\text{2-methylpropanal}} + \cfrac{P_{\text{isobutanol}}}{K_{6D}} + \cdots\right)^3}$$

$$= \cfrac{k_6\left(P_{\text{2-methylpropanal}}P_{H2} - \cfrac{P_{\text{isobutanol}}}{K_{6P}}\right)}{\left(1+\sqrt{K_{5H}P_{H2}} + K_{6A}P_{\text{2-methylpropanal}} + \cfrac{P_{\text{isobutanol}}}{K_{6D}} + \cdots\right)^3}$$

$$k_6 = k_{6s}K_{6A}K_{5H}C_t^3 \ , \ K_{6P} = K_{6D}K_{6s}K_{6A}K_{5H}$$

Reaction 7: 2-butanol(g) $\underset{k_{-7}}{\overset{k_7}{\rightleftharpoons}}$ 2-butene(g) + H_2O(g)   on acid sites of HZSM-5

Adsorption: 2-butanol(g) + * $\underset{k_{-7A}}{\overset{k_{7A}}{\rightleftharpoons}}$ 2-butanol*
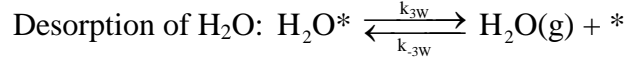
$$r_{7A} = k_{7A}\left(P_{\text{2-butanol}}C_V - \frac{C_{\text{2-butanol*}}}{K_{7A}}\right), \ C_{\text{2-butanol*}} = K_{7A}P_{\text{2-butanol}}C_V$$

Surface reaction: 2-butanol* + * $\underset{k_{-7s}}{\overset{k_{7s}}{\rightleftharpoons}}$ 2-butene* (or 1-butene*) + H_2O*

$$r_{7s} = k_{7s}\left(C_{\text{2-butanol*}}C_V - \frac{C_{\text{2-butene*}}C_{H_2O*}}{K_{7s}}\right)$$

Desorption of butene: 2-butene* $\underset{k_{-7D}}{\overset{k_{7D}}{\rightleftharpoons}}$ 2-butene + *
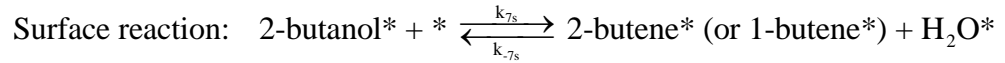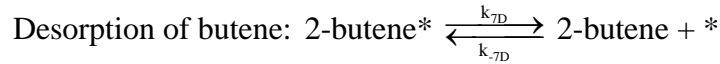
$$r_{7D} = k_{7D}\left(C_{2\text{-butene}*} - \frac{P_{2\text{-butene}}C_V}{K_{7D}}\right), \quad C_{2\text{-butene}*} = \frac{P_{2\text{-butene}}C_V}{K_{7D}}$$

Desorption of H_2O: $H_2O* \underset{k_{-3W}}{\overset{k_{3W}}{\longleftrightarrow}} H_2O(g) + *$

$$r_{3W} = k_{3W}\left(C_{H2O*} - \frac{P_{H2O}C_V}{K_{3W}}\right), \quad K_{3W} = \frac{k_{3W}}{k_{-3W}}, \quad C_{H2O*} = \frac{P_{H2O}C_V}{K_{3W}}$$

$$r_{7s} = k_{7s}\left(C_{2\text{-butanol}*}C_V - \frac{C_{2\text{-butene}*}C_{H_2O*}}{K_{7s}}\right) = k_{7s}\left(K_{7A}P_{2\text{-butanol}}C_V^2 - \frac{\dfrac{P_{2\text{-butene}}C_V}{K_{7D}}\dfrac{P_{H2O}C_V}{K_{3W}}}{K_{7s}}\right)$$

$$= k_{7s}K_{7A}\left(P_{2\text{-butanol}} - \frac{P_{2\text{-butene}}P_{H2O}}{K_{7D}K_{3W}K_{7s}K_{7A}}\right)C_V^2$$

$$C_t = C_V + C_{H2O*} + C_{2\text{-butanol}*} + C_{butene*} + \cdots$$

$$C_t = C_V + \frac{P_{H2O}C_V}{K_{3W}} + K_{7A}P_{2\text{-butanol}}C_V + \frac{P_{2\text{-butene}}C_V}{K_{7D}} + \cdots$$

$$C_V = \frac{C_t}{1 + \dfrac{P_{H2O}}{K_{3W}} + K_{7A}P_{2\text{-butanol}} + \dfrac{P_{2\text{-butene}}}{K_{7D}} + \cdots}$$

$$r_{7s} = k_{7s}K_{7A}\left(P_{2\text{-butanol}} - \frac{P_{2\text{-butene}}P_{H2O}}{K_{7D}K_{3W}K_{7s}K_{7A}}\right)C_V^2$$

$$= k_{7s}K_{7A}\left(P_{2\text{-butanol}} - \frac{P_{2\text{-butene}}P_{H2O}}{K_{7D}K_{3W}K_{7s}K_{7A}}\right)\left(\frac{C_t}{1 + \dfrac{P_{H2O}}{K_{3W}} + K_{7A}P_{2\text{-butanol}} + \dfrac{P_{2\text{-butene}}}{K_{7D}} + \cdots}\right)^2$$

$$= \frac{k_{7s}K_{7A}C_t^2\left(P_{2\text{-butanol}} - \dfrac{P_{2\text{-butene}}P_{H2O}}{K_{7D}K_{3W}K_{7s}K_{7A}}\right)}{\left(1 + \dfrac{P_{H2O}}{K_{3W}} + K_{7A}P_{2\text{-butanol}} + \dfrac{P_{2\text{-butene}}}{K_{7D}} + \cdots\right)^2} = \frac{k_7\left(P_{2\text{-butanol}} - \dfrac{P_{2\text{-butene}}P_{H2O}}{K_{7P}}\right)}{\left(1 + \dfrac{P_{H2O}}{K_{3W}} + K_{7A}P_{2\text{-butanol}} + \dfrac{P_{2\text{-butene}}}{K_{7D}} + \cdots\right)^2}$$

$$k_7 = k_{7s}K_{7A}C_t^2, \quad K_{7P} = K_{7D}K_{3W}K_{7s}K_{7A}$$

Reaction 8: isobutanol(g) $\xrightleftharpoons[k_{-8}]{k_8}$ isobutene(g) + H_2O(g)   on acid sites of HZSM-5

Adsorption: isobutanol(g) + * $\xrightleftharpoons[k_{-8A}]{k_{8A}}$ isobutanol*

$$r_{8A} = k_{8A}\left(P_{isobutanol}C_V - \frac{C_{isobutanol*}}{K_{8A}}\right),\quad C_{isobutanol*} = K_{8A}P_{isobutanol}C_V$$

Surface reaction: isobutanol* + * $\xrightleftharpoons[k_{-8s}]{k_{8s}}$ isobutene* + H_2O*

$$r_{8s} = k_{8s}\left(C_{isobutanol*}C_V - \frac{C_{isobutene*}C_{H_2O*}}{K_{8s}}\right)$$

Desorption of butene: isobutene* $\xrightleftharpoons[k_{-8D}]{k_{8D}}$ isobutene (g) + *

$$r_{8D} = k_{8D}\left(C_{isobutene*} - \frac{P_{isobutene}C_V}{K_{8D}}\right),\quad C_{isobutene*} = \frac{P_{isobutene}C_V}{K_{8D}}$$

Desorption of H_2O: H_2O* $\xrightleftharpoons[k_{-3W}]{k_{3W}}$ H_2O(g) + *

$$r_{3W} = k_{3W}\left(C_{H2O*} - \frac{P_{H2O}C_V}{K_{3W}}\right),\quad K_{3W} = \frac{k_{3W}}{k_{-3W}},\ C_{H2O*} = \frac{P_{H2O}C_V}{K_{3W}}$$

$$r_{8s} = k_{8s}\left(C_{isobutanol*}C_V - \frac{C_{isobutene*}C_{H_2O*}}{K_{8s}}\right) = k_{8s}\left(K_{8A}P_{isobutanol}C_V^2 - \frac{\dfrac{P_{isobutene}C_V}{K_{8D}}\dfrac{P_{H2O}C_V}{K_{3W}}}{K_{8s}}\right)$$

$$= k_{8s}K_{8A}\left(P_{isobutanol} - \frac{P_{isobutene}P_{H2O}}{K_{8D}K_{3W}K_{8s}K_{8A}}\right)C_V^2$$

$$C_t = C_V + C_{H2O*} + C_{isobutanol*} + C_{isobutene*} + \cdots$$

$$C_t = C_V + \frac{P_{H2O}C_V}{K_{3W}} + K_{8A}P_{isobutanol}C_V + \frac{P_{isobutene}C_V}{K_{8D}} + \cdots$$

$$C_V = \frac{C_t}{1 + \dfrac{P_{H2O}}{K_{3W}} + K_{8A}P_{isobutanol} + \dfrac{P_{isobutene}}{K_{8D}} + \cdots}$$

$$r_{8s} = k_{8s} K_{8A} \left(P_{isobutanol} - \frac{P_{isobutene} P_{H2O}}{K_{8D} K_{3W} K_{8s} K_{8A}} \right) \left(\frac{C_t}{1 + \frac{P_{H2O}}{K_{3W}} + K_{8A} P_{isobutanol} + \frac{P_{isobutene}}{K_{8D}} + \cdots} \right)^2$$
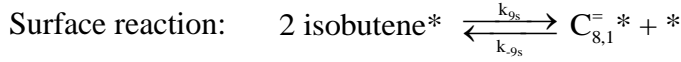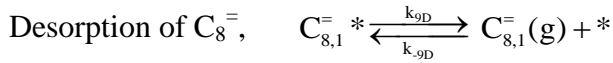
$$= \frac{k_{8s} K_{8A} C_t^2 \left(P_{isobutanol} - \frac{P_{isobutene} P_{H2O}}{K_{8D} K_{3W} K_{8s} K_{8A}} \right)}{\left(1 + \frac{P_{H2O}}{K_{3W}} + K_{8A} P_{isobutanol} + \frac{P_{isobutene}}{K_{8D}} + \cdots \right)^2} = \frac{k_8 \left(P_{isobutanol} - \frac{P_{isobutene} P_{H2O}}{K_{8P}} \right)}{\left(1 + \frac{P_{H2O}}{K_{3W}} + K_{8A} P_{isobutanol} + \frac{P_{isobutene}}{K_{8D}} + \cdots \right)^2}$$

$$k_8 = k_{8s} K_{8A} C_t^2, \ K_{8P} = K_{8D} K_{3W} K_{8s} K_{8A}$$

Reaction 9: isobutene(g) + isobutene(g) $\xrightarrow{k_9}$ $C_{8,1}^{=}(g)$ on acid sites of HZSM-5
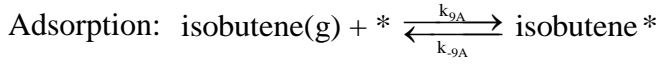
Adsorption: isobutene(g) + * $\underset{k_{-9A}}{\overset{k_{9A}}{\rightleftharpoons}}$ isobutene*

$$r_{9A} = k_{9A} \left(P_{isobutene} C_V - \frac{C_{isobutene*}}{K_{9A}} \right), \ C_{isobutene*} = K_{9A} P_{isobutene} C_V$$

Surface reaction: 2 isobutene* $\underset{k_{-9s}}{\overset{k_{9s}}{\rightleftharpoons}}$ $C_{8,1}^{=}$* + *

$$r_{9s} = k_{9s} \left(C_{isobutene*}^2 - \frac{C_{C_{8,1}*} C_V}{K_{9s}} \right)$$

Desorption of $C_8^{=}$, $C_{8,1}^{=}$* $\underset{k_{-9D}}{\overset{k_{9D}}{\rightleftharpoons}}$ $C_{8,1}^{=}(g)$ + *

$$r_{9D} = k_{9D} \left(C_{C_{8,1}*} - \frac{P_{C_{8,1}} C_V}{K_{9D}} \right), \ C_{C_{8,1}*} = \frac{P_{C_{8,1}} C_V}{K_{9D}}$$

$$r_{9s} = k_{9s} \left(C_{isobutene*}^2 - \frac{C_{C_{8,1}*} C_V}{K_{9s}} \right) = k_{9s} \left(K_{9A}^2 P_{isobutene}^2 C_V^2 - \frac{\frac{P_{C_{8,1}} C_V^2}{K_{9D}}}{K_{9s}} \right) = k_{9s} K_{9A}^2 \left(P_{isobutene}^2 - \frac{P_{C_{8,1}}}{K_{9D} K_{9s} K_{9A}^2} \right) C_V^2$$

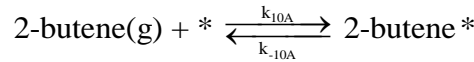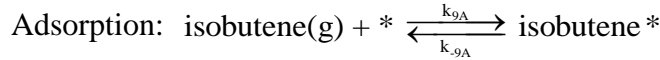$$C_t = C_V + C_{isobutene*} + C_{C_{8,1}*} + \cdots = C_V + K_{9A}P_{isobutene}C_V + \frac{P_{C_{8,1}}C_V}{K_{9D}} + \cdots$$

$$C_V = \frac{C_t}{1 + K_{9A}P_{isobutene} + \dfrac{P_{C_{8,1}}}{K_{9D}} + \cdots}$$

$$r_{9s} = k_{9s}K_{9A}^2 \left(P_{isobutene}^2 - \frac{P_{C_{8,1}}}{K_{9D}K_{9s}K_{9A}^2} \right) \left(\frac{C_t}{1 + K_{9A}P_{isobutene} + \dfrac{P_{C_{8,1}}}{K_{9D}} + \cdots} \right)^2$$

$$= \frac{k_{9s}K_{9A}^2 C_t^2 \left(P_{isobutene}^2 - \dfrac{P_{C_{8,1}}}{K_{9D}K_{9s}K_{9A}^2} \right)}{\left(1 + K_{9A}P_{isobutene} + \dfrac{P_{C_{8,1}}}{K_{9D}} + \cdots \right)^2} = \frac{k_9 \left(P_{isobutene}^2 - \dfrac{P_{C_{8,1}}}{K_{9P}} \right)}{\left(1 + K_{9A}P_{isobutene} + \dfrac{P_{C_{8,1}}}{K_{9D}} + \cdots \right)^2}$$
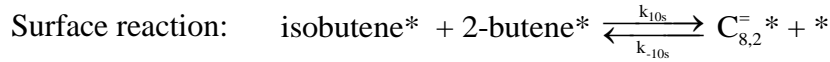
$$k_9 = k_{9s}K_{9A}^2 C_t^2 \ , \ K_{9P} = K_{9D}K_{9s}K_{9A}^2 \ , \ K_{9A} = \frac{1}{K_{8D}}$$

Reaction 10:   isobutene(g) + 2-butene(g) $\xrightarrow{\ k10\ }$ $C_{8,2}^{=}(g)$ on acid sites of HZSM-5
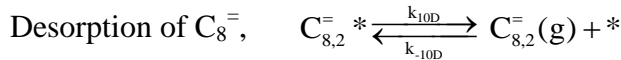
Adsorption: isobutene(g) + * $\underset{k_{-9A}}{\overset{k_{9A}}{\rightleftharpoons}}$ isobutene *

2-butene(g) + * $\underset{k_{-10A}}{\overset{k_{10A}}{\rightleftharpoons}}$ 2-butene *

$$r_{9A} = k_{9A}\left(P_{isobutene}C_V - \frac{C_{isobutene*}}{K_{9A}} \right), \ C_{isobutene*} = K_{9A}P_{isobutene}C_V$$

$$r_{10A} = k_{10A}\left(P_{2\text{-butene}}C_V - \frac{C_{2\text{-butene}*}}{K_{10A}} \right), \ C_{2\text{-butene}*} = K_{10A}P_{2\text{-butene}}C_V$$

Surface reaction: isobutene* + 2-butene* $\underset{k_{-10s}}{\overset{k_{10s}}{\rightleftharpoons}}$ $C_{8,2}^{=}* + *$

$$r_{10s} = k_{10s}\left(C_{isobutene*}C_{2\text{-butene}*} - \frac{C_{C_{8,2}*}C_V}{K_{10s}} \right)$$

Desorption of $C_8^{=}$, $C_{8,2}^{=}* \underset{k_{-10D}}{\overset{k_{10D}}{\rightleftharpoons}} C_{8,2}^{=}(g) + *$

$$r_{10D} = k_{10D}\left(C_{C_{8,2}*} - \frac{P_{C_{8,2}}C_V}{K_{10D}}\right), \ C_{C_{8,2}*} = \frac{P_{C_{8,2}}C_V}{K_{10D}}$$

$$r_{10s} = k_{10s}\left(C_{isobutene*}C_{2\text{-butene}*} - \frac{C_{C_{8,2}*}C_V}{K_{10s}}\right) = k_{10s}\left(K_{9A}P_{isobutene}C_V K_{10A}P_{2\text{-butene}}C_V - \frac{\frac{P_{C_{8,2}}C_V^2}{K_{10D}}}{K_{10s}}\right)$$

$$= k_{10s}K_{9A}K_{10A}\left(P_{isobutene}P_{2\text{-butene}} - \frac{P_{C_{8,2}}}{K_{10D}K_{10s}K_{9A}K_{10A}}\right)C_V^2$$

$$C_t = C_V + C_{isobutene*} + C_{2\text{-butene}*} + C_{C_{8,2}*} + \cdots = C_V + K_{9A}P_{isobutene}C_V + K_{10A}P_{2\text{-butene}}C_V + \frac{P_{C_{8,2}}C_V}{K_{10D}} + \cdots$$

$$C_V = \frac{C_t}{1 + K_{9A}P_{isobutene} + K_{10A}P_{2\text{-butene}} + \frac{P_{C_{8,2}}}{K_{10D}} + \cdots}$$

$$r_{10s} = k_{10s}K_{9A}K_{10A}\left(P_{isobutene}P_{2\text{-butene}} - \frac{P_{C_{8,2}}}{K_{10D}K_{10s}K_{9A}K_{10A}}\right)\left(\frac{C_t}{1 + K_{9A}P_{isobutene} + K_{10A}P_{2\text{-butene}} + \frac{P_{C_{8,2}}}{K_{10D}} + \cdots}\right)^2$$
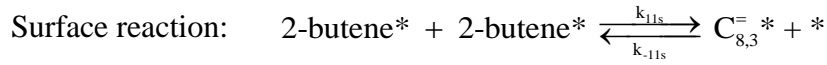
$$r_{10s} = \frac{k_{10}\left(P_{isobutene}P_{2\text{-butene}} - \frac{P_{C_{8,2}}}{K_{10P}}\right)}{\left(1 + K_{9A}P_{isobutene} + K_{10A}P_{2\text{-butene}} + \frac{P_{C_{8,2}}}{K_{10D}} + \cdots\right)^2}$$

$$k_{10} = k_{10s}K_{9A}K_{10A}C_t^2, \ K_{10P} = K_{10D}K_{10s}K_{9A}K_{10A}, \ K_{10A} = \frac{1}{K_{7D}}$$

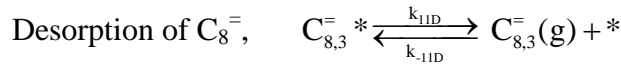**Reaction 11:** 2-butene(g) + 2-butene(g) $\xrightarrow{\text{k}_{11}}$ $C_{8,3}^{=}$(g)   on acid sites of HZSM-5
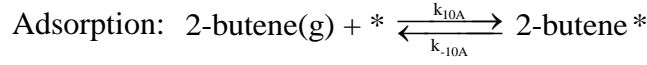
Adsorption: 2-butene(g) + * $\underset{\text{k}_{-10A}}{\overset{\text{k}_{10A}}{\rightleftarrows}}$ 2-butene*

$$r_{10A} = k_{10A}\left(P_{2\text{-butene}}C_V - \frac{C_{2\text{-butene*}}}{K_{10A}} \right), \quad C_{2\text{-butene*}} = K_{10A}P_{2\text{-butene}}C_V$$

Surface reaction: 2-butene* + 2-butene* $\underset{\text{k}_{-11s}}{\overset{\text{k}_{11s}}{\rightleftarrows}}$ $C_{8,3}^{=}$* + *

$$r_{11s} = k_{11s}\left(C_{2\text{-butene*}}^2 - \frac{C_{C_{8,3}}* C_V}{K_{11s}} \right)$$

Desorption of $C_8^=$, $C_{8,3}^{=}$* $\underset{\text{k}_{-11D}}{\overset{\text{k}_{11D}}{\rightleftarrows}}$ $C_{8,3}^{=}$(g) + *

$$r_{11D} = k_{11D}\left(C_{C_{8,3}*} - \frac{P_{C_{8,3}}C_V}{K_{11D}} \right), \quad C_{C_{8,3}*} = \frac{P_{C_{8,3}}C_V}{K_{11D}}$$

$$r_{11s} = k_{11s}\left(C_{2\text{-butene*}}^2 - \frac{C_{C_{8,3}*}C_V}{K_{11s}} \right) = k_{11s}\left(K_{10A}^2 P_{2\text{-butene}}^2 C_V^2 - \frac{\dfrac{P_{C_{8,3}}C_V}{K_{11D}}C_V}{K_{11s}} \right)$$

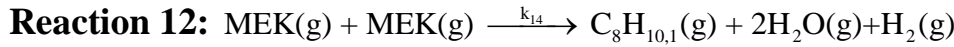$$= k_{11s}K_{10A}^2\left(P_{2\text{-butene}}^2 - \frac{P_{C_{8,3}}}{K_{11D}K_{11s}K_{10A}^2} \right)C_V^2$$

$$C_t = C_V + C_{2\text{-butene*}} + C_{C_{8,3}*} + \cdots = C_V + K_{10A}P_{2\text{-butene}}C_V + \frac{P_{C_{8,3}}C_V}{K_{11D}} + \cdots$$

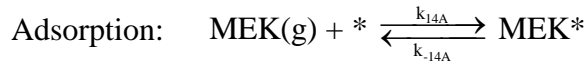$$C_V = \frac{C_t}{1 + K_{10A}P_{2\text{-butene}} + \dfrac{P_{C_{8,3}}}{K_{11D}} + \cdots}$$

$$r_{11s} = k_{11s}K_{10A}^2\left(P_{2\text{-butene}}^2 - \frac{P_{C_{8,3}}}{K_{11D}K_{11s}K_{10A}^2} \right)\left(\frac{C_t}{1 + K_{10A}P_{2\text{-butene}} + \dfrac{P_{C_{8,3}}}{K_{11D}} + \cdots} \right)^2$$

$$r_{11s} = \frac{k_{11s}K_{10A}^2 C_t^2 \left(P_{2\text{-butene}}^2 - \dfrac{P_{C_{8,3}}}{K_{11D}K_{11s}K_{10A}^2} \right)}{\left(1 + K_{10A}P_{2\text{-butene}} + \dfrac{P_{C_{8,3}}}{K_{11D}} + \cdots \right)^2} = \frac{k_{11}\left(P_{2\text{-butene}}^2 - \dfrac{P_{C_{8,3}}}{K_{11P}} \right)}{\left(1 + K_{10A}P_{2\text{-butene}} + \dfrac{P_{C_{8,3}}}{K_{11D}} + \cdots \right)^2}$$
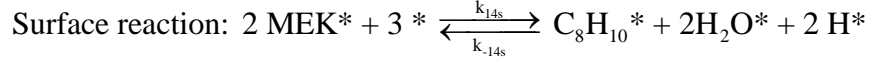
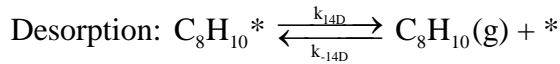$$k_{11} = k_{11s}K_{10A}^2 C_t^2, \quad K_{11P} = K_{11D}K_{11s}K_{10A}^2$$

Reaction 12: $\text{MEK(g)} + \text{MEK(g)} \xrightarrow{\ k_{14}\ } C_8H_{10,1}(g) + 2H_2O(g) + H_2(g)$

on acid sites on HZSM-5, formation of aromatics

Adsorption: $\text{MEK(g)} + * \underset{k_{-14A}}{\overset{k_{14A}}{\rightleftharpoons}} \text{MEK*}$

$$r_{14A} = k_{14A}\left(P_{MEK}C_V - \frac{C_{MEK*}}{K_{14A}} \right), \quad P_{MEK}C_V = \frac{C_{MEK*}}{K_{14A}}, \quad C_{MEK*} = K_{14A}P_{MEK}C_V, \quad K_{14A} = \frac{1}{K_{3D}}$$

Surface reaction: $2\,\text{MEK*} + 3\,* \underset{k_{-14s}}{\overset{k_{14s}}{\rightleftharpoons}} C_8H_{10}* + 2H_2O* + 2\,H*$

$$r_{14s} = k_{14s}\left(C_{MEK*}^2 C_V^3 - \frac{C_{C_8H_{10}*}C_{H_2O*}^2 C_{H*}^2}{K_{14s}} \right)$$

Desorption: $C_8H_{10}* \underset{k_{-14D}}{\overset{k_{14D}}{\rightleftharpoons}} C_8H_{10}(g) + *$

$$r_{14D} = k_{14D}\left(C_{C_8H_{10}*} - \frac{P_{C_8H_{10}}C_V}{K_{14D}} \right), \qquad C_{C_8H_{10}*} = \frac{P_{C_8H_{10}}C_V}{K_{14D}}$$
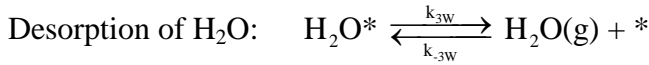
Desorption of H_2O: $H_2O* \underset{k_{-3W}}{\overset{k_{3W}}{\rightleftharpoons}} H_2O(g) + *$

$$r_{3W} = k_{3W}\left(C_{H2O*} - \frac{P_{H2O}C_V}{K_{3W}} \right), \quad K_{3W} = \frac{k_{3W}}{k_{-3W}}, \quad C_{H2O*} = \frac{P_{H2O}C_V}{K_{3W}}$$

Desorption of H_2: $2\,H* \underset{k_{-14H}}{\overset{k_{14H}}{\rightleftharpoons}} H_2(g) + 2\,*$
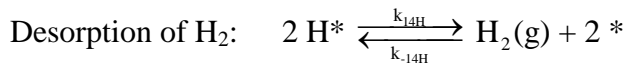
$$r_{14H} = k_{14H}\left(C_{H^*}^2 - \frac{P_{H2}C_V^2}{K_{14H}}\right), \quad K_{14H} = \frac{k_{14H}}{k_{-14H}}, \quad C_{H^*}^2 = \frac{P_{H2}C_V^2}{K_{14H}}, \quad C_{H^*} = \sqrt{\frac{P_{H2}}{K_{14H}}}\,C_V$$

$$r_{14s} = k_{14s}\left(C_{MEK^*}^2 C_V^3 - \frac{C_{C_8H_{10}^*}C_{H_2O^*}^2 C_{H^*}^2}{K_{14s}}\right) = k_{14s}\left(K_{14A}^2 P_{MEK}^2 C_V^5 - \frac{\dfrac{P_{C_8H_{10}}C_V}{K_{14D}}\dfrac{P_{H_2O}^2 C_V^2}{K_{3W}^2}\dfrac{P_{H_2}C_V^2}{K_{14H}}}{K_{14s}}\right)$$

$$= k_{14s}K_{14A}^2\left(P_{MEK}^2 - \frac{P_{C_8H_{10}}P_{H_2O}^2 P_{H_2}}{K_{14D}K_{3W}^2 K_{14H}K_{14s}K_{14A}^2}\right)C_V^5$$

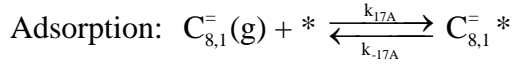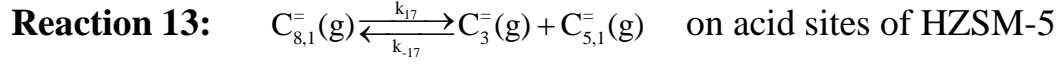$$C_t = C_V + C_{MEK^*} + C_{C_8H_{10}^*} + C_{H_2O^*} + C_{H^*} + \cdots$$

$$C_t = C_V + K_{14A}P_{MEK}C_V + \frac{P_{C_8H_{10}}C_V}{K_{14D}} + \frac{P_{H_2O}C_V}{K_{3W}} + \sqrt{\frac{P_{H_2}}{K_{14H}}}\,C_V + \cdots$$

$$C_V = \frac{C_t}{1 + K_{14A}P_{MEK} + \dfrac{P_{C_8H_{10,1}}}{K_{14D}} + \dfrac{P_{H_2O}}{K_{3W}} + \sqrt{\dfrac{P_{H_2}}{K_{14H}}} + \cdots}$$
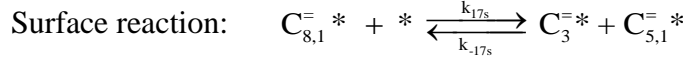
$$r_{14s} = k_{14s}K_{14A}^2\left(P_{MEK}^2 - \frac{P_{C_8H_{10,1}}P_{H_2O}^2 P_{H_2}}{K_{14D}K_{3W}^2 K_{14H}K_{14s}K_{14A}^2}\right)\left(\frac{C_t}{1 + K_{14A}P_{MEK} + \dfrac{P_{C_8H_{10,1}}}{K_{14D}} + \dfrac{P_{H_2O}}{K_{3W}} + \sqrt{\dfrac{P_{H_2}}{K_{14H}}} + \cdots}\right)^5$$

$$= \frac{k_{14s}K_{14A}^2 C_t^5\left(P_{MEK}^2 - \dfrac{P_{C_8H_{10,1}}P_{H_2O}^2 P_{H_2}}{K_{14D}K_{3W}^2 K_{14H}K_{14s}K_{14A}^2}\right)}{\left(1 + K_{14A}P_{MEK} + \dfrac{P_{C_8H_{10,1}}}{K_{14D}} + \dfrac{P_{H_2O}}{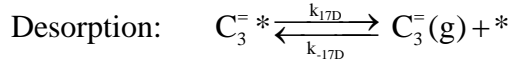K_{3W}} + \sqrt{\dfrac{P_{H_2}}{K_{14H}}} + \cdots\right)^5} = \frac{k_{14}\left(P_{MEK}^2 - \dfrac{P_{C_8H_{10,1}}P_{H_2O}^2 P_{H_2}}{K_{14P}}\right)}{\left(1 + K_{14A}P_{MEK} + \dfrac{P_{C_8H_{10,1}}}{K_{14D}} + \dfrac{P_{H_2O}}{K_{3W}} + \sqrt{\dfrac{P_{H_2}}{K_{14H}}} + \cdots\right)^5}$$

$$k_{14} = k_{14s}K_{14A}^2 C_t^5, \quad K_{14P} = K_{14D}K_{3W}^2 K_{14H}K_{14s}K_{14A}^2, \quad K_{14A} = \frac{1}{K_{3D}}$$
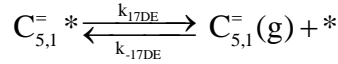
Reaction 13: $\quad C_{8,1}^{=}(g) \xrightleftharpoons[k_{-17}]{k_{17}} C_3^{=}(g) + C_{5,1}^{=}(g) \quad$ on acid sites of HZSM-5

Adsorption: $\quad C_{8,1}^{=}(g) + * \xrightleftharpoons[k_{-17A}]{k_{17A}} C_{8,1}^{=} *$

$$r_{17A} = k_{17A} \left(P_{C_{8,1}^{=}} C_V - \frac{C_{C_{8,1}^{=} *}}{K_{17A}} \right), \ C_{C_{8,1}^{=} *} = K_{17A} P_{C_{8,1}^{=}} C_V, \ K_{17A} = \frac{1}{K_{9D}}$$

Surface reaction: $\quad C_{8,1}^{=} * + * \xrightleftharpoons[k_{-17s}]{k_{17s}} C_3^{=} * + C_{5,1}^{=} *$

$$r_{17s} = k_{17s} \left(C_{C_{8,1}^{=} *} C_V - \frac{C_{C_3^{=} *} C_{C_{5,1}^{=} *}}{K_{17s}} \right)$$

Desorption: $\quad C_3^{=} * \xrightleftharpoons[k_{-17D}]{k_{17D}} C_3^{=}(g) + *$

$$r_{17D} = k_{17D} \left(C_{C_3^{=} *} - \frac{P_{C_3^{=}} C_V}{K_{17D}} \right), \ C_{C_3^{=} *} = \frac{P_{C_3^{=}} C_V}{K_{17D}}$$

$$C_{5,1}^{=} * \xrightleftharpoons[k_{-17DE}]{k_{17DE}} C_{5,1}^{=}(g) + *$$

$$r_{17DE} = k_{17DE} \left(C_{C_{5,1}^{=} *} - \frac{P_{C_{5,1}^{=}} C_V}{K_{17DE}} \right), \ C_{C_{5,1}^{=} *} = \frac{P_{C_{5,1}^{=}} C_V}{K_{17DE}}$$

$$r_{17s} = k_{17s} \left(C_{C_{8,1}^{=} *} C_V - \frac{C_{C_3^{=} *} C_{C_{5,1}^{=} *}}{K_{17s}} \right) = k_{17s} \left(K_{17A} P_{C_{8,1}^{=}} C_V^2 - \frac{\dfrac{P_{C_3^{=}} C_V}{K_{17D}} \dfrac{P_{C_{5,1}^{=}} C_V}{K_{17DE}}}{K_{17s}} \right)$$

$$= k_{17s} K_{17A} \left(P_{C_{8,1}^{=}} - \frac{P_{C_3^{=}} P_{C_{5,1}^{=}}}{K_{17D} K_{17DE} K_{17A} K_{17s}} \right) C_V^2$$

$$C_t = C_V + C_{C_3^{=} *} + C_{C_{5,1}^{=} *} + C_{C_{8,1}^{=} *} \cdots = C_V + \frac{P_{C_3^{=}} C_V}{K_{17D}} + \frac{P_{C_{5,1}^{=}} C_V}{K_{17DE}} + K_{17A} P_{C_{8,1}^{=}} C_V \cdots$$
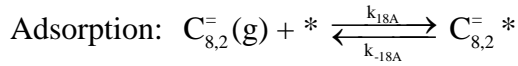
$$C_V = \frac{C_t}{1 + \dfrac{P_{C_3^{=}}}{K_{17D}} + \dfrac{P_{C_{5,1}^{=}}}{K_{17DE}} + K_{17A} P_{C_{8,1}^{=}} + \cdots}$$

$$r_{17s} = k_{17s}K_{17A}\left(P_{C_{8,1}^=} - \frac{P_{C_3^=}P_{C_{5,1}^=}}{K_{17D}K_{17DE}K_{17A}K_{17s}}\right)\left(\frac{C_t}{1 + \dfrac{P_{C_3^=}}{K_{17D}} + \dfrac{P_{C_{5,1}^=}}{K_{17DE}} + K_{17A}P_{C_{8,1}^=} + \cdots}\right)^2$$
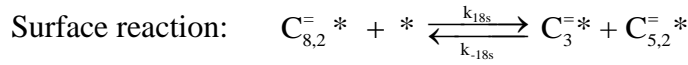
$$= \frac{k_{17s}K_{17A}C_t^2\left(P_{C_{8,1}^=} - \dfrac{P_{C_3^=}P_{C_{5,1}^=}}{K_{17D}K_{17DE}K_{17A}K_{17s}}\right)}{\left(1 + \dfrac{P_{C_3^=}}{K_{17D}} + \dfrac{P_{C_{5,1}^=}}{K_{17DE}} + K_{17A}P_{C_{8,1}^=} + \cdots\right)^2} = \frac{k_{17}\left(P_{C_{8,1}^=} - \dfrac{P_{C_3^=}P_{C_{5,1}^=}}{K_{17P}}\right)}{\left(1 + \dfrac{P_{C_3^=}}{K_{17D}} + \dfrac{P_{C_{5,1}^=}}{K_{17DE}} + K_{17A}P_{C_{8,1}^=} + \cdots\right)^2}$$

$$k_{17} = k_{17s}K_{17A}C_t^2, \ K_{17P} = K_{17D}K_{17DE}K_{17A}K_{17s}, \ K_{17A} = \frac{1}{K_{9D}}$$

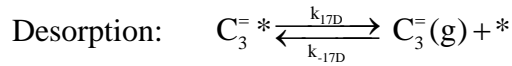**Reaction 14:** $C_{8,2}^=(g) \underset{k_{-18}}{\overset{k_{18}}{\rightleftharpoons}} C_3^=(g) + C_{5,2}^=(g)$ on acid sites of HZSM-5

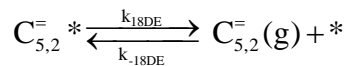Adsorption: $C_{8,2}^=(g) + {}^* \underset{k_{-18A}}{\overset{k_{18A}}{\rightleftharpoons}} C_{8,2}^= {}^*$

$$r_{18A} = k_{18A}\left(P_{C_{8,2}^=}C_V - \frac{C_{C_{8,2}^= {}^*}}{K_{18A}}\right), \ C_{C_{8,2}^= {}^*} = K_{18A}P_{C_{8,2}^=}C_V$$

Surface reaction: $C_{8,2}^= {}^* + {}^* \underset{k_{-18s}}{\overset{k_{18s}}{\rightleftharpoons}} C_3^= {}^* + C_{5,2}^= {}^*$

$$r_{18s} = k_{18s}\left(C_{C_{8,2}^= {}^*}C_V - \frac{C_{C_3^= {}^*}C_{C_{5,2}^= {}^*}}{K_{18s}}\right)$$

Desorption: $C_3^= {}^* \underset{k_{-17D}}{\overset{k_{17D}}{\rightleftharpoons}} C_3^=(g) + {}^*$

$$r_{17D} = k_{17D}\left(C_{C_3^= {}^*} - \frac{P_{C_3^=}C_V}{K_{17D}}\right), \ C_{C_3^= {}^*} = \frac{P_{C_3^=}C_V}{K_{17D}}$$

$$C_{5,2}^= {}^* \underset{k_{-18DE}}{\overset{k_{18DE}}{\rightleftharpoons}} C_{5,2}^=(g) + {}^*$$

$$r_{18DE} = k_{18DE} \left(C_{C_{5,2}^= *} - \frac{P_{C_{5,2}^=} C_V}{K_{18DE}} \right), \; C_{C_{5,2}^= *} = \frac{P_{C_{5,2}^=} C_V}{K_{18DE}}$$

$$r_{18s} = k_{18s} \left(C_{8,2}^= C_V - \frac{C_{C_3^= *} C_{C_{5,2}^= *}}{K_{18s}} \right) = k_{18s} \left(K_{18A} P_{C_{8,2}^=} C_V^2 - \frac{\dfrac{P_{C_3^=} C_V}{K_{17D}} \dfrac{P_{C_{5,2}^=} C_V}{K_{18DE}}}{K_{18s}} \right)$$

$$= k_{18s} K_{18A} \left(P_{C_{8,2}^=} - \frac{P_{C_3^=} P_{C_{5,2}^=}}{K_{17D} K_{18DE} K_{18A} K_{18s}} \right) C_V^2$$

$$C_t = C_V + C_{C_3^= *} + C_{C_{5,2}^= *} + C_{C_{8,2}^= *} \cdots = C_V + \frac{P_{C_3^=} C_V}{K_{17D}} + \frac{P_{C_{5,2}^=} C_V}{K_{18DE}} + K_{18A} P_{C_{8,2}^=} C_V \cdots$$
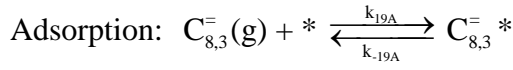
$$C_V = \frac{C_t}{1 + \dfrac{P_{C_3^=}}{K_{17D}} + \dfrac{P_{C_{5,2}^=}}{K_{18DE}} + K_{18A} P_{C_{8,2}^=} + \cdots}$$

$$r_{18s} = k_{18s} K_{18A} \left(P_{C_{8,2}^=} - \frac{P_{C_3^=} P_{C_{5,2}^=}}{K_{17D} K_{18DE} K_{18A} K_{18s}} \right) \left(\frac{C_t}{1 + \dfrac{P_{C_3^=}}{K_{17D}} + \dfrac{P_{C_{5,2}^=}}{K_{18DE}} + K_{18A} P_{C_{8,2}^=} + \cdots} \right)^2$$
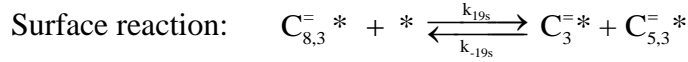
$$= \frac{k_{18s} K_{18A} C_t^2 \left(P_{C_{8,2}^=} - \dfrac{P_{C_3^=} P_{C_{5,2}^=}}{K_{17D} K_{18DE} K_{18A} K_{18s}} \right)}{\left(1 + \dfrac{P_{C_3^=}}{K_{17D}} + \dfrac{P_{C_{5,2}^=}}{K_{18DE}} + K_{18A} P_{C_{8,2}^=} + \cdots \right)^2} = \frac{k_{18} \left(P_{C_{8,2}^=} - \dfrac{P_{C_3^=} P_{C_{5,2}^=}}{K_{18P}} \right)}{\left(1 + \dfrac{P_{C_3^=}}{K_{17D}} + \dfrac{P_{C_{5,2}^=}}{K_{18DE}} + K_{18A} P_{C_{8,2}^=} + \cdots \right)^2}$$

$$k_{18} = k_{18s} K_{18A} C_t^2, \; K_{18P} = K_{17D} K_{18DE} K_{18A} K_{18s}, \; K_{18A} = \frac{1}{K_{10D}}$$
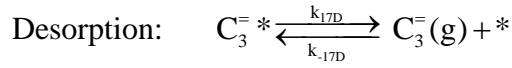
Reaction 15: $\quad C_{8,3}^=(g) \xrightleftharpoons[k_{-19}]{k_{19}} C_3^=(g) + C_{5,3}^=(g) \qquad$ on acid sites of HZSM-5

Adsorption: $\quad C_{8,3}^=(g) + * \xrightleftharpoons[k_{-19A}]{k_{19A}} C_{8,3}^= *$
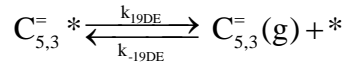
$$r_{19A} = k_{19A}\left(P_{C_{8,3}^=} C_V - \frac{C_{C_{8,3}^= *}}{K_{19A}} \right), \quad C_{C_{8,3}^= *} = K_{19A} P_{C_{8,3}^=} C_V$$

Surface reaction: $\quad C_{8,3}^= * \; + \; * \xrightleftharpoons[k_{-19s}]{k_{19s}} C_3^= * + C_{5,3}^= *$

$$r_{19s} = k_{19s}\left(C_{C_{8,3}^= *} C_V - \frac{C_{C_3^= *} C_{C_{5,3}^= *}}{K_{19s}} \right)$$

Desorption: $\quad C_3^= * \xrightleftharpoons[k_{-17D}]{k_{17D}} C_3^=(g) + *$

$$r_{17D} = k_{17D}\left(C_{C_3^= *} - \frac{P_{C_3^=} C_V}{K_{17D}} \right), \quad C_{C_3^= *} = \frac{P_{C_3^=} C_V}{K_{17D}}$$

$$C_{5,3}^= * \xrightleftharpoons[k_{-19DE}]{k_{19DE}} C_{5,3}^=(g) + *$$

$$r_{19DE} = k_{19DE}\left(C_{C_{5,3}^= *} - \frac{P_{C_{5,3}^=} C_V}{K_{19DE}} \right), \quad C_{C_{5,3}^= *} = \frac{P_{C_{5,3}^=} C_V}{K_{19DE}}$$

$$r_{19s} = k_{19s}\left(C_{C_{8,3}^= *} C_V - \frac{C_{C_3^= *} C_{C_{5,3}^= *}}{K_{19s}} \right) = k_{19s}\left(K_{19A} P_{C_{8,3}^=} C_V^2 - \frac{\dfrac{P_{C_3^=} C_V}{K_{17D}}\dfrac{P_{C_{5,3}^=} C_V}{K_{19DE}}}{K_{19s}} \right)$$

$$= k_{19s} K_{19A}\left(P_{C_{8,3}^=} - \frac{P_{C_3^=} P_{C_{5,3}^=}}{K_{17D} K_{19DE} K_{19A} K_{19s}} \right) C_V^2$$

$$C_t = C_V + C_{C_3^= *} + C_{C_{5,3}^= *} + C_{C_{8,3}^= *} \cdots = C_V + \frac{P_{C_3^=} C_V}{K_{17D}} + \frac{P_{C_{5,3}^=} C_V}{K_{19DE}} + K_{19A} P_{C_{8,3}^=} C_V \cdots$$
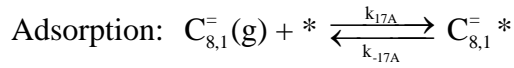
$$C_V = \frac{C_t}{1 + \dfrac{P_{C_3^=}}{K_{17D}} + \dfrac{P_{C_{5,3}^=}}{K_{19DE}} + K_{19A} P_{C_{8,3}^=} + \cdots}$$

$$r_{19s} = k_{19s} K_{19A} \left(P_{C_{8,3}^=} - \frac{P_{C_3^=} P_{C_{5,3}^=}}{K_{17D} K_{19DE} K_{19A} K_{19s}} \right) \left(\frac{C_t}{1 + \dfrac{P_{C_3^=}}{K_{17D}} + \dfrac{P_{C_{5,3}^=}}{K_{19DE}} + K_{19A} P_{C_{8,3}^=} + \cdots} \right)^2$$
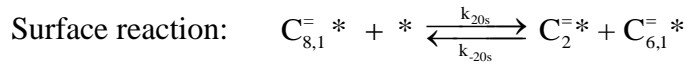
$$= \frac{k_{19s} K_{19A} C_t^2 \left(P_{C_{8,3}^=} - \dfrac{P_{C_3^=} P_{C_{5,3}^=}}{K_{17D} K_{19DE} K_{19A} K_{19s}} \right)}{\left(1 + \dfrac{P_{C_3^=}}{K_{17D}} + \dfrac{P_{C_{5,3}^=}}{K_{19DE}} + K_{19A} P_{C_{8,3}^=} + \cdots \right)^2} = \frac{k_{19} \left(P_{C_{8,3}^=} - \dfrac{P_{C_3^=} P_{C_{5,3}^=}}{K_{19P}} \right)}{\left(1 + \dfrac{P_{C_3^=}}{K_{17D}} + \dfrac{P_{C_{5,3}^=}}{K_{19DE}} + K_{19A} P_{C_{8,3}^=} + \cdots \right)^2}$$

$$k_{19} = k_{19s} K_{19A} C_t^2, \quad K_{19P} = K_{17D} K_{19DE} K_{19A} K_{19s}, \quad K_{19A} = \frac{1}{K_{11D}}$$
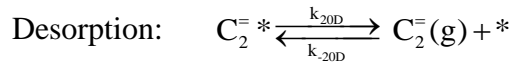
Reaction 16 $\quad C_{8,1}^=(g) \underset{k_{-20}}{\overset{k_{20}}{\rightleftharpoons}} C_2^=(g) + C_{6,1}^=(g) \qquad$ on acid sites of HZSM-5

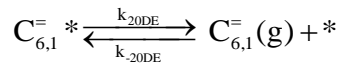Adsorption: $\ C_{8,1}^=(g) + * \underset{k_{-17A}}{\overset{k_{17A}}{\rightleftharpoons}} C_{8,1}^= *$

$$r_{17A} = k_{17A} \left(P_{C_{8,1}^=} C_V - \frac{C_{C_{8,1}^= *}}{K_{17A}} \right), \ C_{C_{8,1}^= *} = K_{17A} P_{C_{8,1}^=} C_V, \ K_{17A} = \frac{1}{K_{9D}}$$

Surface reaction: $\quad C_{8,1}^= * \ + \ * \underset{k_{-20s}}{\overset{k_{20s}}{\rightleftharpoons}} C_2^= * + C_{6,1}^= *$

$$r_{20s} = k_{20s} \left(C_{C_{8,1}^= *} C_V - \frac{C_{C_2^= *} C_{C_{6,1}^= *}}{K_{20s}} \right)$$

Desorption: $\quad C_2^= * \underset{k_{-20D}}{\overset{k_{20D}}{\rightleftharpoons}} C_2^=(g) + *$

$$r_{20D} = k_{20D} \left(C_{C_2^= *} - \frac{P_{C_2^=} C_V}{K_{20D}} \right), \ C_{C_2^= *} = \frac{P_{C_2^=} C_V}{K_{20D}}$$

$$C_{6,1}^= * \underset{k_{-20DE}}{\overset{k_{20DE}}{\rightleftharpoons}} C_{6,1}^=(g) + *$$

$$r_{20DE} = k_{20DE}\left(C_{C_{6,1}^{=}*} - \frac{P_{C_{6,1}^{=}}C_V}{K_{20DE}}\right), \quad C_{C_{6,1}^{=}*} = \frac{P_{C_{6,1}^{=}}C_V}{K_{20DE}}$$

$$r_{20s} = k_{20s}\left(C_{C_{8,1}^{=}*}C_V - \frac{C_{C_2^{=}*}C_{C_{6,1}^{=}*}}{K_{20s}}\right) = k_{20s}\left(K_{17A}P_{C_{8,1}^{=}}C_V^2 - \frac{\frac{P_{C_2^{=}}C_V}{K_{20D}}\frac{P_{C_{6,1}^{=}}C_V}{K_{20DE}}}{K_{20s}}\right)$$

$$= k_{20s}K_{17A}\left(P_{C_{8,1}^{=}} - \frac{P_{C_2^{=}}P_{C_{6,1}^{=}}}{K_{20D}K_{20DE}K_{20s}K_{17A}}\right)C_V^2$$

$$C_t = C_V + C_{C_2^{=}*} + C_{C_{6,1}^{=}*} + C_{C_{8,1}^{=}*} + \cdots = C_V + \frac{P_{C_2^{=}}C_V}{K_{20D}} + \frac{P_{C_{6,1}^{=}}C_V}{K_{20DE}} + K_{17A}P_{C_{8,1}^{=}}C_V + \cdots$$
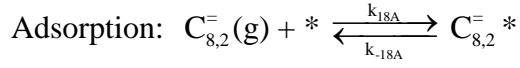
$$C_V = \frac{C_t}{1 + \frac{P_{C_2^{=}}}{K_{20D}} + \frac{P_{C_{6,1}^{=}}}{K_{20DE}} + K_{17A}P_{C_{8,1}^{=}} + \cdots}$$

$$r_{20s} = k_{20s}K_{17A}\left(P_{C_{8,1}^{=}} - \frac{P_{C_2^{=}}P_{C_{6,1}^{=}}}{K_{20D}K_{20DE}K_{20s}K_{17A}}\right)\left(\frac{C_t}{1 + \frac{P_{C_2^{=}}}{K_{20D}} + \frac{P_{C_{6,1}^{=}}}{K_{20DE}} + K_{17A}P_{C_{8,1}^{=}} + \cdots}\right)^2$$
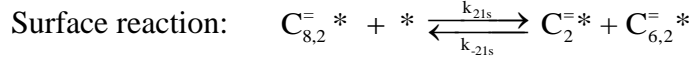
$$r_{20s} = \frac{k_{20s}K_{17A}C_t^2\left(P_{C_{8,1}^{=}} - \frac{P_{C_2^{=}}P_{C_{6,1}^{=}}}{K_{20D}K_{20DE}K_{20s}K_{17A}}\right)}{\left(1 + \frac{P_{C_2^{=}}}{K_{20D}} + \frac{P_{C_{6,1}^{=}}}{K_{20DE}} + K_{17A}P_{C_{8,1}^{=}} + \cdots\right)^2} = \frac{k_{20}\left(P_{C_{8,1}^{=}} - \frac{P_{C_2^{=}}P_{C_{6,1}^{=}}}{K_{20P}}\right)}{\left(1 + \frac{P_{C_2^{=}}}{K_{20D}} + \frac{P_{C_{6,1}^{=}}}{K_{20DE}} + K_{17A}P_{C_{8,1}^{=}} + \cdots\right)^2}$$

$$k_{20} = k_{20s}K_{17A}C_t^2 \ , \quad K_{20P} = K_{20D}K_{20DE}K_{20s}K_{17A} \ , \quad K_{17A} = \frac{1}{K_{9D}}$$
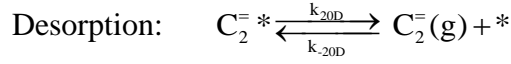
Reaction 17: $\quad C_{8,2}^{=}(g) \underset{k_{-21}}{\overset{k_{21}}{\rightleftharpoons}} C_2^{=}(g) + C_{6,2}^{=}(g) \qquad$ on acid sites of HZSM-5

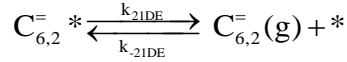Adsorption: $\quad C_{8,2}^{=}(g) + * \underset{k_{-18A}}{\overset{k_{18A}}{\rightleftharpoons}} C_{8,2}^{=} *$

$$r_{18A} = k_{18A}\left(P_{C_{8,2}^{=}} C_V - \frac{C_{C_{8,2}^{=}*}}{K_{18A}}\right), \; C_{C_{8,2}^{=}*} = K_{18A} P_{C_{8,2}^{=}} C_V, \; K_{18A} = \frac{1}{K_{10D}}$$

Surface reaction: $\quad C_{8,2}^{=} * + * \underset{k_{-21s}}{\overset{k_{21s}}{\rightleftharpoons}} C_2^{=}* + C_{6,2}^{=} *$

$$r_{21s} = k_{21s}\left(C_{C_{8,2}^{=}*} C_V - \frac{C_{C_2^{=}*} C_{C_{6,2}^{=}*}}{K_{21s}}\right)$$

Desorption: $\quad C_2^{=} * \underset{k_{-20D}}{\overset{k_{20D}}{\rightleftharpoons}} C_2^{=}(g) + *$

$$r_{20D} = k_{20D}\left(C_{C_2^{=}*} - \frac{P_{C_2^{=}} C_V}{K_{20D}}\right), \; C_{C_2^{=}*} = \frac{P_{C_2^{=}} C_V}{K_{20D}}$$

$$C_{6,2}^{=} * \underset{k_{-21DE}}{\overset{k_{21DE}}{\rightleftharpoons}} C_{6,2}^{=}(g) + *$$

$$r_{21DE} = k_{21DE}\left(C_{C_{6,2}^{=}*} - \frac{P_{C_{6,2}^{=}} C_V}{K_{21DE}}\right), \; C_{C_{6,2}^{=}*} = \frac{P_{C_{6,2}^{=}} C_V}{K_{21DE}}$$

$$r_{21s} = k_{21s}\left(C_{C_{8,2}^{=}*} C_V - \frac{C_{C_2^{=}*} C_{C_{6,2}^{=}*}}{K_{21s}}\right) = k_{21s}\left(K_{18A} P_{C_{8,2}^{=}} C_V^2 - \frac{\dfrac{P_{C_2^{=}} C_V}{K_{20D}} \dfrac{P_{C_{6,2}^{=}} C_V}{K_{21DE}}}{K_{21s}}\right)$$

$$= k_{21s} K_{18A}\left(P_{C_{8,2}^{=}} - \frac{P_{C_2^{=}} P_{C_{6,2}^{=}}}{K_{20D} K_{21DE} K_{21s} K_{18A}}\right) C_V^2$$

$$C_t = C_V + C_{C_2^{=}*} + C_{C_{6,2}^{=}*} + C_{C_{8,2}^{=}*} + \cdots = C_V + \frac{P_{C_2^{=}} C_V}{K_{20D}} + \frac{P_{C_{6,2}^{=}} C_V}{K_{21DE}} + K_{18A} P_{C_{8,2}^{=}} C_V + \cdots$$

$$C_V = \frac{C_t}{1 + \dfrac{P_{C_2^{=}}}{K_{20D}} + \dfrac{P_{C_{6,2}^{=}}}{K_{21DE}} + K_{18A} P_{C_{8,2}^{=}} + \cdots}$$

$$r_{21s} = k_{21s}K_{18A}\left(P_{C_{8,2}^=} - \frac{P_{C_2^=}P_{C_{6,2}^=}}{K_{20D}K_{21DE}K_{21s}K_{18A}}\right)\left(\frac{C_t}{1 + \frac{P_{C_2^=}}{K_{20D}} + \frac{P_{C_{6,2}^=}}{K_{21DE}} + K_{18A}P_{C_{8,2}^=} + \cdots}\right)^2$$
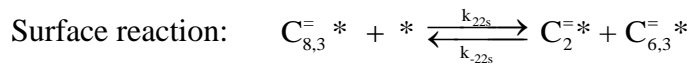
$$r_{21s} = \frac{k_{21s}K_{18A}C_t^2\left(P_{C_{8,2}^=} - \frac{P_{C_2^=}P_{C_{6,2}^=}}{K_{20D}K_{21DE}K_{21s}K_{18A}}\right)}{\left(1 + \frac{P_{C_2^=}}{K_{20D}} + \frac{P_{C_{6,2}^=}}{K_{21DE}} + K_{18A}P_{C_{8,2}^=} + \cdots\right)^2} = \frac{k_{21}\left(P_{C_{8,2}^=} - \frac{P_{C_2^=}P_{C_{6,2}^=}}{K_{21P}}\right)}{\left(1 + \frac{P_{C_2^=}}{K_{20D}} + \frac{P_{C_{6,2}^=}}{K_{21DE}} + K_{18A}P_{C_{8,2}^=} + \cdots\right)^2}$$

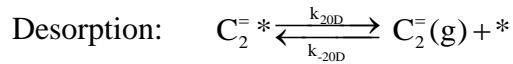$$k_{21} = k_{21s}K_{18A}C_t^2 \ , \ K_{21P} = K_{20D}K_{21DE}K_{21s}K_{18A} \ , \ K_{18A} = \frac{1}{K_{10D}}$$

Reaction 18: $C_{8,3}^=(g) \xrightleftharpoons[k_{-22}]{k_{22}} C_2^=(g) + C_{6,3}^=(g)$ on acid sites of HZSM-5
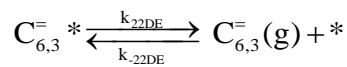
Adsorption: $C_{8,3}^=(g) + * \xrightleftharpoons[k_{-19A}]{k_{19A}} C_{8,3}^= *$
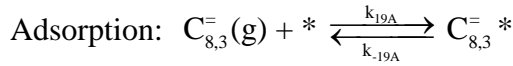
$$r_{19A} = k_{19A}\left(P_{C_{8,3}^=}C_V - \frac{C_{C_{8,3}^= *}}{K_{19A}}\right), \ C_{C_{8,3}^= *} = K_{19A}P_{C_{8,3}^=}C_V, \ K_{19A} = \frac{1}{K_{11D}}$$

Surface reaction: $C_{8,3}^= * \ + \ * \xrightleftharpoons[k_{-22s}]{k_{22s}} C_2^= * + C_{6,3}^= *$

$$r_{22s} = k_{22s}\left(C_{C_{8,3}^= *}C_V - \frac{C_{C_2^= *}C_{C_{6,3}^= *}}{K_{22s}}\right)$$

Desorption: $C_2^= * \xrightleftharpoons[k_{-20D}]{k_{20D}} C_2^=(g) + *$

$$r_{20D} = k_{20D}\left(C_{C_2^= *} - \frac{P_{C_2^=}C_V}{K_{20D}}\right), \ C_{C_2^= *} = \frac{P_{C_2^=}C_V}{K_{20D}}$$

$$C_{6,3}^= * \xrightleftharpoons[k_{-22DE}]{k_{22DE}} C_{6,3}^=(g) + *$$

$$r_{22DE} = k_{22DE}\left(C_{C_{6,3}^=*} - \frac{P_{C_{6,3}^=}C_V}{K_{22DE}}\right), \quad C_{C_{6,3}^=*} = \frac{P_{C_{6,3}^=}C_V}{K_{22DE}}$$

$$r_{22s} = k_{22s}\left(C_{C_{8,3}^=*}C_V - \frac{C_{C_2^=*}C_{C_{6,3}^=*}}{K_{22s}}\right) = k_{22s}\left(K_{19A}P_{C_{8,3}^=}C_V^2 - \frac{\frac{P_{C_2^=}C_V}{K_{20D}}\frac{P_{C_{6,3}^=}C_V}{K_{22DE}}}{K_{22s}}\right)$$

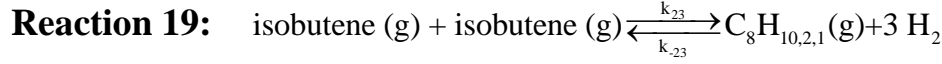$$= k_{22s}K_{19A}\left(P_{C_{8,3}^=} - \frac{P_{C_2^=}P_{C_{6,3}^=}}{K_{20D}K_{22DE}K_{22s}K_{19A}}\right)C_V^2$$

$$C_t = C_V + C_{C_2^=*} + C_{C_{6,3}^=*} + C_{C_{8,3}^=*} + \cdots = C_V + \frac{P_{C_2^=}C_V}{K_{20D}} + \frac{P_{C_{6,3}^=}C_V}{K_{22DE}} + K_{19A}P_{C_{8,3}^=}C_V + \cdots$$

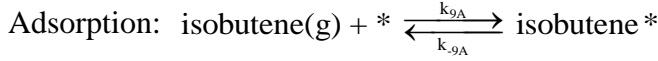$$C_V = \frac{C_t}{1 + \frac{P_{C_2^=}}{K_{20D}} + \frac{P_{C_{6,3}^=}}{K_{22DE}} + K_{19A}P_{C_{8,3}^=} + \cdots}$$

$$r_{22s} = k_{22s}K_{19A}\left(P_{C_{8,3}^=} - \frac{P_{C_2^=}P_{C_{6,3}^=}}{K_{20D}K_{22DE}K_{22s}K_{19A}}\right)\left(\frac{C_t}{1 + \frac{P_{C_2^=}}{K_{20D}} + \frac{P_{C_{6,3}^=}}{K_{22DE}} + K_{19A}P_{C_{8,3}^=} + \cdots}\right)^2$$

$$r_{22s} = \frac{k_{22s}K_{19A}C_t^2\left(P_{C_{8,3}^=} - \frac{P_{C_2^=}P_{C_{6,3}^=}}{K_{20D}K_{22DE}K_{22s}K_{19A}}\right)}{\left(1 + \frac{P_{C_2^=}}{K_{20D}} + \frac{P_{C_{6,3}^=}}{K_{22DE}} + K_{19A}P_{C_{8,3}^=} + \cdots\right)^2} = \frac{k_{22}\left(P_{C_{8,3}^=} - \frac{P_{C_2^=}P_{C_{6,3}^=}}{K_{22P}}\right)}{\left(1 + \frac{P_{C_2^=}}{K_{20D}} + \frac{P_{C_{6,3}^=}}{K_{22DE}} + K_{19A}P_{C_{8,3}^=} + \cdots\right)^2}$$

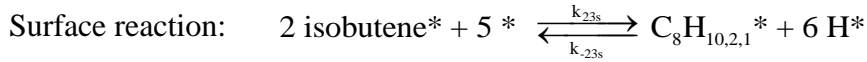$$k_{22} = k_{22s}K_{19A}C_t^2 \ , \ K_{22P} = K_{20D}K_{22DE}K_{22s}K_{19A} \ , \ K_{19A} = \frac{1}{K_{11D}}$$

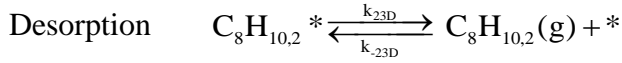**Reaction 19:**   isobutene (g) + isobutene (g) $\underset{k_{-23}}{\overset{k_{23}}{\rightleftharpoons}}$ $C_8H_{10,2,1}$(g)+3 H_2

on acid sites of HZSM-5, formation of aromatics

Adsorption: isobutene(g) + * $\underset{k_{-9A}}{\overset{k_{9A}}{\rightleftharpoons}}$ isobutene *
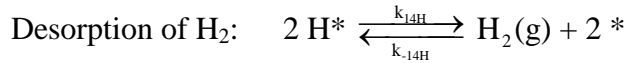
$$r_{9A} = k_{9A}\left(P_{isobutene}C_V - \frac{C_{isobutene*}}{K_{9A}}\right),\ C_{isobutene*} = K_{9A}P_{isobutene}C_V$$

Surface reaction: 2 isobutene* + 5 * $\underset{k_{-23s}}{\overset{k_{23s}}{\rightleftharpoons}}$ $C_8H_{10,2,1}$* + 6 H*

$$r_{23s} = k_{23s}\left(C_{isobutene*}^2 C_V^5 - \frac{C_{C_8H_{10,2,1}*}C_{H*}^6}{K_{23s}}\right)$$

Desorption $C_8H_{10,2}$ * $\underset{k_{-23D}}{\overset{k_{23D}}{\rightleftharpoons}}$ $C_8H_{10,2}$(g) + *

$$r_{23D} = k_{23D}\left(C_{C_8H_{10,2}*} - \frac{P_{C_8H_{10,2,1}}C_V}{K_{23D}}\right),\ C_{C_8H_{10,2,1}*} = \frac{P_{C_8H_{10,2,1}}C_V}{K_{23D}}$$

Desorption of H_2:   2 H* $\underset{k_{-14H}}{\overset{k_{14H}}{\rightleftharpoons}}$ H_2(g) + 2 *

$$r_{14H} = k_{14H}\left(C_{H*}^2 - \frac{P_{H_2}C_V^2}{K_{14H}}\right),\ K_{14H} = \frac{k_{14H}}{k_{-14H}},\ C_{H*}^2 = \frac{P_{H_2}C_V^2}{K_{14H}},\ C_{H*} = \sqrt{\frac{P_{H_2}}{K_{14H}}}C_V$$

$$r_{23s} = k_{23s}\left(C_{isobutene*}^2 C_V^5 - \frac{C_{C_8H_{10,2,1}*}C_{H*}^6}{K_{23s}}\right) = k_{23s}\left(K_{9A}^2 P_{isobutene}^2 C_V^7 - \frac{\frac{P_{C_8H_{10,2,1}}}{K_{23D}}\frac{P_{H_2}^3}{K_{14H}^3}C_V^7}{K_{23s}}\right)$$
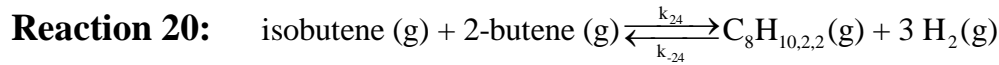
$$C_t = C_V + C_{isobutene*} + C_{C_8H_{10,2,1}*} + C_{H*} + \cdots = C_V + K_{9A}P_{isobutene}C_V + \frac{P_{C_8H_{10,2,1}}C_V}{K_{23D}} + \sqrt{\frac{P_{H_2}}{K_{14H}}}C_V + \cdots$$

$$C_V = \frac{C_t}{1 + K_{9A}P_{isobutene} + \frac{P_{C_8H_{10,2,1}}}{K_{23D}} + \sqrt{\frac{P_{H_2}}{K_{14H}}} + \cdots}$$
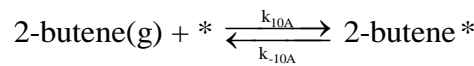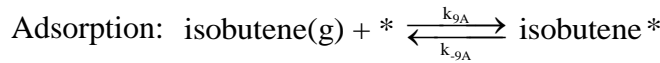
$$r_{23s} = k_{23s}K_{9A}^2 \left(P_{isobutene}^2 - \frac{P_{C_8H_{10,2,1}}P_{H_2}^3}{K_{23D}K_{14H}^3 K_{23s}K_{9A}^2} \right) \left(\frac{C_t}{1 + K_{9A}P_{isobutene} + \frac{P_{C_8H_{10,2,1}}}{K_{23D}} + \sqrt{\frac{P_{H_2}}{K_{14H}}} + \cdots} \right)^7$$

$$r_{23s} = \frac{k_{23s}K_{9A}^2 C_t^7 \left(P_{isobutene}^2 - \frac{P_{C_8H_{10,2,1}}P_{H_2}^3}{K_{23D}K_{14H}^3 K_{23s}K_{9A}^2} \right)}{\left(1 + K_{9A}P_{isobutene} + \frac{P_{C_8H_{10,2,1}}}{K_{23D}} + \sqrt{\frac{P_{H_2}}{K_{14H}}} + \cdots \right)^7} = \frac{k_{23} \left(P_{isobutene}^2 - \frac{P_{C_8H_{10,2,1}}P_{H_2}^3}{K_{23P}} \right)}{\left(1 + K_{9A}P_{isobutene} + \frac{P_{C_8H_{10,2,1}}}{K_{23D}} + \sqrt{\frac{P_{H_2}}{K_{14H}}} + \cdots \right)^7}$$

$$k_{23} = k_{23s}K_{9A}^2 C_t^7 \ , \ K_{23P} = K_{23D}K_{14H}^3 K_{23s}K_{9A}^2, \ K_{9A} = \frac{1}{K_{8D}}$$

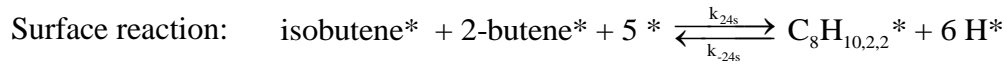**Reaction 20:** isobutene (g) + 2-butene (g) $\xrightleftharpoons[k_{-24}]{k_{24}}$ $C_8H_{10,2,2}(g)$ + 3 $H_2(g)$

on acid sites of HZSM-5, formation of aromatics

Adsorption: isobutene(g) + * $\xrightleftharpoons[k_{-9A}]{k_{9A}}$ isobutene*
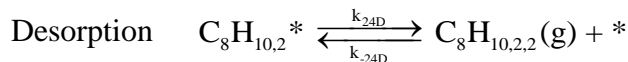
2-butene(g) + * $\xrightleftharpoons[k_{-10A}]{k_{10A}}$ 2-butene*

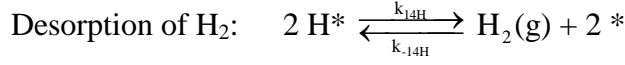$$r_{9A} = k_{9A} \left(P_{isobutene}C_V - \frac{C_{isobutene*}}{K_{9A}} \right), \ C_{isobutene*} = K_{9A}P_{isobutene}C_V$$

$$r_{10A} = k_{10A} \left(P_{2\text{-butene}}C_V - \frac{C_{2\text{-butene}*}}{K_{10A}} \right), \ C_{2\text{-butene}*} = K_{10A}P_{2\text{-butene}}C_V$$

Surface reaction: isobutene* + 2-butene* + 5 * $\xrightleftharpoons[k_{-24s}]{k_{24s}}$ $C_8H_{10,2,2}$* + 6 H*

$$r_{24s} = k_{24s} \left(C_{isobutene*}C_{2\text{-butene}*}C_V^5 - \frac{C_{C_8H_{10,2,2}*}C_{H*}^6}{K_{24s}} \right)$$

Desorption $C_8H_{10,2}$* $\xrightleftharpoons[k_{-24D}]{k_{24D}}$ $C_8H_{10,2,2}(g)$ + *

$$r_{24D} = k_{24D} \left(C_{C_8H_{10,2,2}*} - \frac{P_{C_8H_{10,2,2}} C_V}{K_{24D}} \right), \quad C_{C_8H_{10,2,2}*} = \frac{P_{C_8H_{10,2,2}} C_V}{K_{24D}}$$

Desorption of H_2: $2\,H* \underset{k_{-14H}}{\overset{k_{14H}}{\rightleftharpoons}} H_2(g) + 2\,*$

$$r_{14H} = k_{14H} \left(C_{H*}^2 - \frac{P_{H_2} C_V^2}{K_{14H}} \right), \quad K_{14H} = \frac{k_{14H}}{k_{-14H}}, \quad C_{H*}^2 = \frac{P_{H_2} C_V^2}{K_{14H}}, \quad C_{H*} = \sqrt{\frac{P_{H_2}}{K_{14H}}} C_V$$

$$r_{24s} = k_{24s} \left(C_{\text{isobutene}*} C_{\text{2-butene}*} C_V^5 - \frac{C_{C_8H_{10,2,2}*} C_{H*}^6}{K_{24s}} \right) = k_{24s} \left(K_{9A} P_{\text{isobutene}} K_{10A} P_{\text{2-butene}} C_V^7 - \frac{\dfrac{P_{C_8H_{10,2,2}}}{K_{24D}} \dfrac{P_{H_2}^3}{K_{14H}^3} C_V^7}{K_{24s}} \right)$$

$$C_t = C_V + C_{\text{isobutene}*} + C_{\text{2-butene}*} + C_{C_8H_{10,2,2}*} + C_{H*} + \cdots$$

$$= C_V + K_{9A} P_{\text{isobutene}} C_V + K_{10A} P_{\text{2-butene}} C_V + \frac{P_{C_8H_{10,2,2}} C_V}{K_{24D}} + \sqrt{\frac{P_{H_2}}{K_{14H}}} C_V + \cdots$$
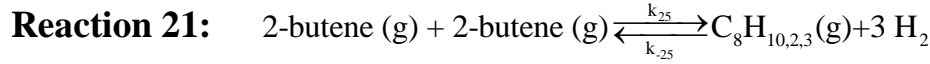
$$C_V = \frac{C_t}{1 + K_{9A} P_{\text{isobutene}} + K_{10A} P_{\text{2-butene}} + \dfrac{P_{C_8H_{10,2,2}}}{K_{24D}} + \sqrt{\dfrac{P_{H_2}}{K_{14H}}} + \cdots}$$

$$r_{24s} = k_{24s} \left(K_{9A} P_{\text{isobutene}} K_{10A} P_{\text{2-butene}} - \frac{\dfrac{P_{C_8H_{10,2,2}}}{K_{24D}} \dfrac{P_{H_2}^3}{K_{14H}^3}}{K_{24s}} \right) C_V^7$$
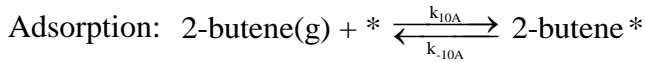
$$= \frac{k_{24s} K_{9A} K_{10A} \left(P_{\text{isobutene}} P_{\text{2-butene}} - \dfrac{P_{C_8H_{10,2,2}} P_{H_2}^3}{K_{24D} K_{14H}^3 K_{24s} K_{9A} K_{10A}} \right) C_t^7}{\left(1 + K_{9A} P_{\text{isobutene}} + K_{10A} P_{\text{2-butene}} + \dfrac{P_{C_8H_{10,2,2}}}{K_{24D}} + \sqrt{\dfrac{P_{H_2}}{K_{14H}}} + \cdots \right)^7}$$

$$r_{24s} = \frac{k_{24} \left(P_{\text{isobutene}} P_{\text{2-butene}} - \dfrac{P_{C_8H_{10,2,2}} P_{H_2}^3}{K_{24P}} \right)}{\left(1 + K_{9A} P_{\text{isobutene}} + K_{10A} P_{\text{2-butene}} + \dfrac{P_{C_8H_{10,2,2}}}{K_{24D}} + \sqrt{\dfrac{P_{H_2}}{K_{14H}}} + \cdots \right)^7}$$
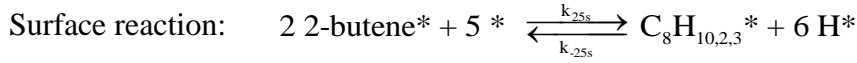
$$k_{24} = k_{24s}K_{9A}K_{10A}C_t^7, \quad K_{24P} = K_{24D}K_{14H}^3 K_{24s}K_{9A}K_{10A}, \quad K_{9A} = \frac{1}{K_{8D}}, \quad K_{10A} = \frac{1}{K_{7D}}$$
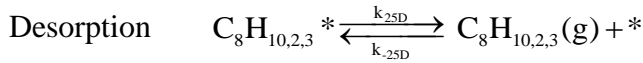
Reaction 21: $\quad$ 2-butene (g) + 2-butene (g) $\underset{k_{-25}}{\overset{k_{25}}{\rightleftharpoons}}$ C$_8$H$_{10,2,3}$(g)+3 H$_2$

on acid sites of HZSM-5, formation of aromatics

Adsorption: 2-butene(g) + * $\underset{k_{-10A}}{\overset{k_{10A}}{\rightleftharpoons}}$ 2-butene *
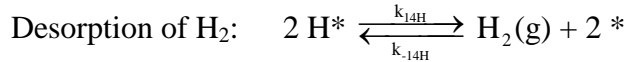
$$r_{10A} = k_{10A}\left(P_{\text{2-butene}}C_V - \frac{C_{\text{2-butene}*}}{K_{10A}} \right), \quad C_{\text{2-butene}*} = K_{10A}P_{\text{2-butene}}C_V$$

Surface reaction: $\quad$ 2 2-butene* + 5 * $\underset{k_{-25s}}{\overset{k_{25s}}{\rightleftharpoons}}$ C$_8$H$_{10,2,3}$* + 6 H*

$$r_{25s} = k_{25s}\left(C_{\text{2-butene}*}^2 C_V^5 - \frac{C_{C_8H_{10,2,3}*}C_{H*}^6}{K_{25s}} \right)$$

Desorption $\quad$ C$_8$H$_{10,2,3}$* $\underset{k_{-25D}}{\overset{k_{25D}}{\rightleftharpoons}}$ C$_8$H$_{10,2,3}$(g) + *

$$r_{25D} = k_{25D}\left(C_{C_8H_{10,2,3}*} - \frac{P_{C_8H_{10,2,3}}C_V}{K_{25D}} \right), \quad C_{C_8H_{10,2,3}*} = \frac{P_{C_8H_{10,2,3}}C_V}{K_{25D}}$$

Desorption of H$_2$: $\quad$ 2 H* $\underset{k_{-14H}}{\overset{k_{14H}}{\rightleftharpoons}}$ H$_2$(g) + 2 *

$$r_{14H} = k_{14H}\left(C_{H*}^2 - \frac{P_{H_2}C_V^2}{K_{14H}} \right), \quad K_{14H} = \frac{k_{14H}}{k_{-14H}}, \quad C_{H*}^2 = \frac{P_{H_2}C_V^2}{K_{14H}}, \quad C_{H*} = \sqrt{\frac{P_{H_2}}{K_{14H}}}C_V$$

$$r_{25s} = k_{25s}\left(C_{\text{2-butene}*}^2 C_V^5 - \frac{C_{C_8H_{10,2,3}*}C_{H*}^6}{K_{25s}} \right) = k_{25s}\left(K_{10A}^2 P_{\text{2-butene}}^2 C_V^7 - \frac{\dfrac{P_{C_8H_{10,2,3}}}{K_{25D}}\dfrac{P_{H_2}^3}{K_{14H}^3}C_V^7}{K_{25s}} \right)$$

$$C_t = C_V + C_{\text{2-butene}*} + C_{C_8H_{10,2,3}*} + C_{H*} + \cdots = C_V + K_{10A}P_{\text{2-butene}}C_V + \frac{P_{C_8H_{10,2,3}}C_V}{K_{25D}} + \sqrt{\frac{P_{H_2}}{K_{14H}}}C_V + \cdots$$

$$C_V = \cfrac{C_t}{1 + K_{10A}P_{\text{2-butene}} + \cfrac{P_{C_8H_{10,2,3}}}{K_{25D}} + \sqrt{\cfrac{P_{H_2}}{K_{14H}}} + \cdots}$$

$$r_{25s} = k_{25s}K_{10A}^2 \left(P_{\text{2-butene}}^2 - \frac{P_{C_8H_{10,2,3}}P_{H_2}^3}{K_{25D}K_{14H}^3K_{25s}K_{10A}^2} \right) \left(\cfrac{C_t}{1 + K_{10A}P_{\text{2-butene}} + \cfrac{P_{C_8H_{10,2,3}}}{K_{25D}} + \sqrt{\cfrac{P_{H_2}}{K_{14H}}} + \cdots} \right)^7$$

$$r_{25s} = \cfrac{k_{25s}K_{10A}^2C_t^7 \left(P_{\text{2-butene}}^2 - \cfrac{P_{C_8H_{10,2}}P_{H_2}^3}{K_{25D}K_{14H}^3K_{25s}K_{10A}^2} \right)}{\left(1 + K_{10A}P_{\text{2-butene}} + \cfrac{P_{C_8H_{10,2}}}{K_{25D}} + \sqrt{\cfrac{P_{H_2}}{K_{14H}}} + \cdots \right)^7} = \cfrac{k_{25} \left(P_{\text{2-butene}}^2 - \cfrac{P_{C_8H_{10,2}}P_{H_2}^3}{K_{25P}} \right)}{\left(1 + K_{10A}P_{\text{2-butene}} + \cfrac{P_{C_8H_{10,2}}}{K_{25D}} + \sqrt{\cfrac{P_{H_2}}{K_{14H}}} + \cdots \right)^7}$$

$$k_{25} = k_{25s}K_{10A}^2C_t^7 \;,\;\; K_{25P} = K_{25D}K_{14H}^3K_{25s}K_{10A}^2 \;,\;\; K_{10A} = \frac{1}{K_{7D}} \;,$$

Assume the species that are not involved in the reaction on the active sites as the inert (just like N_2)

Total active sites on Cu:

$$C_t(Cu) = C_V + C_{H^*} + C_{BDO^*} + C_{acetoin^*} + C_{2\text{-butanedione}^*} + C_{2\text{-butanol}^*} + C_{MEK^*} + C_{2\text{-methylpropanal}^*} + C_{isobutanol^*} + C_{N_2^*}$$

$$+ C_{2\text{-butene}^*} + C_{isobutene^*} + C_{H_2O^*} + C_{C_{8,1}^{=}{}^*} + C_{C_{8,2}^{=}{}^*} + C_{C_{8,3}^{=}{}^*} + C_{C_3^{=}{}^*} + C_{C_{5,1}^{=}{}^*} + C_{C_{5,2}^{=}{}^*} + C_{C_{5,3}^{=}{}^*}$$

$$+ C_{C_2^{=}{}^*} + C_{C_{6,1}^{=}{}^*} + C_{C_{6,2}^{=}{}^*} + C_{C_{6,3}^{=}{}^*} + C_{C_8H_{10,1}{}^*} + C_{C_8H_{10,2}{}^*}$$

$$= C_V + \sqrt{\frac{P_{H2}}{K_{1H}}} C_V + K_{1A} P_{BDO} C_V + \frac{P_{acetoin} C_V}{K_{1D}} + \frac{P_{2,3\text{-butanedione}} C_V}{K_{2D}} + \frac{P_{2\text{-butanol}} C_V}{K_{5D}}$$

$$+ K_{5A} P_{MEK} C_V + K_{6A} P_{2\text{-methylpropanal}} C_V + \frac{P_{isobutanol} C_V}{K_{6D}} + K_{N_2} P_{N_2} C_V + K_{2\text{-butene}} P_{2\text{-butene}} C_V$$

$$+ K_{isobutene} P_{isobutene} C_V + K_{H_2O} P_{H_2O} C_V + K_{C_{8,1}^{=}} P_{C_{8,1}^{=}} C_V + K_{C_{8,2}^{=}} P_{C_{8,2}^{=}} C_V + K_{C_{8,3}^{=}} P_{C_{8,3}^{=}} C_V$$

$$+ K_{C_3^{=}} P_{C_3^{=}} C_V + K_{C_{5,1}^{=}} P_{C_{5,1}^{=}} C_V + K_{C_{5,2}^{=}} P_{C_{5,2}^{=}} C_V + K_{C_{5,3}^{=}} P_{C_{5,3}^{=}} C_V + K_{C_2^{=}} P_{C_2^{=}} C_V + K_{C_{6,1}^{=}} P_{C_{6,1}^{=}} C_V$$

$$+ K_{C_{6,2}^{=}} P_{C_{6,2}^{=}} C_V + K_{C_{6,3}^{=}} P_{C_{6,3}^{=}} C_V + K_{C_8H_{10,1}} P_{C_8H_{10,1}} C_V + K_{C_8H_{10,2}} P_{C_8H_{10,2}} C_V$$

$$C_V = \frac{C_t(Cu)}{\begin{aligned}(1 + &\sqrt{\frac{P_{H2}}{K_{1H}}} + K_{1A} P_{BDO} + \frac{P_{acetoin}}{K_{1D}} + \frac{P_{2,3\text{-butanedione}}}{K_{2D}} + \frac{P_{2\text{-butanol}}}{K_{5D}} \\ &+ K_{5A} P_{MEK} + K_{6A} P_{2\text{-methylpropanal}} + \frac{P_{isobutanol}}{K_{6D}} + K_{N_2} P_{N_2} + K_{2\text{-butene}} P_{2\text{-butene}} \\ &+ K_{isobutene} P_{isobutene} + K_{H_2O} P_{H_2O} + K_{C_{8,1}^{=}} P_{C_{8,1}^{=}} + K_{C_{8,2}^{=}} P_{C_{8,2}^{=}} + K_{C_{8,3}^{=}} P_{C_{8,3}^{=}} \\ &+ K_{C_3^{=}} P_{C_3^{=}} + K_{C_{5,1}^{=}} P_{C_{5,1}^{=}} + K_{C_{5,2}^{=}} P_{C_{5,2}^{=}} + K_{C_{5,3}^{=}} P_{C_{5,3}^{=}} + K_{C_2^{=}} P_{C_2^{=}} + K_{C_{6,1}^{=}} P_{C_{6,1}^{=}} \\ &+ K_{C_{6,2}^{=}} P_{C_{6,2}^{=}} + K_{C_{6,3}^{=}} P_{C_{6,3}^{=}} + K_{C_8H_{10,1}} P_{C_8H_{10,1}} + K_{C_8H_{10,2}} P_{C_8H_{10,2}})\end{aligned}}$$

To be simple, on Cu site,

$$X = (1 + \sqrt{\frac{P_{H2}}{K_{1H}}} + K_{1A}P_{BDO} + \frac{P_{acetoin}}{K_{1D}} + \frac{P_{2,3\text{-butanedione}}}{K_{2D}} + \frac{P_{2\text{-butanol}}}{K_{5D}}$$

$$+ K_{5A}P_{MEK} + K_{6A}P_{2\text{-methylpropanal}} + \frac{P_{isobutanol}}{K_{6D}} + K_{N_2}P_{N_2} + K_{2\text{-butene}}P_{2\text{-butene}}$$

$$+ K_{isobutene}P_{isobutene} + K_{H_2O}P_{H_2O} + K_{C_{8,1}^=}P_{C_{8,1}^=} + K_{C_{8,2}^=}P_{C_{8,2}^=} + K_{C_{8,3}^=}P_{C_{8,3}^=}$$

$$+ K_{C_3^=}P_{C_3^=} + K_{C_{5,1}^=}P_{C_{5,1}^=} + K_{C_{5,2}^=}P_{C_{5,2}^=} + K_{C_{5,3}^=}P_{C_{5,3}^=} + K_{C_2^=}P_{C_2^=} + K_{C_{6,1}^=}P_{C_{6,1}^=}$$

$$+ K_{C_{6,2}^=}P_{C_{6,2}^=} + K_{C_{6,3}^=}P_{C_{6,3}^=} + K_{C_8H_{10,1}}P_{C_8H_{10,1}} + K_{C_8H_{10,2}}P_{C_8H_{10,2}})$$

Hence,

$$C_V = \frac{C_t(Cu)}{X} \text{ for empty sites of Cu}$$

Total active sites on zeolite:

$$C_t(acid) = C_V + C_{H_2O*} + C_{BDO*} + C_{MEK*} + C_{2\text{-butanol}*} + C_{2\text{-butene}*} + C_{2\text{-methylpropanal}*} + C_{isobutanol*} + C_{isobutene*}$$

$$+ C_{C_{8,1}^=*} + C_{C_{8,2}^=*} + C_{C_{8,3}^=*} + C_{C_3^=*} + C_{C_{5,1}^=*} + C_{C_{5,2}^=*} + C_{C_{5,3}^=*} + C_{C_2^=*} + C_{C_{6,1}^=*} + C_{C_{6,2}^=*} + C_{C_{6,3}^=*} + C_{C_8H_{10,1}*} + C_{C_8H_{10,2}*}$$

$$+ C_{N_2*} + C_{H*} + C_{2,3\text{-butanedione}*} + C_{acetoin*}$$

$$C_t(acid) = C_V + \frac{P_{H2O}C_V}{K_{3W}} + K_{3A}P_{BDO}C_V + \frac{P_{MEK}C_V}{K_{3D}} + K_{7A}P_{2\text{-butanol}}C_V + \frac{P_{2\text{-butene}}C_V}{K_{7D}} + \frac{P_{2\text{-methylpropanal}}C_V}{K_{4D}}$$

$$+ K_{8A}P_{isobutanol}C_V + \frac{P_{isobutene}C_V}{K_{8D}} + \frac{P_{C_{8,1}^=}C_V}{K_{9D}} + \frac{P_{C_{8,2}^=}C_V}{K_{10D}} + \frac{P_{C_{8,3}^=}C_V}{K_{11D}} + \frac{P_{C_3^=}C_V}{K_{17D}} + \frac{P_{C_{5,1}^=}C_V}{K_{17DE}} + \frac{P_{C_{5,2}^=}C_V}{K_{18DE}} + \frac{P_{C_{5,3}^=}C_V}{K_{19DE}}$$

$$+ \frac{P_{C_2^=}C_V}{K_{20D}} + \frac{P_{C_{6,1}^=}C_V}{K_{20DE}} + \frac{P_{C_{6,2}^=}C_V}{K_{21DE}} + \frac{P_{C_{6,3}^=}C_V}{K_{22DE}} + \frac{P_{C_8H_{10,1}}C_V}{K_{14D}} + \frac{P_{C_8H_{10,,2,1}}C_V}{K_{23D}} + \frac{P_{C_8H_{10,,2,2}}C_V}{K_{24D}} + \frac{P_{C_8H_{10,,2,3}}C_V}{K_{25D}} + K_N P_{N_2}C_V$$

$$+ \sqrt{\frac{P_{H2}}{K_{14H}}}C_V + K_{2,3\text{-butanedione}}P_{2,3\text{-butanedione}}C_V + K_{acetoin}P_{acetoin}C_V$$

$$C_V = \cfrac{C_t(\text{acid})}{\left(1 + \cfrac{P_{H2O}}{K_{3W}} + K_{3A}P_{BDO} + \cfrac{P_{MEK}}{K_{3D}} + K_{7A}P_{\text{2-butanol}} + \cfrac{P_{\text{2-butene}}}{K_{7D}} + \cfrac{P_{\text{2-methylpropanal}}}{K_{4D}} \\ + K_{8A}P_{\text{isobutanol}} + \cfrac{P_{\text{isobutene}}}{K_{8D}} + \cfrac{P_{C_{8,1}^=}}{K_{9D}} + \cfrac{P_{C_{8,2}^=}}{K_{10D}} + \cfrac{P_{C_{8,3}^=}}{K_{11D}} + \cfrac{P_{C_3^=}}{K_{17D}} + \cfrac{P_{C_{5,1}^=}}{K_{17DE}} + \cfrac{P_{C_{5,2}^=}}{K_{18DE}} + \cfrac{P_{C_{5,3}^=}}{K_{19DE}} \\ + \cfrac{P_{C_2^=}}{K_{20D}} + \cfrac{P_{C_{6,1}^=}}{K_{20DE}} + \cfrac{P_{C_{6,2}^=}}{K_{21DE}} + \cfrac{P_{C_{6,3}^=}}{K_{22DE}} + \cfrac{P_{C_8H_{10,1}}}{K_{14D}} + \cfrac{P_{C_8H_{10,,2,1}}}{K_{23D}} + \cfrac{P_{C_8H_{10,,2,2}}}{K_{24D}} + \cfrac{P_{C_8H_{10,,2,3}}}{K_{25D}}K_N P_{N_2} \\ + \sqrt{\cfrac{P_{H2}}{K_{14H}}} + K_{\text{2,3-butanedione}}P_{\text{2,3-butanedione}} + K_{\text{acetoin}}P_{\text{acetoin}}\right)}$$

To be simple, on acid site:

$$Y = 1 + \cfrac{P_{H2O}}{K_{3W}} + K_{3A}P_{BDO} + \cfrac{P_{MEK}}{K_{3D}} + K_{7A}P_{\text{2-butanol}} + \cfrac{P_{\text{2-butene}}}{K_{7D}} + \cfrac{P_{\text{2-methylpropanal}}}{K_{4D}}$$

$$+ K_{8A}P_{\text{isobutanol}} + \cfrac{P_{\text{isobutene}}}{K_{8D}} + \cfrac{P_{C_{8,1}^=}}{K_{9D}} + \cfrac{P_{C_{8,2}^=}}{K_{10D}} + \cfrac{P_{C_{8,3}^=}}{K_{11D}} + \cfrac{P_{C_3^=}}{K_{17D}} + \cfrac{P_{C_{5,1}^=}}{K_{17DE}} + \cfrac{P_{C_{5,2}^=}}{K_{18DE}} + \cfrac{P_{C_{5,3}^=}}{K_{19DE}}$$

$$+ \cfrac{P_{C_2^=}}{K_{20D}} + \cfrac{P_{C_{6,1}^=}}{K_{20DE}} + \cfrac{P_{C_{6,2}^=}}{K_{21DE}} + \cfrac{P_{C_{6,3}^=}}{K_{22DE}} + \cfrac{P_{C_8H_{10,1}}}{K_{14D}} + \cfrac{P_{C_8H_{10,,2,1}}}{K_{23D}} + \cfrac{P_{C_8H_{10,,2,2}}}{K_{24D}} + \cfrac{P_{C_8H_{10,,2,3}}}{K_{25D}}K_N P_{N_2}$$

$$+ \sqrt{\cfrac{P_{H2}}{K_{14H}}} + K_{\text{2,3-butanedione}}P_{\text{2,3-butanedione}} + K_{\text{acetoin}}P_{\text{acetoin}}$$

Hence,

$$C_V = \frac{C_t(\text{acid})}{Y} \text{ for empty acid sites}$$

Reaction rate of each species:

$$r_{BDO} = \frac{dF_{BDO}}{dW} = -r_{1s} - r_{3s} - r_{4s}$$

$$r_{acetoin} = \frac{dF_{acetoin}}{dW} = r_{1s} - r_{2s}$$

$$r_{MEK} = \frac{dF_{MEK}}{dW} = r_{3s} - r_{5s} - 2r_{14s}$$

$$r_{2\text{-methylpropanal}} = \frac{dF_{2\text{-methylpropanal}}}{dW} = r_{4s} - r_{6s}$$

$$r_{2\text{-butanol}} = \frac{dF_{2\text{-butanol}}}{dW} = r_{5s} - r_{7s}$$

$$r_{isobutanol} = \frac{dF_{isobutanol}}{dW} = r_{6s} - r_{8s}$$

$$r_{2\text{-butene}} = \frac{dF_{2\text{-butene}}}{dW} = r_{7s} - r_{10s} - 2r_{11s} - r_{24s} - 2r_{25s}$$

$$r_{isobutene} = \frac{dF_{isobutene}}{dW} = r_{8s} - 2r_{9s} - r_{10s} - 2r_{23s} - r_{24s}$$

$$r_{C_{8,1}^=} = \frac{dF_{C_{8,1}^=}}{dW} = r_{9s} - r_{17s} - r_{20s}$$

$$r_{C_{8,2}^=} = \frac{dF_{C_{8,2}^=}}{dW} = r_{10s} - r_{18s} - r_{21s}$$

$$r_{C_{8,3}^=} = \frac{dF_{C_{8,3}^=}}{dW} = r_{11s} - r_{19s} - r_{22s}$$

$$r_{C_3^=} = \frac{dF_{C_3^=}}{dW} = r_{17s} + r_{18s} + r_{19s}$$

$$r_{C_{5,1}^=} = \frac{dF_{C_{5,1}^=}}{dW} = r_{17s}$$

$$r_{C_{5,2}^=} = \frac{dF_{C_{5,2}^=}}{dW} = r_{18s}$$

$$r_{C_{5,3}^=} = \frac{dF_{C_{5,3}^=}}{dW} = r_{19s}$$

$$r_{C_2^=} = \frac{dF_{C_2^=}}{dW} = r_{20s} + r_{21s} + r_{22s}$$

$$r_{C_{6,1}^=} = \frac{dF_{C_{6,1}^=}}{dW} = r_{20s}$$

$$r_{C_{6,2}^=} = \frac{dF_{C_{6,2}^=}}{dW} = r_{21s}$$

$$r_{C_{6,3}^=} = \frac{dF_{C_{6,3}^=}}{dW} = r_{22s}$$

$$r_{2,3\text{-butanedione}} = \frac{dF_{2,3\text{-butanedione}}}{dW} = r_{2s}$$

$$r_{C_8H_{10,1}} = \frac{dF_{C_8H_{10,1}}}{dW} = r_{14s}$$

$$r_{C_8H_{10,2}} = \frac{dF_{C_8H_{10,2}}}{dW} = r_{23s} + r_{24s} + r_{25s}$$

$$r_{H_2} = \frac{dF_{H_2}}{dW} = r_{1s} + r_{2s} - r_{5s} - r_{6s} + r_{14s} + 3r_{23s} + 3r_{24s} + 3r_{25s}$$

$$r_{H_2O} = \frac{dF_{H_2O}}{dW} = r_{3s} + r_{4s} + r_{7s} + r_{8s} + 2r_{14s}$$

Table C.1. All parameters from kinetic model.

Parameter	value	unit	parameter	value	unit	parameter	value	unit
k_1	43.10104	mol g^{-1} h^{-1} atm^{-1}	k_9	0	mol g^{-1} h^{-1} atm^{-2}	$1/K_{21P}$	0	atm^{-1}
$1/K_{1P}$	0.304385	atm^{-1}	$1/K_{9P}$	0	atm	$1/K_{21DE}$	0	atm^{-1}
$1/K_{1H}$	6.36E-05	atm^{-1}	$1/K_{9D}$	0	atm^{-1}	k_{22}	18.25801	mol g^{-1} h^{-1} atm^{-1}
K_{1A}	5.605659	atm^{-1}	k_{10}	6.163616	mol g^{-1} h^{-1} atm^{-2}	$1/K_{22P}$	40.93294	atm^{-1}
$1/K_{1D}$	0	atm^{-1}	$1/K_{10P}$	0	atm	$1/K_{22DE}$	0	atm^{-1}
k_2	54.51339	mol g^{-1} h^{-1} atm^{-1}	$1/K_{10D}$	0	atm^{-1}	k_{23}	0	mol g^{-1} h^{-1} atm^{-2}
$1/K_{2P}$	23.74628	atm^{-1}	k_{11}	2.635312	mol g^{-1} h^{-1} atm^{-2}	$1/K_{23P}$	0.33766	atm^{-2}
$1/K_{2D}$	1.127515	atm^{-1}	$1/K_{11P}$	0	atm	$1/K_{23D}$	0	atm^{-1}
k_3	82.50866	mol g^{-1} h^{-1} atm^{-1}	$1/K_{11D}$	0	atm^{-1}	k_{24}	0	mol g^{-1} h^{-1} atm^{-2}
$1/K_{3P}$	0.025904	atm^{-1}	k_{14}	710.507	mol g^{-1} h^{-1} atm^{-2}	$1/K_{24P}$	0	atm^{-2}
$1/K_{3W}$	2.02E-05	atm^{-1}	$1/K_{14P}$	9.055932	atm^{-2}	k_{25}	44.24195	mol g^{-1} h^{-1} atm^{-2}
K_{3A}	141.6312	atm^{-1}	$1/K_{14D}$	75.70594	atm^{-1}	$1/K_{25P}$	0	atm^{-2}
$1/K_{3D}$	0	atm^{-1}	$1/K_{14H}$	1.09E-05	atm^{-1}	$K_{C8,1}$	0	atm^{-1}
k_4	21.98574	mol g^{-1} h^{-1} atm^{-1}	K_{N2}	0.08277	atm^{-1}	$K_{C8,2}$	0	atm^{-1}
$1/K_{4P}$	0	atm^{-1}	K_N	0.020756	atm^{-1}	$K_{C8,3}$	0	atm^{-1}
$1/K_{4D}$	0	atm^{-1}	$K_{2\text{-butene}}$	0.291904	atm^{-1}	K_{C3}	0	atm^{-1}
k_5	51.78992	mol g^{-1} h^{-1} atm^{-2}	$K_{isobutene}$	0	atm^{-1}	$K_{C5,1}$	0	atm^{-1}
$1/K_{5P}$	20.1326	atm	k_{17}	1E-09	mol g^{-1} h^{-1} atm^{-1}	$K_{C5,2}$	0	atm^{-1}
K_{5A}	0.570833	atm^{-1}	$1/K_{17P}$	1.346166	atm^{-1}	$K_{C5,3}$	40.9526	atm^{-1}
$1/K_{5D}$	0	atm^{-1}	$1/K_{17D}$	0	atm^{-1}	K_{C2}	0	atm^{-1}
k_6	10.50697	mol g^{-1} h^{-1} atm^{-2}	$1/K_{17DE}$	0	atm^{-1}	$K_{C6,1}$	0	atm^{-1}
$1/K_{6P}$	0.074096	atm	k_{18}	1E-09	mol g^{-1} h^{-1} atm^{-1}	$K_{C6,2}$	0	atm^{-1}
K_{6A}	13.33063	atm^{-1}	$1/K_{18P}$	0	atm^{-1}	$K_{C6,3}$	4.668586	atm^{-1}

Parameter	Value	Units	Parameter	Value	Units	Parameter	Value	Units
$1/K_{6D}$	0.487861	atm^{-1}	$1/K_{18DE}$	0	atm^{-1}	$K_{C8H10,1}$	0	atm^{-1}
k_7	112.0948	$mol\ g^{-1}\ h^{-1}\ atm^{-1}$	k_{19}	33.57124	$mol\ g^{-1}\ h^{-1}\ atm^{-1}$	$K_{C8H10,2}$	0	atm^{-1}
$1/K_{7P}$	0.017217	atm^{-1}	$1/K_{19P}$	6.603664	atm^{-1}	K_{H2O}	0.53052	atm^{-1}
K_{7A}	0.983089	atm^{-1}	$1/K_{19DE}$	0	atm^{-1}	$K_{acetoin}$	0	atm^{-1}
$1/K_{7D}$	0.006379	atm^{-1}	k_{20}	0	$mol\ g^{-1}\ h^{-1}\ atm^{-1}$	$K_{2,3\text{-}butanedione}$	0	atm^{-1}
k_8	9.546722	$mol\ g^{-1}\ h^{-1}\ atm^{-1}$	$1/K_{20P}$	0	atm^{-1}	$1/K_{24D}$	0	atm^{-1}
$1/K_{8P}$	0	atm^{-1}	$1/K_{20D}$	0	atm^{-1}	$1/K_{25D}$	0	atm^{-1}
K_{8A}	0	atm^{-1}	$1/K_{20DE}$	0	atm^{-1}			
$1/K_{8D}$	31.41782	atm^{-1}	k_{21}	0	$mol\ g^{-1}\ h^{-1}\ atm^{-1}$			

# Appendix D - Supporting information for Chapter 4
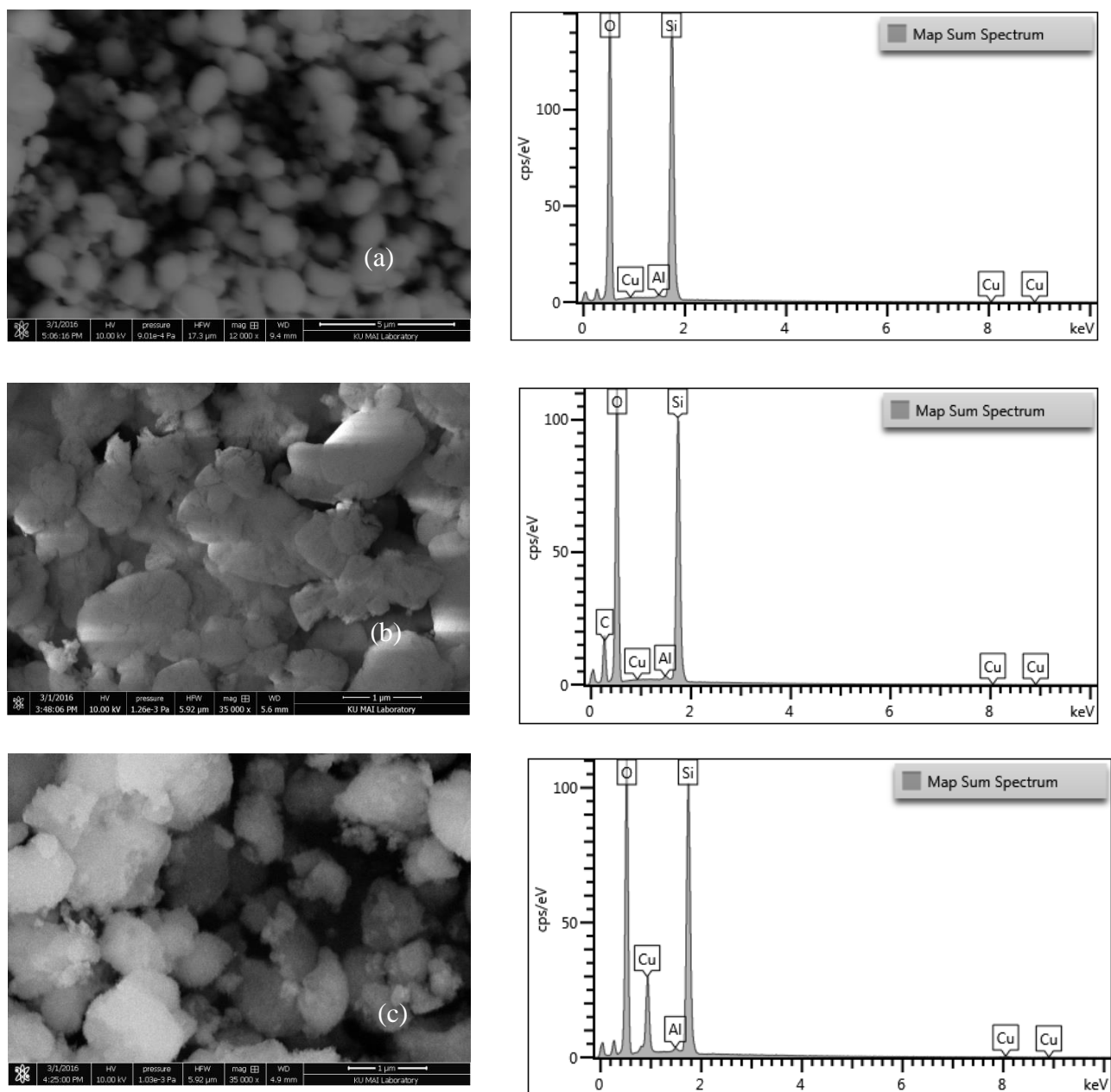
Figure D.1. SEM images and EDS of ZSM-5(280), meso-ZSM-5(280) and Cu/meso-ZSM-5(280). (a) ZSM-5(280); (b) meso-ZSM-5(280); (c) Cu/ZSM-5(280).

Table D.1. EDS result of HZSM-5(280), meso-ZSM-5(280) and Cu/meso-ZSM-5(280).

Sample	Weight percent (%)				Molar ratio
	Al	Si	O	Cu	Si/Al_2O_3
HZSM-5(280)	0.32	47.43	52.25	–	284.8
meso-ZSM-5(280)	0.49	45.96	53.55	–	186
Cu/meso-ZSM-5(280)	0.39	38.17	41.46	19.98	188

From EDS result (**Table D.1**), we can see the Al content increased slightly in the meso-ZSM-5(280), and the molar ratio of SiO_2/Al_2O_3 was decreased from 284.8 to 186, possibly due to the partial desilication during the NaOH treatment (the content of Si decreased slightly from 47.43% to 45.96%).
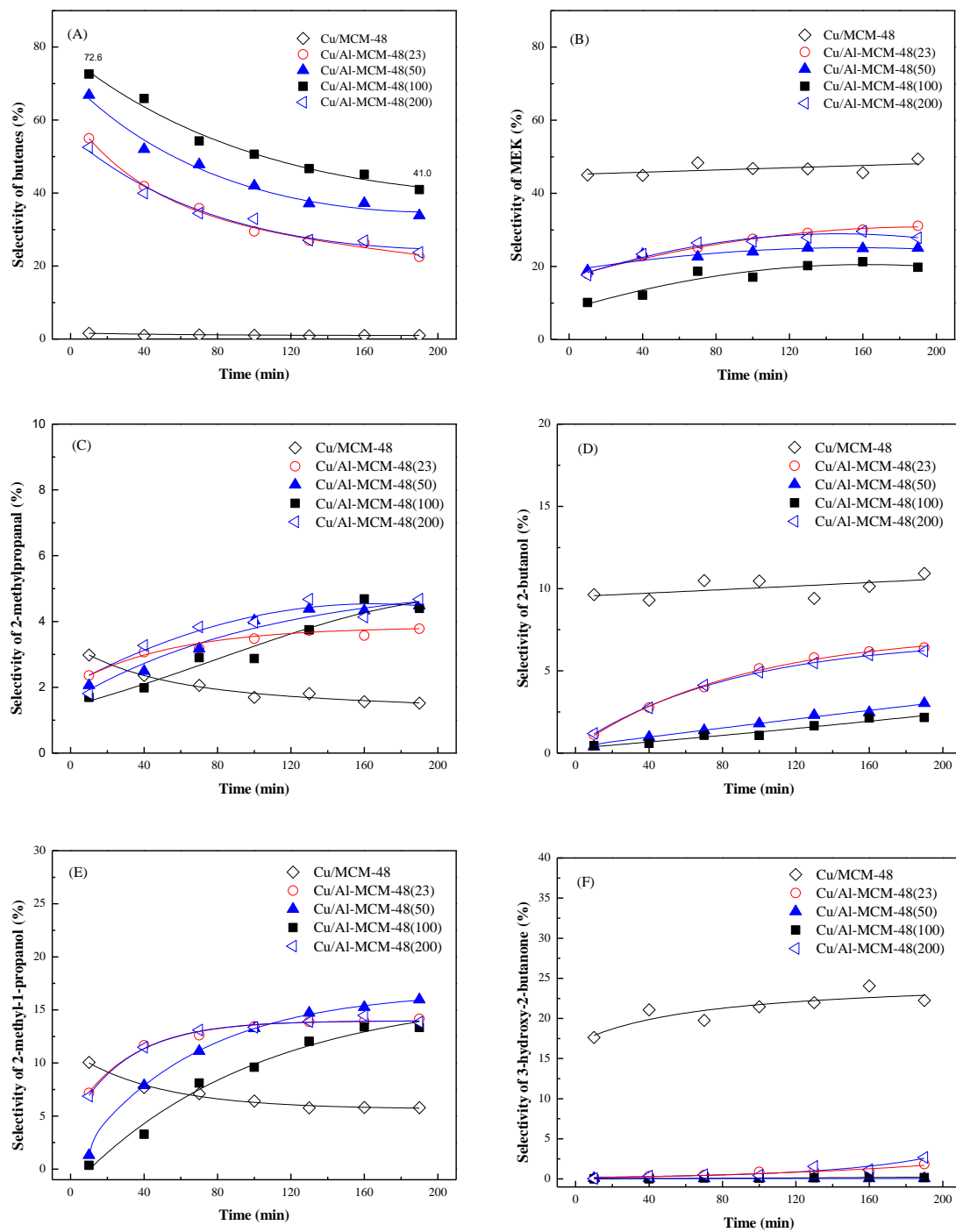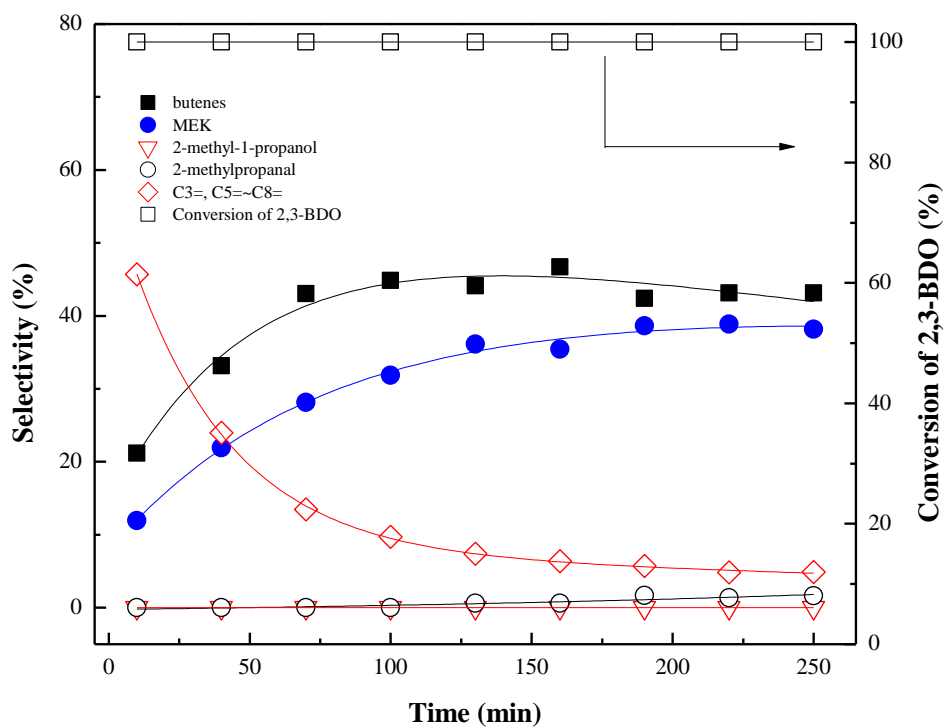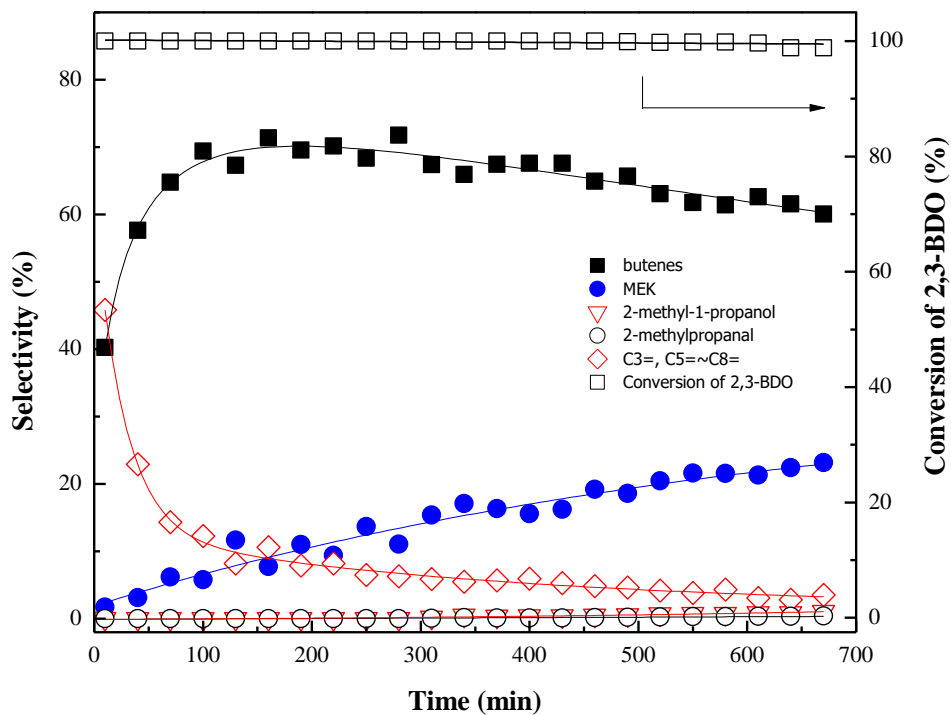
Figure D.2. Catalytic results as a function of time on stream for the conversion of 2,3-butanediol over reduced copper supported on Al-MCM-48 with different SiO$_2$/Al$_2$O$_3$. Reaction conditions: feed rate of 2,3-butanediol, 3.0 mL/h; catalyst weight, 1.0g; H$_2$/2,3-BDO, 5:1; temperature, 250 ^{o}C.
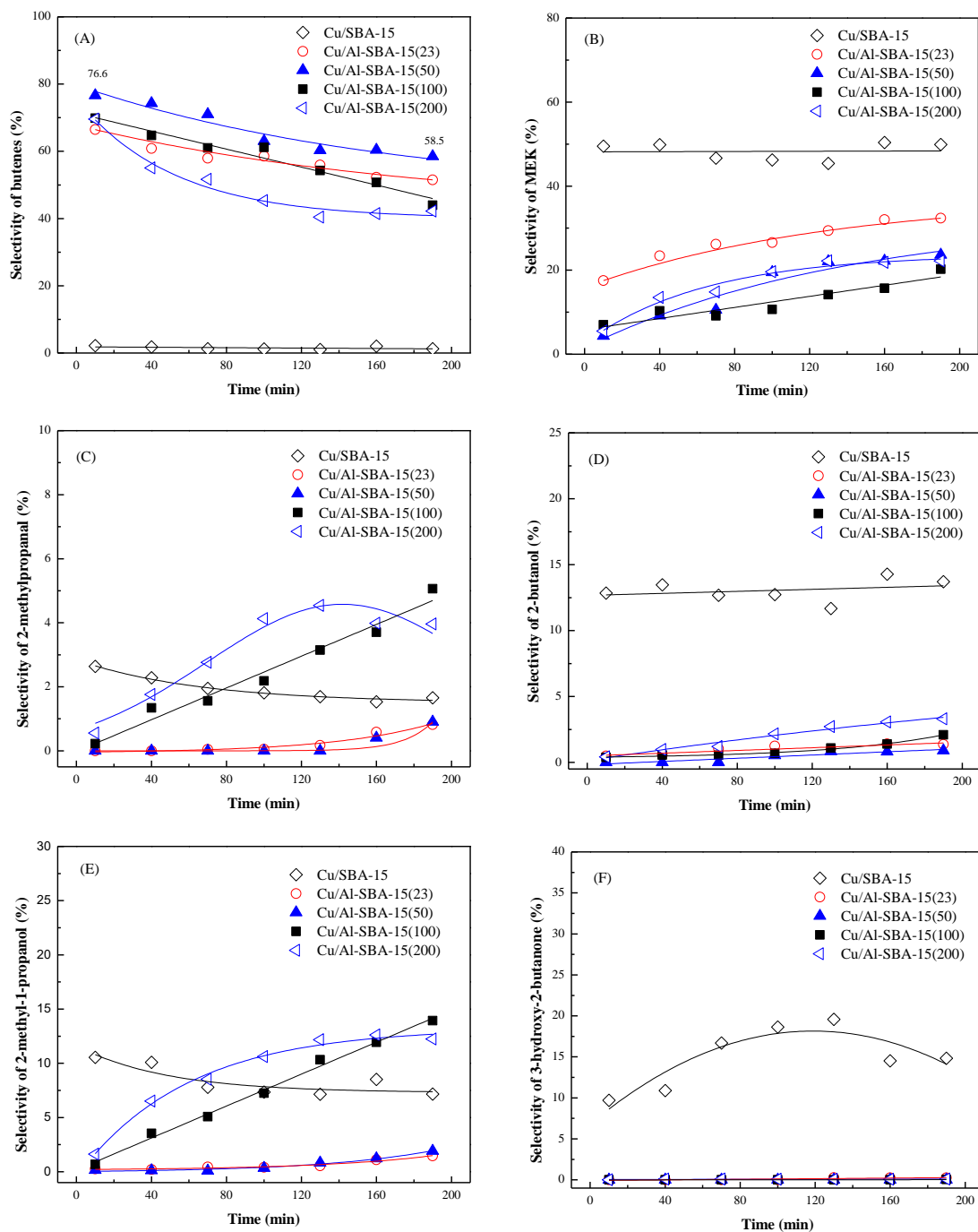
Figure D.3. Catalytic results as a function of time on stream for the conversion of 2,3-butanediol over reduced copper supported on SBA-15 with different SiO_2/Al_2O_3. Reaction conditions: feed rate of 2,3-butanediol, 3.0 mL/h; catalyst weight, 1.0g; H_2/2,3-BDO, 5:1; temperature, 250 ^{o}C.

Figure D.4. Catalytic results as a function of time on stream for the conversion of 2,3-butanediol over reduced copper supported on mesoporous ZSM-5(50). Reaction conditions: feed rate of 2,3-butanediol, 3.0 mL/h; catalyst weight, 1.0g; H_2/2,3-BDO, 5:1; temperature, 250 ^{o}C.
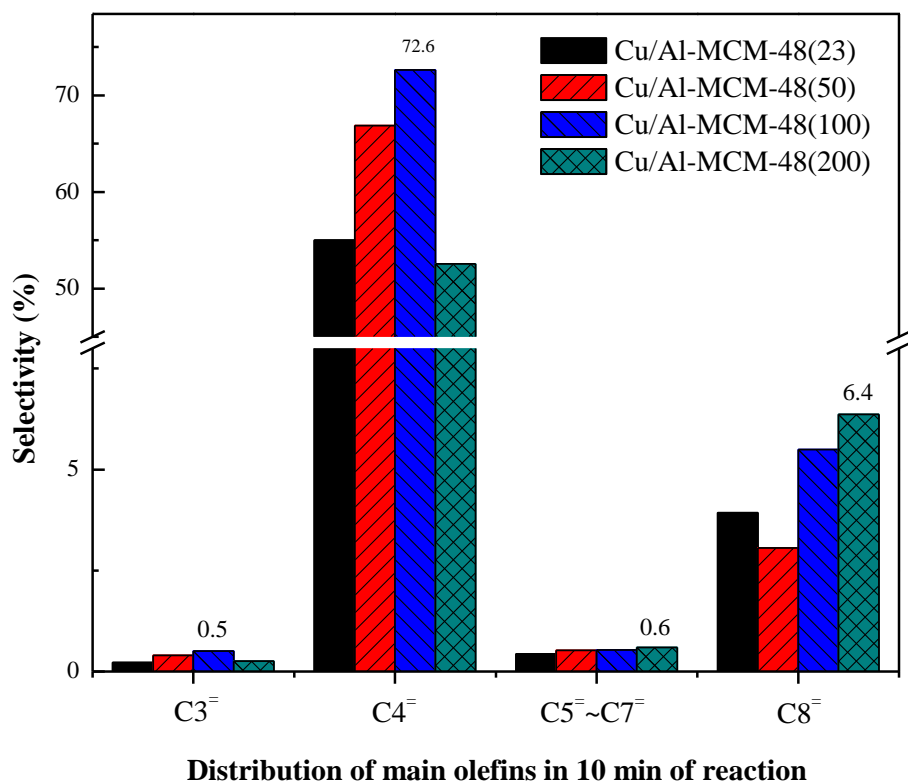
Figure D.5. Catalytic results as a function of time on stream for the conversion of 2,3-butanediol over reduced copper supported on mesoporous ZSM-5(280). Reaction conditions: feed rate of 2,3-butanediol, 3.0 mL/h; catalyst weight, 1.0g; H_2/2,3-BDO, 5:1; temperature, 250 ^{o}C.

Figure D.6. Comparison of selectivities of $C3^=$, $C4^=$, $C5^=-C7^=$ and $C8^=$ at initial 10 min over Cu/Al-MCM-48 with different SiO_2/Al_2O_3.
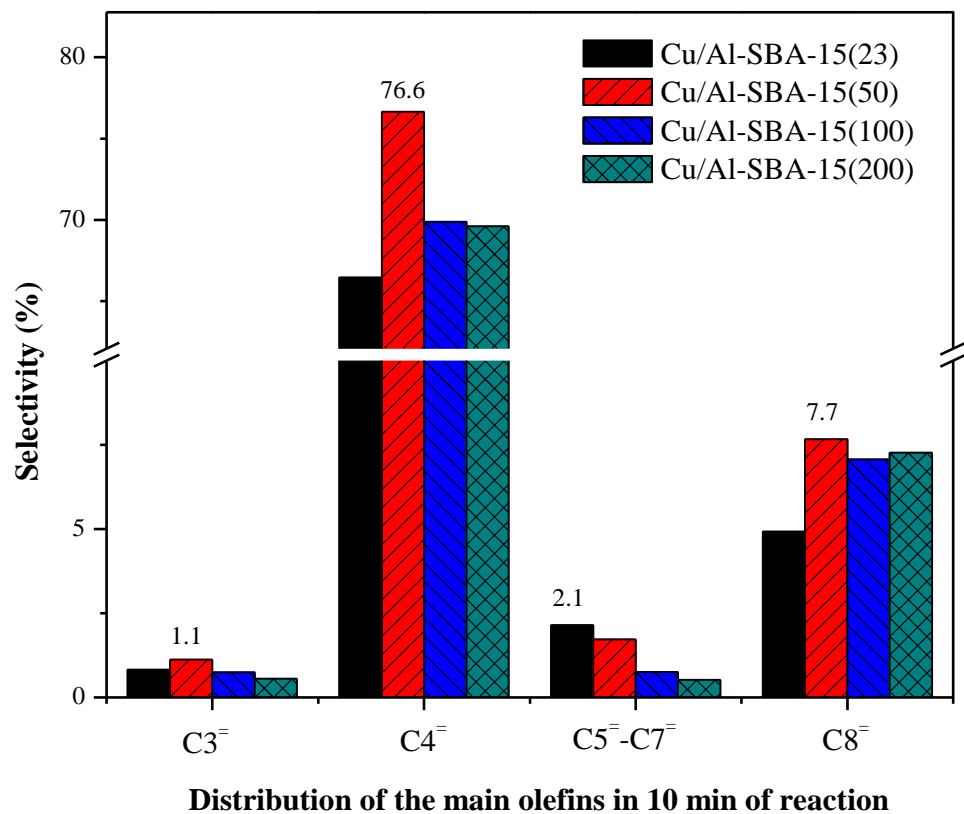
Figure D.7. Comparison of selectivities of $C_3^=$, $C_4^=$, $C_5^=-C_7^=$ and $C_8^=$ at initial 10 min over Cu/Al-SBA-15 with different SiO_2/Al_2O_3.